Resolving and mathematizing energetic gradients that facilitate cytoskeletal self-assembly

Thesis by
Ana Isabel Duarte

In Partial Fulfillment of the Requirements for the
Degree of
Doctor of Philosophy

CALIFORNIA INSTITUTE OF TECHNOLOGY
Pasadena, California

2026
Defended September 9, 2025

Ana Isabel Duarte
ORCID: 0000-0003-3726-3018

ACKNOWLEDGEMENTS

To Rob Phillips: my advisor, my collaborator, my friend

Rob, exactly six years ago from my defense date, September 9, 2019, you said the words that commenced my Caltech experience. I remember the sentiment vividly. It was the first minutes of bootcamp and you welcomed all of us saying how lucky you felt to be with us. This struck me as especially odd since we were a gaggle of students you had never met. You also said that we should remember how lucky we are too. It is a privilege, which you urged us not to forget, to be surrounded by talented colleagues in a place that holds significant scientific legacy. Every day of the eight-day bootcamp, you began by repeating to us how lucky you felt to be endeavoring in science together. I have not forgotten, and Rob, I must tell you I am the most lucky. I feel fortunate to have spent my graduate studies at Caltech; but much more than this, it is a true honor to work alongside you.

When I joined your group, I knew you did premier science, but I really had no idea how exceptional of a mentor you would be. While simultaneously being extremely rigorous with high expectations, it is evident that you care deeply about your students as people. In fact, I know you consider us your collaborators rather than your students. I did not realize how seriously you meant this until halfway through my PhD journey.

But first, I will make a digression. Once, you told me you love when students reach their "3rd year cry," the time when people start to break down and have the scary realization that nobody can save them but themselves. For me, graduate school has been a rollercoaster, and I definitely experienced setbacks, which I know you know. You were right that I had to do the work to get back up again. But every time I fell, you were beside me offering me a hand. You have my full trust and for that I thank you. With each of these moments, you viewed me as an individual and found the places I needed to grow. You taught me the value of "bloody drills for bloodless battles," a mantra I intend to uphold.

I am not sure why it took me so long to internalize and embrace the trust and confidence you had in me, which you offered each day of my time with you at the lab. I know self-doubt played a part, but perhaps I was too focused and preoccupied with the many road bumps along the way, doubting my ability to overcome them. All the while I missed your subtle, but concrete support of me. I am embarrassed to

admit it took a while for it all to click with me. But you never wavered, your support was constant. It started to click with me after Biarritz. This is when I realized how genuinely you wanted me to see myself as working "with" you and not "for" you. I recall the moment you said you wanted to do the N-dimensional sphere lesson in Marseille. You then asked me not only to create the lesson plan for the next day's session, but you also asked me to teach it to the class. For anyone who is in your orbit, it is patently obvious how much you value teaching. You would not hand over a teaching assignment to someone who would undermine your teaching philosophy, especially among your colleagues. In this moment, you believed in me more than I did and pushed me to my full potential. Thank you for this. I am deeply honored each time you ask for feedback from me, whether it is on grants or my thoughts on how to navigate teaching in the modern age, or when you assign tasks to me that are important to you, or when you trust me to give a presentation on the spot, etc. I hope in the years to come I show up for you often and repay you for all you have done for me.

There are many lessons I've learned from you over the course of my time at Caltech. Here are a few that resonate most with me and have become daily mantras throughout my graduate studies. Let's start with "little steps for little feet." This idea felt revolutionary to me, especially as a young scientist. One would think that hitting a home run was required in all experiments at Caltech. But your philosophy about taking small, manageable actions to achieve a larger goal was far more productive, reliable, and meaningful. Looking back, I see how much of a difference these small steps made when looking at our work at its full scale. Without these minute steps, one cannot fully understand or answer larger complexities.

Next, I value your scientific skepticism that allows us to have trust in the work we do, but that also require us to verify our work, repeatedly. You talk about how flight crews say "arm and cross check," ensuring that the doors are in fact closed. Your work and your expectations for us is no different. I admire that your rigorous standards cannot be surpassed, which ultimately means that our work can be trusted and relied upon by all.

I also appreciate how much you value multidisciplinary collaboration varying scientific approaches. It does not matter if the discipline is rooted in biology, physics, or somewhere else, or whether the perspective is coming from theoretical or experimental applications. What matters to you is achieving greater understanding of our work by growing and expanding our knowledge baseline. For instance, when

I first joined the group, I did not immediately appreciate the benefit of having so many visitors to the lab. But over time, I realized how useful it was to have ongoing exchanges with guests from different parts of the world with varying scientific backgrounds. It certainly broadened my knowledge and enhanced my work.

Of course, these multidisciplinary collaborations, which seemed so frequent, were terrifying to me because it also meant that I, along with my lab mates, would have to exchange our ideas, concepts, and processes about our work with our guests. I now know all of this was part of your "bloody drills for bloodless battles" philosophy. Each time we did these events we were perfecting our craft. And I grew as a person. Through presentations, talks, and meetings with scientists from all over the world, I gained experience in collaboration and confidence in my ability to exchange ideas with others. This is inspiring to me as I move forward because you have taught me that the answers we seek can be found in places beyond our walls.

This brings me to the way you run our group. You often emphasize iterations over perfection, which is a subject I frequently struggle with. I want everything to be perfect, but you have shown me that repetition, restatements, tryouts, reiterations, etc., lead to better results in the long run. At a personal level, you have helped me to let go of perfection and encouraged me to seek and accept help from others. It is true that everything feels a little more approachable and doable when perfection is not in the way.

I also appreciate the way you have instilled in our group that kindness is superior to unconstructive criticism, teaching us to be lovers not haters. You have shown us how to be critical, but never at the expense of shutting down creativity, input, or collaboration. You value science as a team sport and it has been exciting playing the sport on your team.

Finally, I turn away from these preceding professional notes to underscore how much I admire you as a person. One thing that is true to me about you is your insatiable curiosity and your sense of wonderment. This is at the core of who you are. You constantly seek adventures, explore the world, and appreciate the beauty of the natural world. You made it a point to share some magical moments with us, like bringing us within stroking distance of dolphins deep off the coast of Long Beach, taking us to Mount Wilson to closely view the planets, stars, and galaxies, encouraging us to fully explore different cultures as we traveled abroad to teach at European universities, and simply making time for group hikes for comradery while learning about the geology around us. You are a true naturalist at heart. Your

curiosity and excitement are contagious. It reminds me of the reasons I am drawn to the world of science.

Your resiliency as a human inspires me, encouraging me to keep climbing because all things are possible. You have taught me to be confident and to stay on course when the going gets tough. Rob, I have absorbed all your lessons like a sponge. Your philosophies are now integrated in my ethos. I will carry all your teachings forward in my career so that others will continue to benefit from your work. Let the Phillips legacy live on.

Thank you for doing floor stretches with me in between teaching 12-hour long classes abroad while jet-lagged.

Thank you for the pranks you pull at the lab and the way you giggle and shrug, reminding us to not take things so seriously.

Thank you for making science exciting and a place filled with possibility.

Thank you for all the fun moments we have shared.

Thank you for being you.

To my committee

I am very thankful for my thesis committee, Professors Matt Thomson, Dave Hsieh, and Ryan Patterson for ushering me through my PhD program. Your participation in my candidacy exam was transformative and affirming of my quest to become a member of the scientific community. I felt challenged but supported. While your questions at times stretched my capacity to find satisfactory answers, I felt your desire to help me develop into a scientist. You were there to launch me, not stump me. Thank you for fostering a safe, curious, and exciting environment. I left the exam with more confidence and re-energized for my research.

I also want to thank each of you individually:

Matt, thank you for your abundance of enthusiasm. You have always been encouraging, especially when I first joined the active matter coalition. Your creativity inspires me to push scientific boundaries. I really valued when we did joint group meetings and left discussions with you highly motivated.

Dave, thank you for going above and beyond to make yourself present in my milestone degree checkpoints. Your dedication to students is admirable, and should I secure a faculty position someday, I hope to model this. To this end, I am grateful for

your advocacy work supporting minority physicists. Seeing you running events like Future have made me feel very included at Caltech.

Ryan, I am very appreciative of your willingness to transcend departmental boundaries and engage with me over biophysics. I was very impressed by the deep questions you asked me during my candidacy, despite my work being unrelated to your group's research. Your perspectives were thus uniquely valuable in my project's progress which I thank you for.

To my labmates, collaborators, and mentees

Thank you for walking with me through this journey. I am deeply appreciative for how encouraging and spirited you all are.

I wish to especially thank my project collaborators: Rob Phillips, Gabriel L. Salmon, Heun Jin Lee, Soichi Hirokawa, Rachel A. Banks, Amin Tajik, Minakshi Ashok, Henk Postma, Matt Thomson, and Bibi Najma.

Additionally, I am thankful for all my labmates over past six years: Bill Ireland, Niko McCarty, Muir Morrison, Griffin Chure, Suzy Beeler, Vahe Galstyan, Manuel Razo, Scott Saunders, Rachel A. Banks, Grace Solini, Soichi Hirokawa, Avi Flamholz, Bibi Najma, Gabriel L. Salmon, Rebecca Rousseau, Tom Röschinger, Kian Faizi, Rosalind Pan, Minakshi Ashok, Sara Mahdavi, Mohammadamin Tajik, and Doran Sekaran.

And, I had the great opportunity to mentor four talented students: Victor Gomez, Catherine Ji, Maya Martinez Lurvey, and Sophia Parker. Thank you all for helping me discover my passion for teaching and mentorship.

I would like to express further gratitude to several of these members who have especially impacted my time at Caltech.

Heun Jin Lee: Thank you for the wisdom you have imparted over the years. I admire your diligence and stubbornness in the lab and aspire to take this forward with me.

Rachel Banks: You are so confident, brave and determined. I have looked up to you since my first day in grad school and try to emulate these characteristics, which I learned from you. I am grateful for all the laughs we have shared along the way.

Soichi Hirokawa: Thank you for always being the butt of everyone's jokes! Your good natured spirit made day to day life so fun. You are also an incredible teacher and someone I feel lucky to have been mentored by. I hope to see you in Connecticut soon.

Gabriel "Lucifer" Salmon: As you always say, I am thankful to be co-conspirators with you in both science and life. I feel privileged to have gone on so many adventures with you. You are always a sounding board for me and are constantly ready to provide chocolate and back scratchy hugs. My first day at Caltech, during prospective visit days, I saw you deliver a beautiful group meeting. I was in such awe of you then and am still in awe of you today! I cannot wait to see all you will do.

Amin Tajik: In many ways I think of you as an older brother. You are deeply caring and always look out for me. You also have been a shoulder to cry on and a friend who picks me up after a hard day. Thank you for your endless enthusiasm and love.

Tom Röschinger: You are a nucleation point for us as a group. When things feel disjoint, you always find ways to bring us together. Thank you for always baking me a birthday cake and finding ways to make me smile.

Sara Mahdavi: Thank you for the many chaotic adventures. I will never forget running through Minneapolis together. You're ability to roll with the punches is highly impressive! I've also loved being your office mate and experiencing your quick wit, which always brings a laugh.

Minakshi Ashok: You have grown so much in the past three years and I am proud to have seen it. I especially admire all the work you have done to be the truest version of yourself. I am very inspired by this.

To my friends

Adam Shaw: You always bring the RUCKUS! You have made really gloomy days at Caltech happy ones. Thank you for always being ready for shenanigans.

Jane Wu: Its been a treat becoming your friend AND your bridesmaid! I love how quick you are to laugh and how you don't take life too seriously. A moment that really stuck with me is when the bustle on your wedding dress came undone and the train fell in some mud. You said "its ok, let's just dance and have fun." It was such a good reminder to me to focus on the important moments and people in life.

Brian Lee: I did not ever think we would be friends and I am so so glad I was wrong. I realize now how deeply you care about the people you love. I also admire your candidness and know you will tell me exactly what you think. This makes me really trust you. I am touched that I made it into your circle and am so excited to live closer to you soon!

Andreas Butler: You are possibly the quirkiest person I know, which is something I adore about you. While your crazy hypotheticals are very comedic, they also challenge me to think in new ways. Your creativity radiates through the group. I have also realized what a loyal friend you are. Thank you for showing up both consistently and when it is important. You bring much joy into my life.

Steven Stradley: Thank you for embracing me into your sphere. It has been a treat to explore the arts in LA with you. Thank for being a glue keeping David's Disciples together. You fastidiousness has led to a really special family for me in California.

Colin Morrell: Thank you for letting me crack your shell and become your friend! I have loved growing closer to you and spending time together at Pilates, cooking, and hiking. I also admire how you have navigated anxiety in grad school. Your confidence abounds now and I am very motivated by it.

Hannah Manetsch: You care so deeply about people. I feel I can tell you anything without you judging me. I hope you know you can do the same with me. Being your friend has been one of the biggest treats in all of grad school. You bring an abundance of love and light to my world. Also, I admire the grace with which you navigated challenges at Caltech. I am so inspired by you.

Madison Howard: You are the ultimate girl's girl! Thank you for radiating positivity. I know I can call you whenever I need a little joy in my day. I love how you find happiness in the small things all around us. I feel honored to be your friend and very sad to be moving far. But, I am very excited for when you will visit me and we can continue our dates.

Kim Pham: Thank you for your constant support! You are always ready to jump in and help whether it be making sure my suit fits perfect or ensuring we make it to Yosemite. You are also so creative, pay attention to the details, and know how to transform something bland into somehing beautiful, both in crafts and in life. Thank you for becoming a dear friend!

Michelle Qian: We have grown a lot together. You are a consistent pillar in my time at Caltech. Thank you for being by my side at my worst and sticking around to see me at my best. I feel grateful for the kindness and love you have consistently shown me. Thank you for so spontaneously asking if I wanted to go to Banff with you and starting a friendship I cherish. I am excited for all the adventures we will continue to have.

André Nicolov: Thank you for being my last friend at UW and my first friend at

Caltech. It is a treat that our journeys have so closely mirrored each other. From being 1/24th of the way there to now being done, I am touched we did it all together. Thank you for being a person I can turn to when I need to decompress. The many hours we have spent sitting in your car have been extremely restorative to me and something I wont forget. And, thank you for always spilling tea with me.

Dan Sokratov: I am glad for how we were able to reconnect in the middle of grad school. There are not many people where after a chunk of time apart you can come back together and still feel close. You are someone I truly believe will stand the test of time as a friend. I am always here for you and know you are here for me too.

Sarah House: You are incredibly brave. I am inspired by how hard you work to make healthy choices when life deals you its worst. Your quest of self improvement motivates me to do the same. I also love spending time with you. Between dancing, eating mango ice, and having deep talks, I cherish you.

Jackie Tessler: My first ever friend, whether our lives are in or out of sync, I love you. I am thankful that we have our whole lives to grow together. You are my pseudo-sister. I miss the days when we lived two blocks away, but am thankful that even when we are apart, you support me and always root for me.

To my family

Robin, Tom, and John: Thank you for embracing me into your family. I have been so comforted to have you so close and know I have people nearby who care for me. The adventures we have shared are major highlights of the past six years and offered a reprieve from the chaos. You are always ready to have fun, but whether it is extravagant or simply playing farkle, I am touched by how you put people first above all else.

Mike and Gretchen: You lead with love and care, things I want to emulate. Upon first visiting you in Kansas, I immediately felt at home. In the spirit of Molly Ellen, each day with you is the best day ever because you know how to make it that way! Your open minds and happy nature brings much joy to my world.

Grandma: I love you and am thankful for all the support you have shared with me throughout my journey. I feel privileged you now live at home and I get to see you more often. Just being in your company eating breakfast and playing cards are moments I treasure.

Abuelita: Muchas gracias por todo tu amor. Yo lo siento todos los días. Hoy te

tengo en mis pensamientos. Abrazos y besos. Te amo muchichichisimo.

Sofie: My beloved pup, thank you for being my study companion and licking my tears when I am sad. I hope you can feel all my love.

To Mommy

Lately, I keep having memories of walking through the woods with you. We would look at nature and you would ask what I was curious about. You instilled in me an innate instinct to wonder, which is of course mission critical for the PhD. You also are such an advocate for equity and inclusion in education, which has made a large impact on me and my worldview. But also, thank you for always reminding me to hold onto my joy, and for being a wealth of happiness in my life. Your silliness is a gift that gives life its color. There is no day that goes by where I don't feel your love. Thank you for always putting me first. I love you.

To Papi

I would not be in physics if it were not for you, so really I owe this whole journey to you. Thank you for dreaming so big that I believed I could achieve anything. Without your relentless love and support, I do not think I would be in a position to earn a PhD. You tell me the hard truths. But, you are always there, with your hand on my back, pushing me up the mountain when I feel I am failing. We are Montañas, mountain people, and we can do hard things. Thank you for helping me see the whole of the moon. I love you.

To Chandler

Thank you for being by my side every step of the way through this journey. We survived two apocalypses and grad school together. It is an honor to have grown with you throughout the last six years. You are the person I cry to, the person I want to celebrate with, and the person I confide in. I hope you feel as much support from me as I have felt from you. Sometimes I catch myself looking at you wondering how I got so lucky. You have made me grow. You taught me how to think the best of people and prioritize relationships. The care I see you pouring into your community motivates me. While your comedic delivery lights up a room, it is not the thing that makes you special to me. I love the way you think. You have a criticality that makes you very discerning; but, you also see style and beauty in the world. You feel deeply and search for experiences that will give you both newer and richer emotional experiences. And, I can see how much you value relationships. You will go to great

lengths to make others smile, often ignoring the cost it has on you. I admire the person you are. It is a gift to have your love. Thank you for always striving to make me happy. Just being around you makes me happy. For all the things that are to come, I cannot wait to do them with you. I love you.

To the women who showed me I could

Sarah Keller: You are so savvy and know how to advocate for yourself in the world of academia. Very frequently I think to myself "what would Sarah do?" You have shown me how you can lead putting people first. Thank you for all the coaching and care you put into my career. I hope to be half the mentor you are and promise to pass the love forward.

Mariana Smit Vega Garcia: The first and only Latina professor I have had, I look up to you greatly. Thank you for the kindness and love you shared with me, especially when I faced my first disappointments in academia. You have shown that this path was possible for me.

Leslayann Schecterson: Thank you for taking such a large chance on me. You made science fun and inspired my love for research. I do not think I would have pursued research as a career had it not been for you.

Tracy Petroske: Thank you for all the days you stayed with me after school trying to help me grasp kinematics. You believed in me when I didn't. I am so grateful to you for imparting your love of physics on me and for the kindness with which you supported me.

PUBLISHED CONTENT AND CONTRIBUTIONS

[1] **Ana Isabel Duarte**, Gabriel L. Salmon, Heun Jin Lee, Bibi Najma, Minakshi Ashok, Soichi Hirokawa, Rachel A Banks, Matt Thomson, and Rob Phillips. "ATP consumption in space and time in microtubule-motor structures." In: *in preparation* (2025).
A.I.D. designed and performed research, contributed new reagents and analytic tools, analyzed data, and wrote the paper.

[2] Gabriel L*. Salmon, **Ana Isabel Duarte***, and Rob Phillips. "Fundamental power requirements to build or maintain biochemical gradients." In: *in preparation* (2025).
A.I.D. co-performed research, data analysis, and cowrote the paper. (*equal contribution).

[3] Soichi Hirokawa, Heun Jin Lee, Rachel A Banks, **Ana Isabel Duarte**, Bibi Najma, Matt Thomson, and Rob Phillips. "Motor-driven microtubule diffusion in a photobleached dynamical coordinate system." In: *Proceedings of the National Academy of Sciences* 122.24 (2025), e2417020122. DOI: 10.1073/pnas.2417020122.
A.I.D. analyzed data and contributed new reagents/analytic tools.

TABLE OF CONTENTS

LIST OF ILLUSTRATIONS

Number *Page*

LIST OF TABLES

Chapter 1

INTRODUCTION

"What work is worth dedicating your twenties to?" This question, oft posed by my thesis advisor, Rob Phillips, has resonated with me throughout my six years at Caltech. After some introspection into the question of what motivates me, I came to an answer that is perhaps pedestrian: I find the unknown compelling. Naivete which creates a sense of magic and awe, attracts me to problems. And then, an accompanying itchiness tied to unresolved questions summons stubbornness. This internal one-two punch makes it easy to devote my twenties to science. But now, we must ask, what is the most unknown problem to invest in.

Of course, we may not agree here; however, I am hard pressed to find something more mystical and more uncharted than the natural world's ability to sustain life. I am far from the first to share this feeling. I would be remiss here if I did not mention the great Erwin Schrödinger, who delivered a series of lectures entitled "What is life?" where he expressed his own fascination, noting "These facts are easily the most interesting that science has revealed in our day." Despite being a founder of the field of quantum mechanics, even he could not escape wondering "how can the events in space and time which take place within the spatial boundary of a living organism be accounted for by physics and chemistry?" [1]. Regardless of their field of study, many of the great thinkers have been intrigued by questions that surround the ability to distinguish living from non-living systems. I present here a very brief sampling of charming stories, that I do not assert are complete, but rather, that give an impression for how long humans have been wondering about the nature of life.

Beginning with Antony van Leeuwenhoek, this Dutch scientist of the late 1600s used a microscope to explore the world inside a drop of rain water. Here, he found what we know today as microbes. He was entranced to find that these little particles inside water could move and change shape, noting "When these *animalcula* or living Atoms did move, they put forth two little horns, continually moving themselves" [2]. Thus began an adventure searching for the animalcula in water collected from different sources and, comedic to the present day reader, collecting infused pepper water with a pepper, due to van Leeuwenhoek's interest in the " pungency of pepper upon our tongue." Examining the different sources, he began tabulating the differences in size,

shape, quantity, swimming speed, and more. Upon reading his correspondence, it is clear van Leeuwenhoek was entranced by the dynamical nature of the animalcula including their motion and ability to bend their shape, which motivated him to consider these tiny specimens as a new part of the phenomena of life.

Precisely 150 years later, Robert Brown published a study motivated by a very similar spirit, watching the motion of pollen grains[3]. As a botanist, tasked with enumerating as many possible species as he could while traveling, Brown became enamored with collecting and observing pollen under his microscope. The lively movement of the grains inspired Brown's initial thought that the grains were living. However, in continuing the examinations of pollen after the source plant had died, he revised his thoughts stating he "expected to find these molecules in all organic bodies: and accordingly on examining the various animal and vegetable tissues, whether living or dead, they were always found to exist." This finding caused Brown to revaluate his notion of what constituted as living and he started exploring the motion of particulates from inanimate sources like glass. Despite finding that these movements occurred in all forms of tiny matter, Brown was still curious how the motions impacted living systems. He "was desirous of ascertaining whether the mobility of the particles existing in organic bodies was in any degree affected by the application of intense heat to the containing substance." Of course, as we know today, heat, or thermal energy, is precisely the driver of diffusion. Yet, this line of questioning is interesting for two reasons: First, despite Brown's identification as a botanist, he found himself forced to ask physical questions of living systems. Second, his studies, nominally about the role of pollen in plants, touch upon the larger theme of what characteristics define matter as living and what processes facilitate life.

Several decades later, Charles Darwin published his revolutionary work, "On the Origin of Species"[4]. Like Brown, throughout his travels, Darwin explored different species and worked to understand their relations. As we well know, he reached the conclusion "that each species had not been independently created, but had descended, like varieties, from other species." In conceptualizing the notion of lineages, Darwin was left wondering about what properties make different types of life unique. He suggested categorizing species by evaluating "whether any form be sufficiently constant and distinct from other forms, to be capable of definition." This led him to take note of the traits that were preserved among living systems noting, "all living things have much in common, in their chemical composition, their

germinal vesicles, their cellular structure, and their laws of growth and reproduction." These observations ride on the underlying mystery of what constitutes life. Simply reflecting upon the title of this historical work, "On the Origin of Species," we realize Darwin is fundamentally asking where does life begin and how did it diverge from non-living matter?

Moving about another 100 years forward, we return to our discussion of Schrödinger, who delivers his lecture series "What is life?"[1]. Schrödinger ruminates on how living matter is distinct due to its "orderly and lawful behavior of matter, not based exclusively on its tendency to go over from order to disorder, but based partly on existing order that is kept up." This astute sentiment still puzzles us today. Noting his statement that living systems exhibit "admirable regularity and orderliness, unrivaled by anything we meet with in inanimate matter," it feels we must explore the rudimentary cause of this difference by probing the physical parameters we know to be at play in creating orderliness. The amount of order in a system can be described by the system's entropy, which is intimately connected to energy. If perhaps, we could better understand how living systems use and direct their energy, we may be able ascertain hints toward how life is sustained.

In his final chapter, Schrödinger professes "We must therefore not be discouraged by the difficulty of interpreting life by the ordinary laws of physics... we must be prepared to find a new type of physical law prevailing in it." Today, there are many great works aimed to better understand life through the exploration of energy. Here, I provide a smattering of studies that I, once again, do not profess to be complete, but that I find highly inspiring in answering Schrödinger's call to action.

One category of studies includes recent work that investigates a biological system's energy expenditure through calorimetry [5]. This technique measures the power, or energy per time, via temperature sensing in a fluid sample. Exciting work from 2019 quantified the heat output of zebrafish embryos using this method. Amazingly, the result directly informs us how much power these cells are using at a given time. While impressive in its own right, this work additionally explores the cost of mitotic cell cycles. On top of the basal energy level, the authors find oscillations in the power output of their samples. They suspected that these oscillations may be connected to the cell cycle. By adding pharmacological inhibitors, they test how perturbing cell cycle oscillations modifies the measured power oscillations, and indeed find the oscillations disappear. This work, probing both energetics at the cellular level and the individual cellular processes level, takes us a large step closer to understanding

how the basic unit of life, cells, rely on energy.

Subsequent work aims to continue probing the energetic consumption of individual cellular processes. This is very useful to the scientific community as we can begin to create a cellular budget, mapping how much energy cells use for any given function. Determining the energy partitioned to an individual process can be challenging, requiring high enough resolution to measure small heat outputs from small samples. Scientists designed and built a picocalorimeter that reports power outputs at picowatt sensitivities with microliter volumes [6]. With this tool in hand, researchers measured the thermal dissipation of an *in vitro*, active nematic fluid, containing motor proteins and microtubules, which are critical to cell division, transport, and cellular structure [7]. Through this work, they discovered 10^9 times more energy is dissipated than they predicted based on estimating the power of viscous flows. This work echoes Schrödinger's sentiment that living systems do not always play by the standard physical laws. These systems are maintained in a nonequilibrium steady state, defying the state of maximum entropy demanded in equilibrium. From this result we see how probing the physical laws that we accept as a community can help us interpret living systems and dictate where life seems to harness physics a little differently.

Simultaneously, others have investigated cellular energetics through the study of metabolism. These works hinge upon knowledge of the chemical pathways that intake oxygen and carbon sources, intermediately produce ATP, and output heat and byproducts like NADH. Upon measuring molecules inputted or outputted in metabolism, one can infer the associated energy flux based upon stoichiometry. A 2021 review paper does a beautiful job highlighting works featuring metabolic based techniques [8]. A central theme to this review is the value of measuring gradients in addition to global measurements. Using respirometers to quantify oxygen concentration or calorimeters to measure heat both describe energy fluxes across the entire system, what we refer to as a global measurement. When asking questions involving individual cellular processes, measurements that offer spatial knowledge can be useful in understanding where energy is localized. Some of the same authors wrote a paper developing a technique to image NADH molecules across mouse oocytes [9]. Using fluorescence lifetime imaging, this study explores the emergence of NADH gradients upon imposing various metabolic stresses to oocytes. This breakthrough result opens the door for future work to estimate ATP gradient formation across the oocyte, leading toward an understanding of where

cells allocate energy.

Inspired by the spirit of these great thinkers, both historical and modern, I hope to join the peloton of those using physical approaches to explore the most fundamental of biological questions: what does it mean to be alive? In the thesis that follows, I describe three interconnected stories. These threads strive to paint a unified picture of the energetic and mechanical assembly of motor proteins and microtubules into structures that resemble mitotic spindles, the complex molecular machines that segregate chromosomes during cell division. In the work described, we introduce a new method for direct measurement of ATP molecules in space and time, building upon the field's excitement towards witnessing gradients in isolated processes. We additionally write mathematical models exploring the physics of building and maintaining gradients in non-equilibrium steady states. And, in the spirit of comprehensively understanding our system, we explore the material properties of dynamic network formation.

All of the work described here uses an *in vitro* motor-microtubule model system. It has been well established that combining motor proteins and microtubules with ATP, spontaneous network formation will occur [10, 11]. Tuning the concentration ratios of motors to microtubules, two different structural regimes are observed [12]. The first is termed a nematic regime. Here, microtubules align in very long bundles resulting in swirly, filamentous patterns. A second type of network occurs in what is called a polar regime. Here, radially symmetric star-shaped structures are formed, which are called asters. The poles of the mitotic spindle are in this regime. All the work described in this thesis is in the polar, aster regime. Previous research in our lab aimed to control when and where we create structures. To achieve this goal, a 2019 study from the Matt Thomson lab in collaboration with our group engineered motor proteins to have an optogenetic protein linker attached on their tail [13]. When illuminating the linker, it undergoes a conformational change that, like a puzzle piece, allows it to attach to a linker on another motor's tail [14]. With this system, we can project any pattern of light onto a sample and initiate structure formation in the illuminated regions.

In Chapters 2 and 3, we measure spatiotemporal gradients of ATP molecules in dynamically forming asters. We introduce a fluorescent-based ATP reporter into our experimental system, which binds and releases ATP without hydrolysis. Upon excitation, the fluorescent signal of the probe changes based on the binding state of ATP, providing a direct readout of ATP gradients across an aster. With this measure-

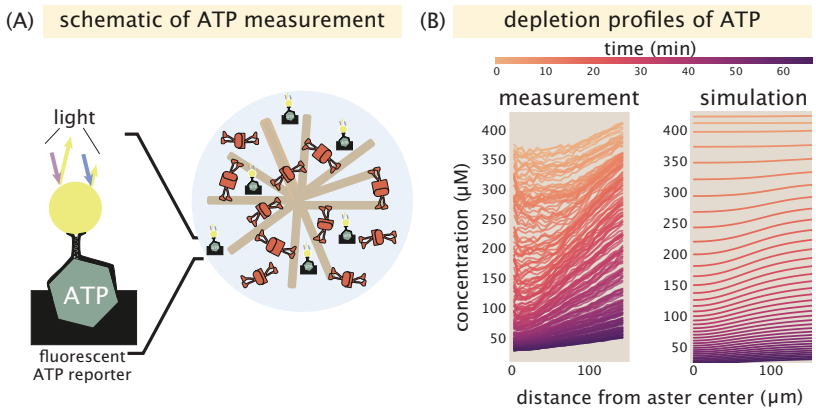

Figure 1.1: **Measuring ATP in space and time.** (A) Cartoon model of the ATP measurement scheme. (B) Experimental and simulated results showing emergent ATP gradients along the aster radius.

ment in hand, we work to interpret the cost of aster formation with reaction-diffusion modeling, finite element simulations, and systematic estimations of dissipative processes. A summary of this project is depicted in Figure 1.1.

Motivated to understand the gradients we observe in the previous chapters, in Chapter 4, we use statistical physics to develop a theory of biological gradients. We write flux-based equations that compare the molecular kinetics due to diffusion versus active transport. This allows us to predict the energy paid to simply maintain gradients as well as the additional costs required to steepen gradients. Through the mathematical description we provide, we aim to shed insight into the energetic expense of creating and sustaining gradients, allowing living systems to exist in non-equilibrium steady states. A preview of the story to come is depicted in Figure 1.2.

A comprehensive understanding of gradient formation in our system requires knowledge of the aster's material properties. Chapters 5 and 6 describe a project that used photobleaching techniques to observe advection and diffusive spreading during active network contraction. This study investigates which mechanism dominates upon tuning motor speeds by varying motor species and ATP concentrations. Regardless of motor speed, we find the role of advection is greater than diffusion. However, interestingly, we find that the rate of diffusion scales with motor speeds, indicating diffusion in this contracting network is an active process. Exploring deformations of contracting regions in the aster provide a material based perspective from which we build our understanding of the formation of gradients. In Figure 1.3 we provide

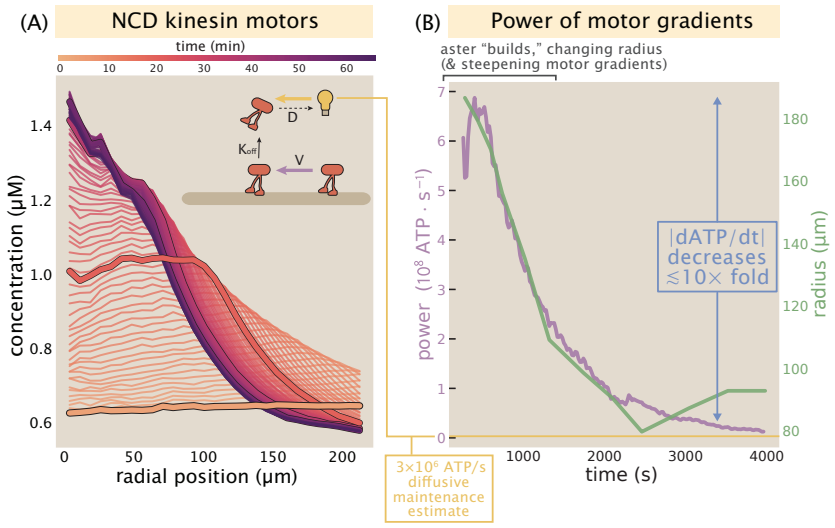

Figure 1.2: **Motor gradients emerge at the expense of ATP dissipation.** (A) Measurements of motor proteins in a developing aster. The cartoon inset highlights the competition between advection toward the center of the structure versus diffusion. (B) Measurements of the power dissipated from the building and maintenance of an aster. We note upon forming a steady-state gradient, the power expenditure drops nearly an order of magnitude.

a graphical overview of this work.

References

[1] Erwin Schrodinger. *What is life?: With mind and matter and autobiographical sketches*. Cambridge University Press, 2012.

[2] Anthony van Leeuwenhoeck. "Observations, communicated to the publisher by Mr. Antony van Leewenhoeck, in a Dutch letter of the 9th Octob. 1676. here English'd: concerning little animals by him observed in rain-well-sea- and snow water; as also in water wherein pepper had lain infused." In: *Philosophical Transactions* 12 (1677), pp. 821–831.

[3] Robert Brown. "A brief account of microscopical observations made in the months of June, July and August 1827, on the particles contained in the pollen of plants; and on the general existence of active molecules in organic and inorganic bodies." In: *Philosophical Magazine* 4.21 (1827), pp. 161–173.

[4] Charles Darwin. *On the Origin of Species*. Oxford University Press London, New York and Toronto, 1859.

[5] Jonathan Rodenfels, Karla M. Neugebauer, and Jonathon Howard. "Heat oscillations driven by the embryonic cell cycle reveal the energetic costs of signaling." In: *Developmental Cell* 48.5 (2019), pp. 646–658.

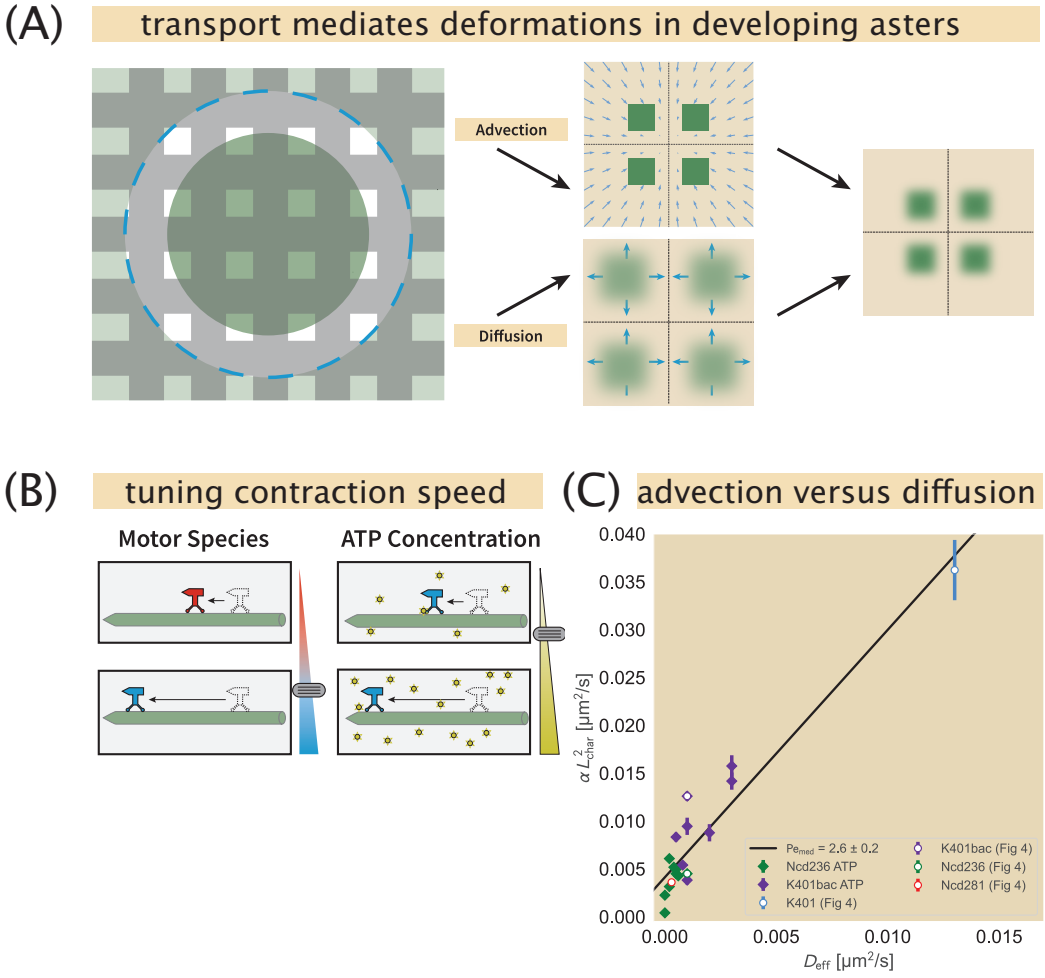

Figure 1.3: **Photobleaching grid patterns allow visual and quantitative comparisons of the dominant transport mechanisms.** (A) Cartoon scheme of the photobleaching system. Tracking unit cell deformations allow an analysis of the roles of advection versus diffusion. (B) Representation of the parameters that modulate motor speed. (C) The magnitude of advection and diffusion scale linearly with each other.

[6] Jinhye Bae et al. “A micromachined picocalorimeter sensor for liquid samples with application to chemical reactions and biochemistry.” In: *Advanced Science* 8.5 (2021), p. 2003415.

[7] Peter J. Foster et al. “Dissipation and energy propagation across scales in an active cytoskeletal material.” In: *Proceedings of the National Academy of Sciences* 120.14 (2023), e2207662120.

[8] Xingbo Yang et al. “Physical bioenergetics: Energy fluxes, budgets, and constraints in cells.” In: *Proceedings of the National Academy of Sciences* 118.26 (2021), e2026786118.

[9] Xingbo Yang, Gloria Ha, and Daniel J Needleman. “A coarse-grained NADH redox model enables inference of subcellular metabolic fluxes from fluorescence lifetime imaging.” In: *Elife* 10 (2021), e73808.

[10] François J. Nédélec et al. “Self-organization of microtubules and motors.” In: *Nature* 389.6648 (1997), pp. 305–308.

[11] Thomas Surrey et al. “Physical properties determining self-organization of motors and microtubules.” In: *Science* 292.5519 (2001), pp. 1167–1171.

[12] Johanna Roostalu et al. “Determinants of polar versus nematic organization in networks of dynamic microtubules and mitotic motors.” In: *Cell* 175.3 (2018), pp. 796–808.

[13] Tyler D. Ross et al. “Controlling organization and forces in active matter through optically defined boundaries.” In: *Nature* 572.7768 (2019), pp. 224–229.

[14] Gurkan Guntas et al. “Engineering an improved light-induced dimer (iLID) for controlling the localization and activity of signaling proteins.” In: *Proceedings of the National Academy of Sciences* 112.1 (2015), pp. 112–117.

Chapter 2

ATP CONSUMPTION IN SPACE AND TIME IN MICROTUBULE-MOTOR STRUCTURES

2.1 Abstract

Living matter produces a variety of beautiful spatiotemporal structures and patterns that are not present in their nonliving counterparts. Often, these ordered, non-equilibrium steady states are sustained through the consumption of energy. Careful examination of when and where living systems direct energy consumption helps us understand the principles dictating such ordering and can motivate development of non-equilibrium theories that apply to living matter. Here, we investigate the energetic cost of assembling an ordered aster from a disordered, uniform mixture of cytoskeletal microtubules and kinesin motors. Using a fluorescent ATP sensor, we perform a careful measurement of ATP consumption through space and time on an in vitro cytoskeletal network. Our experiments resolve the emergence of radial ATP gradients. We successfully predict how a given motor profile generates these ATP distributions using reaction-diffusion models in conjunction with finite element simulations. With our results, we compare the power per volume required by our cytoskeletal networks with the known power per volume expenditure in cells, leading to the hypothesis that one of the primary energy drains in the context of these systems is the production and maintenance of spatial motor gradients. Our direct quantification of energetic fluxes across space unlocks future explorations of what steady states are accessible to cells, and how the cytoskeleton drives broad spatial organization.

2.2 Introduction

One of the main drivers maintaining the rich patterns in living matter is a steady investment of energy. For example, the existence of morphogen gradients in developmental patterning is paid for through a steady flux of protein synthesis and degradation. Similarly, cytoskeletal-motor systems hydrolyze ATP and GTP to achieve processes ranging from intracellular transport, to cell motility, to chromosome segregation. Motivated by these processes, we were inspired to develop a physical understanding of the connection between energy fluxes and the emergence of biological order in space and time in the context of the particular example of

microtubule-motor assemblies.

The energetic basis of the processes within living cells are based upon a few fundamental energy currencies, which can be thought of as a sort of biological batteries. This metaphor is useful because it reminds us that batteries are indifferent to the particulars of what they are wired up to – they can drive anything from the light in a flashlight to motorized toys. Biological processes are powered by several key biological batteries including membrane potentials, redox reactions and trinucleotide hydrolysis. Indeed, for the molecular motor driven reactions that power the structures of the cytoskeleton, ATP and GTP hydrolysis are central. Thus, we were curious about how ATP consumption in space and time drives the dynamics of structure formation.

Recently, it has become possible to measure the total energy consumption of both living organisms and the molecular machinery that drive them [1, 2, 3, 4]. We aimed to complement these foundational studies by investigating the spatial distribution of energy consumption. In particular, here we report the visualization of spatial, ATP concentration gradients across cytoskeletal networks, giving insight into how structure, composition and morphology drive energy dissipation.

We use motor-microtubule assemblies as a highly controllable and tunable system due to their minimal components and self-organizing properties in vitro as well as their biological ubiquity. An abundance of work has established that connected dimeric motor domains can cross-link microtubules, creating ordered networks [5, 6, 7, 8]. To control the position, size and start of microtubule cross-linking, we optogenetically link motor proteins together as shown in Figure 2.1, as previously developed in our labs [8]. Motors harness energy to drag microtubules into ordered structures by hydrolyzing an ATP molecule for each step they take along the microtubule. We measure the energy consumed by the motors throughout space and time using a fluorescent, QUEEN-based ATP probe [9] as shown in Figure 2.1.

In addition, to complement the measurements and to provide a framework for understanding them, we develop a reaction-diffusion equation that describes the emergent ATP spatiotemporal gradients and explore the implications of that model with finite element calculations. Combining our experimental and theoretical results, we determine that the measured network formation power is indeed many orders of magnitude greater than the theoretical power of equilibrium processes.

We note that the work presented in the remainder of the paper is written with the

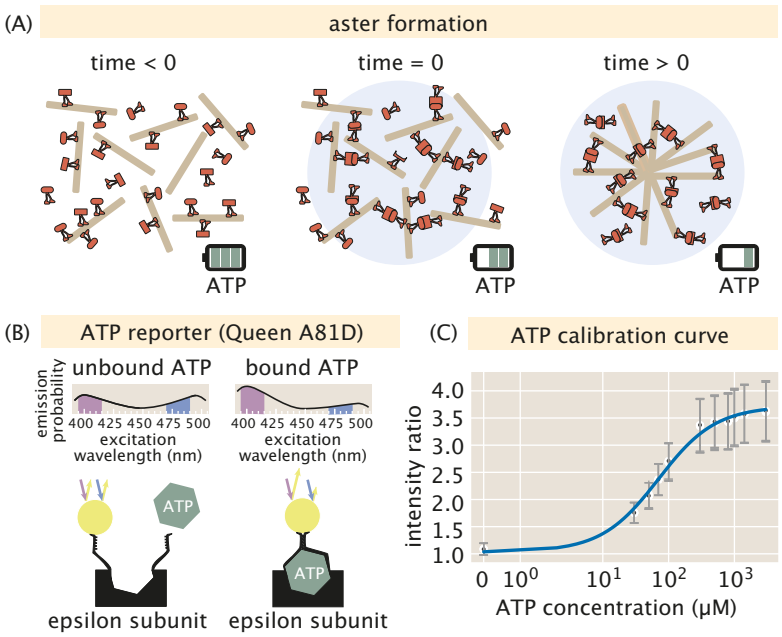

Figure 2.1: **Schematic of the experimental system used to measure spatiotemporal evolution of ATP.** (A) The formation of an aster using light activated motor dimerization. Before light activation, motors independently walk on microtubules hydrolyzing ATP. At $t = 0$ a circular light pattern is projected onto the sample. Motor proteins inside the illuminated region dimerize, crosslinking microtubules. As time elapses, microtubules are dragged into an aster resulting in the depletion of ATP. (B) The binding mechanism for ATP to the ATP probe. Binding ATP to the probe causes the number of emission counts due to an excitation of 405 nm light to increase, while emission counts from 480 nm light excitation decreases. By comparing the ratio of the emission counts at 405 nm and 480 nm light excitations, the concentration of ATP can be inferred. (C) A calibration curve mapping known ATP concentrations to fluorescent light intensity ratios. Each black circle represents the mean ratio value for a given image and gray error bars report the standard deviation of the image.

intention of providing the essential narrative structure in the paper itself. In parallel, the Supplementary Material is written with the aim of making every technical detail of how the experiments were done, how the data was analyzed, how conclusions were drawn and how the data was interpreted using quantitative models completely and rigorously transparent.

2.3 ATP Concentrations in Space and Time

The key elements of our experimental design are shown in Figure 2.1. As noted above, using spatially and temporally controlled illumination, we can generate patterns such as the radially symmetric aster shown in the schematic. Our principal experimental goal is to measure the rate of consumption of ATP as a function of position and time, a goal that is realized by using the fluorescent, ratiometric ATP reporter [9] depicted in Figure 2.1(B). The probe mechanism creates a change in the protonation state [10] of the fluorophore when ATP binds [11], triggering a shift in the fluorophore's absorption spectrum [12]. By using known standards, as shown in Figure 2.1(C), we can construct a calibration curve that now permits us to measure the ATP concentration in a given spatial region. Given that the characteristic scale of ATP concentrations in our experiments are of order 100 μM, we see that our ATP probe can measure ATP consumption in a spatially resolved fashion since, as seen in the calibration curve, the ATP reporter is sensitive in precisely the concentration ranges over which the reporter is effective. Note that in the Supplemental Information, we give an extremely detailed description of how we handled uneven illumination and photobleaching, a prerequisite to a calibration curve like that shown in Figure 2.1(C). In addition, there we also describe how we used two-dimensional images to make approximate three-dimensional inferences.

This measurement scheme equips us to simultaneously resolve the quantity of both ATP and motors over space and time while asters form, as shown for representative time courses in Figs. 2.2(A) and (B). As motors step along and exert torques on microtubules, they accumulate in the centers of assembling asters, creating self-organized polar order and material flow, as witnessed in the time course of Fig. 2.2(A). Concurrently, our measurements report how an initially uniform concentration of ATP is steadily reduced, as shown by Fig. 2.2(B). Importantly, the depletion of ATP is manifestly nonuniform over space, forming a steepening gradient of ATP, with less ATP in the aster center than at its periphery. These concentration fields are displayed as radial profiles in Fig. 2.2(C) and Fig. 2.2(D), registering rich time and space dependencies.

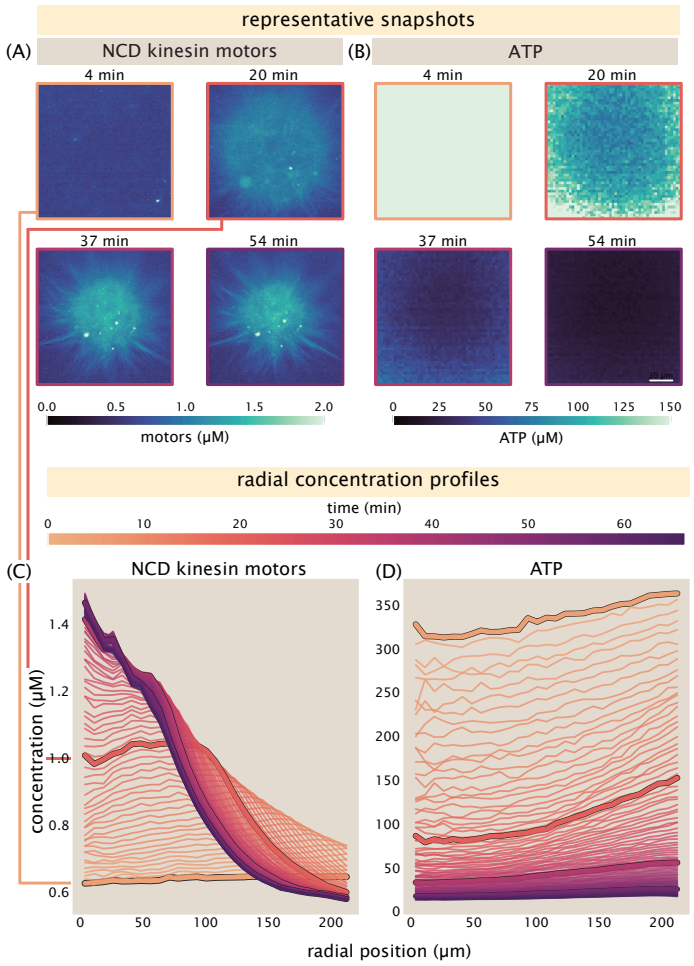

Figure 2.2: **Experimental measurements resolve coupled gradients of motors and ATP across space and time.** (A) Experimentally measured spatial distributions of molecular motors and (B) ATP over four timepoints during the self-organization of an aster. As time evolves, motor proteins concentrate near the aster center; a coupled ATP gradient develops, with greatest depletion in the aster's center where motors are most abundant. (C) Radial concentration profiles of motors and (D) ATP using the same data as in (A) and (B), once angularly averaged, have been highlighted with thick strokes outlined in black at each respective time. These gradients reveal clear, rich nonuniformities over time and space.

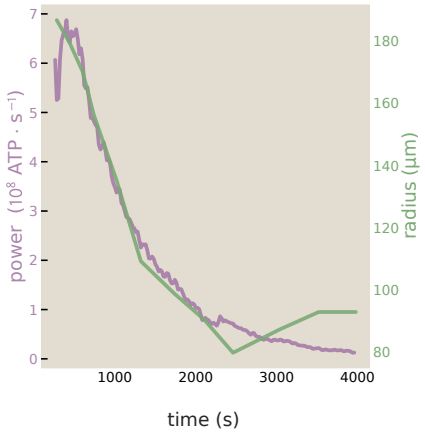

Figure 2.3: **The power of aster formation.** The number of ATPs consumed per second is plotted as a function of time in purple. The green line on top reports the aster radius over time. Under these conditions (0.6 μM motors and 500 μM initial ATP), the magnitude of power tends to follow the size of the aster, consuming ATP faster while first aggressively contracting, and reaching a baseline power level once the aster is no longer dramatically changing size.

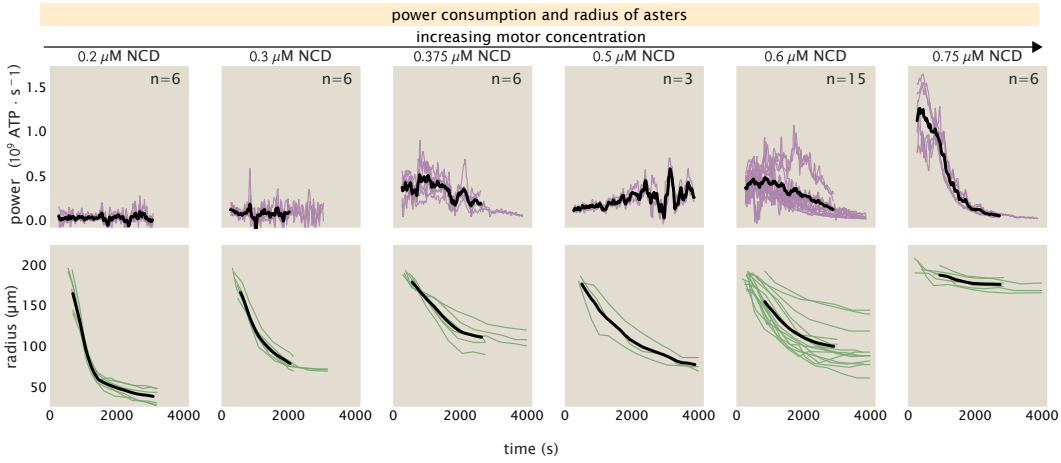

Figure 2.4: **Sizes and power demands of asters across varying motor concentrations.** Top: Measured rates of ATP depletion (top, in purple traces) and characteristic aster sizes (bottom, in green traces) over time across increasing total motor concentrations (as columns from left to right). Distinct experimental replicates are each shown as thin lines to reflect the typical reproducibility of the phenomenonlogy of aster trajectories in each condition, with the number of replicates indicated in the upper right corner. The median trajectories are depicted as black lines. The representative trajectory depicted earlier in Figs. 2.2 and 2.3 is among the trajectories shown in the penultimate (0.6 μM motors) column of this plot.

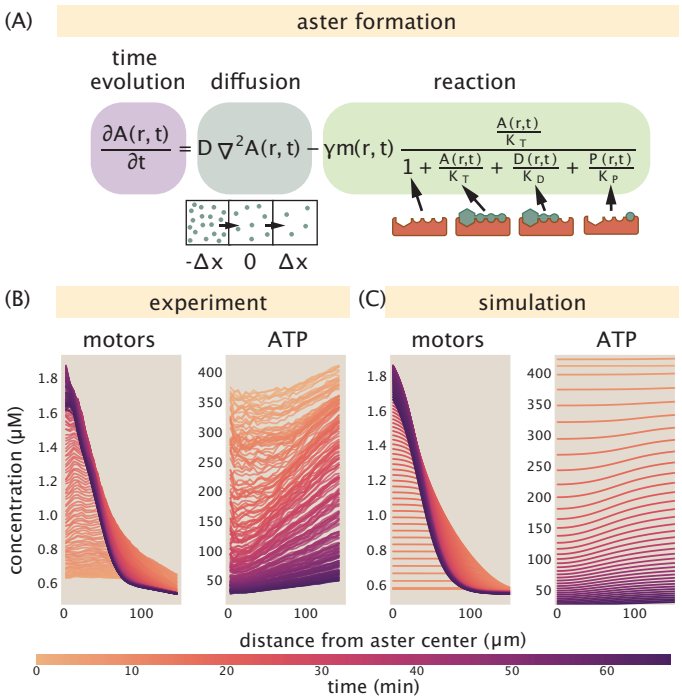

Figure 2.5: **Experimental measurements and Finite Element simulations of ATP concentration in space and time.** (A) The reaction-diffusion equation used to simulate ATP concentration is written with illustrations of the diffusive term and the binding states of ATP (A), ADP (D) and phosphate (P) to the motor protein schematized in red. (B) The radial concentration profile of motors and ATP as measured experimentally. (C) The radial concentration profile of motors and ATP as computed using finite element calculations of a continuum reaction-diffusion equation. As time evolves, motor proteins become concentrated near the aster center while ATP depletes. Both the experiment and simulation reveal an ATP gradient with the greatest depletion in the aster center, where motors are most concentrated.

Another way of visualizing the results of our measurements is to take the ATP data from successive instants and convert it to a power. As shown in Figure 2.3, the power can be evaluated directly in units of ATP/s, making it possible to compare directly to other measurements, as well as estimates of what the energy from hydrolysis events is used to pay for. Next, we ask how one might develop quantitative intuition for the distribution of the ATP in the aster in both space and time.

How do presiding physical parameters, such as the total abundance of motors and initial ATP, control the dissipative and geometric trajectories of asters as they form? To approach this question, we varied the concentration of molecular motors and measured how the rates of ATP depletion over time changed. Across a $\gtrsim$ 3-fold range of sub-micromolar motor concentrations, motors and microtubules varied the

extent to which they macroscopically built prominently recognizable asters over longer than an hour, as visualized by the bottom row of Fig. 2.4 showing aster radii over time. Concomitantly, these structures across motor concentrations shows very different trajectories of power consumption over time, as reported by the power trajectories given by the top row of Fig. 2.4.

These experiments also contribute a measure of the variability attending aster formation, a stochastic process, over biological and technical replicates; individual aster trajectories under repeated conditions are shown as thin lines in Fig. 2.4. While the contraction rates and ATP depletion rates are largely macroscopically reproducible for many total motor concentrations, the reproducibility of these aster formation radial and dissipative trajectories also appeared to vary based on the ambient amount of motors. For instance, we observed particuarly large inter-aster variation at 0.6 μM motors, as shown by the more difergent trajectories of the penultimate column of Fig. 2.4. We note with curiosity that this regime of greater variability appears to be just at the cusp of transitioning from asters that readily contract (giving the appreciable changes to aster radii, at motor concentrations $\lesssim$ 0.6 μM motors) to those that barely macroscopically contract (yielding the only slight changes to aster radii, at motor concentrations $>$ 0.6 μM motors).

The profiles revealed in Figure 2.5 characterize the radial and temporal dependence of both the motors and the ATP. As seen in the dynamical equation in Figure 2.5(A), the change of concentration in some small material volume element can be attributed both to ATP molecules entering and leaving that small region and to the hydrolysis of those ATP molecules by molecular motors that are in the material volume element of interest. More precisely, as shown in the figure, we can write a reaction-diffusion equation that captures the rate of change of ATP in a material volume element. As shown by the box underneath the equation in Figure 2.5(A), a material volume element of interest has molecules both leaving and entering as a result of diffusion, as described in more detail in the Supplement. The reaction term uses a Michaelis-Menten-like dynamics for the rate of ATP consumption by motors. However, the denominator of that term also includes terms that reflect competitive inhibition of the reaction due to ADP and P_i. The local hydrolysis rate is proportional to the density of motors and to the concentration of ATP itself. Note that there is another more pernicious dynamic taking place during our experiments, namely, photobleaching. We have several sections in the Supplemental Information that describe how we measure and account for photobleaching, including thorough finite

element simulations of a diffusion-photobleaching equation in Section 3.8.

One convenient way to analyze the solutions to such equations in diverse geometries is by appealing to numerical methods. In our case, we used the finite element method to compute the space-time history of the ATP as shown in Figure 2.5(C). As seen in the figure, for reasonable parameter choices (the details of parameter selection are described in the Supplement), the time evolution of the ATP field is in reasonable accord with our measurements. One question that naturally arises is to ask what that ATP hydrolysis "pays for?" Of course, mechanistically, we know that the ATPs are being consumed by motors as they carry out their walk along microtubules. But here we mean it differently. That energy is dissipated through elementary processes such as ordering and contraction of the microtubule network. How much energy do these processes cost? Microscopically, a huge variety of dissipative processes are taking place during the microtubule-motor rearrangements attending aster formation. As shown in Figure 2.3 the power varies considerably at different stages of the aster formation process. To that end, we explore the power associated with a variety of processes that we imagine are taking place concurrently and would cost different amounts at different stages of the aster formation process. Indeed, as seen in Figure 2.6 there are a number of possible estimates that one can make in units of ATP/s that reflect what ATP hydrolysis might be used to "pay for." Each of these estimates (and several others) is spelled out in detail in the Supplemental Information in Section 4.2 and here we simply describe the concept of each calculation and how much power consumption it implies.

Given the measured power, we were intrigued to compare it to the power associated with a variety of elementary dissipative processes that take place during aster formation as shown in Figure 2.6. For example, as is evident from the radius as a function of time in Figure 2.3, the volume of the microtubule aster is decreasing over time. As shown in Figure 2.6(A) and described in detail in Section 4.2, we can perform a simple estimate of the power associated with this contraction as the pV work done divided by the elapsed time. We find that the pV power is five orders of magnitude smaller than the measured power. As shown in Figure 2.6(B), a second dissipative process is the frictional sliding of the various microtubules during the contraction process. A naive estimate is obtained by replacing a given microtubule by a corresponding sphere of the same dimensions and to work out the Stokes drag. As in the case of the pV power, this results in a power that is five orders of magnitude smaller than the measured power of Figure 2.3. As discussed

in Section 4.2, a better estimate can be made in which the microtubule is treated as a rod rather than a sphere and in this case the computed power is even smaller. Another approach to estimating the power is offered by field theories of nematic ordering in which the state of the system is characterized by the spatially varying tensor $Q_{ij}(\mathbf{f}, t)$. This estimate is trickier to make since the parameters in such a field theory of motor-microtubule systems are not well known. Nevertheless, as seen in Figure 2.6(C) (and described in more detail in the Supplement), the power we estimate associated with such ordering is many orders of magnitude smaller than the measured power. The final dissipative process highlighted in Figure 2.6(D) is that of maintaining a nonequilibrium gradient of motors radially outward from the center of the aster. One way to think about such a gradient is that if there were not some active transport carrying motors towards the aster center, then diffusion would smooth out that gradient. As we show in Section 4.2, there is a well defined prescription for estimating the power to maintain such a gradient and we find that it is of the same order of magnitude as the measured powers. This interesting result suggests the hypothesis that a significant fraction of the ATP hydrolysis consumed by the motors is "spent" to build and then maintain this gradient.

2.4 Discussion

It is practically a cliche to note that living organisms are "out of equilibrium." But we also find that this compact, binary statement, while true, is largely unhelpful. Equilibrium ideas are even used to describe the conditions in a star, and it behooves us to have quantitative measures of what we mean by the word "nonequilibrium" in different contexts. For example, although a bacterium can be thought of as a furnace burning fuel at a rate of 10^5 W/m^3, for single cells and even embryos, this power consumption leads to a temperature change relative to the external world of less than 10^{-7} K. Though each ATP hydrolysis event leads to a local temperature change of ≈ 10 K in a 1 nm^3 volume, that temperature change relaxes away at time scales far less than a microsecond. Similarly, the concentration gradients of morphogens are very shallow implying that the "out of equilibrium" concentration gradient is barely discernible at the molecular scale. To see this, we imagine discretizing the anterior-posterior axis of the fly embryo into little 1 μm^3 boxes, the measured gradients are so gentle that two adjacent 1 μm^3 boxes near the anterior part of the embryo would have an average of 60 and 59 molecules, respectively. The point here is that the question of the extent to which biological systems depart from equilibrium is both important and subtle.

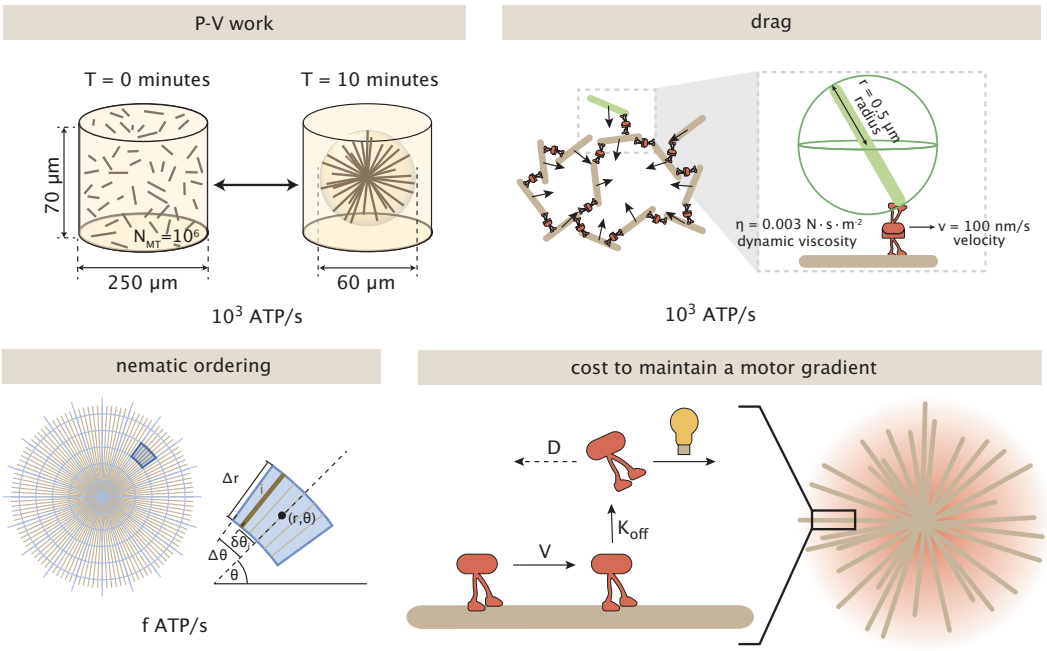

Figure 2.6: **Mechanistic processes taking place during aster formation and their estimated power.** Each schematic considers a different dissipative processes that occurs during the formation of an aster. (A) Schematic of the power of compressing an "ideal gas" of microtubules. (B) The power of dragging microtubules through a viscous medium. (C) Power estimate for inducing nematic ordering in a random array of microtubules. (D) The power to maintain a concentration gradient of motors in the aster.

In recent years, renewed efforts have been made both experimentally and theoretically to explore the deep question of when and where energy is being consumed within cells and what the energy consumption is used for. A seminal study in the 1970s by Stouthammer already recognized the huge energetic burden of protein synthesis in fast growing cells [13]. This process sets a baseline of roughly 10^6ATP/(μm^2 s) because to produce the $\approx$ few $\times\, 10^2$ peptide bonds per protein each of which costs 4 ATP equivalents for the roughly few $\times\, 10^6$ proteins per cell results in a total cost of $\approx$ few $\times\, 10^9$ ATPs over the 1000 seconds of the cell cycle. Recent experiments in bacteria illustrated how in starved cells after roughly 24 hours they die due to a loss of membrane potential. Here too, we can make simple estimates of the power required to maintain the transmembrane potential against membrane leakage. Stated simply, the flux of ions out of the cell can be estimated as $dn/dt = JA$, where $J = p\Delta c$. Using the very low permeability to ions of roughly $p \approx 10^{-9}$ nm/s, we find that the net loss of ions occurs at a rate of 1 - 10 ions/s. Using the relation $\Delta Q = C\Delta V$, we can estimate that in under 24 hours the membrane potential will be

nearly completely lost. The power to maintain the membrane potential against such leakage is a tiny value of 10s of ATPs per second.

We argue that the management of energy expenditure in space and time is of critical importance for understanding everything from the development of membrane potentials to the fidelity of biological polymerization to the assembly of structures such as the spindle. Recently, both calorimetry and fluorescence approaches have made it possible to dissect the dissipation in living cells. Such measurements generally tell a similar story, namely, that the scale of measured dissipation is often orders of magnitude larger than the dissipation one might expect by considering elementary processes such as flow [1].

In this paper, we rigorously measured such energy consumption in space and time in the specific context of a microtubule-motor system. Our measurements resolving large spatially varying power consumptions, understood from a slew of theoretical contexts, provoke immediate questions, both empirically and conceptually.

Empirically, precisely how dramatically do spatial gradients of ATP and ATP consumption rates develop and persist inside whole cells (whether metabolically replete or stressed)? Our work directly quanties the growth and extinguishment of dramatic dissipative gradients from an initial unreplenished ambient ATP pool by a dominant sink process (namely, motors). Whole cells, however, couple the equivalents of these sink processes with metabolic sources (including mitochondria). It is a fascinating, abiding question for our field, whose urgency is sharpened by our work, to ask whether or how the conspiracy of both sources and sinks manifests appreciable gradients (or not) of biochemical sources of energy. Our measurements establish that gradients might be eminently physiologically plausible. Yet, the sustainment and quantitative extent of extant gradients inside cells must be explicitly measured across metabolic conditions to understand the true physiological consequences of such gradients.

Conceptually, if cells spend more energy than they appear to "need" to to accomplish certain key tasks, can explicit spatial readouts of their dissipation reveal other functional priorities that constrain them? Could new control schemes for physiology across organelles be unlocked by such metabolic gradients in space? At the level of fundamental nonequilibrium physics, how can amazing recent theoretical progress in stochastic thermodynamics (e.g., as discussed in [14]), whose results are very frequently spaceless, be updated to incorporate the rich new consequences of spatial effects?

We anticipate rapid fundamental discoveries await these basic questions informed by developing "spatial metabolomics" tools that measure ATP or its equivalents in real units on biologically-relevant length- and time-scales.

References

[1] Peter J. Foster et al. "Dissipation and energy propagation across scales in an active cytoskeletal material." In: *Proceedings of the National Academy of Sciences* 120.14 (2023), e2207662120.

[2] Jonathan Rodenfels, Karla M. Neugebauer, and Jonathon Howard. "Heat oscillations driven by the embryonic cell cycle reveal the energetic costs of signaling." In: *Developmental Cell* 48.5 (2019), pp. 646–658.

[3] Qiwei Yu, Dongliang Zhang, and Yuhai Tu. "Inverse power law scaling of energy dissipation rate in nonequilibrium reaction networks." In: *Physical Review Letters* 126.8 (2021), p. 080601.

[4] Yuansheng Cao et al. "The free-energy cost of accurate biochemical oscillations." In: *Nature Physics* 11.9 (2015), pp. 772–778.

[5] François J. Nédélec et al. "Self-organization of microtubules and motors." In: *Nature* 389.6648 (1997), pp. 305–308.

[6] Thomas Surrey et al. "Physical properties determining self-organization of motors and microtubules." In: *Science* 292.5519 (2001), pp. 1167–1171.

[7] Johanna Roostalu et al. "Determinants of polar versus nematic organization in networks of dynamic microtubules and mitotic motors." In: *Cell* 175.3 (2018), pp. 796–808.

[8] Tyler D. Ross et al. "Controlling organization and forces in active matter through optically defined boundaries." In: *Nature* 572.7768 (2019), pp. 224–229.

[9] Hideyuki Yaginuma and Yasushi Okada. "Live cell imaging of metabolic heterogeneity by quantitative fluorescent ATP indicator protein, QUEEN-37C." In: *BioRxiv* (2021), pp. 2021–10.

[10] Takeharu Nagai et al. "Circularly permuted green fluorescent proteins engineered to sense Ca2+." In: *Proceedings of the National Academy of Sciences* 98.6 (2001), pp. 3197–3202.

[11] Hideyuki Yaginuma et al. "Diversity in ATP concentrations in a single bacterial cell population revealed by quantitative single-cell imaging." In: *Scientific Reports* 4.1 (2014), p. 6522.

[12] Roger Y. Tsien. "The green fluorescent protein." In: *Annual Review of Biochemistry* 67.1 (1998), pp. 509–544.

[13] A. H. Stouthamer. “Theoretical study on amount of ATP required for synthesis of microbial cell material.” In: *Antonie Van Leeuwenhoek Journal of Microbiology* 39.3 (1973), pp. 545–565.

[14] Massimiliano Esposito, Upendra Harbola, and Shaul Mukamel. “Nonequilibrium fluctuations, fluctuation theorems, and counting statistics in quantum systems.” In: *Reviews of Modern Physics* 81.4 (2009), pp. 1665–1702.

Chapter 3

SUPPLEMENTARY INFORMATION FOR ATP CONSUMPTION IN SPACE AND TIME IN MICROTUBULE-MOTOR STRUCTURES

3.1 Materials and Methods

Sample Chambers for Aster, ATP Calibration, and ATP Hydrolysis Experiments

For both the aster and ATP hydrolysis experiments, a flow cell was created by placing parafilm spacers between a microscope slide and a cover glass. A mild heat treatment at 65 °C was applied to facilitate the adhesion of parafilm to the glass surfaces, resulting in a flow cell that is approximately 70 – 100 μm in height and has a volume of approximately 5 μL. To prevent nonspecific protein adsorption onto the glass, the glass surfaces were coated with an acrylamide brush [1]. The reaction mixture was loaded into each channel by capillarity and sealed with a fast-setting silicone polymer (Picodent Twinsil Speed).

Sample Preparation and Reaction Mixture for Aster and ATP Hydrolysis Experiments

For aster experiments involving Ncd motors, the reaction mixture consisted of Ncd-mCherry-micro, Ncd-mCherry-iLID, 2.8 μM A81D, and microtubules (1.5 μM tubulin). We systematically varied the final concentrations of each Ncd motor type from 0.2 μM to 0.75 μM, supplemented with 500 μM of MgATP (Sigma A9187). Additionally, aster experiments were conducted with K401-mCherry-micro, K401-iLID, 2.8 μM A81D, and microtubules (1.6 μM tubulin), resulting in a final concentration of 0.25 μM for each motor type with 1000 μM of MgATP.

For ATP hydrolysis experiments, we varied the concentration of MgATP (ranging from 50 μM to 1420 μM), ADP (ranging from 0 μM to 1420 μM), and potassium phosphate (pH 7.0, ranging from 0 mM to 40 mM) using 1 μM Ncd-mCherry-micro, 1.4 μM A81D, and microtubules (1.5 μM tubulin).

The concentrations are specifically associated with protein monomers in the cases of Ncd-mCherry-micro and Ncd-mCherry-iLID, along with K401-mCherry-micro and K401-iLID, whereas tubulin represents the protein dimer.

For both aster and ATP hydrolysis experiments, the reaction mixture consisted of 66.7 mM PIPES at pH 6.8, 4.7 mM $MgCl_2$, 0.83 mM EGTA, a crowding agent (20-22% glycerol, Sigma, G5516), a surface passivating agent (0.50 mg/mL Pluronic F-127, Sigma, P2443), and an oxygen-scavenging system to prevent photobleaching (0.37 mg/mL pyranose oxidase, Sigma, P4234; 7.2 mg/mL glucose, Thermo Fisher Scientific, USA; 9 μg/mL catalase, Sigma, C40; 5.4 mM DTT, Thermo Fisher Scientific, USA; 2.0 mM Trolox, Sigma, 238813).

Sample preparation and handling were performed in a dark room with red light to minimize early light activation of the optogenetic proteins. We prepared the reaction mixture right before loading it into the flow cell and sealed it using Picodent Twinsil Speed. The experiments were repeated at least three times at room temperature (approximately 25°C).

Activation and Imaging Protocol for aster and ATP hydrolysis experiments

In experiments focusing on aster formation, we selected one position within the flow channel, which is illuminated by an excitation region with a diameter of 400 μm. In the case of experiments related to ATP hydrolysis, the entire field of view is illuminated. GTypically, one experiment is conducted per flow channel.

The fluorescent motors (mCherry labeled) and the A81D ATP probe were imaged simultaneously every 20 seconds using a $\times$10 objective. The exposure time values for 405nm and 480nm excitations were 33-150 ms and 50-160 ms, respectively, and 100-300 ms for 587 nm mCherry excitation.

ATP Calibration Assays

For our ATP hydrolysis experiments, we used a ratiometric fluorescent ATP probe, QUEEN 7μ mutant, A81D) [2], which allows the estimation of ATP levels in the reaction mixture. In these assays, we quantified the fluorescence intensity of A81D, which serves as a reporter system coupled with a fluorophore to monitor ATP hydrolysis by Ncd-mCherry-micro or K401-mCherry-micro motor proteins in our experiments.

For ATP calibration experiments, we examine the relationship between the QUEEN 405/480 ratio and MgATP concentration, ranging from 0 μM to 3000 μM. We used 1.4-2.8 μM A81D with GMP-CPP-stabilized microtubules (1.5 μM tubulin) in the reaction mixture at various MgATP concentrations. The composition of the reaction

mixture for ATP calibration is the same as outlined in section 3.1, excluding motor proteins.

Epifluorescence imaging was performed every 20s using excitation filters (405 and 480 nm) and a $\times 10$ objective. The exposure time values for 405nm and 480nm excitation are 33-150ms and 50-160ms, respectively. Typically, five positions within the same flow cell were chosen for averaging. The experiments are performed at room temperature (approximately 25°C).

Flow Chamber, Sample Preparation, and Imaging Protocol for Microtubule Gliding Assays

The flow chambers were constructed as previously described [3]. In brief, we built a chamber by assembling an amino-silanized coverslip and an acrylamide-coated microscope slide separated by melted parafilm spacers.

We treated the amino-silanized glass surface with glutaraldehyde to attach antibodies. For this purpose, the chamber was incubated with 10% (v/v) glutaraldehyde (Sigma, G7776) for 30 minutes. After removing unreacted glutaraldehyde by rinsing the chamber with MilliQ water, it was then incubated with a 0.02 mg/ml solution of anti-FLAG antibody (F3165, Sigma) to specifically bind motor proteins to the glass surface. The remaining exposed surface was blocked with a 0.2% (w/v) Pluronic F-127 (Sigma, P2443) and 2 mg/ml β-casein (Sigma, C6905) solution for 5 minutes. Motors were bound to the surface by incubating Ncd-YFP-iLID FLAG-tag motor proteins (at $\approx$ 1 nM in 10 mg/ml bovine serum albumin (BSA, JT Bakers), 1 mM DTT, and 500 μM mgATP in M2B buffer (80 mM PIPES, 1 mM EGTA, 2 mM $MgCl_2$)) for 5 minutes. Unbound motors were washed out with M2B, and then AlexaFluor 647 labeled GMP-CPP stabilized microtubules in M2B with 1mM DTT were flowed in. After 5 minutes of incubation at room temperature, the flow cell was rinsed with M2B to remove unbound microtubules.

The imaging buffer consisted of M2B buffer with 0.5 mg/ml β-casein, 0.50 mg/mL Pluronic F-127, 3 mM $MgCl_2$, 2 mM Trolox, and an oxygen scavenging system (0.37 mg/ml pyranose oxidase, 7.2 mg/ml glucose, 9 μg/ml catalase, 5.4 mM DTT, 2.0 mM Trolox). In microtubule gliding experiments, we varied the concentrations of mgATP (ranging from 20 μM to 5000 μM), ADP (ranging from 0 μM to 5000 μM), and potassium phosphate (pH 7.0, ranging from 0 mM to 40 mM). Following the addition of the reaction mixture, the flow cell was sealed using Picodent Speed. The experiments were repeated at least three times at room temperature (approximately

25°C).

Image acquisition of AlexaFluor 647-labeled microtubules was performed in a sealed chamber using Total Internal Reflection Fluorescence (TIRF) microscopy with an HCX PL Apo 100×/1.47 TIRF objective. Imaging was performed at one frame per second for 100 seconds. We also imaged Ncd motor proteins (YFP labeled) bound to the glass surface. Individual microtubules were tracked using custom-written Python code to determine their speed.

3.2 Image Analysis

Here we detail our image processing method. We aim to be very careful in checking how our operations modify the data. The predominant goal of the following text is to identify where variation sources occur in our data and how to remove such variation.

The analyzed dataset measures ATP concentration through a fluorescently labeled ATP probe, Queen A81D [2]. The probe contains a superfolder GFP attached to the epsilon subunit of an ATP synthase and capitalizes on the dual excitation peaks of GFP. When ATP binds to the epsilon subunit, there are increased emissions from the 405 nm excitation, and in the unbound state there are increased emissions from the 480 nm excitation state. Taking the ratio of light intensities at 405 nm and 480 nm, an ATP calibration can be created by fitting a curve to the intensity ratio versus ATP concentration, as is shown in Figure 3.10 below. Note that each image should not contain any spatial dependence, as we are measuring the fluorescence of homogeneous mixtures of ATP, the ATP probe, and motor proteins. Without microtubules present, there cannot be any ATP hydrolysis or structure formation.

Background Subtraction

Cameras artificially add an offset to the intensity values of an image to ensure that no pixels are recorded as having less than zero signal [4]. We identify this offset by taking a "dark image," where we close the camera shutter, preventing light from reaching the camera. We use the averaged image of multiple dark images, as shown in Figure 3.1, as the background image subtracted from all fluorescent images.

Figure 3.1: **Camera offset is found by taking a "dark image."** The average of six images are taken with the camera shutter closed. The average offset value is 1913.8 intensity counts. This image is subtracted from all fluorescent images. The horizontal lines present in the image roughly appear at the same place in all images.

Uneven Illumination Correction

Microscopy images of uniform samples can often have artificial gradients of intensity across space. Commonly, this artifact arises from vignetting cast by magnification tubes, non-uniform light sources, and off axis light [5]. Here, we work to distinguish the fraction of an image's variance that is due to a spatial gradient, implying uneven illumination, rather than local fluctuations.

To search for the origin of variation, we will divide our image into a grid. As we prove in Section 3.2, the total variance, σ^2_{tot}, of the image will equal the average variance within a grid block, $\left\langle \sigma^2_{\text{in}} \right\rangle$ plus the variance of the average grid block value, σ^2_{btwn},

$$\sigma^2_{\text{tot}} = \left\langle \sigma^2_{\text{in}} \right\rangle + \sigma^2_{\text{btwn}}. \tag{3.1}$$

If the variance within grid blocks dominates the total variance term, then most of the variation in an image arises from the noise of nearby pixel values, see the second row of Figure 3.2. However, if the variance between grid blocks (the variance of grid block average values) dominate, the image variance is attributable to intensity differences across regions of the image. Since we explore homogeneous ATP images here, we expect all the variance to be within grid blocks. If instead most of the variance is between blocks, this is a sign of uneven illumination, which manifests as a gradient of intensity from one side of the image to the other, see the first row of Figure 3.2. Thus, we can use this grid block method as a metric for the amount of

uneven illumination present in an image.

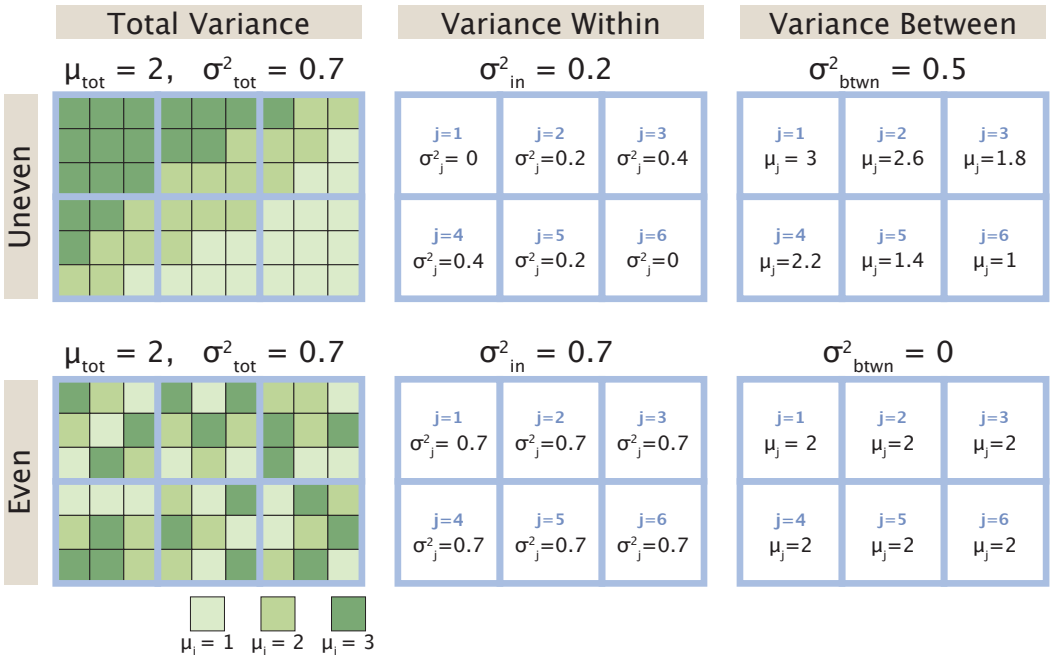

Figure 3.2: **Partitioning of variance for unevenly versus evenly illuminated images.** Here, we go through the exercise of finding the variance within and between blocks for two synthetic images. We assign each pixel value in the first column to have a value between one and three. By eye, we would consider the image in the first row to be unevenly illuminated, since there is an intensity gradient across the image. We would consider the image in the second row to be evenly illuminated, since there is no apparent intensity pattern. Splitting the image into six grid blocks of nine pixels each, we quantify our assumptions. The second column reports the variance of pixels within each grid block. Taking the average of these variances, we report σ^2_{in}, our metric for the variance within grid blocks (as defined by Equation 3.9). In the third column, the mean value of each grid block is reported. Taking the variance of these means gives σ^2_{btwn}, our metric for the variance between grid blocks (as defined by Equation 3.10). While the total image mean and variance for both images are the same, we find that more variance is between blocks in the first row and all the variance is within blocks in the second row. Thus when an image is unevenly illuminated, the variance between blocks dominates.

When dividing our image into into B blocks each containing N_B pixels, we must take note of the variance partitioning in the limits $N_B = 1$ and $N_B = N$, where N is the total number of pixels in the image. In the limiting case that each block only contains one pixel, $N_B = 1$, the variance within a block will be zero and the variance between blocks will equal the total variance of the image. In the opposite limit, where there is one large block containing all pixels, $N_B = N$, the variance

within the block is the total variance of the image and there is no variance between blocks. Thus, we must pick and intermediate N_B block size. In Equation 3.2, we graph the fraction of the variance within blocks versus the number of pixels per block. We find, somewhat surprisingly, that the data fits well to a cubic function of the logarithm of ATP concentration. Since we are looking for a middle ground block size that does not favor variance partitioning in either limit, we look near the inflection points of the curves. In Equation 3.3, we plot the fraction of variance within grid blocks versus the number of pixels per block for all measured ATP conditions. The light gray boxes contain the inflection points of all curves in both bound and unbound ATP channels. In this region, the slopes of all curves are low, implying that regardless of the choice of box size, the fraction of variance within blocks is about the same. Thus, we arbitrarily select the midpoint of the gray box (on a linear scale) as the block size we will use to compare the changes of variance partitioning when correcting images.

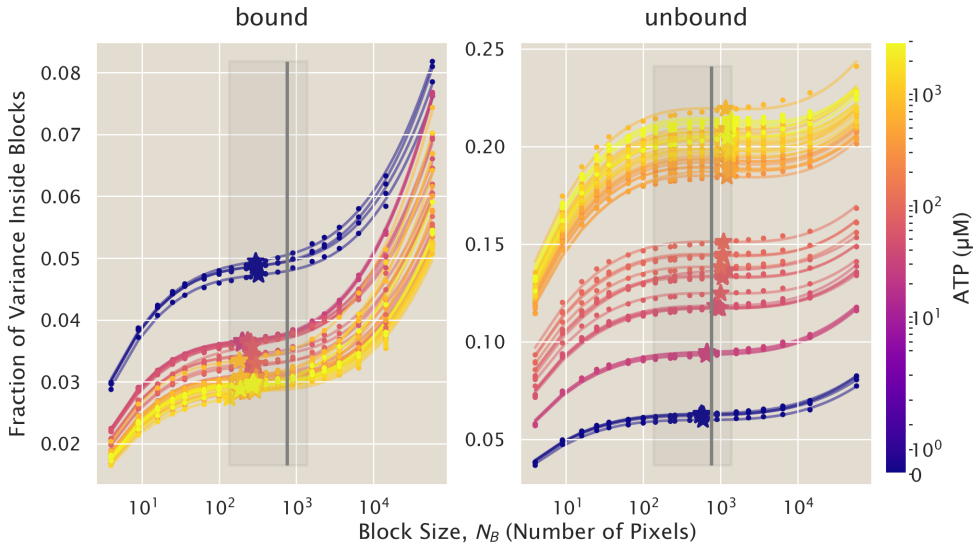

Figure 3.3: **The variance within grid blocks varies with the size of the grid block.** We measure how the variation within a block changes with the number of pixels per grid block (represented by circular markers). The trend fits well to a cubic polynomial of the form $\sigma^2_{\text{in}} = ax^3 + bx^2 + cx + d$, where $x = \ln(N_B)$ and N_B is the number of pixels in a grid block. Each solid line fits the data for a single image and is color coded by the concentration of ATP in the sample. We plot the inflection point for each fit (represented by star markers). The gray box is the region containing all the inflection points from both the bound and unbound channel's images. The gray line plots the midpoint (on a linear scale) of the gray box region. The value of the curves at the gray line as compared to the value at line's inflection point is nearly the same. So, we take this value as an arbitrary size by which we can compare the variance partitioning within versus between blocks as we perform uneven illumination corrections on our images.

From Figure 3.3, we see a very small amount of the variance is located within grid blocks, meaning the vast majority of variance is between grid blocks, implying uneven illumination. We now correct the uneven illumination by fitting a 2D quadratic polynomial of the form,

$$\text{2Dquad}(x, y) = ax^2 + by^2 + cxy + dx + ey + f, \tag{3.2}$$

as described by [6], to our image. Next, we create a normalization matrix from our 2D quadratic polynomial fit,

$$\alpha = \frac{\langle \text{2Dquad}(x, y) \rangle}{\text{2Dquad}(x, y)}, \tag{3.3}$$

where we divide the average polynomial fit value by the value of each filter pixel

value. We then multiply the original image by this filter to find an evened image,

$$\mathrm{im}_{\mathrm{ev}} = \alpha \cdot \mathrm{im}. \tag{3.4}$$

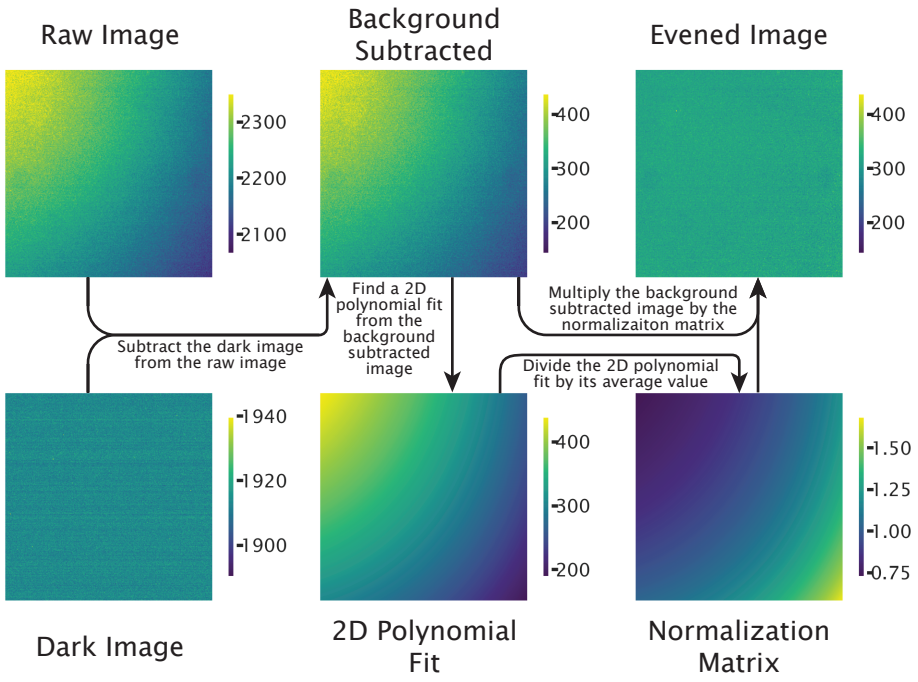

Figure 3.4: **Uneven illumination correction process.** We detail the pipeline to correct uneven illumination in images of homogeneous ATP samples. A camera shutter closed, "dark," image is subtracted from the "Raw Image" to create the "Background Subtracted" image. Then, a 2D polynomial is fit to the "Background Subtracted" image using Equation 3.2. A normalization matrix is created from the 2D polynomial fit using Equation 3.3. Finally, the "Background Subtracted" image is multiplied by the normalization matrix to create an "Evened Image."

By eye, the post-filter image, "Evened Image," in Figure 3.4, does not appear to retain any of the light gradient present in the "Raw Image." We can confirm numerically that after correction, nearly all the image variance is within blocks. In Figure 3.5, the fraction of variance within blocks is plotted for all images, with most images containing over 98% of their variance within grid blocks.

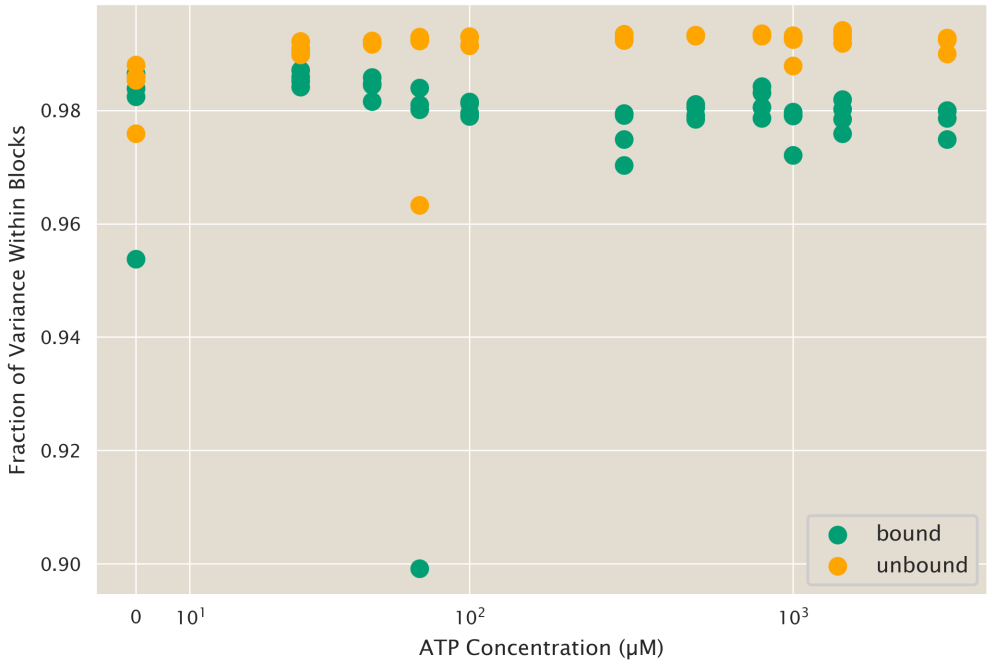

Figure 3.5: **Nearly all of the image variance is located within grid blocks after correction.** After applying a 2D polynomial filter to the images, over 85% of variance is located within grid blocks, and over 98% for most images. There is no apparent correlation between variance fraction and ATP concentration. Green dots mark data from images taken in the bound ATP channel, while orange dot mark data from the unbound ATP channel.

Most of the variance before correction occurred along the $y = -x$ diagonal, as seen in Figure 3.4. Visually, we see the result of the 2D polynomial filter in Figure 3.6, which plots the intensity value of the image versus the distance along the $y = -x$ diagonal, represented by the multiplication of the x and y pixel coordinate. Indeed, we see a negative slope before correction and an approximately zero slope after correction.

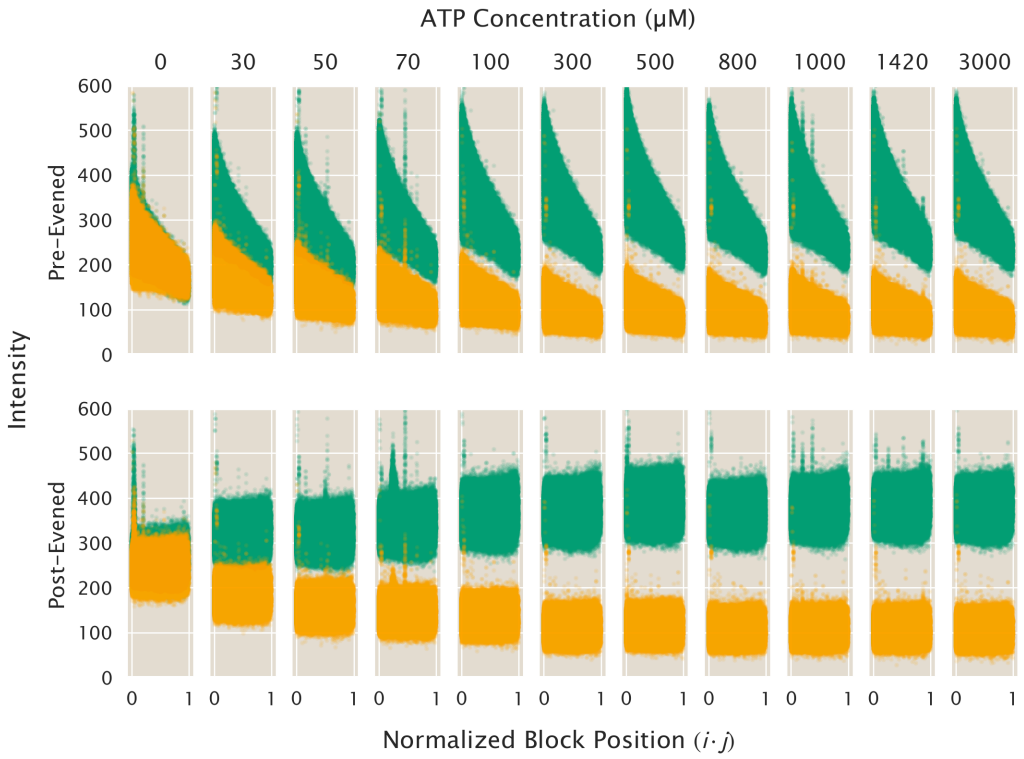

Figure 3.6: **Intensity trend with pixel location.** The intensity value of a pixel versus the location of the pixel is plotted along the upper left to lower right diagonal of the image, as assigned by the multiplication of the pixel coordinates, $i \cdot j$. The green dots represent data from the bound ATP channel (excitation 405 nm) and the orange dots present data from the unbound channel (excitation 480 nm). In the top row of plots, images taken before uneven illumination correction, regardless of ATP concentration or imaging channel, show a negative slope. In the second row, images after uneven illumination correction have approximately no slopes, indicating that the filter correctly removed any illumination bias along the diagonal.

Regardless of the gradient direction, for an image of a homogeneous ATP sample to be even, we would expect grid block averages should be the same across the image. This would imply that there is not a correlation between the intensity of the block and it's location. In Figure 3.7A and Figure 3.7B, we mark the average value for every grid block of every image. The average values are color coded by their grid block's location, which is mapped out in Figure 3.7C. For each ATP concentration, there is no clear trend in the intensity based on block location (with the exception of the corner blocks – the deepest purple and red dots – which are subject to edge effects).

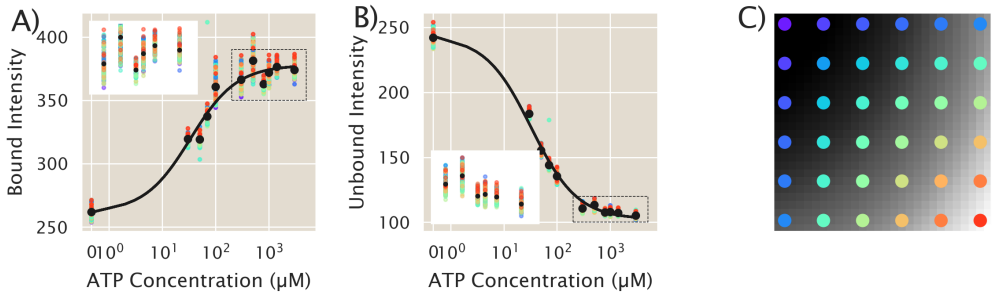

Figure 3.7: **After correction, grid block values of homogeneous ATP images do not depend on block location.** The average grid block intensity values for all images are plotted with respect to the ATP concentration of the sample, where A) reports data from the bound ATP channel and B) reports data from the unbound ATP channel. The data points are color coded by the location of their grid block. Black dots are the average value for each ATP concentration. A subset of data is plotted in the white inset of both figure A) and B) for a zoomed in view of the data spread. The data in the inset is denoted by the dotted black rectangle. A map of the grid block location by color is shown in C) overlayed on an unevened ATP image.

We additionally fit intensity versus ATP concentration for each grid block using a Michaelis-Menten curve of the form,

$$I = (I([\text{ATP}] = \infty) - I([\text{ATP}] = 0)) \frac{[\text{ATP}]}{K_\text{M} + [\text{ATP}]} + I([\text{ATP}] = 0), \qquad (3.5)$$

where I is the intensity of the block, and K_M is the Menten constant. We plot the the fit parameters versus the block position in Figure 3.8. Again, there is no significant trend based on the region of the image and the fit parameters are roughly centered about the mean fit parameter.

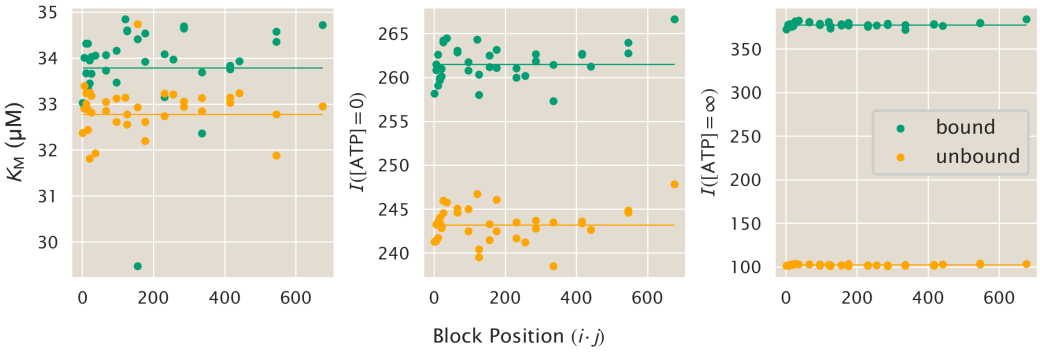

Figure 3.8: **Michaelis-Menten fit parameters of the evened image do not have a trend.** We fit the intensity versus ATP concentration to a Michaelis-Menten curve of the form of Equation 3.5. Plotting the fit parameters versus grid block position, as denoted by multiplying the i, j coordinates of a grid block, we find no trend based on position. The bound ATP channel is plotted in green, while the unbound channel is orange. The fit to the averaged evened images are represented by a horizontal line.

We now have confidence in our ability to correct any image of a homogeneous ATP sample. Taking a 2D polynomial fit of the image, we find the gradient of light and create a normalization matrix to remove it. However, if our image was not of a uniform sample, gradients in light may be due to features of the experiment and thus the image's 2D polynomial fit may not only contain information on uneven illumination. However, if the normalization matrices of homogeneous ATP samples are the same across multiple images and across ATP concentrations, these matrices could be applied to remove uneven illumination from experimental images with real gradients. We compute the normalization matrices for homogeneous images across a range of ATP concentrations. In Figure 3.9, we plot the mean value of 36 grid blocks distributed through the image, where each ATP concentration value has four repeats. The standard deviation is very low, a fraction of a percent, compared to the mean value, indicating the same normalization matrix could be used to describe images taken at a variety of ATP concentrations. However, we do note that each light channel should have its own filter correction as the mean normalizaiton values for images taken at 405 and 480 channel emissions differ.

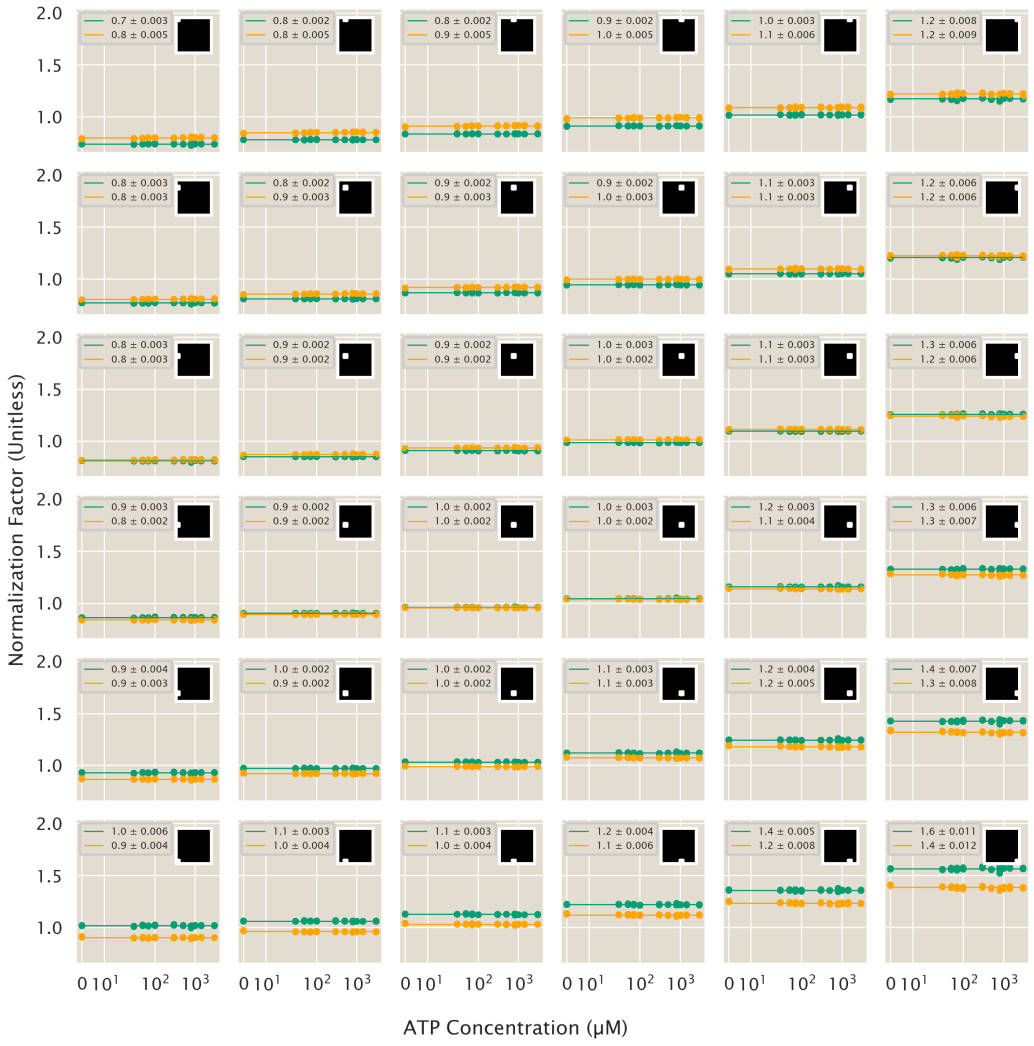

Figure 3.9: **The normalization matrices across ATP concentrations report the same value at a given grid block.** Each subplot charts the average intensity value for a given grid block where the inset shows the location of the grid block within the image. The horizontal lines plot the evened image average and the standard deviation is low, a fraction of a percent compared to the mean, indicating the average of filters well represent each filter.

In this data set, we measure the intensity values reported by the ATP probe for a range of known ATP concentrations. Thus, from these images, we can establish a calibration of the intensity values for given ATP concentrations. Taking the ratio of the bound to unbound image intensity values, we fit the data to a Michaelis-Menten function,

$$R = (R_{\max} - R_{\min}) \frac{\frac{[\mathrm{ATP}]}{K_{\mathrm{M}}}}{1 + \frac{[\mathrm{ATP}]}{K_{\mathrm{M}}}} + R_{\min}, \tag{3.6}$$

where R is the intensity ratio of the bound and unbound channels, [ATP] is the concentration of ATP, and K_M is the Michaelis-Menten constant, as shown in Figure 3.10.

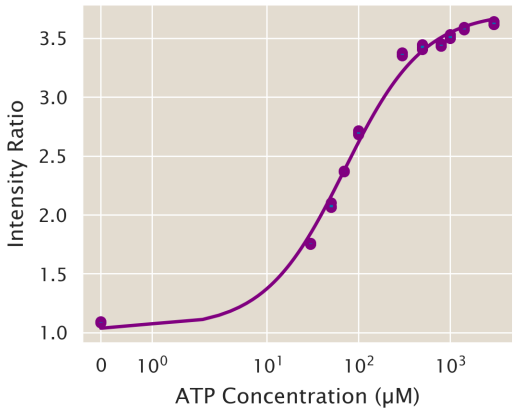

Figure 3.10: **ATP Calibration Curve.** Intensity versus ATP concentration values are plotted where each ATP concentration has four replicates. The data is fit to a Michaelis-Menten curve of the form of Equation 3.6. Here, $K_M = 70\,\mu$M, $R_{max} = 3.7$, and $R_{min} = 1$.

We are left to ask what are the error bars on our calibration? In answering this question, we additionally ask how the standard deviation of intensity values scale with increasing ATP concentration. We plot the histograms of intensity values for the evened images in Figure 3.11. We find that as the ATP concentration increases, so does the mean, while the standard deviation remains nearly constant. We plot the Gaussian distribution given our histogram's mean and standard deviation and find the intensity is well predicted by a Gaussian of the form,

$$\frac{1}{\sqrt{2\pi\sigma}} \exp\left(\frac{-(x-\mu)^2}{2\sigma^2}\right). \tag{3.7}$$

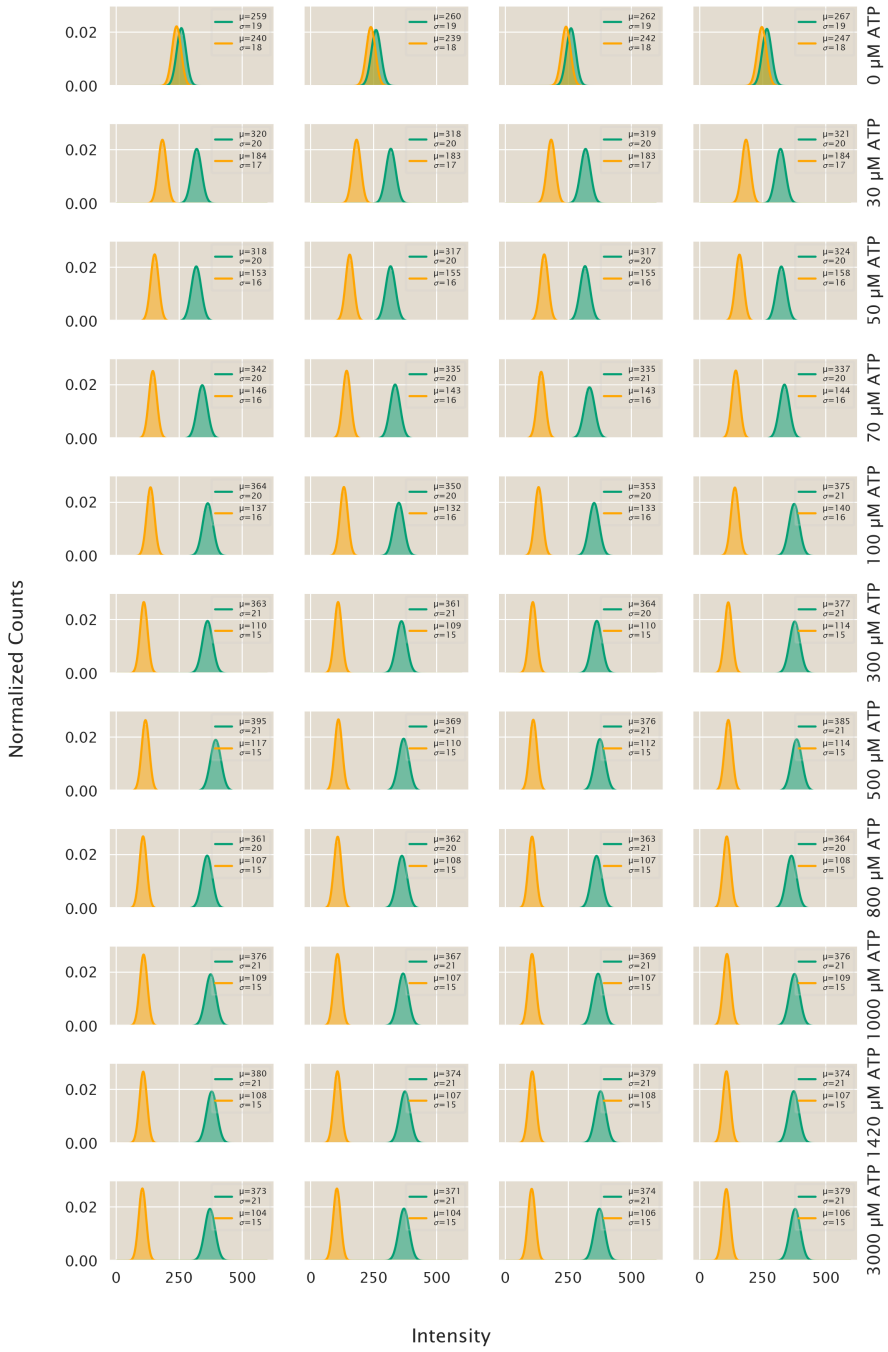

Figure 3.11: **Intensity histograms of evened images are Gaussian distributed.** Each row contains intensity distributions for four replicate images at a given ATP concentration. Plugging the mean and standard deviations of the histograms into Equation 3.7, a Gaussian curve describing the distribution is plotted by the solid line. With increasing ATP concentration, there is little change in the standard deviation relative to the mean. Green curves represent the bound excitation channel, while orange curves represent the unbound excitation channel.

While dividing two Gaussian functions does not result in a Gaussian, we find the ratio of bound to unbound intensities can still be approximated by a Gaussian, as shown in Figure 3.12. We now find there is a significant broadening in the histograms, indicating that as the ATP concentration increases, so too does the ratio mean and standard deviation.

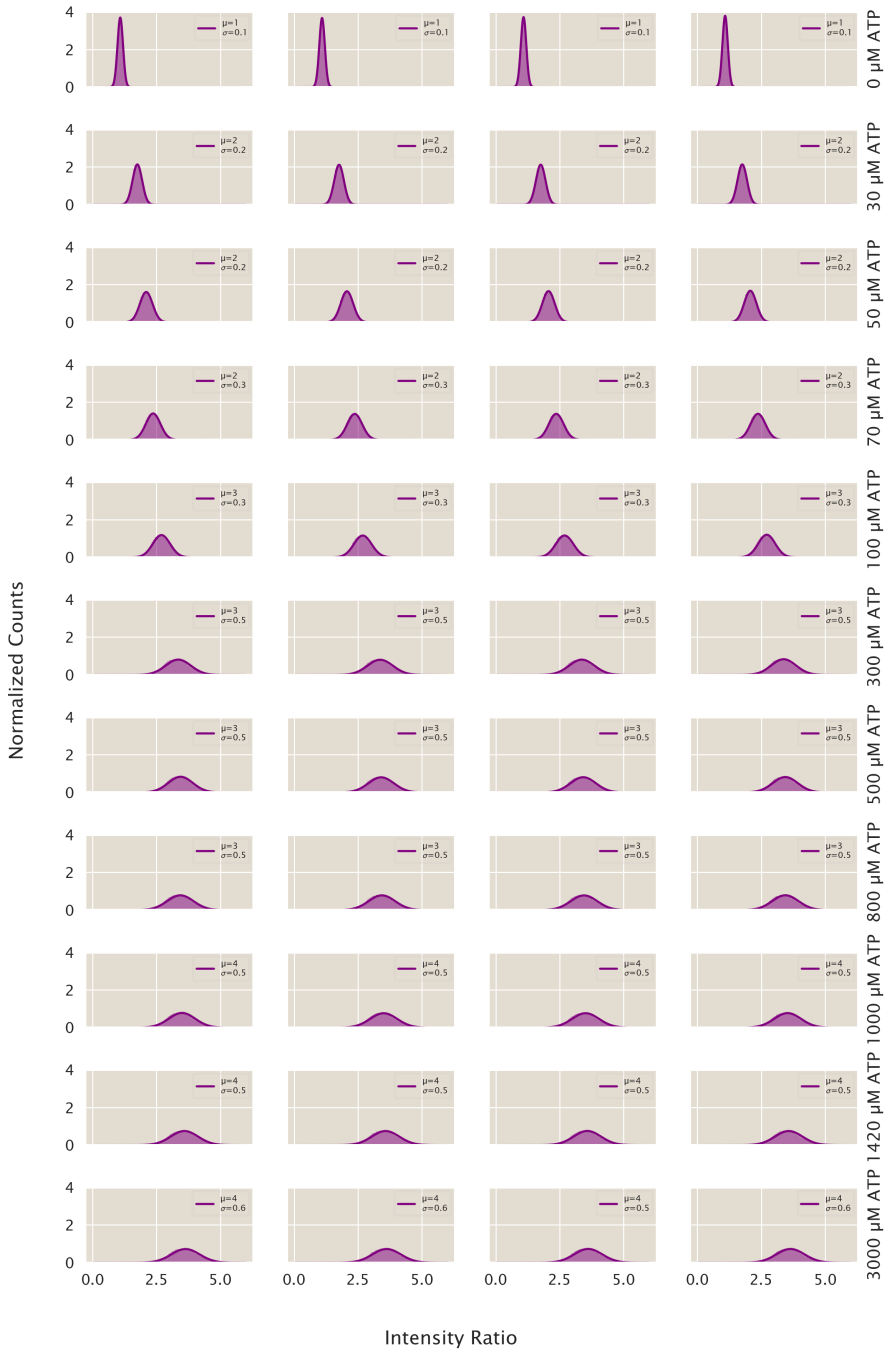

Figure 3.12: **Intensity ratios are Gaussian distributed.** Each row contains intensity ratio distributions for four replicate images at a given ATP concentration. Plugging the mean and standard deviations of the histograms into Equation 3.7, a Gaussian curve describing the distribution is plotted by the solid line. As ATP concentration increases, there is significant broadening of the ratios histogram, such that the standard deviation increases.

Understanding how the standard deviation scales with the mean of the intensity ratio distribution can help inform us how to compute the error of our calibration at various ATP concentrations. In Figure 3.13, the standard deviation is shown to trend linearly with the mean of the histograms. For the intensity values measured by the bound and unbound channels, there is a very small slope, 0.02, such that the standard deviation is relatively unaffected by the mean. However, for the ratio of these two channels, the slope is, 0.18, which results in notable changes in the standard deviation for our range of ATP concentrations. Thus, our next step will be to use these results to model the error on our ATP calibration fit.

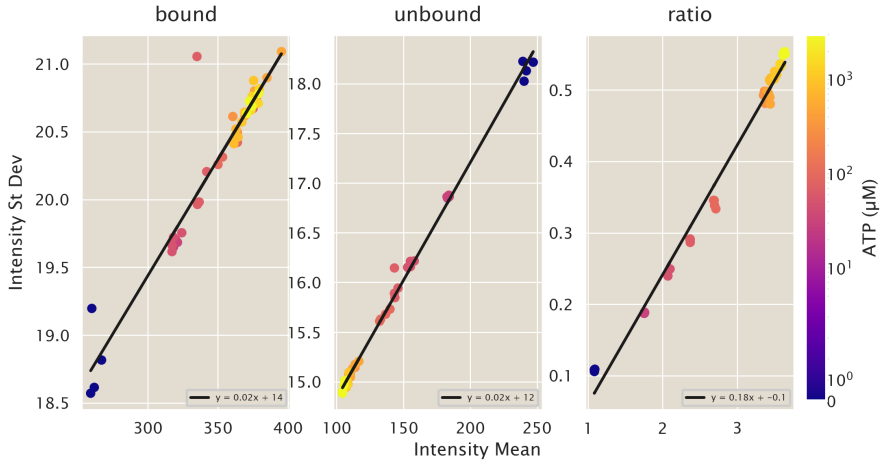

Figure 3.13: **The mean and standard deviation of intensity histograms are linearly related.** Here we plot the standard deviation versus the mean across ATP concentrations and linearly fit the data (black line). For both the bound and unbound intensity channels, there is a weak positive slope of 0.02 between the mean and standard deviation of the intensity distributions. However, there is a larger slope of 0.18 for the distribution of the ratio of intensities. Thus, the linear relation describes the broadening of the histograms seen in Figure 3.12 .

Proof the Total Variance is the Sum of the Variances Within and Between Grid Blocks

The total variance of the image, can be written as

$$\sigma^2_{\text{tot}} = \frac{1}{N}\sum_{i}^{N}(I_i - \langle I \rangle)^2 \tag{3.8}$$

where i sums over each pixel, I_i is the intensity value of a given pixel, and $\langle I \rangle$ is the average intensity value of all pixels in the image. To understand if most of the

variance in the images occur within given regions of the image or between regions of the image, we divide the image into a grid with B blocks each containing N_B pixels. Inside of a given grid block, indexed j, the variance is

$$\sigma^2_{\text{in}} = \sigma^2_{\text{j}} = \frac{1}{N_B} \underbrace{\sum_{i}^{N_B}}_{\text{in } j} \left(I_i - \langle I \rangle_j\right)^2, \tag{3.9}$$

which sums over all pixels, i, that are within block j, and where $\langle I \rangle_j$ is the average of pixel intensity values within block j. Finally, we define the variance between blocks as,

$$\sigma^2_{\text{btwn}} = \frac{1}{B} \sum_{j}^{B} \left(\langle I \rangle_j - \langle I \rangle\right)^2. \tag{3.10}$$

Let us rewrite the form of the total variance to see how it relates to the variance inside and between blocks,

$$\sigma^2_{\text{tot}} = \frac{1}{B} \sum_{j}^{B} \frac{1}{N_B} \underbrace{\sum_{i}^{N_B}}_{\text{in } j} \left(I_i - \langle I \rangle\right)^2. \tag{3.11}$$

Expanding the square yields,

$$\sigma^2_{\text{tot}} = \frac{1}{B} \sum_{j}^{B} \frac{1}{N_B} \underbrace{\sum_{i}^{N_B}}_{\text{in } j} \left(I_i^2 - 2I_i \langle I \rangle + \langle I \rangle^2\right). \tag{3.12}$$

We add and subtract $-2I_i \langle I \rangle_j + \langle I \rangle_j^2$ to simplify terms to the form of inside block variance. Highlighting terms in red that become the inside block variance,

$$\begin{aligned}
\sigma^2_{\text{tot}} &= \frac{1}{B} \sum_{j}^{B} \frac{1}{N_B} \underbrace{\sum_{i}^{N_B}}_{\text{in } j} \left(I_i^2 - 2I_i \langle I \rangle + \langle I \rangle^2 \, {\color{red}-2I_i \langle I \rangle_j + \langle I \rangle_j^2} + 2I_i \langle I \rangle_j - \langle I \rangle_j^2\right) \\
&= \frac{1}{B} \sum_{j}^{B} \frac{1}{N_B} \underbrace{\sum_{i}^{N_B}}_{\text{in } j} \left({\color{red}\left(I_i - \langle I \rangle_j\right)^2} - 2I_i \langle I \rangle + \langle I \rangle^2 + 2I_i \langle I \rangle_j - \langle I \rangle_j^2\right) \\
&= \frac{1}{B} \sum_{j}^{B} \left({\color{red}\sigma_j^2} + \frac{1}{N_B} \underbrace{\sum_{i}^{N_B}}_{\text{in } j} \left(2I_i \left(\langle I \rangle_j - \langle I \rangle\right) - \langle I \rangle_j^2 + \langle I \rangle^2\right) \right).
\end{aligned} \tag{3.13}$$

Bringing all terms that do not depend on i out of the first sum,

$$\sigma_{\text{tot}}^2 = \frac{1}{B}\sum_j^B \left(\sigma_j^2 - \langle I \rangle_j^2 + \langle I \rangle^2 + \frac{2}{N_B}\left(\langle I \rangle_j - \langle I \rangle\right) \underbrace{\sum_i^{N_B}}_{\text{in } j} I_i \right). \tag{3.14}$$

Note that $\frac{1}{N_B}\underbrace{\sum_i^{N_B}}_{\text{in } j} I_i$ is simply $\langle I \rangle_j$, so we can write

$$\sigma_{\text{tot}}^2 = \frac{1}{B}\sum_j^B \left(\sigma_j^2 - \langle I \rangle_j^2 + \langle I \rangle^2 + 2\left(\langle I \rangle_j - \langle I \rangle\right)\langle I \rangle_j \right). \tag{3.15}$$

With some algebra, we can simplify our expression,

$$\begin{aligned}
\sigma_{\text{tot}}^2 &= \frac{1}{B}\sum_j^B \left(\sigma_j^2 - \langle I \rangle_j^2 + \langle I \rangle^2 + 2\langle I \rangle_j^2 - 2\langle I \rangle_j \langle I \rangle \right) \\
&= \frac{1}{B}\sum_j^B \left(\sigma_j^2 + \langle I \rangle_j^2 - 2\langle I \rangle_j \langle I \rangle + \langle I \rangle^2 \right) \\
&= \frac{1}{B}\sum_j^B \left(\sigma_j^2 + \left(\langle I \rangle_j - \langle I \rangle\right)^2 \right) \\
&= \frac{1}{B}\sum_j^B \sigma_j^2 + \frac{1}{B}\sum_j^B \left(\langle I \rangle_j - \langle I \rangle\right)^2.
\end{aligned} \tag{3.16}$$

Interestingly, the second term on the right hand side is exactly Equation 3.10, the variance between blocks,

$$\sigma_{\text{tot}}^2 = \frac{1}{B}\sum_j^B \sigma_j^2 + \sigma_{\text{btwn}}^2. \tag{3.17}$$

We can interpret the first term as the average of the variances within blocks,

$$\sigma_{\text{tot}}^2 = \left\langle \sigma_{\text{in}}^2 \right\rangle + \sigma_{\text{btwn}}^2. \tag{3.18}$$

Thus, the total variance in the image is average variance inside blocks plus the variance between blocks. Now, we have a direct way to determine how much variance is between blocks, implying uneven illumination.

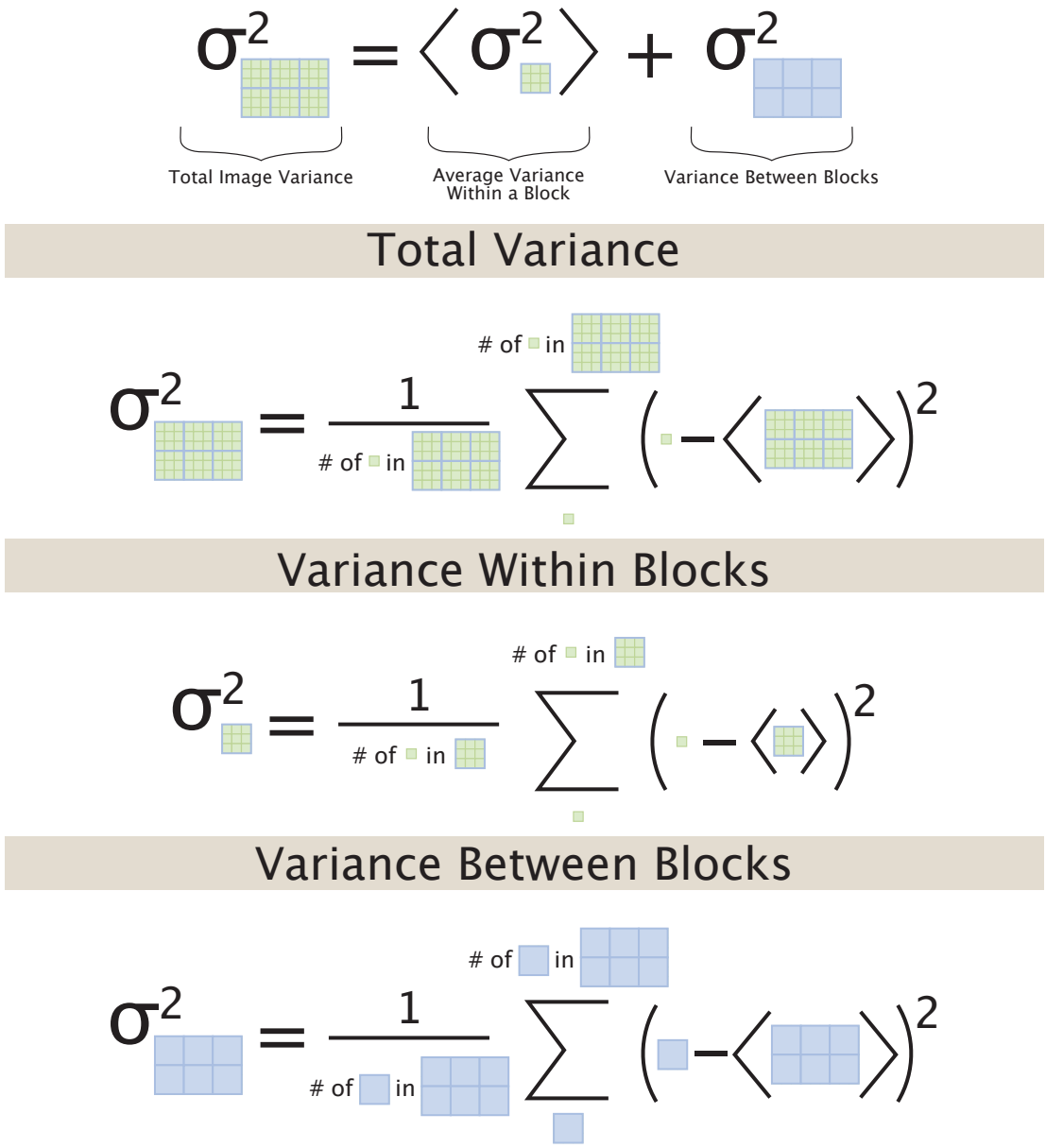

Figure 3.14: **Graphical representation of variance between and within blocks.** The top panel is the equation for the total variance in terms of the variance within a block and between blocks. The subsequent three panels graphically depict the definition of each type of variance, where a single green block represents one pixel, i, and a blue block represents one grid block, j, containing N_{B} pixels.

3.3 Conceivable Geometric and Optical Distortions Arising from 2D Images of 3D Distributions

Monitoring the rapidly changing, and optically labile, chemical reactions driving aster formation with microscopy imposes fundamental technical constraints on our

measurements. Specifically, while asters are formed by molecular motors, microtubules, and ATP arranged in rich three-dimensional structures, imaging these distributions fully in three dimensions over our conditions of biochemical interest would significantly constrain the fastest changes resolvable in these spatial fields. In addition, acquiring 3D data (via many tightly-spaced 2D images in an axial dimension) imposes a significantly larger burden of excitatory photons that can photobleach and further perturb fluorescently-labeled molecules like those we monitor. Consequently, to capture fine changes in aster structure over space and time, the bulk of our measurements are in the form of two-dimensionsal epifluorescence images of developing asters. These images are collected while focused at a central axial plane through the aster.

To interpret this slew of experimental results, in principle, we must account for the difference between our 3D objects of interest and the 2D epifluorescence microscopy images representations of these structures. Here, in the sections that follow, we assess the possible consequences/distortions following from these two-dimensional acquisitions, both conceptually in general, and empirically for our specific imaging conditions. To augur what follows, our analyses largely show that the conceptually-possible differences between two-dimensional data and three-dimensional distributions are in fact empirically negligible, largely due to the narrowness of the optical point spread functions convolving these images compared to the shape of the raw underlying structures we image.

Our discussion that follows proceeds in three parts. First, we consider the ideal case where the optical weighting function along the axial dimension is zero everywhere except the focal plane actually sampled, meaning the acquired 2D image precisely matches the equivalent 3D slice (with no distortion). Second we consider the opposing case where the weighting function is uniform along the axial dimension, resulting in a uniform projection when integrating over each slice in the axial dimension. Lastly, we consider the most realistic case falling between these two limits, where a nonzero, nonuniform, weighting function accumulates fluorescence signal from slices above and below the focal plane, giving a convolution with the signal at the focal plane. In imaging practice, we numerically verify that the narrowness of this weighting function (relative to the objects of interest) makes this case closely approximate the first case of a bona fide slice through the underlying three dimensional distribution.

General form of a 2D image projection

In general, a two dimensional image $\hat{I}(x, y)$ collected at spatial position (x, y) is an integral of a true underlying source profile $I(x', y', z')$ from sources at positions (x', y', z'), where each source is weighted by some optical weighting function $f(x', y', z')$ throughout space,

$$\hat{I}(x, y) = \int_{-\infty}^{\infty} \int_{-\infty}^{\infty} \int_{-\infty}^{\infty} I(x', y', z')\ f(x', y', z')\, \mathrm{d}x'\mathrm{d}y'\mathrm{d}z'. \tag{3.19}$$

Specific imaging cases

In a first ideal case, when the weighting function is simply a Dirac delta function over the axial dimension centered at the focal plane at z, namely $f(x', y', z') = \delta(x - x')\delta(y - y')\delta(z - z')$, the image $\hat{I}^{(1)}(x, y)$ is exactly the corresponding focal slice through the three dimensional profile,

$$\hat{I}^{(1)}(x, y) = \int_{-\infty}^{\infty} \int_{-\infty}^{\infty} \int_{-\infty}^{\infty} I(x', y', z')\ \delta(x - x')\delta(y - y')\delta(z - z')\, \mathrm{d}x'\mathrm{d}y'\mathrm{d}z' \tag{3.20}$$

$$= I(x, y, z). \tag{3.21}$$

In a second opposing case, the image accumulates signal uniformly over sources along the axial dimension, namely $f(x', y', z') = \delta(x - x')\delta(y - y') \times 1$. This gives an image $I^{(2)}(x, y)$ of the form,

$$\hat{I}^{(2)}(x, y) = \int_{-\infty}^{\infty} \int_{-\infty}^{\infty} \int_{-\infty}^{\infty} I(x', y', z')\ \delta(x - x')\delta(y - y')\, \mathrm{d}x'\mathrm{d}y'\mathrm{d}z' \tag{3.22}$$

$$= \int_{-\infty}^{\infty} \mathrm{d}z'\ I(x, y, z). \tag{3.23}$$

When the underlying distributions $I(x, y, z)$ are axially- symmetric or spherically-symmetric ($\equiv I(\rho, \theta)$ or $\equiv I(r)$), such images two dimensional images $\hat{I}$ adopt the forms of Abel transformations [7]. In principle, the underlying $I(r)$ or $I(\rho, \theta)$ can be recovered by an inverse Abel transformation [7, 8] on the measured two-dimensional image $\hat{I}$, though in practice, the numerical success of these schemes is a delicate and often fraught inverse problem.

In a third, intermediate, and most realistic case, we acknowledge that the sources from above and below the focal plane at z can contribute with nonzero weight to the measured signal at z, and also further acknowledge the possible contributions of sources at transverse positions (x', y') distinct from the query position (x, y). Specifically, the optical weighting function of a source at (x', y', z') is a point-spread function (set by the microscope) well modeled as depending only on the displacement $(x - x', y - y', z - z')$ to the query point (x, y). This gives an image $\hat{I}^{(3)}(x, y)$ of the form,

$$\hat{I}^{(3)}(x, y) = \int_{-\infty}^{\infty} \int_{-\infty}^{\infty} \int_{-\infty}^{\infty} I(x', y', z') f(x - x', y - y', z - z') \, \mathrm{d}x' \mathrm{d}y' \mathrm{d}z'. \quad (3.24)$$

Models of the point spread function $f(x-x', y-y', z-z')$ corresponding to circular apertures appropriate for microscope objectives are available [9, 10, 11] to varying levels of analytical and numerical detail, including the popular Born and Wolf model expressed in terms of Airy and Bessel functions. Often a very good approximation to these empirical circumstances is a Gaussian decay factorizable in transverse and axial dimensions with anisotropic widths, namely,

$$f(x - x', y - y', z - z') = \mathrm{psf}_{\mathrm{tr}}(x - x', y - y' | \sigma_{\mathrm{tr}}^2) \times \mathrm{psf}_{\mathrm{ax}}(z - z' | \sigma_{\mathrm{ax}}^2). \quad (3.25)$$

Case Two: Abel Transformation

When the optical weighting function is not purely localized at the focal plane, but instead is uniform throughout the axis of the imaging volume, the distortion of a three-dimensional profile is conceivably appreciable. Image sources at axial positions far away from the focal plane are convolved with sources actually residing at the focal plane, in principle posing an intractable ill-posed inverse problem: there are many different underlying 3D distributions consistent with a given 2D measured image. However, intriguingly, when the underlying distribution $I(x, y, z)$ is spherically-symmetric or axially-symmetric, a measured two-dimensional profile $\hat{I}(\rho, \theta)$ uniquely specifies the original three-dimensional profile, a relationship expressed by the so called Abel transformation and its complement, the inverse Abel transformation. Here, we explicitly describe how a radially-symmetric image (e.g., of spherically-symmetric aster) manifests a two dimensional projection forming an Abel transformation, under this pessimistic scenario when the optical weighting function does not decay away from the focal plane as rapidly as expected from epifluorescence microscopy. We also remark on qualitative features that can be analytically shown to survive in such a two dimensional uniformly-weighted projection. We provide this discussion to give maximally conservative statements about how

two dimensional images still report on key features of three dimensional structures, even in the counterfactual setting where distant image sources are weighted equally to those appearing on the focal plane.

Imagining a 3D, spherical aster where we possess an omniscient knowledge of the concentration profile, we ask what will be the concentration profile reported by a microscope 2D image? To solve, we integrate the height, over z (in cylindrical coordinates), of a skyscraper cutting through the aster sphere. For a given skyscraper address with cylindrical coordinates (ρ, θ), we calculate the concentration of the image pixel value corresponding to the skyscraper,

$$\hat{I}(\rho, \theta) = \int_0^h dz\, I(\rho, \theta, z). \tag{3.26}$$

Since there is radial symmetry in θ, we can remove the θ dependence in the integral such that,

$$\hat{I}(\rho) = \int_0^{2\pi} d\theta \int_0^h dz\, I(\rho, z) = 2\pi \int_0^h dz\, I(\rho, z). \tag{3.27}$$

We now change to spherical coordinates, rather than cylindrical, since we consider the aster to be a sphere. Thus, the concentration as a function of r, which depends on ρ and z, can be written as,

$$\hat{I}(\rho) = 2\pi \int_0^h dz\, I(r(\rho, z)). \tag{3.28}$$

Since for a given skyscraper ρ is constant, we can change the integration variable from z to r with the equation,

$$r^2 = \rho^2 + z^2. \tag{3.29}$$

Differentiating with respect to r,

$$2r = 2z\frac{dz}{dr} \Rightarrow dz = \frac{r}{z}dr. \tag{3.30}$$

Using the substitution, $z = \sqrt{r^2 - \rho^2}$,

$$dz = \frac{r}{\sqrt{r^2 - \rho^2}}dr. \tag{3.31}$$

Thus, the concentration at a given 2D image radius, ρ of a 3D aster is,

$$\hat{I}(\rho) = 2\pi \int_\rho^{\sqrt{\rho^2+h^2}} dr\, I(r)\frac{r}{\sqrt{r^2 - \rho^2}}. \tag{3.32}$$

As a sanity check, we can ensure that a uniform concentration in 3D, $I(r, \theta, \phi) = I_0$ is still uniform in 2D. Plugging this constant into equation 3.34,

$$\hat{I}(\rho) = 2\pi I_0 \int_{\rho}^{\sqrt{\rho^2+h^2}} dr \, \frac{r}{\sqrt{r^2 - \rho^2}}, \tag{3.33}$$

and performing a u-substitution where $u = \sqrt{r^2 - \rho^2}$ and $du = r/\sqrt{r^2 - \rho^2}$,

$$\hat{I}(\rho) = 2\pi I_0 \int_0^h du = 2\pi I_0 h. \tag{3.34}$$

We can ensure that if we simply integrated over a constant sample from the perspective of the microscope, we would obtain the same constant,

$$\hat{I}(\rho, \theta) = \int_0^h dz \, I_0 = I_0 h, \tag{3.35}$$

and assuming spherical symmetry,

$$\hat{I}(\rho) = \int_0^{2\pi} d\theta \, I_0 h = 2\pi I_0 h. \tag{3.36}$$

The transform defined in equation 3.34, is called an Abel Transform, and has an analytical inverse function, under the condition that $I(r) \to 0$ faster than $\frac{1}{r}$ [8].

3.4 Empirical Deconvolution on an Aster

Here we acknowledge the contributions of intensity signals from nearby pixels on a queried pixel as directed by a finite width point spread function. The majority of data in this study analyzes 2D images that pass through the aster center. Figure 3.15 depicts an image of this type. In analyzing the intensity "smearing" that occurs from neighboring pixels, it is important to not only evaluate the contribution of other pixels in the same plane but also pixels in planes above and below the pixel of interest. In this section, we evaluate how the results of deconvolution on 3D image stacks of an aster modify the intensity value of the resultant image. We acquire images of an aster motor distribution every $0.5\,\mu$m in the axial direction. We then perform a deconvolution procedure using an ImageJ plugin, Deconvolution Lab2 [9], employing the Richardson-Lucy deconvolution method. As inputs, we provide an image or image stack and also a point spread function. For circular apertures, the point spread function has been shown to be an Airy function [10]. However, for ease of use, practitioners often approximate these functions with a Gaussian. We demonstrate the results of deconvolving with both of these methods.

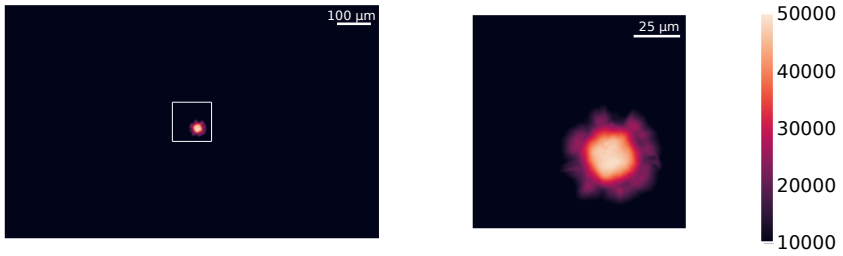

Figure 3.15: **Image of the center of an aster for deconvolution.** As an example image for deconvolution, the center plane of a z-stack of a fully formed aster is shown. On the left, the full figure dimensions are shown, while on the right, a cropped view of the center of the image is shown, corresponding to the white square on the left. We note the aster is not perfectly centered within the image which is typical for asters as they dynamically form. Our deconvolution method needs to work regardles of the aster centering.

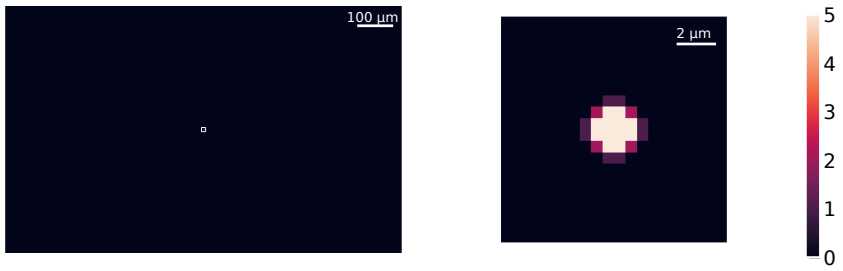

Figure 3.16: **Generated Airy point spread function.** Using the PSF Generator in ImageJ with the Born and Wolf 3D model, we have created a point spread function based on our microscope's optical parameters. The images here are the center slice of the 3D PSF where the left shows the full size of the image and the right is cropped to the center to show the bright center of the PSF.

We generate an Airy PSF using an ImageJ PSF Generator plugin [12]. The plugin requests as inputs the refractive index, which we set to 1 for an air objective, the wavelength of light, which we input as 480 nm, the numerical aperture of the objective, which we set to 0.45, and the nanometer to pixel conversions in each dimension, which for the x and y dimensions, we take to be 578 nm/px and for the z dimension we use 500 nm/px. In Figure 3.16 we show an example of the Airy PSF at the center plane.

Using Deconvolution Lab2, we perform 50 iterations of Richardson-Lucy deconvolution, at first only in 2D, on the sample image shown in Figure 3.15 and deconvolve with the Airy PSF shown in Figure 3.16. In Figure 3.17(A) we show the result of this deconvolution when implemented this way. In Figure 3.17(B) we plot the trace

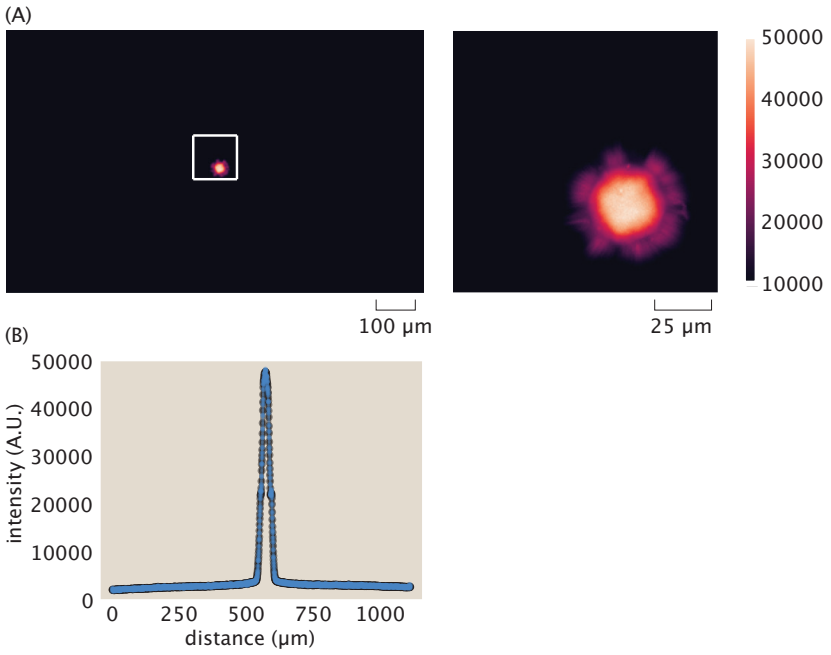

Figure 3.17: **Deconvolving using an Airy PSF in ImageJ reveals a similar output to the raw image input.** (A) The full deconvolution output and cropped deconvolution output are depicted. (B) Taking a cut line through the center of the aster for both the raw image (in black) and the deconvolved output (in blue), we find near perfect agreement in intensity signal. This indicates that the convolution done by the microscope had very little effect on the image.

of a cut line through the center of the aster for the initial raw image in black and the Fiji deconvolved Airy PSF in blue. We find that this deconvolution returns a value practically identical to the raw image trace.

Complementary to using the Airy function, we explore the results of using a Gaussian as already described earlier in the context of synthetic data. In Figure 3.18 we fit the length parameters for the Gaussian to the Airy PSF generated in ImageJ and find that the transverse direction has a length scale of $\sigma_{\text{tr}} = 0.33\ \mu$m and the axial dimension has a length scale of $\sigma_{\text{ax}} = 2.32\ \mu$m. These characteristic widths, and the conceit of Gaussian approximations, to the point spread function are highly consistent with reported values and procedures in related literature; e.g., references [13, 14] report similar widths of $0.3 \sim \mu$m to the transverse character of experimental point spread functions under related conditions.

Upon deconvolving with the Gaussian point spread function, as shown in Figure 3.19, the output again appears nearly identical to the raw image as shown in Figure 3.15.

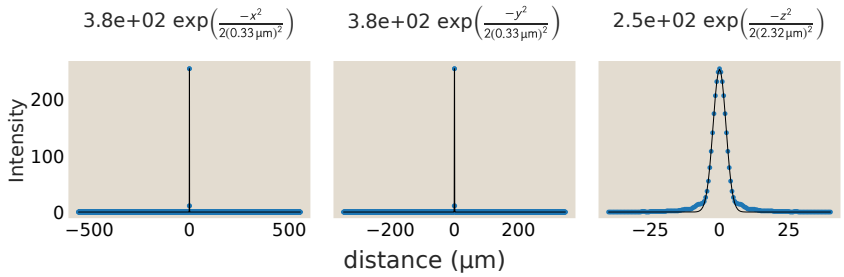

Figure 3.18: **Gaussian length scales are determined by fitting the generated Airy point spread function.** Gaussian functions provide a very good fit to the decay of the point spread function in space. The transverse plane has a small length scale, only 0.33 μm, while the axial direction has a longer, but still small length scale of 2.32 μm.

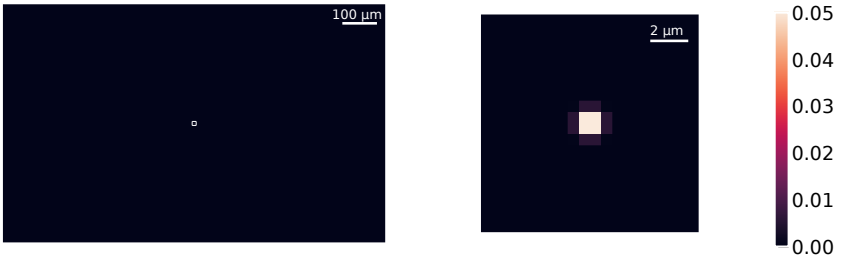

Figure 3.19: **GaussPSF with length scales as determined by the Airy function fits.**

These tests of 2D deconvolutions give us a sense that any effect of convolution by the microscope is minimal. However, it is important to check modifications created by convolutions in the axial dimension, especially since this is the widest dimension of the point spread function, as can be seen in Figure 3.18. To this end, we perform 100 iterations of Richardson-Lucy deconvolution for both the generated Airy PSF and the fit Gaussian PSF. Again, we plot the cut lines through the center of the aster in Figure 3.21 and find little deviation from the raw image. The Gaussian deconvolution again looks identical to the raw image, but for the Airy deconvolution, there is a slight difference at the center of the aster. Here, the Airy deconvolved output produces higher intensities in the aster core and becomes less smooth.

Rather than taking a cut line, we also plot the polar averages of the images centered about the aster with respect to the aster radius shown in Figure 3.22. Once again, we largely see agreement with the raw images. The 3D airy deconvolution is again the only deconvolved output that show any difference with an increased intensity at the aster center.

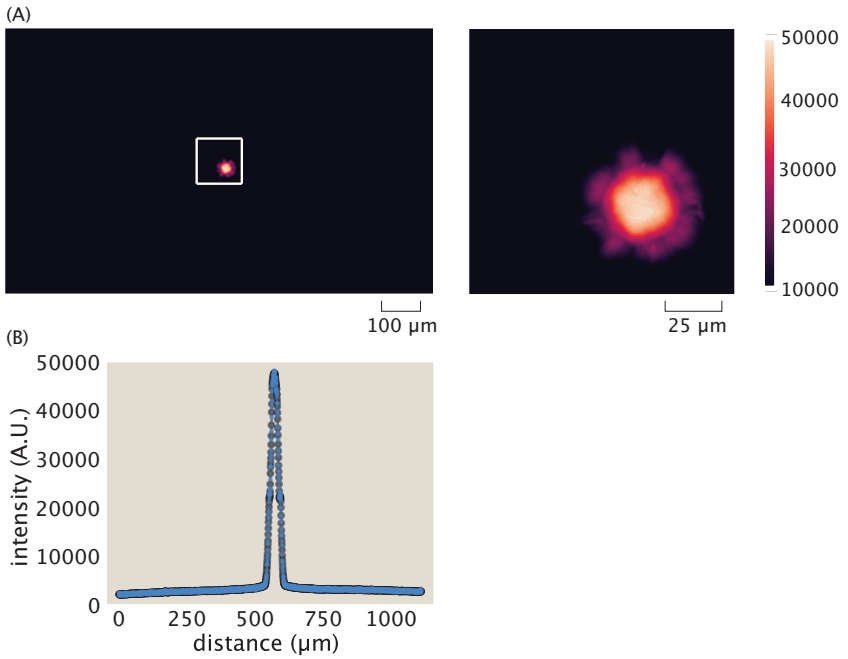

Figure 3.20: **Deconvolving using a Gaussian PSF reveals a similar looking output to the raw image input.** (A) The full deconvolution output and cropped deconvolution output are depicted. (B) Taking a cut line through the center of the aster for both the raw image (in black) and the deconvolved output (in blue), we find near perfect agreement in intensity signal. This indicates that the convolution done by the microscope had very little effect on the image.

Having learned that the quantitative impact of deconvolution in two or three dimensions in real aster images of interest is extremely numerically modest, we now explicitly verify that the ambient background level of fluorescence signal does not change the (small) impact of deconvolution. Figure 3.23 compares how performing background subtraction before or after deconvolution affects the recovered fluorescence profiles. The raw, deconvolved, and background-subtracted then deconvolved traces of Figure 3.23(A) agree up to the background offset, and very small numerical noise. This agreement, arguing that deconvolution and background subtraction largely commute numerically, shows that the presence of an ambient signal background in real aster images leaves the result of deconvolution essentially unchanged (up to exactly the background offset). We further visualize this agreement in Figure 3.23(B) by plotting the difference between the deconvolved image $D[I]$ and the background-subtracted then deconvolved image $D[I - \langle I_{\text{bg}} \rangle]$, relative to the background level $\langle I_{\text{bg}} \rangle$. Over the central line profile of the aster, this difference is very close to unity throughout the image, namely $\frac{D[I]-D[I-\langle I_{\text{bg}} \rangle]}{\langle I_{\text{bg}} \rangle} \approx 1$.

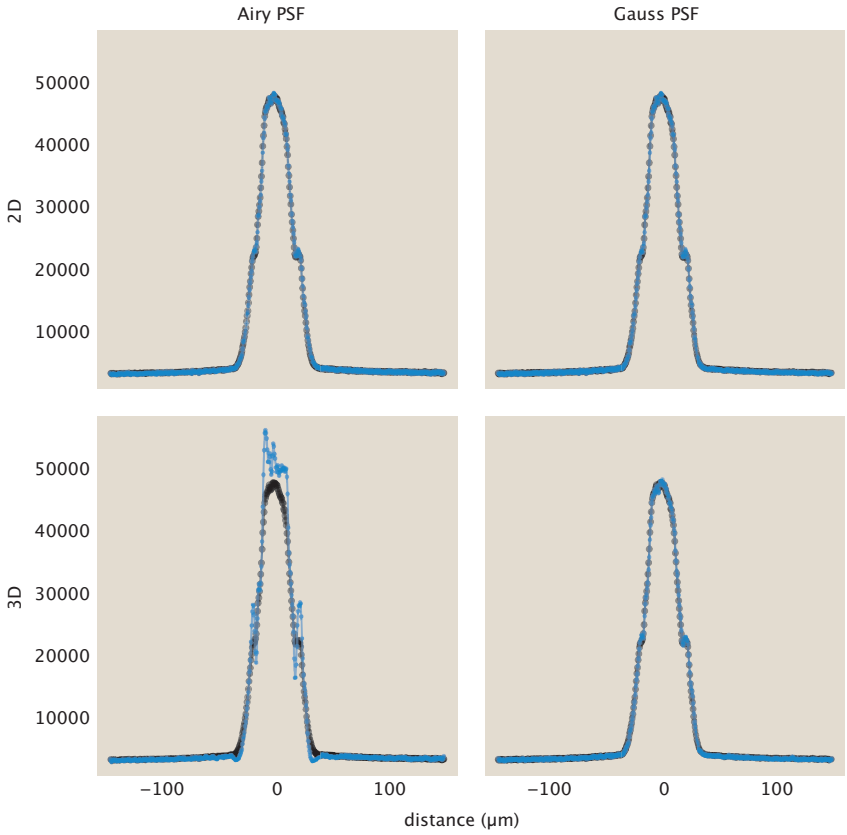

Figure 3.21: **3D deconvolution in ImageJ for Airy or Gaussian PSFs show little deviation from the original image.** For all plots, we include the raw image intensity cutline in black and the deconvolved cutline in blue. The top row highlights the ImageJ 2D deconvolutions while the bottom row highlights their 3D counterparts.

This finding that a background does not nontrivially modify the result of deconvolution (for relevant aster data of interest) complements generic numerical guarantees applying to Richardson-Lucy deconvolution. Studying the deconvolution operation in the context of astronomical images, Prato and coworkers [15] establish that performing Richardson-Lucy deconvolution conserves intensity flux both locally and globally in input images, when the background of the image is zero. Our numerical analysis suggests that the latter proviso that background is zero may not be required for these algorithms on our class of data.

In sum, we find deconvolving has little to no impact on the image. This is especially clear in Figure 3.22 where only the 3D Airy deconvolution shows any discrepancy between the raw and deconvolved images. And even here, there is a maximum of approximately a 10% difference between the intensity values within 15 μm of the aster center. Based on these results, we do not find it imperative to include a

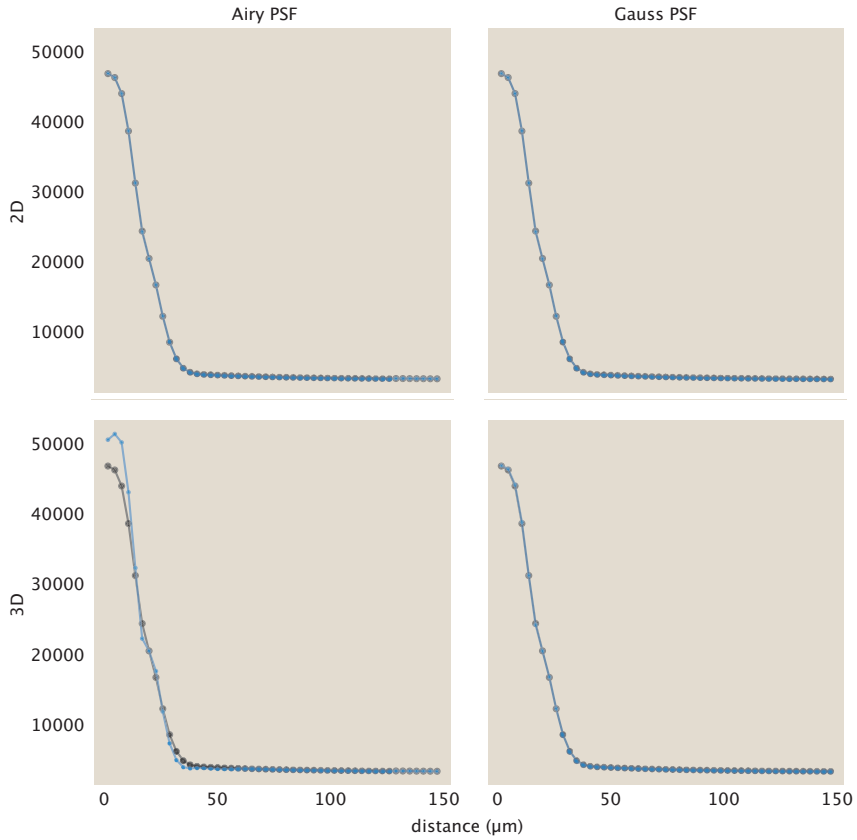

Figure 3.22: **Polar averaging deconvolved outputs also largely agree with the raw polar averages.** We take the averaged intensity of volume normalized radial shells and plot how the intensity changes with respect to the distance from the aster center. In black, we show the traces of the raw image and in blue the traces of the deconvolved output. Largely, the deconvolved images in both 2D, on the top row, and in 3D, on the bottom row, match the raw image.

deconvolution procedure when analyzing aster data.

3.5 Effects of Convolution on Image Formation

We were curious to better understand why the deconvolution algorithms led to very modest changes in our measurements. To investigate these questions more deeply, in this section, we examine synthetic data that we subject to the deconvolution procedure to dissect the physics of the deconvolution process.

As noted in the previous section, the formation of an image in a microscope includes convolution with the microscope's point spread function. The point spread function provides a mathematical description of how light from a point source is affected by diffraction and other optical limitations as it passes through the optical path of the

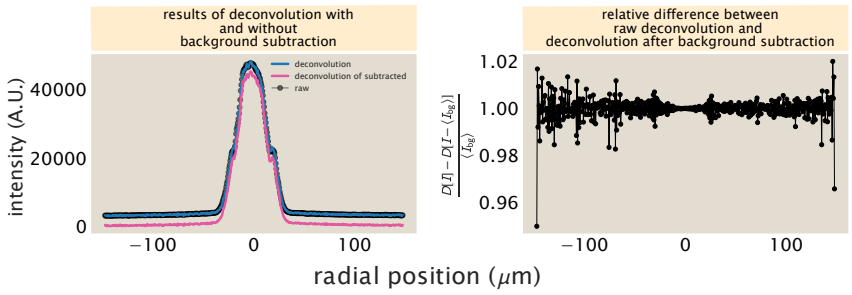

Figure 3.23: **Subtraction of ambient background fluorescence leaves deconvolution results unchanged**. (A) Profiles (slices) of fluorescence along a a line through an aster's center before deconvolution (in black, denoted I); after deconvolution (in blue, denoted $\mathcal{D}[I]$ where $\mathcal{D}$ is the deconvolution operation); and when deconvolution is performed after the ambient $\langle I_{\text{bg}} \rangle$ average level of fluorescence in the regions of space outside the aster is subtracted, $\mathcal{D}[I - \langle I_{\text{bg}} \rangle]$,shown in pink. These traces affirm that the subtraction of ambient fluorescence before or after deconvolution does not affect the shape of the intensity fluorescence profile. These deconvolutions were performed in two dimensions using an Airy-function based point-spread function in DeconvolutionLab2 (via Imagej), as described above. (B) The difference $\frac{D[I]-D[I-\langle I_{\text{bg}} \rangle]}{\langle I_{\text{bg}} \rangle}$ of the blue and black traces in panel (A) relative to the ambient $\langle I_{\text{bg}} \rangle$ level of fluorescence. The fact that this value is consistently very close to unity affirms that $D[I] - D[I - \langle I_{\text{bg}} \rangle] \approx \langle I_{\text{bg}} \rangle$, namely that the background subtraction operation is essentially commutative with respect to deconvolution.

microscope. This convolution causes the resultant image to appear smoother, or blurred, compared to the object itself. As this work measures the number of ATPs at a given location in time via fluorescence, it is important to determine how the PSF spreads and attenuates fluorescence signal, affecting the apparent localization and intensity of ATPs. To get a feeling for the impact of convolution, we mimic the image acquisition procedure on synthetic data. In particular, we specify a symmetric sphere of fluorescent motor proteins whose concentration decays radially. We model the motor concentration field using an exponential decay corresponding to the object

$$\text{obj} = \exp\left(\frac{-\sqrt{x^2 + y^2 + z^2}}{\lambda_o}\right), \tag{3.37}$$

where λ_o is the decay length, which we take to be $\approx 30\,\mu$m for a fully formed aster. For convenience, we do not normalize the object, ensuring that at the origin the intensity value is one.

Our first objective is to explore how convolution modifies the "measured" intensities. To perform a convolution mimicking the imaging process in the microscope, we define a point spread function as a 3D Gaussian. We assume that the point spread

function has different length scales in the transverse (x-y) plane compared to the axial (z) direction. The form of our synthetic point spread function is

$$\mathrm{psf}(x,y,z) = \mathrm{psf}_{\mathrm{tr}}(x,y)\times\mathrm{psf}_{\mathrm{ax}}(z) = \frac{1}{2\pi\sigma_{\mathrm{tr}}^2}\exp\left(\frac{-(x^2+y^2)}{2\sigma_{\mathrm{tr}}^2}\right)\times\frac{1}{\sqrt{2\pi\sigma_{\mathrm{ax}}^2}}\exp\left(\frac{-z^2}{2\sigma_{\mathrm{ax}}^2}\right). \tag{3.38}$$

We estimate the length scale for the transverse point spread function based on the minimum resolvable distance. For a self-luminous light source of incoherent light, which encompasses fluorescent signals, the minimum distance is

$$\sigma_{\mathrm{tr}} \approx \frac{0.61\lambda}{\mathrm{N.A.}}, \tag{3.39}$$

where λ is the wavelength of light and N.A. is the numerical aperture [10]. For our setup, we use a wavelength of 513 nm and our objective has an N.A. of 0.45. These parameters yield the transverse length scale,

$$\sigma_{\mathrm{tr}} = \frac{0.61\times 513\ \mathrm{nm}}{0.45} = 695\ \mathrm{nm} \approx 0.7\,\mu\mathrm{m}. \tag{3.40}$$

For the axial length scale, we compute the depth of focus as

$$\sigma_{\mathrm{ax}} \approx \frac{\lambda\, n}{\mathrm{N.A.}^2}, \tag{3.41}$$

as stated in [16], where n is the index of refraction, which we take as $n = 1$ for an air objective. Plugging in values, we estimate

$$\sigma_{\mathrm{ax}} \approx \frac{0.513\ \mu m\times 1}{(0.45^2)} \approx 2.5\ \mu m. \tag{3.42}$$

Now that we have the parameters describing the point spread function in hand, we now turn to examining its effects. The convolution of the object with the point spread function is characterized by the integral

$$\mathrm{im}(x,y,z) = \int_{-\infty}^{\infty}\int_{-\infty}^{\infty}\int_{-\infty}^{\infty}\mathrm{obj}(x',y',z')\mathrm{psf}(x-x',y-y',z-z')\,\mathrm{d}x'\mathrm{d}y'\mathrm{d}z' \tag{3.43}$$

which amounts to weighting each point in the image with all points in the object, each appropriately multiplied by the point spread function itself.

We use the scipy package, *scipy.signal.convolve* to perform this convolution. We set the "mode" keyword argument to "same" which ensures the returned convolved matrix has the same size as the inputted object. The microscope would acquire an image that reflects the center slice of the convolution. We compare the center slice

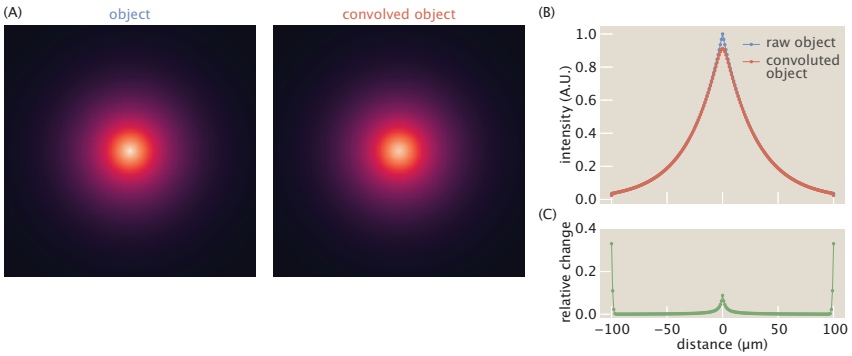

Figure 3.24: **Exploring the effects of convolution with the point spread function for synthetically generated data.** (A) Images of the center plane for both the raw object, a radially decaying exponential sphere of motors, and the convolved image with a Gaussian point spread function. (B) More quantitatively, we plot the intensity of both the object and convolved object along a cut line passing through the object origin. (C) We find most of the relative change, as defined as $\frac{\text{obj}-\text{obj}\star\text{psf}}{\text{obj}}$, occurs in the center of the object. The peaks at the ends are due to edge effects in the convolution.

of the synthetic specified object and the convolved object in figure 3.24(A). By eye it is difficult to distinguish the two slices from one another. To be more precise, we draw a cutline through the center of the object as depicted in figure 3.24(B). The difference after convolution is still quite minimal, though we do see a difference near the center such that the convolved image becomes smoothed and has a lower intensity value. We demonstrate the relative change in figure 3.24(C) as the difference of the convolved object from the raw object divided by the raw object,

$$\Delta I = \frac{\text{obj} - \text{obj} \star \text{psf}}{\text{obj}}. \tag{3.44}$$

There is about a 10% change in the signal at the center of the object and very little change beyond 10 μm outside the center. The spikes at the ends of the plot are due to edge effects occurring from convolution.

The variation in the image intensity as a result of the convolution with the point spread function appears to be minimal, and is only noticeable at the very center. This begs the question: how necessary is incorporating the corrections due to the point spread function in the analysis of our images, and specifically, how will this procedure alter our measured concentrations? To that end, we perform a sweep of sigma values to determine at what Gaussian length scales convolution significantly alters the intensity reported in the image as contrasted with the intensity of the object.

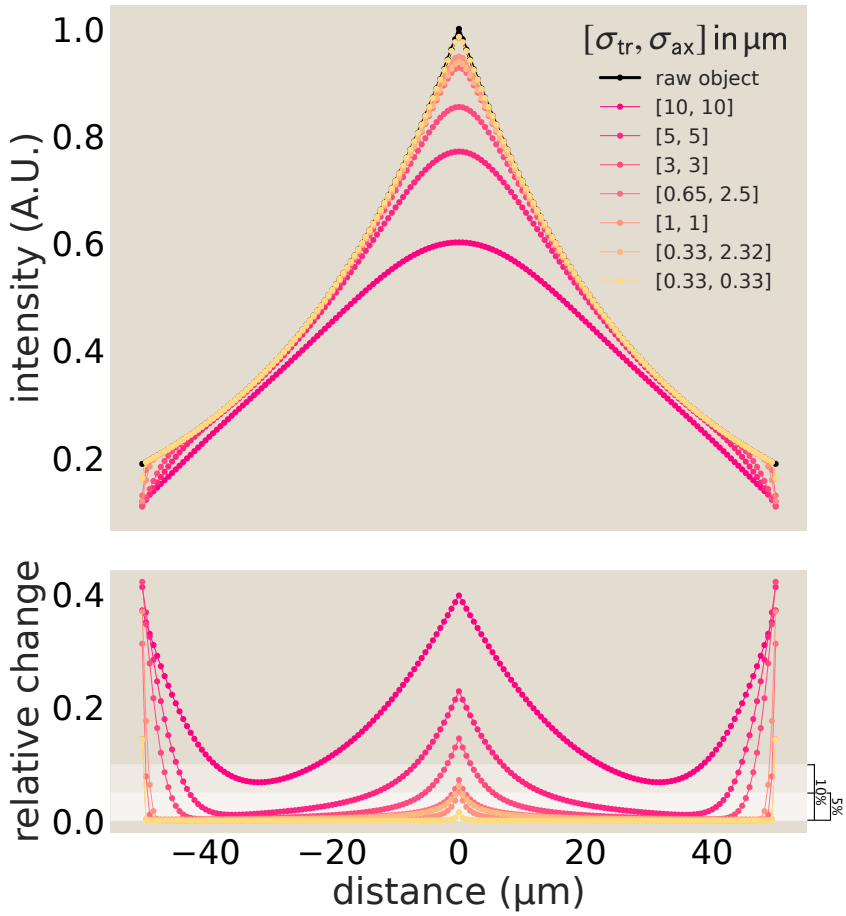

Figure 3.25: **Comparison of object and object convoluted with Gaussian point spread function.** (A) The profile of the synthetic object is plotted in black with convolved "images" with varying PSF length scales overlayed. For small length scales, $\sigma < 3\,\mu$m, the "image" does a good job of approximating the object. The discrepancies are highlighted in (B) where we plot the relative change between the image and object. Most of the variation occurs in the center. Increases at the edges are thought to be boundary effects.

From the data reported in figure 3.25, we find that when convolving with small σ values ($\sigma \leq 3\,\mu$m), the resultant traces are very similar to the original object. The bottom plot gives the relative change of the intensity values after convolving as described in equation 3.44. Except for the edges of the plot, where we believe boundary effects create increases, convolutions with small σ values reveal discrepancies of under ten percent.

3.6 Probe Blurring

It is important to take into account the on/off times of ATP to the ATP reporter to understand how reported ATP gradients may be affected by the probe. We can do an estimate to determine how far a probe can travel while bound to an ATP. We estimate the diffusion constant of the ATP probe to be $D = 45\,\mu\text{m}^2/\text{s}$ in section 3.11. We then need to take into account the binding rates for the ATP reporter. We use the reporter Queen-7μ A81D which has a reported dissociation constant of $K_\text{d} = 7.02 \times 10^{-2}$ mM [17]. The on and off rates for this mutant is not listed, however, the authors do list the rates for other mutants. Queen-2m has a reported on rate of $k_\text{on} = 2.7 \times 10^{-2}\,\text{mM}^{-1}\text{s}^{-1}$ and an off rate of $k_\text{off} = 9.4 \times 10^{-2}\,\text{s}^{-1}$ [18]. Queen-37C has a reported on rate of $k_\text{on} = 3.5 \times 10^{-2}\,\text{mM}^{-1}\text{s}^{-1}$ and an off rate of $k_\text{off} = 1.7 \times 10^{-1}\,\text{s}^{-1}$ [2]. Based on these reported off rates, the bound time of an ATP to a probe is roughly,

$$t_\text{b} = \frac{1}{k_\text{off}} = \frac{1}{0.1\,\text{s}^{-1}} \approx 10\,\text{s}. \tag{3.45}$$

Given that we image the aster every 20 s, the bound time is long. The distance the probe can travel during the bound time of ATP is on the order of

$$l_\text{b} = \sqrt{Dt_\text{b}} = \sqrt{45\,\mu\text{m}^2/\text{s} \times 10\,\text{s}} \approx 20\,\mu\text{m}. \tag{3.46}$$

This length scale is also long since the gradients we measure are also on the order of few $\times\, 10\,\mu$m. Thus, diffusing probes bound to ATP could contribute to a significant smoothing of gradients as bound probes diffuse.

To better understand this, we can write a model for the ATP bound probes over space and time. In this model, we take into account the diffusion of bound probes, the dissociation of the ATP to the probe, and the binding of an ATP to the probe,

$$\frac{\partial Q_\text{b}}{\partial t} = D\nabla^2 Q_\text{b} - k_\text{off} Q_\text{b} + k_\text{on} Q_\text{b} A. \tag{3.47}$$

3.7 Finite Element Simulations of Continuum Models

Our work is predicated on an interplay between experimental measurements and a theoretical description of our results. As seen in the main body of the paper, we have considered an elementary reaction-diffusion model that describes the spatiotemporal evolution of ATP as a result of the consumption of ATP by the motors as well as the diffusion of ATP.

Although the equations are simply stated, for the case in which the motor distribution is varying in space and time, the solution of these equations is prohibitive except in

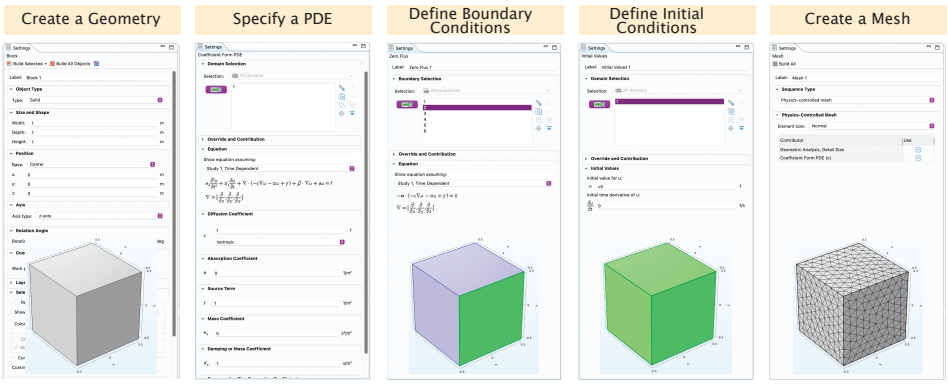

Figure 3.26: **Setting up a finite element calculation in COMSOL.** The use of COMSOL is dependent upon a series of steps that in total make it possible to solve some partial differential equation of interest. The five columns show how to create a geometry, specify which partial differential equation we are solving, how to define boundary conditions and initial conditions and how to set up the finite element mesh.

the most highly idealized circumstances. As a result, we were interested in having a robust numerical approach to solving the continuum equations describing our experiments, including the effects of photobleaching, in the context of the complex geometry of our microscope coverslips and optically activated aster regions.

To that end, in several different contexts we used the finite element method to carry out numerical solutions of our reaction-diffusion-photobleach equations. Part of the power of the finite element method is that it allows us the flexibility to consider arbitrary geometries and to quickly move between different effects by tuning the relevant partial differential equations. In particular, we have used the commercial finite element software known as COMSOL. As seen in Figure 3.26, to carry out a simulation of interest, we need to set up the calculations by describing the geometry, choosing which partial differential equations to solve, what the boundary and initial conditions are and how to mesh our region of interest.

In the main body of the paper, we showed how the finite element method was used to compute the depletion over time of ATP as a result of a gradient in the distribution of motors. Later in the SI, we will discuss how we used the finite element method to make careful simulations of how photobleaching might have influenced our measurement of the ATP concentration.

3.8 Photobleaching

From an experimental perspective, one of the main objectives of the present work is to determine the concentration of ATP at different positions and times within our microtubule-motor system. However, since our method of making that measurement uses fluorescence, it is incumbent upon us to quantify the unwanted effects of photobleaching, which leads to a reduction in fluorescent signal, as opposed to the physical reduction we are really interested in due to ATP consumption.

To understand and account for the character and extent of photobleaching affecting our measurements, we consider these dynamics from several angles. First, we perform control experiments quantifying the intensity reduction in a uniform mixture of fluorescent ATP probes absent any motor activity. We understand the quantitative phenomenology reported by these experiments by building models accounting for the role of a reservoir outside the excitation region, both via simple kinetic and finite element modeling.

Phenomenology of Photobleaching from Control Experiments

We prepare an ATP calibration experiment, as described in section 3.1, such that we pipette a fixed, known quantity of ATP into the same reaction mixture as an aster experiment; however, we do not include motor proteins, thereby preventing any ATP hydrolysis from occurring. We then image the sample using the same time dynamics as aster experiments, namely matching laser intensity currents, 1000 mA, exposure times, 150 – 160 ms, and the interval between image acquisition, 20 s. Upon collecting image data, we process it using the pipeline described in section 3.2 to do background subtraction (section 3.2) and uneven illumination corrections (section 3.2). We then average the intensity value of each image and plot the intensity values over time. This produces scatter plots such as those shown in Figure 3.27. We see empirically from the lines in Figure 3.27 that photobleaching in our system is very well described by fitting a single exponential plus a constant of the form

$$f_p(t) = \frac{I(t)}{I_0} = (1 - I_\infty)e^{-t/\tau} + I_\infty, \tag{3.48}$$

where $I(t)$ is the intensity at time t, I_0 is the intensity at the start of the experiment, I_∞ is the intensity as time approaches infinity, and τ is the characteristic decay constant in time.

To fit this decay due to photobleaching, we first divide all data points by the initial value of the intensity, I_0, which, for a strictly monotonic function, is the

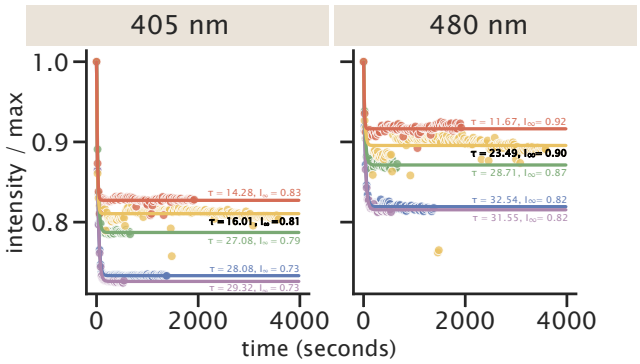

Figure 3.27: **Examples of representative, appreciably-variable, raw photobleaching trajectories across (putatively-identical) experiments, and accompanying fits.** Fluorescence intensities $I(t)$ of 405 nm (left column) and 480 nm (right column) excitation channels were each fit adequately to an exponential decay, Equation 3.48, with a single timescale τ and a long-time offset I_∞ (once normalized by maximum intensity values at time zero, I_0). Lines show best-fit curves and dots are raw data. Each color represents an experimental repeat for data taken at $500\mu M$ ATP and at 20 s intervals.

maximum value of the data. Thus, we pin the time zero intensity to 1. Using scipy.optimize.minimize, we find the parameter set, $\underline{p} = (p_0, p_1, \ldots, p_n)$, for a fitting function, $f_p(t)$, that minimizes the sum of the square of the residuals,

$$\text{SSR} = \sum_t (I(t) - f_p(t))^2, \tag{3.49}$$

where $I(t)$ is the value of the intensity at a time t. From here on, we will define the variables of the parameter set such that $p_0 = \tau$, $p_1 = I_\infty$.

Why does photobleaching adopt this form of an initial exponential decay to a plateau of about 80% of the initial intensity? Ordinarily, photobleaching in a uniformly-illuminated, confined chamber could instead be modeled by a single exponential decay,

$$f_p(t) = e^{-t/\tau}, \tag{3.50}$$

since the only thing that could change the state of the probe is bleaching according to the dynamical equation,

$$\frac{dI}{dt} = -\frac{1}{\tau} I. \tag{3.51}$$

However, our situation is more nuanced because the excitation region is small compared to the size of the chamber, meaning non bleached probes can diffuse in, slowing the time scale of intensity decay. We show that a single exponential indeed fits poorly to our data in Figure 3.28(A). But, as we commented before in

Eq. 3.48, a single exponential plus a constant seems to do the trick. One may be concerned about whether this model is physically reasonable since at sufficiently long timescales, the underlying physical picture would still expect that all the probes to have been bleached. To reckon with this question, in section 3.8, we show that when diffusive replenishment is invoked in a first order kinetic model where probes adopt two (bleached or unbleached) states, the decay of visible (unbleached) probe is modeled by a double exponential,

$$f_p(t) = (1 - I_\infty)e^{-t/\tau} + I_\infty e^{-t/\tau_2}, \tag{3.52}$$

where τ_2 is a second emergent timescale in the physical problem. If this second time constant τ_2 is very long, the behavior describing the photobleaching dynamics is well approximated by a single exponential plus a constant. In Figure 3.28(C), a double exponential fit seems to fit just as well as a single exponential plus a constant as shown in Figure 3.28(B). However, we note that the the solver kept the initial guess for τ_2, the long decay constant. In adjusting initial guesses and solver tolerances, we conclude that experimental data do not offer sufficiently long time courses for the solver to get a good fit for this parameter. However, we do know it is much much longer than the timescale of our experiment. Indeed, in Figure 3.29, we show that for $\tau_2 > 3 \times 10^5$, the squared sum of residuals for most replicates have reached a plateau and there is no further refinement of this parameter to achieve. If our experiment contained data at much longer times, we could more clearly witness the effect of the second decay constant.

Sensitivity of photobleaching to experimental conditions

When correcting for photobleaching in aster data, one of the things we need to check is if the photobleaching decay fits vary with ATP concentration. In Figure 3.30, we plot the fit parameters as a function of ATP concentration. There is no clear trend with ATP, indicating that the probe photobleaching process is not ATP-concentration dependent. Thus, regardless of an aster's ATP concentration, we can process images using appropriate globally-inferred parameters to the photobleaching decay curves.

We also examine how the fit parameters scale with modulating the time interval between light excitations. We expect that for shorter times between pulses, the bleaching of probes will be more continuous leading to shorter decay constants, while for longer intervals between light pulses the time constant should take much longer to see reduction in light intensity, which we have simulated in section 3.8. In Figure 3.31, we find the decay constant, τ, scales about linearly with the interval be-

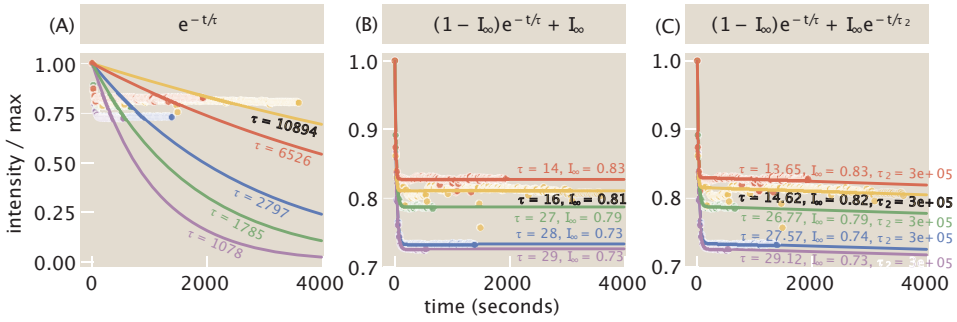

Figure 3.28: **Photobleaching data fit to several functional forms.** (A) Single exponential fits do not do an acceptable job of capturing the intensity depletion due to photobleaching and lead to large values of the decay constant. (B) Fitting to a single exponential plus a constant provides a satisfactory fit to the form of measured intensity reduction. (C) A double exponential plus a constant also fits the measured intensity decline, though the solver does not capture the second, longer decay constant very well. All data in these plots are taken at 500 μM ATP and at 20 s intervals. Each color represents the data from the same experimental repeats as depicted in Figure 3.27. Values for τ and τ_2 have units of seconds and values for I_∞ are unitless, since the intensities are normalized by the maximum intensity I_0 at time zero.

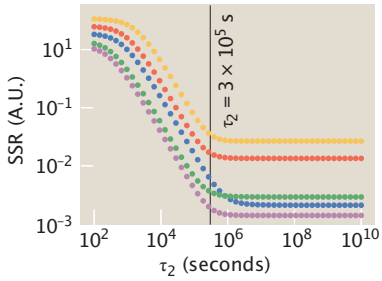

Figure 3.29: **Evaluation of fit for a second decay constant.** Using the fit parameters in Figure 3.27, we plot how the minimization of the sum of the square of the residuals (SSR) to the data depends on the value of a second decay constant, τ_2. For values larger than approximately 3×10^5 seconds, the SSR reaches a minimization limit beyond which there is no further improvement to the fit . Each color represents the data from the same experimental repeats as depicted in Figure 3.27.

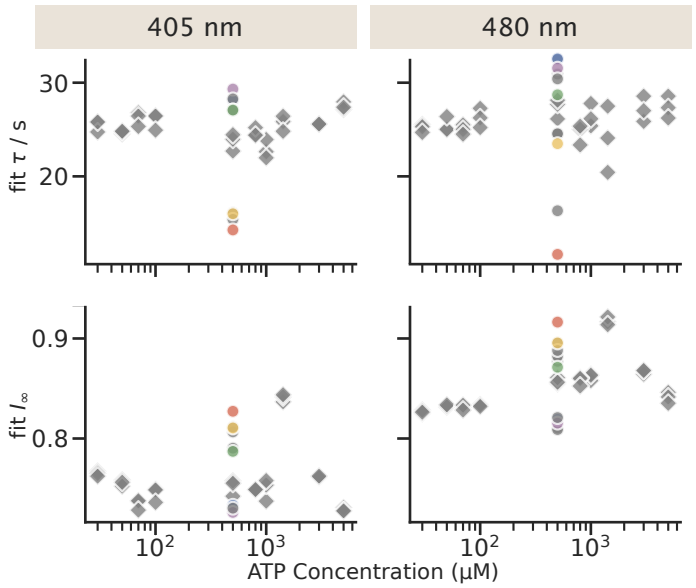

Figure 3.30: **ATP dependence of the fit parameters for photobleaching.** The fit constants, τ and I_∞, of the function, $I(t)/I_0 = (1 - I_\infty)e^{-t/\tau} + I_\infty$, are plotted as a function of ATP concentration. None of the fit parameters seem to have a clear trend as a function of ATP concentration. Circular points and diamond-shaped points display data from experiments conducted on separate dates. All data points are taken with the same imaging parameters. Each color represents the data from the same experimental repeats as depicted in Figure 3.27.

tween light excitations. In contrast, there is only small variation in the I_∞ parameter with respect to the pulsing interval.

Amid the variation in these parameters discussed above, key quantitative regularities emerge. Across experiments, all the photobleaching decay time constants are shorter than $\tau \lesssim 35$ s. In addition, all plateau intensity values I_∞ vary by less than 20%. Together, these two facts have the consequence that the late time behaviors of photobleaching trajectories agree within a few tens of percent of each other. This result can be understood by referring to equation 3.48, $I(t)/I_0 = (1 - I_\infty)e^{-t/\tau} + I_\infty$. After waiting a few decay constants—reached early in the experiment even for the slowest photobleaching trajectory—the first term $(1 - I_\infty)e^{-t/\tau}$ vanishes. Since the remaining plateau constant, I_∞, varies only mildly (by less than 20%), the overall trajectories ultimately agree within a few tens of percent of each other after long enough times.

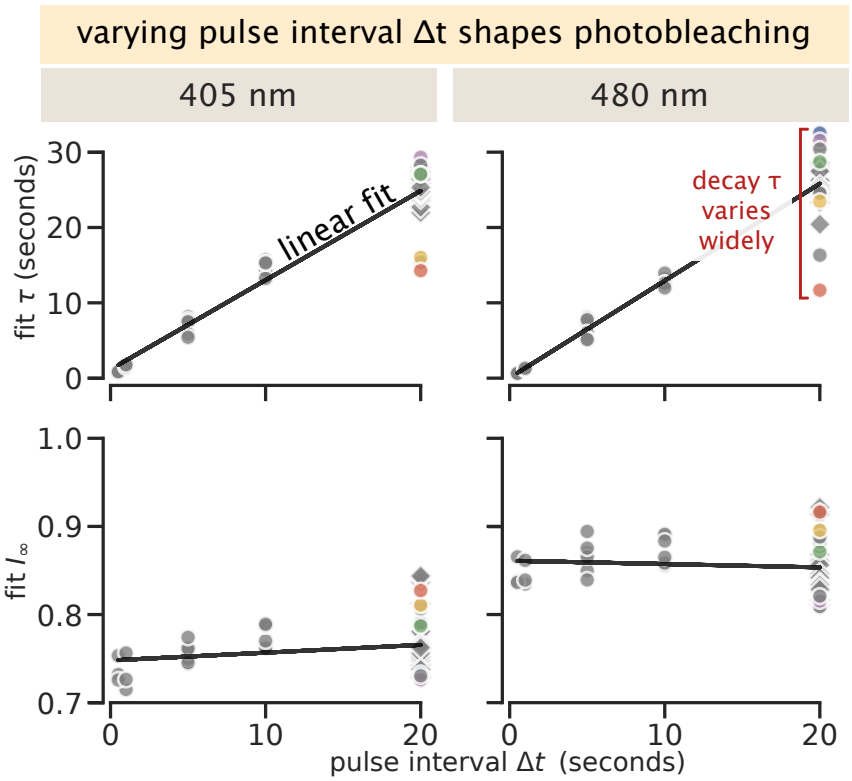

Figure 3.31: **Intrinsic and systematic variability of photobleaching kinetic parameters across days and excitation pulse intervals Δt.** On average, the fit decay time τ and offset I_∞ vary linearly with the interval Δt between excitation pulses in the measurement, as reported by acceptable linear fits between these parameters to the pulse interval Δt (shown as black lines). Five distinctly colored examples, the same experimental repeats as described by Figure 3.27, are taken at the pulse interval of $\Delta t = 20$ s, the interval typically used between frames in aster experiments, are highlighted, evidencing wide and ultimately meaningful variability in photobleaching kinetics across experiments. Circular points and diamond-shaped points display data from experiments conducted on separate dates.

Photobleaching correction procedure

With the form of the time-dependent intensity reduction in hand, we can now account for the amount of depletion due to photobleaching over time to recover the "true" intensity. In particular, we interpret the measured intensity as the product of a weighting function and the true intensity if fluorophores were not bleached. Namely, when $\tilde{I}$ is the true intensity and I is the measured intensity,

$$\tilde{I}(t) = \frac{I(t)}{f_p(t)} = \frac{I(t)}{(1 - I_\infty)e^{-t/\tau} + I_\infty}. \tag{3.53}$$

Since our probe calibrations are ratios of image intensities collected at two wavelengths, we can independently correct images from each wavelength and then take

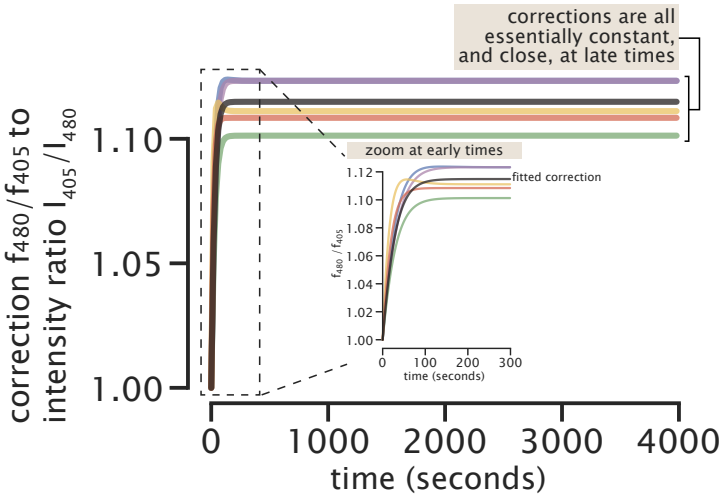

Figure 3.32: **Variation in the ratiometric photobleaching correction implied by variability in photobleaching experimental fits.** Specifically, each fluorescence channel offers a photobleaching fit function $f(t) = I(t)/I_{\max} = (1-I_\infty)\exp[-t/\tau]+I_\infty$. The measured fluorescence intensity ratio $r(t) = I_{405}(t)/I_{480}(t)$ would be corrected by the ratiometric correction $f_{480}(t)/f_{405}(t)$—and then is ultimately transformed to ATP concentration by a separate nonlinear concentration calibration function. Experimental variability in the raw kinetic parameters τ and I_∞ of each fluorescence channel thus propagate in rich ways to the shape of the ratiometric correction function. Notice even the appearance of non-monotonicity in time in the yellow and blue experimental fits' correction curves, which is facilitated by mismatches in the timescales of bleaching in the 405 nm and 480 nm channels. Each line is colored with the same scheme as the repeats described by Figure 3.27 and an additional line, the dark gray, plots the correction function when τ and I_∞ are set by the value of the linear fit at 20 seconds in Figure 3.31.

the ratio. This means the effective correction to the overall ratio is $\frac{f_{480}(t)}{f_{405}(t)}$, yielding,

$$\frac{\tilde{I}_{405}(t)}{\tilde{I}_{480}(t)} = \frac{I_{405}(t)\,f_{480}(t)}{I_{480}(t)\,f_{405}(t)}. \tag{3.54}$$

In Figure 3.32 we plot the correction values over time for five characteristic experimental replicates. In addition, we plot the consensus of the fitted parameters, τ and I_∞, as determined by the linear fit evaluated at the acquisition interval, 20 seconds, in Figure 3.31. The kinetic variability in fit parameters across experiments propagates to implied corrections. The differences are most apparent at early times before the fit functions plateau. We can see how these corrections modify the number of ATP versus time for a sample aster experiment in Figure 3.33.

As expected, the corrected ATP readouts are greater than the uncorrected mea-

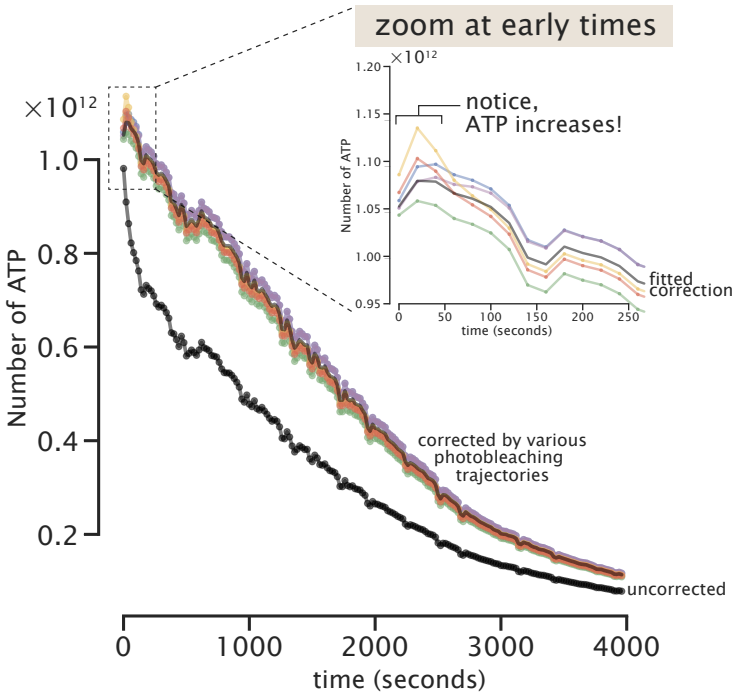

Figure 3.33: **Implications of variability across experimental photobleaching trajectories for inferred ATP abundance over time.** The black trajectory shows the number of ATP molecules over time of a representative aster if photobleaching were left uncorrected. The colored curves above are the same underlying aster data subjected to exemplary but diverse ratiometric photobleaching corrections (ensuing from those in Figure 3.32 and colored correspondingly). The dark gray curve, is the result of correcting using the τ and I_∞ values of the linear fit at 20 seconds in Figure 3.31. Notice that all corrected trajectories show an apparent *increase* in ATP over at least the first pair of data points, with, e.g., the blue and purple trajectories sustaining this apparent increase in ATP over at least two time points. Given that motors are continually consuming ATP, we expect the appearance of such an increase in ATP is pathological/nonphysical, emphasizing how profoundly photobleaching trajectories confound the resolution of ATP dynamics at early time points.

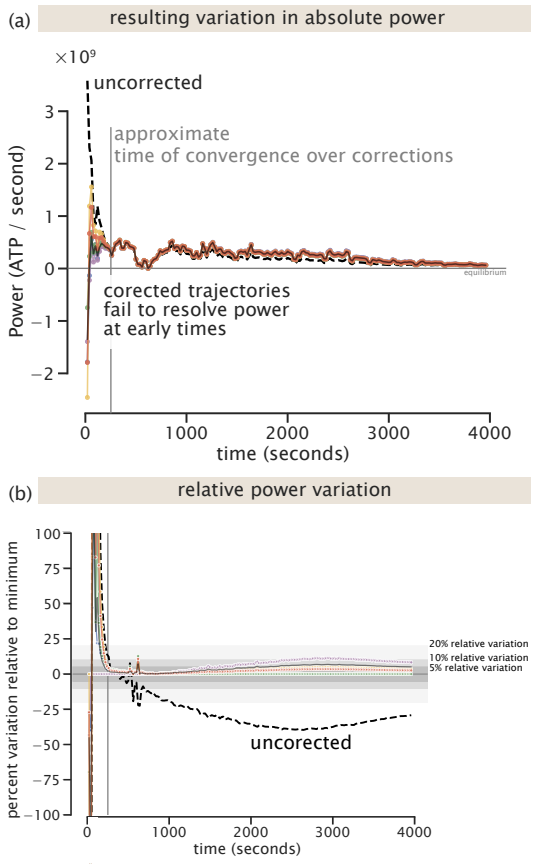

Figure 3.34: **Implications of variability across experimental photobleaching trajectories for inferred power consumption (ATP/second) over time.** (a) The black trajectory shows the consumption rate of ATP molecules over time of a representative aster if photobleaching were left uncorrected. The colored curves are the same underlying aster data subjected to exemplary but diverse ratiometric photobleaching corrections (ensuing from those in Figure 3.32 and colored correspondingly). The dark gray curve, is the result of correcting using the τ and I_∞ values of the linear fit at 20 seconds in Figure 3.31. Notice the dramatic ambiguity in even the *sign* of the ATP consumption rate, atop the quantitative disagreement across corrections, at early times. However, after a few characteristic photobleaching time constants (approximately $t \gtrsim 250\ s$, indicated by the gray line), the diversely-corrected curves closely agree. (b) In determining a cutoff time for where the varied photobleach corrected ATP curves agree, we plot the percent variation at each time for each power curve as compared to the curve with the minimum power. The variation is computed as $\frac{\text{power}_i(t)-\min(t)}{\min(t)} \times 100$, where i indexes over each corrected curve and $\min(t)$ refers to the minimum value of power at a given time t. The variation curves are laid upon three shaded regions depicting 5, 10, and 20 percent variation.

surement, yet still deplete over time as the aster consumes ATP. However, control photobleaching trajectories vary considerably across replicates and conditions at early time points. In Figure 3.33, these discrepancies manifest in corrected ATP trajectories until roughly 250 seconds ($\sim$ 4 min). Further, some candidate corrections could even spuriously show a mild increase in ATP over the earliest time points. (We regard such an apparent increase as nonphysical, given the continual consumption of ATP by motors.) This potential problem is even more apparent when examining power (namely the derivative of ATP over time), as shown in Figure 3.34. Crucially, however, after roughly 250 seconds (nearly ten times longer than the fit decay constant τ values), power trajectories across all candidate corrections align nearly identically. This concordance of the inferred ATP and power trajectories only after 250 seconds recommends that these trajectories are reliably resolvable after this short initial period.

In Figure 3.35, we see that the initial period is early in the meaningful development of the aster structures. Figure 3.35(C) depicts the the state of motor and ATP gradients at the proposed cutoff time. The motor image does not yet show any structure formation, reinforcing our recommendation to start analyzing data after the initial $t \gtrsim 250$ s period. Taking a closer look at amount of gradients developed in ATP, the grey lines in Figure 3.35(A) and (B) show the ATP profiles at all measured time points before the cutoff. After correcting for photobleaching, we find that although ATP does begin depleting, ATP throughout the system is still abundant. Additionally nearly all the gradient formation in ATP occurs after the cutoff. Given that nearly all development of spatial gradients, in both ATP and motors, occur after the cutoff and ATP is still at meaningful abundances, we proceed with our analysis examining data following this practical cutoff.

Theory of the Experiment: Analysis of Photobleach-Diffusion Equations

To develop intuition for the way in which photobleaching alters our fluorescence signal and hence could contaminate our measurement, we worked to develop a "theory of the experiment" to compute how the dynamics of the effect we are trying to measure (i.e. ATP consumption) couple with the unwanted effects of photobleaching. This effort is one of many such examples within our laboratory where we have repeatedly found it very useful to do our best job of writing down a quantitative theoretical description of the experiment and using that description to calibrate our experiments themselves [19, 20]. This is not a substitute for the actual experimental correction described in the previous section 3.8, but rather a

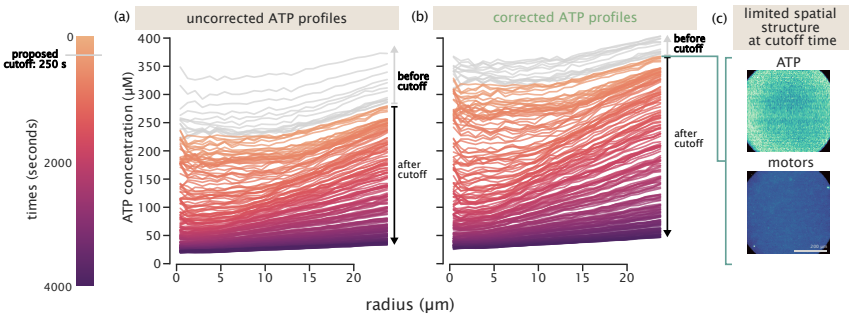

Figure 3.35: **ATP traces over space and time, with and without an exemplary photobleaching correction, relative to a proposed cutoff time—before which we propose deeming ATP dynamics quantiatively-unresolvable.**(a) Spatiotemporal profiles of ATP if no photobleaching correction were applied. (b) Spatiotemporal profiles of ATP under an exemplary photobleaching correction (corresponding to the green example photobleaching trajectory fit in the preceding figures in this section. In panels (a) and (b), profiles before the proposed cutoff time of 250 s—the same cutoff indicated by in Figure 3.34 by the vertical gray line—are colored in grey (leaving the remaining profiles, which we propose retaining, colored by time). (c) For these representative aster data, the spatial profiles of both ATP and motors have developed only modest spatial gradients at the proposed cutoff time (250 seconds, 13 frames). This means the retained data contain the bulk of interesting spatiotemporal gradient formation attending the aster formation.

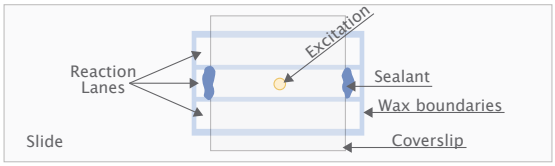

Figure 3.36: **Anatomy of the experimental chamber.** To create our experimental chamber, we cut 3 mm × 18mm lanes out of parafilm wax. We sandwich the wax sheet between a coverslip and a slide leaving the ends of the lanes exposed. This allows us to flow a reaction mixture into each lane. We seal the reaction in the lanes using picodent twinsill speed, a polymeric seal.

complementary approach for developing intuition for the scale and dynamics of the photobleaching effect.

In this section, we show how to set up quantitative models of the photobleaching and diffusion of our fluorescent probes and how the model equations can be solved as the basis of proposed photobleaching corrections in our experiments. First, in the ensuing sections 3.8 and 3.8, we write a model for the fluorescent probe independent of space, where the probe adopts two states, bleached or unbleached. This model can be used to account for the character of photobleaching in our experiments.

Figure 3.36 shows the geometry of one of our experimental devices. As shown, the experimental system is a giant reservoir encompassing a small region where illumination destroys the visibility of some molecules through photobleaching. This geometry sets up conditions for photobleaching to compete with bulk replenishment from the reservoir, as we now explore.

Photobleaching in a reservoir takes the form of a double exponential

When exciting a region of our sample, there is some rate, k_{bleach}, at which probes in this region are photobleached. These probes are then lost from the pool of probes we can account for through fluorescence. Within the excitation region, there is some concentration of fluorescent probes, c_{in}, and outside of this region, there is additional pool of fluorescent probes with concentration, c_{out}. Probes can diffuse between these regions with rates k_{in} and k_{out}. We write a model for the kinetics of probe movement. The time dependence of non-bleached probes in the illumination region is

$$\frac{dc_{\text{in}}(t)}{dt} = -k_{\text{bleach}}c_{\text{in}}(t) - k_{\text{out}}c_{\text{in}}(t) + k_{\text{in}}c_{\text{out}}(t), \tag{3.55}$$

while the time dependence of non-bleached probes outside the illumination region is,

$$\frac{dc_{\text{out}}(t)}{dt} = k_{\text{out}}c_{\text{in}}(t) - k_{\text{in}}c_{\text{out}}(t). \tag{3.56}$$

Writing the system of equations as in matrix form results in

$$\frac{d}{dt}\begin{bmatrix} c_{\text{in}} \\ c_{\text{out}} \end{bmatrix} = \begin{bmatrix} -k_{\text{bleach}} - k_{\text{out}} & k_{\text{in}} \\ k_{\text{out}} & -k_{\text{in}} \end{bmatrix}\begin{bmatrix} c_{\text{in}} \\ c_{\text{out}} \end{bmatrix}, \tag{3.57}$$

and applying the ansatz,

$$\begin{aligned} c_{\text{in}}(t) &= c_{\text{in}}^{(0)}e^{\sigma t} \\ c_{\text{out}}(t) &= c_{\text{out}}^{(0)}e^{\sigma t}, \end{aligned} \tag{3.58}$$

we can solve the system of equations as an eigenvalue problem. Plugging in the ansatz into the matrix form,

$$\sigma e^{\sigma t}\begin{bmatrix} c_{\text{in}}^{(0)} \\ c_{\text{out}}^{(0)} \end{bmatrix} = e^{\sigma t}\begin{bmatrix} -k_{\text{bleach}} - k_{\text{out}} & k_{\text{in}} \\ k_{\text{out}} & -k_{\text{in}} \end{bmatrix}\begin{bmatrix} c_{\text{in}}^{(0)} \\ c_{\text{out}}^{(0)} \end{bmatrix}, \tag{3.59}$$

which we rearrange to find

$$0 = \begin{bmatrix} -k_{\text{bleach}} - k_{\text{out}} - \sigma & k_{\text{in}} \\ k_{\text{out}} & -k_{\text{in}} - \sigma \end{bmatrix}\begin{bmatrix} c_{\text{in}}^{(0)} \\ c_{\text{out}}^{(0)} \end{bmatrix}. \tag{3.60}$$

Taking the determinant,

$$\begin{aligned} 0 &= (-k_{\text{bleach}} - k_{\text{out}} - \sigma)(-k_{\text{in}} - \sigma) - k_{\text{in}}k_{\text{out}} \\ &= \sigma^2 + (k_{\text{bleach}} + k_{\text{in}} + k_{\text{out}})\sigma + k_{\text{in}}(k_{\text{bleach}} + k_{\text{out}}) - k_{\text{in}}k_{\text{out}} \\ &= \sigma^2 + (k_{\text{bleach}} + k_{\text{in}} + k_{\text{out}})\sigma + k_{\text{in}}k_{\text{bleach}}. \end{aligned} \tag{3.61}$$

Solving for the roots of σ,

$$\sigma = -\frac{1}{2}(k_{\text{bleach}} + k_{\text{in}} + k_{\text{out}}) \pm \frac{1}{2}\sqrt{(k_{\text{bleach}} + k_{\text{in}} + k_{\text{out}})^2 - 4k_{\text{in}}k_{\text{bleach}}}. \tag{3.62}$$

Plugging this partial differential equation into Mathematica and solving for $c_{\text{in}}(t)$, we find,

$$c_{\text{in}}(t) = \frac{c_0 \exp\left(-\frac{(\alpha+\gamma)t}{2}\right)}{2\gamma}\left(\beta - \beta\exp(\gamma t) + \gamma + \gamma\exp(\gamma t)\right), \tag{3.63}$$

where, for ease of reading, we define the constants

$$\begin{aligned} \alpha &\equiv k_{\text{bleach}} + k_{\text{in}} + k_{\text{out}}, \\ \beta &\equiv k_{\text{bleach}} - 3k_{\text{in}} + k_{\text{out}}, \\ \gamma &\equiv \sqrt{-4k_{\text{bleach}}k_{\text{in}} + (k_{\text{bleach}} + k_{\text{in}} + k_{\text{out}})^2} = \sqrt{-4k_{\text{bleach}}k_{\text{in}} + \alpha^2}. \end{aligned} \tag{3.64}$$

We simplify the form of $c_{\text{in}}(t)$ by distributing the exponential prefactor,

$$c_{\text{in}}(t) = \frac{c_0}{2\gamma}\left(\beta e^{-(\alpha+\gamma)t/2} - \beta e^{-(\alpha-\gamma)t/2} + \gamma e^{-(\alpha+\gamma)t/2} + \gamma e^{-(\alpha-\gamma)t/2}\right). \tag{3.65}$$

Combining the terms in the parenthesis by exponentials,

$$c_{\text{in}}(t) = \frac{c_0}{2\gamma}\left((\gamma+\beta)e^{-(\alpha+\gamma)t/2} + (\gamma-\beta)e^{-(\alpha-\gamma)t/2}\right). \tag{3.66}$$

This equation establishes that the visible abundance of probes in the monitored region, $c_{\text{in}}(t)$, can be described as a double exponential with two characteristic timescales τ_1 and τ_2, given by,

$$\begin{aligned} \tau_1^{-1} &= (\alpha+\gamma)/2 \\ &= \frac{1}{2}\left(k_{\text{bleach}} + k_{\text{in}} + k_{\text{out}} + \sqrt{-4k_{\text{bleach}}k_{\text{in}} + (k_{\text{bleach}} + k_{\text{in}} + k_{\text{out}})^2}\right) \end{aligned} \tag{3.67}$$

and

$$\begin{aligned} \tau_2^{-1} &= (\alpha-\gamma)/2 \\ &= \frac{1}{2}\left(k_{\text{bleach}} + k_{\text{in}} + k_{\text{out}} - \sqrt{-4k_{\text{bleach}}k_{\text{in}} + (k_{\text{bleach}} + k_{\text{in}} + k_{\text{out}})^2}\right). \end{aligned} \tag{3.68}$$

We remark that since $\gamma \geq 0$, we see that $\tau_1^{-1} \geq \tau_2^{-1}$ and so $\tau_1 \leq \tau_2$. That is, the more rapid decay process is captured by the first timescale τ_1.

In Section 3.8, we find that the predictions of this model do a reasonable job of describing the photobleaching in our experiments. Specifically, our data is best fit to a double exponential with a short and a long time constant, corresponding to $\tau_2 \gg \tau_1$ and yielding an effective plateau in fluorescence on experimental timescales.

To further grapple with other origins of photobleaching, we also explored what modifications to the model are introduced by probes sticking to the glass coverslip or slide. Next, we include our findings here for those practitioners interested.

Photobleaching with surface bound probes in a reservoir takes the form of a triple exponential

As above, we write model for the bleaching dynamics inside and outside the excitation region, but now also take into account an additional effect where probes can be bound to the surface and do not diffuse. These probes can still bleach when inside the excitation region. We denote the concentration of probes inside the excitation region with variable $c_{\text{s-in}}$ and outside the excitation region as, $c_{\text{s-out}}$. We include two more rate constants, k_{on} and k_{off}, for the rates of binding and unbinding to the surface. Thus, our system of equations is now,

$$\begin{aligned}
\frac{dc_{\text{in}}(t)}{dt} &= -k_{\text{bleach}}c_{\text{in}}(t) - k_{\text{out}}c_{\text{in}}(t) + k_{\text{in}}c_{\text{out}}(t) - k_{\text{on}}c_{\text{in}}(t) + k_{\text{off}}c_{\text{s-in}}(t),\\
\frac{dc_{\text{out}}(t)}{dt} &= k_{\text{out}}c_{\text{in}}(t) - k_{\text{in}}c_{\text{out}}(t) - k_{\text{on}}c_{\text{out}}(t) + k_{\text{off}}c_{\text{s-out}}(t),\\
\frac{dc_{\text{s-in}}(t)}{dt} &= -k_{\text{bleach}}c_{\text{s-in}}(t) + k_{\text{on}}c_{\text{in}}(t) - k_{\text{off}}c_{\text{s-in}}(t),\\
\frac{dc_{\text{s}}(t)}{dt} &= k_{\text{on}}c_{\text{out}}(t) - k_{\text{off}}c_{\text{s-out}}(t).
\end{aligned} \tag{3.69}$$

Writing the system of equations as in matrix form, we have

$$\frac{d}{dt}\begin{bmatrix} c_{\text{in}} \\ c_{\text{out}} \\ c_{\text{s-in}} \\ c_{\text{s-out}} \end{bmatrix} = \begin{bmatrix} -k_{\text{bleach}} - k_{\text{out}} - k_{\text{on}} & k_{\text{in}} & k_{\text{off}} & 0 \\ k_{\text{out}} & -k_{\text{in}} - k_{\text{on}} & 0 & k_{\text{off}} \\ k_{\text{on}} & 0 & -k_{\text{bleach}} - k_{\text{off}} & 0 \\ 0 & k_{\text{on}} & 0 & -k_{\text{off}} \end{bmatrix} \begin{bmatrix} c_{\text{in}} \\ c_{\text{out}} \\ c_{\text{s-in}} \\ c_{\text{s-out}} \end{bmatrix}. \tag{3.70}$$

As a first guess, we assume the binding kinetics to the surfaces are very slow, slower than the duration of the experiment. So we simplify this system of equations

such that where surface bound probes are only subject to bleaching and do not communicate with the pool of other probes. Thus our system of equations is,

$$\begin{aligned}
\frac{dc_{\text{in}}(t)}{dt} &= -k_{\text{bleach}}c_{\text{in}}(t) - k_{\text{out}}c_{\text{in}}(t) + k_{\text{in}}c_{\text{out}}(t),\\
\frac{dc_{\text{out}}(t)}{dt} &= k_{\text{out}}c_{\text{in}}(t) - k_{\text{in}}c_{\text{out}}(t),\\
\frac{dc_{\text{s-in}}(t)}{dt} &= -k_{\text{bleach}}c_{\text{s-in}}(t),\\
\frac{dc_{\text{s-out}}(t)}{dt} &= 0.
\end{aligned} \tag{3.71}$$

Thus, the concentration of surface bound probes outside the excitation region is constant in time, and we can ignore the last equation. Now referring to the surface bound probes in the excitation region as c_{s}, we write the system of equations in matrix form,

$$\frac{d}{dt}\begin{bmatrix} c_{\text{in}} \\ c_{\text{out}} \\ c_{\text{s}} \end{bmatrix} = \begin{bmatrix} -k_{\text{bleach}} - k_{\text{out}} & k_{\text{in}} & 0 \\ k_{\text{out}} & -k_{\text{in}} & 0 \\ 0 & 0 & -k_{\text{bleach}} \end{bmatrix}\begin{bmatrix} c_{\text{in}} \\ c_{\text{out}} \\ c_{\text{s}} \end{bmatrix}. \tag{3.72}$$

As above, we prescribe the ansatz that the concentrations of each species change exponentially in time,

$$\begin{aligned}
c_{\text{in}}(t) &= c_{\text{in}}^{(0)}e^{\sigma t}\\
c_{\text{out}}(t) &= c_{\text{out}}^{(0)}e^{\sigma t}\\
c_{\text{s}}(t) &= c_{\text{s}}^{(0)}e^{\sigma t}
\end{aligned} \tag{3.73}$$

we can solve the system of equations as an eigenvalue problem. Plugging in the ansatz into the matrix form,

$$\sigma e^{\sigma t}\begin{bmatrix} c_{\text{in}}^{(0)} \\ c_{\text{out}}^{(0)} \\ c_{\text{s}}^{(0)} \end{bmatrix} = e^{\sigma t}\begin{bmatrix} -k_{\text{bleach}} - k_{\text{out}} & k_{\text{in}} & 0 \\ k_{\text{out}} & -k_{\text{in}} & 0 \\ 0 & 0 & -k_{\text{bleach}} \end{bmatrix}\begin{bmatrix} c_{\text{in}}^{(0)} \\ c_{\text{out}}^{(0)} \\ c_{\text{s}}^{(0)} \end{bmatrix}, \tag{3.74}$$

which we rearrange to find

$$0 = \begin{bmatrix} -k_{\text{bleach}} - k_{\text{out}} - \sigma & k_{\text{in}} & 0 \\ k_{\text{out}} & -k_{\text{in}} - \sigma & 0 \\ 0 & 0 & -k_{\text{bleach}} - \sigma \end{bmatrix}\begin{bmatrix} c_{\text{in}}^{(0)} \\ c_{\text{out}}^{(0)} \\ c_{\text{s}}^{(0)} \end{bmatrix}. \tag{3.75}$$

Taking the determinant,

$$\begin{aligned} 0 &= \Big((-k_{\text{bleach}} - k_{\text{out}} - \sigma)(-k_{\text{in}} - \sigma) - k_{\text{in}}k_{\text{out}}\Big)\Big(- k_{\text{bleach}} - \sigma\Big) \\ &= \Big(\sigma^2 + (k_{\text{bleach}} + k_{\text{in}} + k_{\text{out}})\sigma + k_{\text{in}}(k_{\text{bleach}} + k_{\text{out}}) - k_{\text{in}}k_{\text{out}}\Big)\Big(- k_{\text{bleach}} - \sigma\Big) \\ &= \Big(\sigma^2 + (k_{\text{bleach}} + k_{\text{in}} + k_{\text{out}})\sigma + k_{\text{in}}k_{\text{bleach}}\Big)\Big(- k_{\text{bleach}} - \sigma\Big). \end{aligned} \tag{3.76}$$

Solving for the roots of σ, the first set of big parenthesis is the same quadratic equation as before, giving the two roots,

$$\sigma = -\frac{1}{2}(k_{\text{bleach}} + k_{\text{in}} + k_{\text{out}}) \pm \frac{1}{2}\sqrt{(k_{\text{bleach}} + k_{\text{in}} + k_{\text{out}})^2 - 4k_{\text{in}}k_{\text{bleach}}}. \tag{3.77}$$

And the second big parenthesis yields a third root which is simply,

$$\sigma = -k_{\text{bleach}}. \tag{3.78}$$

Accordingly, very interestingly, bleaching with a population of probes stuck to a surface simply adds an exponential to the model, yielding a triple exponential function. To ask whether our control experiment data showed conspicuous signals of such surface sticking, we also subjected them to the triple exponential model, but concluded the fits were no better than fitting to a double exponential. Given that second time constant values already exceed the duration of the experiment, our data alone do not garner further information about a third timescale, if one should participate.

Time-dependent bleaching rates from periodic excitations

Our models in the preceding sections 3.8 and 3.8 investigated the case where the rate of photobleaching k_{b} is continuous and constant in time. In a real experiment monitoring aster formation, however, the sample is illuminated only in pulses over time, yielding frames of movies. Accordingly, the rate at which probes bleach is time dependent, so that the decay of fluorescence intensity $u(t)$ is given by the ordinary differential equation,

$$\frac{\mathrm{d}u(t)}{\mathrm{d}t} = -k_{\text{b}}(t)u(t), \tag{3.79}$$

where $k_{\text{b}}(t)$ is the rate of photobleaching. Our experiments acquire images every 20 seconds, where light only excites the sample when an image is being taken presenting a fixed exposure time of 150 ms. To understand how such time-varying bleaching

rates shape trajectories of photobleaching, we now explore properties of a simple model evoking the periodic excitations of experiments. Crucially, this understanding also delivers standard benchmark solutions that validate the numerical accuracy and stability of our most realistic, precise, and spatially-explicit simulations from finite element methods that follow next, in section 3.8.

First, to capture pulsatile excitations, we prescribe an example time-dependent photobleaching rate function as,

$$k(t) \equiv k_{\mathrm{b}} \frac{1 + \sin(2\pi t/\tau)}{2}, \tag{3.80}$$

where τ is the period of light pulses. This function is visualized in Figure 3.37(C). The rate of photobleaching is a periodic function between 0 and k_{b}. In this simple test, we do not account for diffusion of probes, only considering a degradation rate due to bleaching. The ODE for the concentration of bright probes is thus,

$$\frac{\mathrm{d}u(t)}{\mathrm{d}t} = -k(t)u(t) = -\frac{k_{\mathrm{b}}u(t)}{2}\left(1 + \sin\left(\frac{2\pi t}{\tau}\right)\right). \tag{3.81}$$

We can solve for $u(t)$ by using the separation of variables technique, resulting in the expression

$$\int_{u(0)}^{u(t)} \frac{\mathrm{d}u(t')}{u(t')} = \int_0^t -\frac{k}{2}\mathrm{d}t' + \int_0^t -\frac{k}{2}\sin\left(\frac{2\pi t'}{\tau}\right)\mathrm{d}t'. \tag{3.82}$$

Integrating both sides, we find

$$\ln\left(\frac{u(t)}{u(0)}\right) = -\frac{k}{2}t + \frac{k\tau}{4\pi}\left(\cos\left(\frac{2\pi t'}{\tau}\right) - 1\right). \tag{3.83}$$

Finally, exponentiating both sides, we arrive at the time dependent concentration given by

$$u(t) = u(0)\exp\left(-\frac{k}{2}t + \frac{k\tau}{4\pi}\left(\cos\left(\frac{2\pi t'}{\tau}\right) - 1\right)\right). \tag{3.84}$$

We plot this result as the black lines in Figure 3.37.

We can compare the numerical solution to the ODE in Equation 3.81 using the forward Euler method,

$$u(t + \Delta t) = u(t) - \frac{k_{\mathrm{b}}}{2}\Delta t\, u(t)\left(1 + \sin\left(\frac{2\pi t}{\tau}\right)\right). \tag{3.85}$$

Computing the numerical solution in python, we plot the result as the green circles in Figure 3.37(A). Both the numerical and analytic solutions are indistinguishable.

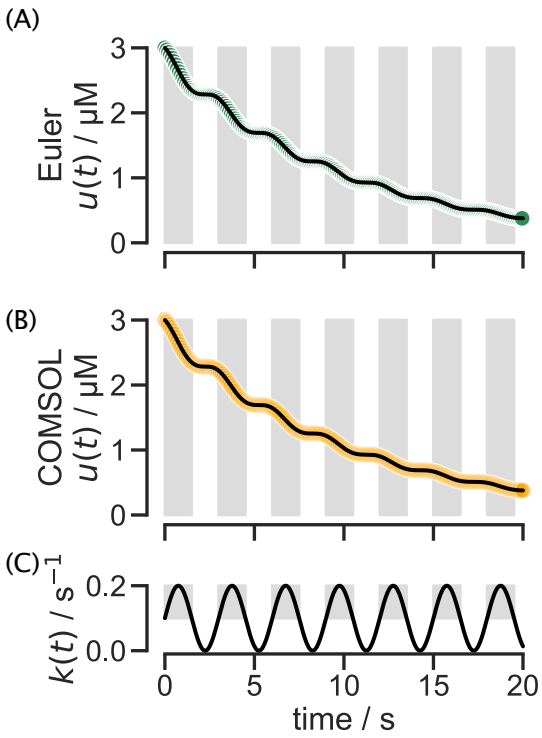

Figure 3.37: **Numerically solving the intensity decay due to photobleaching when pulsing light matches the analytic solution for both the forward Euler method and FEM.** (A) The numerical solution, via the forward Euler method, for Equation 3.81 is plotted by the green circles under the analytical solution represented with a black line. (B) The numerical solution, via the finite element method, for Equation 3.81 is plotted by the orange circles under the analytical solution represented with a black line. (C) The driving pulse of the form of Equation 3.80 is plotted with the gray shading highlighting the half periods of greater bleaching contributions.

In general, we remark that this sinusoidally-varying bleaching rate is a special case of an integrating factor behavior, namely, Eq. 3.79 has the solution,

$$u(t) = u_0 \exp\left[-\int_0^{t'} dt' k(t')\right] \tag{3.86}$$

$$\equiv u_0 \exp\left[-\langle k(t)\rangle t\right], \tag{3.87}$$

where u_0 is the value of the intensity at time zero, and in the second line we defined $\langle k(t)\rangle$ as a time averaged bleaching rate, $\langle k(t)\rangle \equiv \frac{1}{t}\int_0^t dt' k(t')$ up to time t. This behavior makes explicit that the observed intensity decay due to some time-varying photobleaching rate up to a time t can be understood as effectively an exponential decay with a time-averaged bleaching rate. Thus, the overall effect of illumination by pulses is largely to trace out a softened decay curve set by an effective duty cycle of the illumination over the experimental timescale.

Finite element simulations of our photobleaching models

Having understood how a first-order kinetic description of bleaching balanced with reservoir replenishment (sections 3.8 and 3.8) and time-varying bleaching rates (section 3.8) manifest effectively plateauing intensity trajectories, we now graduate our modeling to a full description that explicitly accounts for the depletion and transport of fluorescent probes across space. We move from the ordinary differential equations of sections 3.8 and 3.8 to a partial differential equation treatment of the full reaction diffusion equations underlying our experimental conditions.

To develop both this full theory of our experiment and develop an understanding for the continuum mechanics of our system, we harness the power of the finite element method (FEM) already introduced in section 3.7. To validate our simulations, in the next section 3.8, we perform benchmarking checks with analytic solutions to the pulsatile dynamical context discussed in section 3.8. Afterwards, in section 3.8, we thoroughly explore the effects of modulating the diffusion constant and bleach rate on the time dynamics of intensity depletion.

Validating finite element numerical conditioning with pulsing model benchmark

Before examining the full three-dimensional complexity of our problem, we first do numerical "controls" by comparing analytic and FEM solutions to the same simplified problem discussed in section 3.8. Importantly, this verifies that these simulations are numerically well conditioned and behaved for experimentally relevant conditions.

In COMSOL, we defined a cylindrical geometry in which we applied Equation 3.81. We specify a uniform concentration initial condition and impose zero flux on the boundaries. Using the time dependent solver, we specify the start time, stop time and step size with the relative tolerance set to match the step size. We plot the results of the simulation, averaged over the cylinder, in Figure 3.37(B) as the orange circles. Again we find that the numerical solution using FEM is indistinguishable from the analytical solution.

Adding a layer of complexity, we now include diffusion in our COMSOL model and ensure that our simulations accurately describe the pulsing nature of our experiment. We now add a larger cylinder to the geometry which contains the reservoir of ATP probes but is never excited by light. Probes from this larger cylinder can diffuse into the smaller cylinder where light excitation can bleach the probes. We simulate

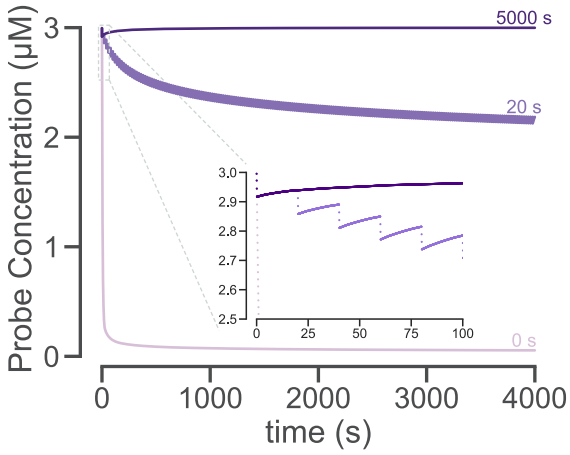

Figure 3.38: **Examining the limits of interval times, we find simulations agree with expectations.** We simulate the depletion of bright probe concentration due to photobleaching with a diffusion constant of $40\,\mu m^2/s$ and a bleaching rate of $0.02\,s^{-1}$ with three different intervals of time between pulses. In the limit of having an infinite time between pulses, or just a single pulse, we set the interval to be longer than the simulation time. The resultant curve (the darkest purple) initially undergoes decay with the other two curves, but after 20 seconds, recovers and plateaus back at the starting concentration. The middle trace plots the depletion when the light pulses every 20 seconds. The zoomed in inset of early times show a drop in concentration during each pulse and recovery for the interval between pulses. The second limit, having no time between light pulses (the lightest purple), shows monotonic depletion of bright probe concentration where a steady photobleaching smoothly depletes the bright probes regardless of their ability to diffuse.

two limits for which we already know the solutions, infinitely long and short times between pulses. When the interval between pulses is infinitely large, we would expect that as soon as the light turns off, we see recovery in the concentration of bright probes that remains constant for the rest of time. This is a FRAP experiment. The darkest line in Figure 3.38 shows just this. After one pulse which ends at 20 seconds, the concentration smoothly increases and then plateaus at about the starting concentration. In the opposite limit, when there is no interval between pulses, meaning the light is continuously on, the concentration of bright probes decays monotonically with no recovery, as seen by the lightest curve in Figure 3.38. Our experiment exists in an intermediate range, where light is pulsed every 20 seconds. The medium purple curve depicts this in Figure 3.38. We can see periodic intensity depletion and then recovery in the time between depletion. This is apparent in the zoomed-in inset.

Finite element simulations of photobleaching and transport

We now use the finite element analysis to more precisely understand the dynamics of photobleaching in our experiments, acknowledging all relevant experimental effects. In particular, our experimental setup demands a "bleach-diffusion" equation treatment since the cover slip forms a "reservoir" of fluorescent molecules that can diffuse into the bleaching region. As a result, we have two competing time scales, namely, that of the photobleaching itself and the time scale over which diffusion of molecules from the reservoir can replenish the photobleached region. In the simulations that follow, we examine the dynamics that results from tuning these two time scales independently.

We set up a COMSOL simulation with the geometric constraints of our experiment. We model the excitation region as a small cylinder, with the depth of the chamber and diameter of the light pulse, inside a larger cylinder, with a diameter of the width of the chamber, see Figure 3.39. The use of the cylindrical geometry is simply a matter of convenience for the calculations since it makes it easier to set up and visualize when the problem has this symmetry.

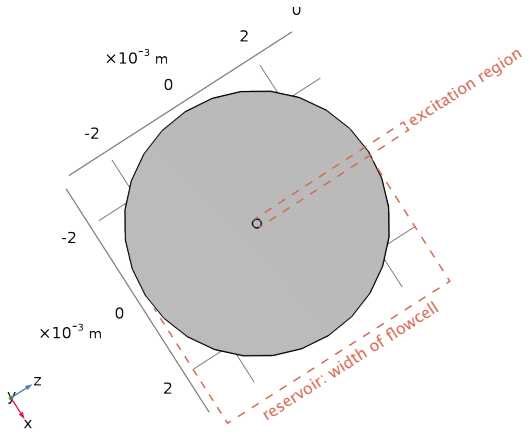

Figure 3.39: **Aerial view of cylindrical geometry in COMSOL for photobleaching simulations.** We model photobleaching experiments with two concentric cylinders. The larger has a diameter of the width of the flow cell where the sample is deposited. This larger cylinder acts as a reservoir of ATP probes. The much smaller cylinder is the region where we pulse light excitations. It is inside this region where bleachign occurs.

This simulation explores the change of concentration $u(\mathbf{r}, t)$ of bright probes through space and time when there is no aster formation. We create a reaction containing microtubules, ATP, the ATP probe, but no motor proteins to prevent ATP hydrolysis

and any structure formation. In this scenario, probes should be allowed to freely diffuse everywhere. Probes in the excitation region are subject to bleaching at a constant rate. Hence, in our simulations of this problem, we define two coefficient form partial differential equations, one to act in each region of the geometry. In the central region, there is both bleaching and diffusion, while in the exterior region, there is simply diffusion. The COMSOL form of "coefficient form partial differential equations" is

$$e_a \frac{\partial^2 u}{\partial t^2} + d_a \frac{\partial u}{\partial t} + \nabla \cdot (-c\nabla u - \alpha u + \gamma) + \beta \cdot \nabla u + au = f. \tag{3.88}$$

Inside the excitation region, probes can diffuse and undergo bleaching. Thus, we set $d_a = 1$, $c = D$, $a = -k_{\text{bleach}}$, and all other constants to zero such that

$$\frac{\partial u}{\partial t} - D\nabla^2 u + k_{\text{bleach}} = 0. \tag{3.89}$$

Outside the excitation region, probes cannot be bleached, so as a second coefficient form PDE, we set $d_a = 1$ and $c = D$, with all other constants set to zero, such that

$$\frac{\partial u}{\partial t} - D\nabla^2 u = 0. \tag{3.90}$$

We set the boundary conditions of the outer cylinder to have zero flux. At time zero, we fix the concentration across the geometry to a constant concentration, c_0.

When setting up our simulation, there are further technical specifications needed to fully describe the physical model. For those interested in precisely repeating our numerical simulations, we report the specific details of our COMSOL implementation of this problem in the following shaded box.

Specifics of Simulation Set-up:

- To capture the discrete on/off nature of pulsing the excitation light, we utilize the Events Interface in COMSOL. Events trigger the solver to reassess the step size at specified times.
  - There are two event types, explicit and implicit, available in COMSOL. Here we use two explicit events, since we know the precise timings of the light stage. Implicit events should be used when the event of interest is a response to the simulation dynamics.
  - We create a discrete states variable called ONOFF, which we initially set to a value of 1. This corresponds to the light being on.

We then create an explicit event, which turns the light off such that ONOFF = 0, which is set at time $t_{\text{excite}} = 150$ ms and repeats with an interval $t_{\text{int}} = 20$ s. A second explicit event is set to turn the light back on at $t_{\text{int}} = 20$ s, by setting ONOFF = 1, and repeats with the interval $t_{\text{int}} = 20$ s.

- We use the Coefficient Form PDE physics to describe our model. We define two separate PDEs to simulate the bright probe concentrations in each cylinder.
  - Our first PDE is defined to act upon the smaller cylinder. In this region, probes can diffuse and also be bleached by the light pulses thus, our model is
  $$\frac{\partial c}{\partial t} = D\nabla^2 c - k_{\text{bleach}} \times \text{ONOFF}. \tag{3.91}$$
  - The second PDE acts upon the larger cylinder excluding the inner smaller cylinder's volume. Here probes can only diffuse, thus we use the model
  $$\frac{\partial c}{\partial t} = D\nabla^2 c. \tag{3.92}$$
- We use a physics controlled mesh with a “Fine" element size.
- To solve the equation, we use the Time Dependent Solver with output times from 0 – 4000 s at a step size of 0.05 s. We apply a user controlled relative tolerance of 0.01. For the absolute tolerance, we use a "Scaled" global method with the "Factor" tolerance method set to a tolerance factor of 0.1. We leave the derivative tolerance method to be "Automatic."

One goal of this simulation is to understand how the parameter values for k_{bleach} and D change the time dynamics of photobleaching. We run a variety of simulations sweeping the parameter values of k_{bleach} and D as shown in Figures 3.40 and 3.41. We find that as we increase k_{bleach} and as we increase D, the steepness of the decay decreases and there is a higher concentration of bright probes at the end of the simulation. We fit the simulation curves to a single exponential plus a constant as seen in Figure 3.40. The fits are described by the equations

$$\frac{u}{u_0} = (1 - I_\infty)\exp(-t/\tau_1) + I_\infty, \tag{3.93}$$

in Figure 3.40 and a double exponential in Figure 3.41 which is described by

$$\frac{u}{u_0} = (1 - I_\infty)\exp(-t/\tau_1) + I_\infty \exp(-t/\tau_2), \tag{3.94}$$

where u_0 is the initial concentration of bright probes. We find a better agreement to the double exponential fit. Regardless of the fit type, we find the fit parameters for the fast decay constant, τ_1, and the infinite time value of the concentration, I_∞, reflect the trends in the bleaching rate and diffusion constants. The increasing steepness that results from increasing k_{bleach} and D is reflected by a decreasing τ_1. Similarly the higher ending concentration of bright probes that correlates with higher k_{bleach} and D values is reflected by an increasing I_∞ value.

Complementing our exploration of the form of the decay in probe brightness with time, we can take a more granular look into the spatial depletion profile as shown in Figures 3.42 and 3.43. Here, we draw a straight line the length of the larger cylinder diameter which passes through the center point of the geometry. Plotting the bright probe concentration as a function of position on the line, we can observe the form of depletion throughout the simulation. We find that as the diffusion constant increases, the well created by light pulsing in the inner circle becomes shallower. This makes sense because a higher diffusion constant allows bright probes to quickly replenish the darkened well. As the bleaching rate increases, the well becomes deeper. With more probes bleached per shot of light, the deficit of bright probes in the well is more significant. The simulations with zero diffusion, $D = 0$ show some noise due to numerical instability, especially at the discontinuous edges of the region of light excitation. These plots may raise concern that when treating images for photobleaching, there may need to be a spatial dependence on the corrective function. However, we find in the regions of the images we use, the spatial effects are minimal. Figure 3.43 zooms in on the light excitation region and also shows the width of the approximate final aster size. At early times, when the aster is first contracting and is about the size of the light excitation region, the concentration profile is mostly flat with little spatial dependence. At later times when there more curvature in the well, we highlight the percent change in bright probe concentration in the aster size region is maximally one percent. Thus, we do not believe applying a spatially-explicit correction to photobleaching is necessary for these experiments.

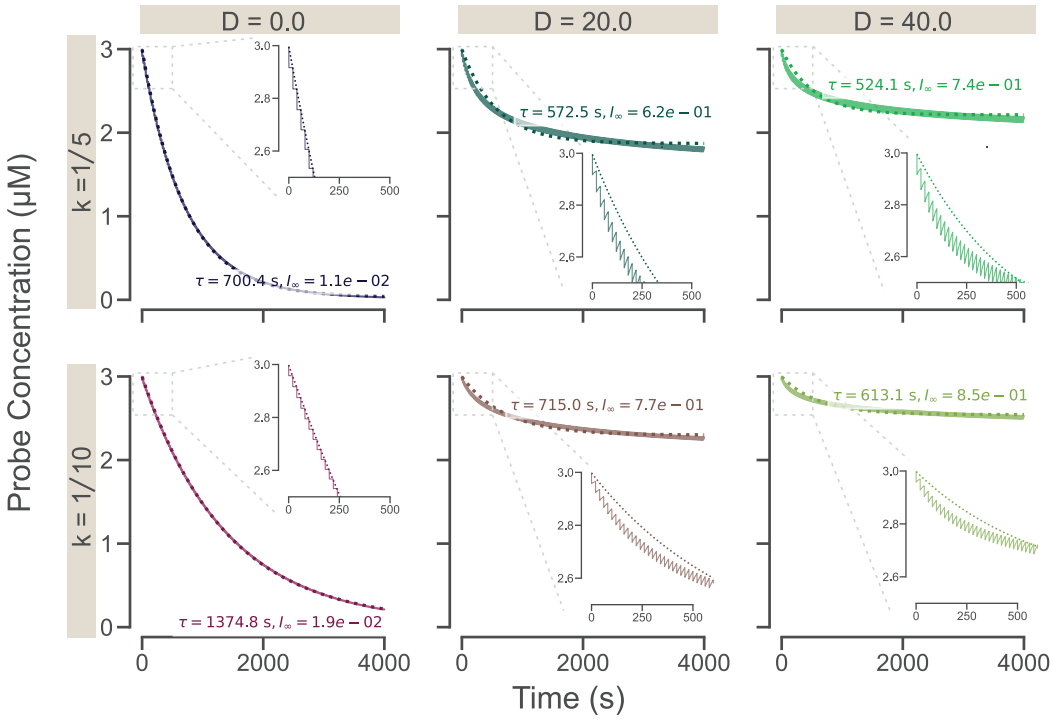

Figure 3.40: **Fitting COMSOL simulations of the bright ATP probe intensity to a single exponential plus a constant.** We simulate the depletion of bright probes due to photobleaching for a sweep of bleaching rates and diffusion constants. Fitting the time traces, which report the concentration of bright probes averaged over the light excitation region, we find a single exponential plus a constant, equation 3.93, fits the traces moderately well. We witness trends in the fit parameters such that the decay constant τ increases with increasing k_{bleach} and D, while I_∞ increases with increasing D but decreases with increasing k_{bleach}. The insets for each plot show a zoomed in blow up of the early times to visualize the initial depletion and recovery cycles corresponding to the pulses. The single exponential plus constant fits don't capture the initial decay well for non-zero diffusion.

Estimates of Photobleaching Dynamics

We conclude this section with a series of estimates aimed to give intuition into the dynamics of photobleaching in our system. Specifically, towards a sense of scale for the extent of photobleaching under these conditions, we approximate the number of fluorescent probes that might be subject to different scenarios of photophysically-challenging illumination. These estimates are based on simplifying assumptions, but we find they provide useful context by suggesting a feeling for the scales of the problem. We have included these results here and urge the reader to attempt their own version of these estimates.

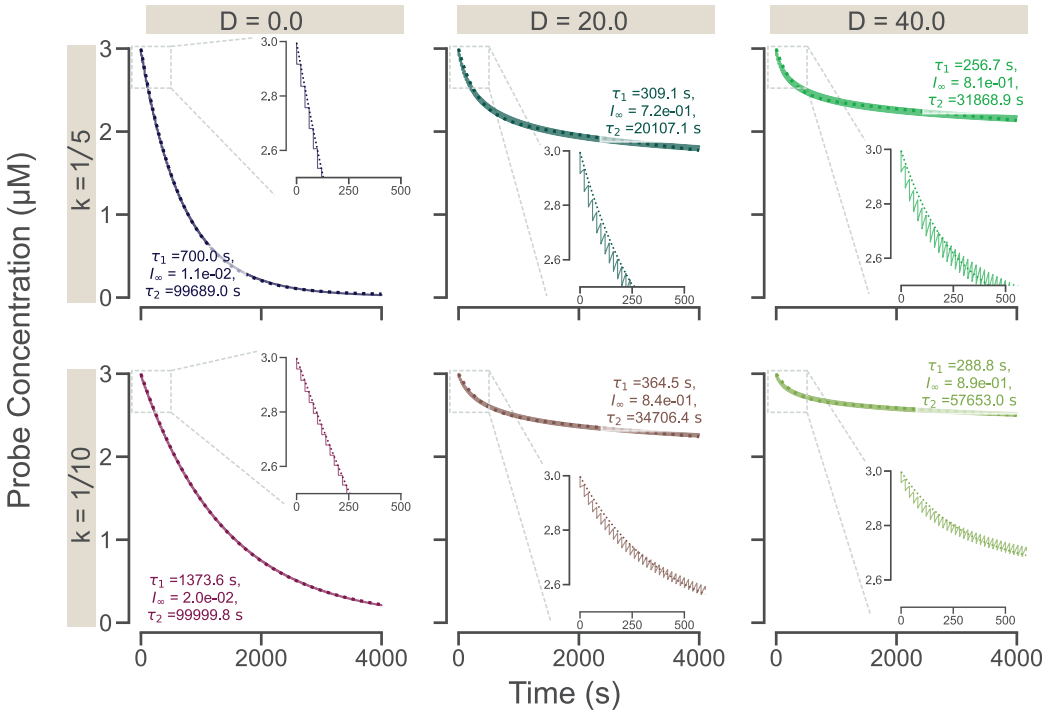

Figure 3.41: **Fitting COMSOL simulations of the ATP probe intensity decay due to photobleaching to a double exponential.** We simulate the depletion of bright probes due to photobleaching for a sweep of bleaching rates and diffusion constants. Fitting the time traces, which report the concentration of bright probes averaged over the light excitation region, we find a double exponential plus a constant, equation 3.94, fits the traces quite well, and better than the single exponential plus a constant. We witness trends in the fit parameters such that the decay constant τ_1 increases with increasing k_{bleach} and D, while I_∞ increases with increasing D but decreases with increasing k_{bleach}. The insets for each plot show a zoomed in blow up of the early times to visualize the initial depletion and recovery cycles corresponding to the pulses. The double exponential fits well capture the initial decay.

How many photons are emitted per excitation pulse?

As measured by a power meter, the power of our microscope's light excitation is $\approx 200\,\mu$W. The power meter's collection area is larger than the size of the pulse, so we take the area of illumination to be the area over which the power is distributed. The area of illumination is

$$A = 1920\,\text{px} \times 1200\,\text{px} \times \left(\frac{0.59\,\mu\text{m}}{\text{px}}\right)^2 \approx 10^6\,\mu\text{m}^2. \tag{3.95}$$

Thus, the incident power per area is

$$\frac{P}{A} = \frac{200\,\mu\text{W}}{10^6\,\mu\text{m}^2} = 2 \times 10^{-10}\,\frac{\text{W}}{\mu\text{m}^2}. \tag{3.96}$$

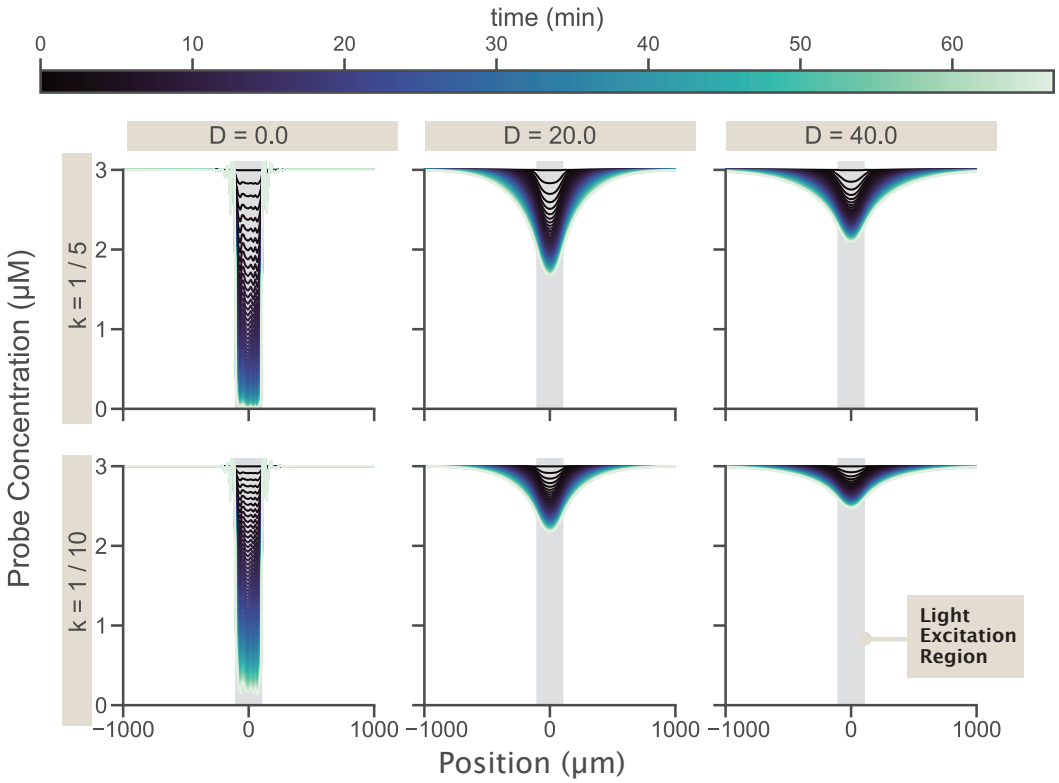

Figure 3.42: **Plotting the bright probe concentration across space shows how simulation parameters impact the depletion well formed.** We draw a cut line that spans the diameter of the larger cylinder at the midpoint of the cylinder height. Each line in the figure represents the concentration of bright probes in space for a given timepoint. We find the depth of the well depleted correlates with increasing bleaching rates and decreasing diffusion constants.

Each pulse is emitted for $\approx 150\,\text{ms}$, thus the energy per area of each pulse is,

$$\sigma_{\text{pulse}} \equiv \frac{P\Delta t}{A} = 2\times 10^{-10}\,\frac{\text{W}}{\mu\text{m}^2}\times 0.15\,\text{s} = 3\times 10^{-11}\,\frac{\text{J}}{\mu\text{m}^2}. \tag{3.97}$$

The wavelength of the light pulse is $\lambda \approx 400\,\text{nm}$, giving a single photon energy of

$$E_{\text{photon}} = \frac{hc}{\lambda} = \frac{(7\times 10^{-34}\,\text{J}\cdot\text{s})(3\times 10^{8}\,\text{m/s})}{4\times 10^{-7}\,\text{m}} \approx 5\times 10^{-19}\,\frac{\text{J}}{\text{photon}}. \tag{3.98}$$

Thus, the number of photons per μm^2 of a light pulse is,

$$\frac{\sigma_{\text{pulse}}}{E_{\text{photon}}} = \frac{3\times 10^{-11}\,\text{J}/\mu\text{m}^2}{5\times 10^{-19}\,\text{J/photon}} = 6\times 10^{7}\,\frac{\text{photons}}{\mu\text{m}^2}. \tag{3.99}$$

For an illumination area of $A \sim 10^6\ \mu\text{m}^2$, this implies there are a total of about 6×10^{13} total emitted photons per pulse.

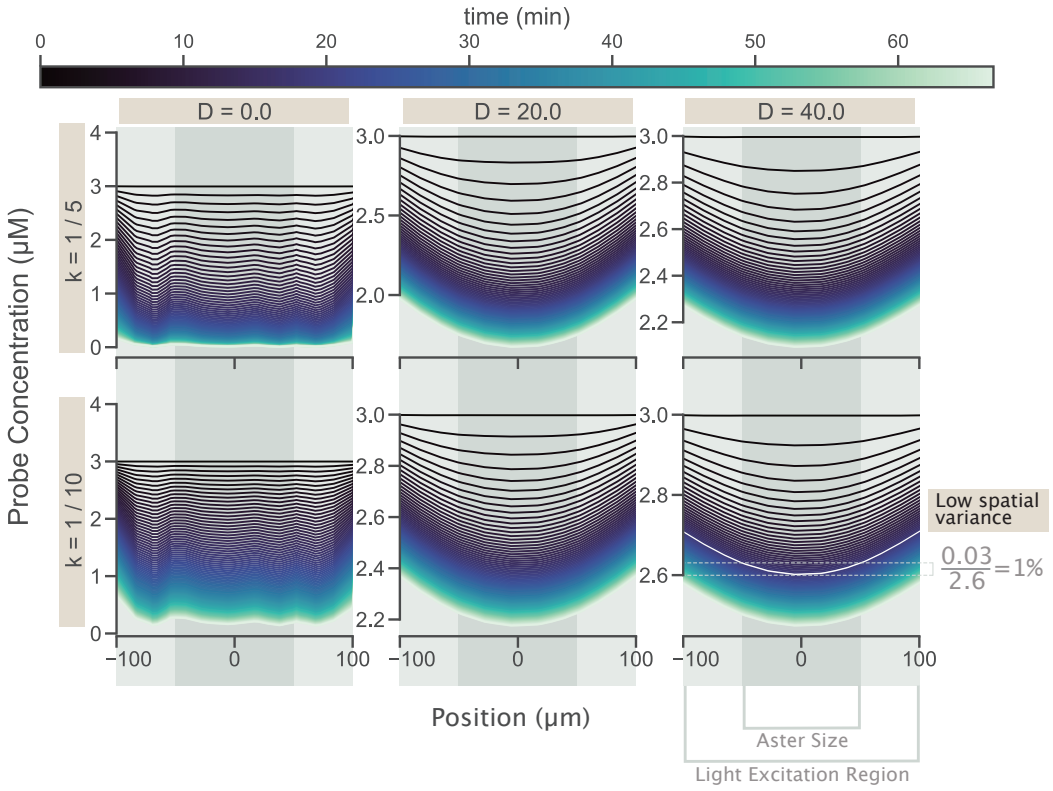

Figure 3.43: **Zooming in on the spatial depletion well created by photobleaching, there is little variation within the region of interest.** If there is high levels of variation throughout space in concentration of bright probe, we would need to correct for photobleaching with a spatial dependent function. Zooming in on the light excitation region, where our analysis occurs, we find that the extent of spatial variation is small. At early times (blacker lines), the aster is approximately the size of light excitation region, but the concentration traces are mostly flat, implying little variation. For later times (bluer lines), the traces are curvier. But during these times the aster is smaller, around the width of the dark grey region. In the bottom right plot, we show for a given time around 20 minutes (highlighted by the white trace), the variation is still small, only one percent in the aster region.

How many fluorescent probes are in the illumination area?

The concentration of ATP probes in our experiment is $2.8\,\mu$M. Given the illumination area of the excitation pulse in equation 3.95 and the depth of the experimental chamber as $d \approx 100\,\mu$m, the volume of illumination is

$$V = Ad = 10^6\,\mu\text{m}^2 \times 100\,\mu\text{m} = 10^8\,\mu\text{m}^3. \tag{3.100}$$

Thus, the number of probes illuminated is

$$\#\text{ of probes} = 2.8\,\mu\text{M}\left(\frac{10^3\mu\text{m}^3}{\mu\text{M}}\right)\left(10^8\,\mu\text{m}^3\right) \approx 3\times 10^{11}\text{ probes}. \tag{3.101}$$

How many photons are absorbed by probes according to the concentration of the sample?

The Beer-Lambert Law models the intensity reduction due to light passing through a solution. For some incident light intensity, I_0, the transmitted light intensity I, can be computed by solving

$$\log_{10}\left(\frac{I_0}{I}\right) = \epsilon l c, \tag{3.102}$$

where ϵ is the molar extinction coefficient of the solute, l is the depth of the sample chamber, and c is the concentration of solute. The extinction coefficient of QUEEN ATP reporters is listed as $\epsilon = 24,870\ \text{M}^{-1}\,\text{cm}^{-1} \approx 2\times 10^{-6}\ \mu\text{M}^{-1}\,\mu\text{m}^{-1}$ [2]. Our flow cell chambers have a depth on the order of $100\,\mu$m and the concentration of probes are about $3\,\mu$M. Inputting these values, we find the fraction of intensity that is transmitted,

$$\frac{I_0}{I} \approx 10^{(2\times 10^{-6}\,\mu\text{M}^{-1}\,\mu\text{m}^{-1})(3\,\mu\text{M})(100\,\mu\text{m})} = 10^{6\times 10^{-4}} = 1.001. \tag{3.103}$$

This means only 1 out of every 1000 incident photons are actually absorbed by fluorescent probes.

If the probes were to queue, such that one probe receives all incoming photons until it bleaches before the next probe receives any photons, how many probes die in a single pulse?

On average, common fluorescent proteins exhibit photobleaching quantum yields of order 10^{-5} (see references [21, 22]), meaning they can photobleach once they have received of order 10^5 photons. Given that a single pulse emits 6×10^{13} photons, which the adsorption fraction of the previous section implies gives 6×10^{10} adsorbed

photons, the number of probes that can be bleached in a single pulse may be very roughly estimated as,

$$\#\text{ of bleached probes} = \frac{6\times10^{13}\text{ incident photons}\frac{1\text{ adsorbed photon}}{10^3\text{ incident photons}}}{10^5\text{ photons per bleached probe}} = 6{\times}10^5\text{ bleached probes.} \tag{3.104}$$

From this, we find the fraction of bleached probes,

$$p_b = \frac{6\times10^5\text{ bleached probes}}{3\times10^{11}\text{ total probes}} = 2\times10^{-6}. \tag{3.105}$$

This is an upper bound assuming the photons are not distributed evenly. However it implies that a single pulse does little to deplete the probe intensity.

How does the intensity of the sample change as a function of the fraction of bleached probes per excitation assuming instantaneous diffusion?

In reality, the transport of fresh unbleached probes from the reservoir into the illuminated (bleached) region is neither instantaneous nor infinitely slow, but somewhere in between. Since these limiting idealized cases bound the real behavior in experiments, it is useful to get a sense of how they each behave. To wit, consider the first case where diffusive replenishment is infinitely fast. What would be the corresponding shape and quantitative rate of the resulting intensity decay?

Assuming diffusion is instantaneous, the intensity of the sample after a single pulse is the weighted average of the illuminated and not illuminated areas, A_{illum} and $A_{\text{not illum}}$, weighted by the fraction of bleached probes, p_b,

$$\langle I(n=1)\rangle = \frac{(1-p_b)I_0A_{\text{illum}} + I_0A_{\text{not illum}}}{A_{\text{illum}} + A_{\text{not illum}}} = I_0\left(1 - \frac{p_b}{1+\frac{A_{\text{not illum}}}{A_{\text{illum}}}}\right). \tag{3.106}$$

For multiple pulses, the average intensity of the sample will be

$$\langle I(n)\rangle = I_0\left(1 - \frac{p_b}{1+\frac{A_{\text{not illum}}}{A_{\text{illum}}}}\right)^n. \tag{3.107}$$

In our system, $A_{\text{illum}} = 10^6\,\mu\text{m}^2$, as defined in equation 3.95 and the not illuminated area (size of the chamber minus the illuminated area) is

$$A_{\text{not illum}} = (3\times10^3\,\mu\text{m})(18\times10^3\,\mu\text{m}) - 10^6\,\mu\text{m}^2 = 53\times10^6\,\mu\text{m}^2. \tag{3.108}$$

So, the ratio of areas is $\approx \frac{1}{50} = 0.02$. Thus any changes to the sample's average intensity occur very slowly. We can see this more clearly by noting that $1-x \approx e^{-x}$

for small x. This limit is true given that

$$\frac{p_b}{1+\frac{A_{\text{not illum}}}{A_{\text{illum}}}} \approx \frac{2\times10^{-6}}{1+0.02} \approx 2\times10^{-6}. \tag{3.109}$$

Thus, we can rewrite Equation 3.110 as,

$$\langle I(n)\rangle = I_0 \exp\left(-\frac{np_b}{1+\frac{A_{\text{not illum}}}{A_{\text{illum}}}}\right), \tag{3.110}$$

where the decay constant as a function of the number of pulses is long,

$$\frac{1+\frac{A_{\text{not illum}}}{A_{\text{illum}}}}{p_b} \approx 5\times10^5 \text{ pulses}. \tag{3.111}$$

If the short timescale of photobleaching we fit in the experiment is entirely due to surface bound probes, what area of the surface would be covered in probes?

To inform the physical possibility that probes may stick to the surface of the experimental chamber and be subject to photobleaching but not replenishment, as discussed with the model in section 3.8, we ask about the number of probes associated with a cross-sectional area of the surface. The rapid initial decay in photobleaching as measured by our control experiments drops by 20 percent. Assuming this is all due to probes stuck to the surface photobleaching, we estimate the number of probes required to create this effect. The concentration of probe in the reaction mix is 2.8 μM. The illumination region is 1920x1200 pixels with a scaling of 0.59 um per pixel. And, the height of the flow cell is 100 um. Thus, the per micron cubed number of probe molecules is,

$$N_{\text{per}\,\mu\text{m}^3} = f\ \mu\text{M} \times \frac{1000/\mu\text{m}^3}{\mu\text{M}} = f\times10^3/\mu\text{m}^3. \tag{3.112}$$

The area of illumination is

$$A = 1920\,\text{px}\times1200\,\text{px}\times\left(\frac{0.59\,\mu\text{m}}{\text{px}}\right)^2 \approx 10^6\,\mu\text{m}^2 \tag{3.113}$$

and the volume is

$$V = 10^6\,\mu\text{m}^2\times100\,\mu\text{m} = 10^8\,\mu\text{m}^3 \tag{3.114}$$

so the number of probes in the excitable region is

$$N = N_{\text{per}\,\mu\text{m}^3}\times V = f\times10^{11}. \tag{3.115}$$

For the rapid decay in the empirical photobleaching curves to be fully accounted for by surface-mediated probe bleaching, how many probes must be stuck to the surface? Since the total fluorescence decay observed is on the order of 20 percent, there would need to be

$$N_{\text{surf}} = 0.2 \times N \approx 10^{11} \tag{3.116}$$

probes stuck to the surfaces of the experimental chamber to fully account for the observed decay. We estimate the radius of each probe to be 2 nm in equation 3.204, so we approximate the area of each probe as $4 \times 10^{-5}\ \mu\text{m}^2$. Thus the total area taken up by surface bound probes is

$$A_{\text{surf probes}} = 4 \times 10^{6}\ \mu\text{m}^2, \tag{3.117}$$

implying the surface would be fully decorated in probes. We find this surface-associated density physically highly implausible.

Center Tracking

To accurately determine how concentrations change with the aster radius, it is important to accurately identify the center of an aster. Images of fluorescently labeled motor proteins in asters generally show a bright core region with fainter arms. Especially while developing, asters show diffuse, ovular boundaries. These boundaries of asters are not always geometrically contiguous or universally high in contrast with the background over the aster region. These features fundamental to real asters deeply complicate the use of automated segmentation and tracking of asters using even sophisticated image analysis pipelines and thresholding procedures. Specifically, for instance, we built and assessed a battery of semisupervised thresholding and tracking pipelines, but all methods failed to achieve satisfactory identification of asters and positions across the experimental conditions and replicates we measured. Accordingly, to ensure that this segmentation and tracking is performed robustly for every dataset, we performed manual segmentation and tracking of all asters as they formed across all data. Specifically, to accomplish this, we drew elliptical boundaries of asters over a dense number of key frames in each aster movie (using an instance of the open source Computer Vision Annotation Tool (CVAT)), and where relevant performed simple temporal interpolation of these aster boundaries between explicitly tracked key frames. This produced excellent and internally consistent tracking results. Since every ellipse furnishes both a minor and major axis for the aster, to summarize the overall radial size of the aster (e.g., as reported in the main text figures), we report the geometric mean of these two axis lengths.

3.9 Effects of Competitive Inhibition by ADP and Phosphate on ATP Hydrolysis Rates

States and Weights Modeling of ATP Hydrolysis

To quantitatively dissect the relationship between motor proteins and ATP, we develop a model describing the concentration of ATP throughout space and time. ATP can diffuse and undergo hydrolysis due to motor proteins throughout our system; however, ATP cannot regenerate. The diffusive term is straight forward and takes the form of Fick's Law, $D\nabla^2 A$. The reaction term needs to take into account the rate at which ATP can bind to a motor, along with the probability of binding. As a first pass, we model this reaction term just taking into account the statistical mechanics of ATP binding to a motor. However, this fails to acknowledge the dynamics of ATP being converted to ADP and phosphate. We elaborate on the ATP only model to include competitive inhibition resulting from ADP, as well as phosphate.

ATP Only Model – Assume No Products Present

We use a states and weights approach, as outlined in reference [23], to determine the probability of an ATP molecule binding to a motor protein for T ATP molecules in a lattice with Ω sites, one of which is the motor protein binding site. In this case, there are two states for the motor protein, as depicted in Figure 3.44. It can be unbound with energy $E = 0$ and multiplicity $\frac{\Omega!}{T!(\Omega-T)!} \approx \frac{\Omega^T}{T!}$ for $\Omega >> T$. Alternatively the motor protein can be bound, with an energy of $E = \epsilon_T$ and multiplicity $\approx \frac{\Omega^{(T-1)}}{(T-1)!}$. Putting this together, we find the probability of binding is

$$p_{\text{bound}} = \frac{\frac{\Omega^{(T-1)}}{(T-1)!}e^{-\beta\epsilon_T}}{\frac{\Omega^T}{T!} + \frac{\Omega^{(T-1)}}{(T-1)!}e^{-\beta\epsilon_T}}. \tag{3.118}$$

We simplify the probability by multiplying the numerator and denominator by $\frac{T!}{\Omega^T}$ to get

$$p_{\text{bound}} = \frac{\frac{T}{\Omega}e^{-\beta\epsilon_T}}{1 + \frac{T}{\Omega}e^{-\beta\epsilon_T}}. \tag{3.119}$$

To convert Ω, the number of "lattice sites", to a volume, we multiply the numerator and denominator by $\frac{\Delta V}{\Delta V}$, the small volume each lattice site represents. By specifying $c_0 = \frac{1}{\Delta V}$ and $[\text{ATP}] = \frac{T}{\Omega\Delta V}$, our probability now depends on concentrations and becomes

$$p_{\text{bound}} = \frac{\frac{[\text{ATP}]}{c_0} e^{-\beta\epsilon_T}}{1 + \frac{[\text{ATP}]}{c_0} e^{-\beta\epsilon_T}}. \tag{3.120}$$

Lastly, we define a constant $K_\text{T} = c_0 e^{\beta\epsilon_\text{T}}$ which gives the result

$$p_{\text{bound}} = \frac{\frac{[\text{ATP}]}{K_\text{T}}}{1 + \frac{[\text{ATP}]}{K_\text{T}}}, \tag{3.121}$$

in the form of a Michaelis-Menten (Langmuir) binding curve. Thus the constant K_T is interpreted as the concentration at which the chance of an ATP binding to a motor is fifty percent.

State	Energy	Multiplicity	Weight
	0	$\frac{\Omega^\text{T}}{T!}$	$\frac{\Omega^\text{T}}{T!}$
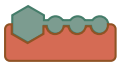	ϵ_T	$\frac{\Omega^{(\text{T}1)}}{(T-1)!}$	$\frac{\Omega^{(\text{T}1)}}{(T-1)!}\exp\left(-\beta\epsilon_\text{T}\right)$

Figure 3.44: **States and weights of ATP binding to motors.** Energy, multiplicity and weights for the binding states of a single motor in a lattice with Ω sites and T ATP molecules.

ADP Competitive Inhibition – Assume a Single Product

We now add in the effect of accumulating ADP into our model. If ADP binds to the motor, ATP cannot bind which creates competitive inhibition. Similar to our treatment of the ATP only system, we write down probability in terms of the weights of each state. This system has three states: the motor protein is unbound, ATP is bound, or ADP is bound, as shown in Figure 3.45. Once again, we denote the lattice sites as Ω, the number of ATP molecules as T, and the number of ADP molecules as D. We write the probability of the ATP bound state as

$$p_{\text{bound}} = \frac{\frac{\Omega^{T-1}\Omega^D}{(T-1)!D!}\exp\left(-\beta\epsilon_\text{T}\right)}{\frac{\Omega^T\Omega^D}{T!D!} + \frac{\Omega^{T-1}\Omega^D}{(T-1)!D!}\exp\left(-\beta\epsilon_\text{T}\right) + \frac{\Omega^T\Omega^{(D-1)}}{T!(D-1)!}\exp\left(-\beta\epsilon_\text{D}\right)}. \tag{3.122}$$

Multiplying the numerator and denominator by $\frac{T!D!}{\Omega^T\Omega^D}$ simplifies the expression to

$$p_{\text{bound}} = \frac{\frac{T}{\Omega}\exp\left(-\beta\epsilon_\text{T}\right)}{1 + \frac{T}{\Omega}\exp\left(-\beta\epsilon_\text{T}\right) + \frac{D}{\Omega}\exp\left(-\beta\epsilon_\text{D}\right)}. \tag{3.123}$$

We can convert this into a concentration friendly equation through the substitutions $[\text{ATP}] = \frac{T}{\Omega\Delta V}$, $[\text{ADP}] = \frac{D}{\Omega\Delta V}$, and $K_{T,D} = \frac{1}{\Delta V} e^{\beta\epsilon_{T,D}}$, which results in

$$p_{\text{bound}} = \frac{\frac{[\text{ATP}]}{K_T}}{1 + \frac{[\text{ATP}]}{K_T} + \frac{[\text{ADP}]}{K_D}}. \tag{3.124}$$

Equation 3.124 is of a similar form to equation 3.121, but has an extra term in the denominator corresponding to the likelihood of binding ADP. Thus as more ATP turns to ADP, the probability of ATP binding to the motor decreases.

Note that if we consider a model of ATP and phosphate with no ADP present, the form should be the same as in Equation 3.124 where [ADP] is replaced with $[\text{P}_i]$ and K_D is replaced with K_P.

State	Energy	Multiplicity	Weight
	0	$\frac{\Omega^\text{T}}{T!}\frac{\Omega^\text{D}}{D!}$	$\frac{\Omega^\text{T}}{T!}\frac{\Omega^\text{D}}{D!}$
	ϵ_T	$\frac{\Omega^{(\text{T-1})}}{(T-1)!}\frac{\Omega^\text{D}}{D!}$	$\frac{\Omega^{(\text{T-1})}}{(T-1)!}\frac{\Omega^\text{D}}{D!}\exp\left(-\beta\epsilon_\text{T}\right)$
	ϵ_D	$\frac{\Omega^\text{T}}{T!}\frac{\Omega^{(\text{D-1})}}{(D-1)!}$	$\frac{\Omega^\text{T}}{T!}\frac{\Omega^{(\text{D-1})}}{(D-1)!}\exp\left(-\beta\epsilon_\text{D}\right)$

Figure 3.45: **States and weights for competitive inhibition of ADP on a motor.** Energy, multiplicity and weights for three binding states: unbound motor, bound ATP, and bound ADP. Assume a lattice with Ω sites, one of which is the motor protein, T ATP molecules and D ADP molecules.

ADP and Phosphate Competitive Inhibition – Assume Both Products are Present

We can go a step further with this model by considering both hydrolysis products, ADP and phosphate, to be present in solution. This creates two new inhibition states: phosphate is bound, or phosphate and ADP are bound. We follow a similar procedure as in the ADP only model, though now we must take into account three species, ATP (T), ADP (D), and phosphate (P). As depicted in Figure 3.46, let us define the energies of the bound phosphate, and the ADP and phosphate bound states, as ϵ_P and $\epsilon_{\text{D·P}} = \epsilon_\text{D} + \epsilon_\text{P} + \sigma'$, respectively. Here we guess the energy of both

species binding is the sum of the individual binding energies, plus or minus some interaction energy, σ'. For, again, Ω binding sites, the probability of an ATP being bound to the motor is:

$$p_{\text{bound}} = \underbrace{\frac{\Omega^{T-1}\Omega^{D}\Omega^{P}}{(T-1)!D!P!}\exp\big(-\beta\epsilon_{\text{T}}\big)}_{\text{ATP Bound}} \cdot \Bigg[\underbrace{\frac{\Omega^{T}\Omega^{D}\Omega^{P}}{T!D!P!}}_{\text{Unbound}} + \underbrace{\frac{\Omega^{T-1}\Omega^{D}\Omega^{P}}{(T-1)!D!P!}\exp\big(-\beta\epsilon_{\text{T}}\big)}_{\text{ATP Bound}} + \underbrace{\frac{\Omega^{T}\Omega^{(D-1)}\Omega^{P}}{T!(D-1)!P!}\exp\big(-\beta\epsilon_{\text{D}}\big)}_{\text{ADP Bound}} + \underbrace{\frac{\Omega^{T}\Omega^{D}\Omega^{(P-1)}}{T!D!(P-1)!}\exp\big(-\beta\epsilon_{\text{P}}\big)}_{\text{P Bound}} + \underbrace{\frac{\Omega^{T}\Omega^{(D-1)}\Omega^{(P-1)}}{T!(D-1)!(P-1)!}\exp\big(-\beta(\epsilon_{\text{D}}+\epsilon_{\text{P}}+\sigma')\big)}_{\text{ADP and P Bound}} \Bigg]^{-1}. \tag{3.125}$$

We can simplify this expression by multiplying the numerator and denominator by $\frac{T!D!P!}{\Omega^{T}\Omega^{D}\Omega^{P}}$, which gives us

$$p_{\text{bound}} = \frac{\frac{T}{\Omega}\exp\left(-\beta\epsilon_{\text{T}}\right)}{1+\frac{T}{\Omega}\exp\left(-\beta\epsilon_{\text{T}}\right)+\frac{D}{\Omega}\exp\left(-\beta\epsilon_{\text{D}}\right)+\frac{P}{\Omega}\exp\left(-\beta\epsilon_{\text{P}}\right)+\frac{DP}{\Omega\Omega}\exp\left(-\beta(\epsilon_{\text{D}}+\epsilon_{\text{P}}+\sigma')\right)}. \tag{3.126}$$

Once more converting to units of concentration, we take $[\text{ATP}] = \frac{T}{\Omega\Delta V}$, $[\text{ADP}] = \frac{D}{\Omega\Delta V}$, $[\text{P}] = \frac{P}{\Omega\Delta V}$, $K_{T,D,P} = \frac{1}{\Delta V}e^{\beta\epsilon_{T,D,P}}$, and define $\sigma = e^{\beta\sigma'}$ which results in

$$p_{\text{bound}} = \frac{\frac{[\text{ATP}]}{K_T}}{1+\frac{[\text{ATP}]}{K_T}+\frac{[\text{ADP}]}{K_D}+\frac{[\text{P}]}{K_P}+\frac{[\text{ADP}][\text{P}]}{\sigma K_D K_P}}. \tag{3.127}$$

This model demonstrates how products of ATP hydrolysis compete with the motor binding sites. As more possible states emerge, the probability of ATP will binding to the motor protein reduces. We can directly see an impact on ATP hydrolysis by defining the hydrolysis rate as the probability of binding ATP multiplied by the maximum hydrolysis rate. This is written as

$$\Gamma\left([\mathrm{ATP}],[\mathrm{ADP}],[\mathrm{P}_i]\right) = \gamma \cdot \frac{\frac{[\mathrm{ATP}]}{K_\mathrm{T}}}{1 + \frac{[\mathrm{ATP}]}{K_\mathrm{T}} + \frac{[\mathrm{ADP}]}{K_\mathrm{D}} + \frac{[\mathrm{P}]}{K_\mathrm{P}} + \frac{[\mathrm{ADP}][\mathrm{P}]}{\sigma K_\mathrm{D} K_\mathrm{P}}}, \tag{3.128}$$

where γ is the ATP hydrolysis per motor per second for saturating ATP conditions with zero product concentrations.

State	Energy	Multiplicity	Weight
	0	$\frac{\Omega^\mathrm{T}}{T!}\frac{\Omega^\mathrm{D}}{D!}\frac{\Omega^\mathrm{P}}{P!}$	$\frac{\Omega^\mathrm{T}}{T!}\frac{\Omega^\mathrm{D}}{D!}\frac{\Omega^\mathrm{P}}{P!}$
	ϵ_T	$\frac{\Omega^{(\mathrm{T}-1)}}{(T-1)!}\frac{\Omega^\mathrm{D}}{D!}\frac{\Omega^\mathrm{P}}{P!}$	$\frac{\Omega^{(\mathrm{T}-1)}}{(T-1)!}\frac{\Omega^\mathrm{D}}{D!}\frac{\Omega^\mathrm{P}}{P!}\exp\left(-\beta\epsilon_\mathrm{T}\right)$
	ϵ_D	$\frac{\Omega^\mathrm{T}}{T!}\frac{\Omega^{(\mathrm{D}-1)}}{(D-1)!}\frac{\Omega^\mathrm{P}}{P!}$	$\frac{\Omega^\mathrm{T}}{T!}\frac{\Omega^{(\mathrm{D}-1)}}{(D-1)!}\frac{\Omega^\mathrm{P}}{P!}\exp\left(-\beta\epsilon_\mathrm{D}\right)$
	ϵ_P	$\frac{\Omega^\mathrm{T}}{T!}\frac{\Omega^\mathrm{D}}{D!}\frac{\Omega^{(\mathrm{P}-1)}}{(P-1)!}$	$\frac{\Omega^\mathrm{T}}{T!}\frac{\Omega^\mathrm{D}}{D!}\frac{\Omega^{(\mathrm{P}-1)}}{(P-1)!}\exp\left(-\beta\epsilon_\mathrm{P}\right)$
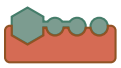	$\epsilon_{\mathrm{D}\cdot\mathrm{P}}$	$\frac{\Omega^\mathrm{T}}{T!}\frac{\Omega^{(\mathrm{D}-1)}}{(D-1)!}\frac{\Omega^{(\mathrm{P}-1)}}{(P-1)!}$	$\frac{\Omega^\mathrm{T}}{T!}\frac{\Omega^{(\mathrm{D}-1)}}{(D-1)!}\frac{\Omega^{(\mathrm{P}-1)}}{(P-1)!}\exp\left(-\beta\epsilon_{\mathrm{DP}}\right)$

Figure 3.46: **States and weights for competitive inhibition of ADP and phosphate on a motor.** Energy, multiplicity and weights for five binding states: unbound motor, bound ATP, bound ADP, bound phosphate, and bound ADP and phosphate. Once more, assume a lattice with Ω sites, one of which is the motor protein, T ATP molecules, D ADP molecules, and P phosphate molecules.

Testing Our Model Against Published Data

Fitting Motor Speeds Versus ATP Concentrations

The paper *Inhibition of kinesin motility by ADP and phosphate supports a hand-over-hand mechanism* by Schief et al. [24], examines how the speed of kinesin motors vary with ADP and phosphate concentrations. This measurement is very useful to us because speed is proportionally related to ATP hydrolysis rates through the motor step size. The authors define the speed of motors as

$$S = d \cdot k_\mathrm{cat} \frac{[\mathrm{ATP}] - \frac{[\mathrm{ADP}][\mathrm{P_i}]}{K_\mathrm{eq}}}{K_\mathrm{M} + [\mathrm{ATP}]}, \tag{3.129}$$

where d is the motor step size, k_{cat} is the per second hydrolysis rate, K_M is the Menten constant, K_{eq} is the equilibrium constant for hydrolysis, and all terms in brackets are concentrations. Hydrolysis of ATP highly favors the forward direction with $K_{eq} = 4.9 \cdot 10^{11}$ µM [24], thus the second term in the numerator is negligible, as no concentrations considered exceed 10^6 µM. We now write the speed as

$$S = d \cdot k_{cat} \frac{[ATP]}{K_M + [ATP]}. \tag{3.130}$$

We scan the measured data from Schief et al. and test if our model fits to it. We first examine Figure 2 from Schief et al., which depicts motor speeds versus ATP concentrations for different levels of hydrolysis products. We fit the data to equation 3.130, where k_{cat} and K_M are the fitting parameters. We determine k_{cat} for the no product data (Figure 3.47 black curve) and then keep it fixed for all other data sets, thus all other data only has one fitting parameter, K_M.

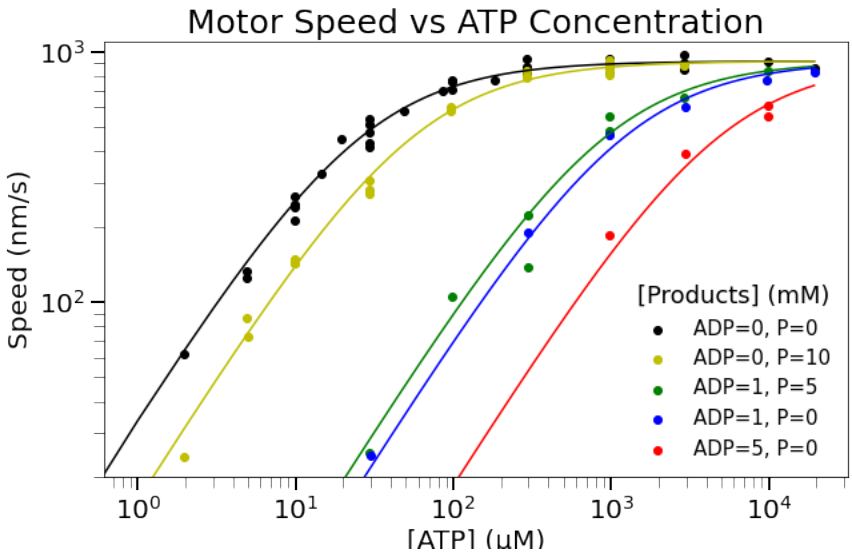

Figure 3.47: **Motor speeds for a given ATP concentration depends on the concentrations of ADP and phosphate.** Here, we replicate Figure 2 from Schief et al. The data points were determined by scanning the original figure with WebPlotDigitizer. The lines are fit to a Michaelis-Menten function. For the black curve (where the product concentrations are zero), we fit both k_{cat} and K_T parameters. For all other curves where products are present, we fit a single parameter, K_M, and use k_{cat}, from the no product condition, as an input for this function.

We can express our hydrolysis expression from equation 3.128 in the form of equation 3.130 with the following substitutions:

$$\begin{aligned}\Gamma &= \frac{S}{d},\\ k_{\text{cat}} &= \gamma,\\ K_{\text{M}} &= K_{\text{T}}\left[1 + \frac{[\text{ADP}]}{K_{\text{D}}} + \frac{[\text{P}]}{K_{\text{P}}} + \frac{[\text{ADP}][\text{P}]}{\sigma K_{\text{D}} K_{\text{P}}}\right].\end{aligned} \tag{3.131}$$

With these substitutions, we can determine the binding constants for each species. We find K_{T} from the no products experiment (Figure 3.47 black curve), which is simple,

$$K_{\text{M}} = K_{\text{T}}. \tag{3.132}$$

To determine $K_{\text{D,P}}$, we use the equation

$$K_{\text{D,P}} = [\text{ADP, P}]\left(\frac{K_{\text{M}}}{K_{\text{T}}} - 1\right)^{-1}, \tag{3.133}$$

(Figure 3.47 blue, red, and yellow curves). Finally to determine sigma, we write

$$\sigma = \frac{[\text{ADP}][\text{P}]}{K_{\text{D}} K_{\text{P}}}\left(\frac{K_{\text{M}}}{K_{\text{T}}} - 1 - \frac{[\text{ADP}]}{K_{\text{D}}} - \frac{[\text{P}]}{K_{\text{P}}}\right)^{-1}, \tag{3.134}$$

(Figure 3.47 green curve). This means the equation to find $K_{\text{D·P}}$ is

$$K_{\text{D·P}} = [\text{ADP}][\text{P}]\left(\frac{K_{\text{M}}}{K_{\text{T}}} - 1 - \frac{[\text{ADP}]}{K_{\text{D}}} - \frac{[\text{P}]}{K_{\text{P}}}\right)^{-1}. \tag{3.135}$$

The tabulated parameters are listed in Table 3.1

Through this analysis, we find that the values of K_{T} and K_{D} are about equivalent, perhaps this is due to similar chemical structure. It can thus be expected that the presence of ADP in our assay will cause significant slowing in the motor hydrolysis rate. On the other hand, K_{P} is two orders of magnitude larger than K_{T}, implying a small chance of phosphate binding to the motor protein. While we can expect some inhibition due to phosphate, it appears that competitive inhibition due to ADP dominates.

Strangely, $K_{\text{D·P}}$, and thus σ, is negative. It is also very large, four orders of magnitude larger than K_{T}. A negative binding constant would mean that the presence of both ADP and phosphate reduces competitive inhibition for the motor protein, while only having one of the species present creates increases the inhibition. This does not

Figure 3.47 Parameter Fits		
Parameter	Value	Description
γ	$114.5s^{-1}$	Fitted Parameter
$K_{\text{M (Black)}}$	26.2µM	Fit for 0 mM ADP, 0 mM P
$K_{\text{M (Yellow)}}$	55.8µM	Fit for 0 mM ADP, 10 mM P
$K_{\text{M (Blue)}}$	1.2mM	Fit for 1 mM ADP, 0 mM P
$K_{\text{M (Red)}}$	4.9mM	Fit for 5 mM ADP, 0 mM P
$K_{\text{M (Green)}}$	930µM	Fit for 1 mM ADP, 5 mM P
K_{T}	26.2µM	Equation 3.132
K_{D}	24.5µM	Equation 3.133
K_{P}	8.9mM	Equation 3.133
$K_{\text{D·P}}$	−714mM	Equation 3.135
σ	−3.3µM	Equation 3.134

Table 3.1: All the fitted parameters from Figure 3.47 are reported, along with the resulting Menten constants for each species.

seem physical. At best we would expect that the ADP and phosphate always bind together, so the total inhibition is equivalent to inhibition of ADP alone, as this is the more dominant inhibitor. Mathematically, this value for $K_{\text{D·P}}$ does not jibe with our model because it requires that σ is a negative value. We defined $\sigma = e^{-\beta\sigma'}$, where σ' is an interaction energy for the duel binding of ADP and phosphate. A negative σ implies an imaginary σ'.

Regardless of the sign, the magnitude of $K_{\text{D·P}}$ indicates that the inhibition due to ADP and P being bound is much smaller than the effect of either product alone and could possibly be negligible. Schief et al. only present one data set (green) with both products present in solution. These experiments seem worth replicating to understand if there is some behavior that is incorrectly incorporated into our model.

Figure 3.48 examines how the fit changes for different values of $K_{\text{D·P}}$. Setting $K_{\text{D·P}} = \infty$, thereby neglecting the interaction term, is the next best fit to the data after setting $K_{\text{D·P}} = \sigma \cdot K_{\text{D}} \cdot K_{\text{P}}$. Both taking the absolute value of σ and setting $\sigma = 1$ produce worse fits.

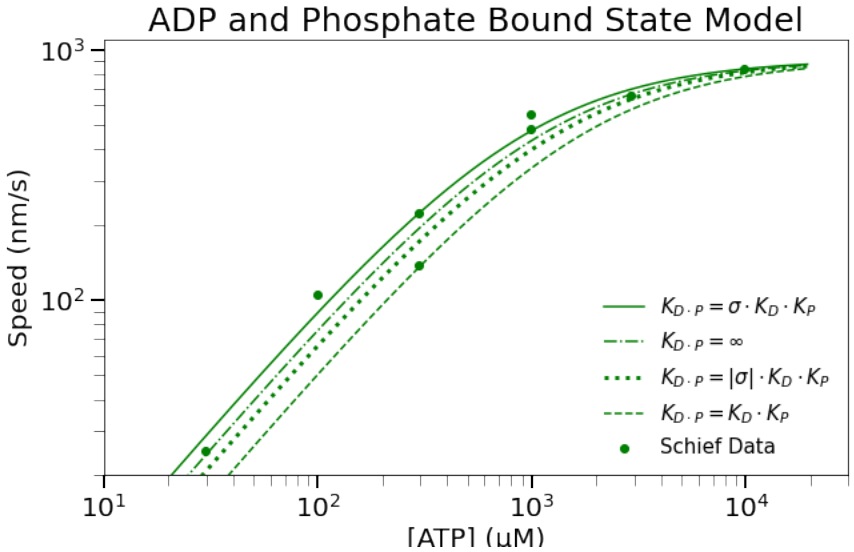

Figure 3.48: **Exploration of $K_{\mathrm{D\cdot P}}$ values for the ADP and phosphate bound state**. We examine the fits from varying the σ value in $K_{\mathrm{D\cdot P}}$. Using $\sigma = -713$ mM as found from our model, we get the best fit to the data. However, because a negative σ does not seem physical, we explore how setting σ to 713 mM, 1, and ∞ change the fits. We find that entirely neglecting the ADP/Phosphate bound state, setting $\sigma = \infty$ is the next best fit to the data. This is followed by taking $|\sigma| = 713$ mM, as the magnitude reduces the amount of inhibition experienced. Lastly, ignoring an interaction energy, setting $\sigma = 1$ produces the worst fit, as it maximizes the inhibition due to each product.

Additionally from Table 3.1, we learn about the hydrolysis rate of the motors in question. Our model quotes a rate of 114.5 ATP hydrolyzed per second per motor, for saturating ATP conditions with no products in solution. Previous work also using full length *Drosophila* conventional kinesin measures consistent hydrolysis rates with our fitted rate [25].

Fitting Motor Speeds Versus Product Concentrations

The authors took additional data investigating motor speeds versus various levels of products at various ATP levels. Using our model, we fit the data to

$$S = d \cdot \gamma \frac{\frac{[\mathrm{ATP}]}{K_T}}{1 + \frac{[\mathrm{ATP}]}{K_\mathrm{T}} + \frac{[\mathrm{ADP, P}]}{K_{\mathrm{D,\,P}}}}, \tag{3.136}$$

where we fit one parameter, $K_{\mathrm{D,\,P}}$. The first set of data, depicted in Figure 3.49, illustrates the variation in motor speed for different phosphate concentrations. Motor

speeds drop with increasing phosphate, especially as ATP concentrations drop, which implies inhibition is occurring.

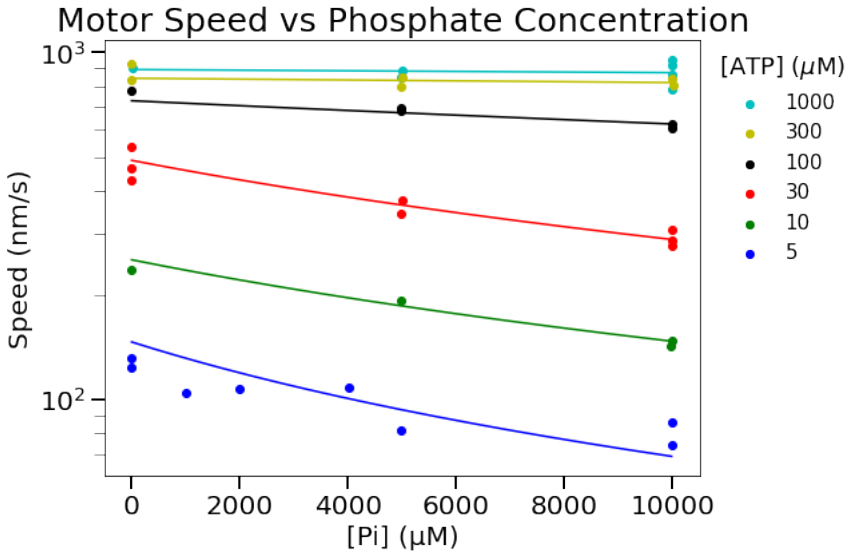

Figure 3.49: **Motor speeds are reduced with increasing phosphate concentrations.** Here, we replicate Figure 4A from Schief et al. The data points were determined by scanning the original figure with WebPlotDigitizer. The lines are fit to a Michaelis-Menten function. For each curve we fit a single parameter, K_P , and use k_{cat} and K_T, from Table 3.1, as inputs.

Our fits result in the K_P values quoted in Table 3.2. This data set produces an average K_P of 11.3 mM, comparable to the 8.9 mM value found from the previous data set in Table 3.1. There does not appear to be a trend in the K_P value with ATP concentration.

K_P Fitted Values for Various ATP Concentrations	
ATP Concentration (μM)	K_P (mM)
1000	12.2
300	27.9
100	12.5
30	6.8
10	10.1
5	7.4
Average	11.3

Table 3.2: Here we report upon the fits of K_P from the data in Figure 3.49. We do not find a correlation with ATP concentrations, as expected from our model.

The authors also examined the variation in speed with ADP concentration, as depicted in Figure 3.50. Once again, we have plotted the digitized data from Schief et al. and fit the points to our model in equation 3.136. Motor speeds drop significantly with higher levels of ADP present. Again, this is more drastic for lower ATP concentrations.

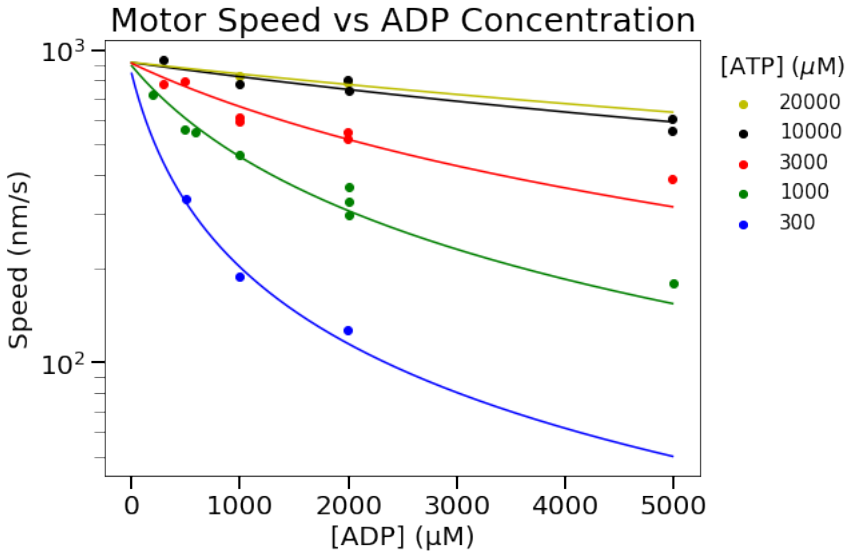

Figure 3.50: **Motor speeds are significantly reduced with increasing ADP concentrations.** Here, we replicate Figure 4B from Schief et al. The data points were determined by scanning the original figure with WebPlotDigitizer. The lines are fit to a Michaelis-Menten function. For each curve we fit a single parameter, K_D, and use k_{cat} and K_T, from Table 3.1, as inputs.

Table 3.3 reports the fitted K_D values. On average, $K_D = 23.6$ matching the $K_D = 24.5$ from table 3.1. Again, K_D values do not appear correlated with ATP concentration.

Comparison of Our Model to the Schief Model

We now compare our model with the model used in Schief et al. (2004) The authors defined k_{cat} and K_M as

$$k_{cat} = \frac{k_{cat}^{00}}{1 + \frac{[ADP]}{K_{ii}^{ADP}} + \frac{[P_i]}{K_{ii}^{P}} + \frac{[ADP][P_i]}{K_{ii}^{ADP\cdot P}}}, \tag{3.137}$$

and

$$\frac{K_M}{k_{cat}} = \frac{K_M^{00}}{k_{cat}^{00}} \left[1 + \frac{[ADP]}{K_i^{ADP}} + \frac{[P_i]}{K_i^{P}} + \frac{[ADP][P_i]}{K_i^{ADP\cdot P}}, \right] \tag{3.138}$$

K_D Fitted Values for Various ATP Concentrations	
ATP Concentration (mM)	K_D (μM)
20	14.7
10	23.8
3	23.0
1	26.7
0.3	25.4
Average	23.6

Table 3.3: Here we report upon the fits of K_D from the data in Figure 3.50. We do not find a correlation with ATP concentrations, as expected from our model.

respectively. The subscript 00 denotes the constants when the products are at zero concentration. The subscript i describes competitive inhibition by the products on the motor protein impacting the Menten term. The subscript ii is described as non-competitive inhibition which modifies the overall stepping rate and the Menten constant. Inputting equations 3.137 and 3.138 into equation 3.130, we find

$$S = d \cdot \frac{k_{\text{cat}}^{00}}{1 + \frac{[\text{ADP}]}{K_{\text{ii}}^{\text{ADP}}} + \frac{[\text{P}_\text{i}]}{K_{\text{ii}}^{\text{P}}} + \frac{[\text{ADP}][\text{P}_\text{i}]}{K_{\text{ii}}^{\text{ADP·P}}}} \cdot \frac{[\text{ATP}]}{\frac{K_{\text{M}}^{00} k_{\text{cat}}^{00}}{k_{\text{cat}}^{00}} \frac{1 + \frac{[\text{ADP}]}{K_{\text{i}}^{\text{ADP}}} + \frac{[\text{P}_\text{i}]}{K_{\text{i}}^{\text{P}}} + \frac{[\text{ADP}][\text{P}_\text{i}]}{K_{\text{i}}^{\text{ADP·P}}}}{1 + \frac{[\text{ADP}]}{K_{\text{ii}}^{\text{ADP}}} + \frac{[\text{P}_\text{i}]}{K_{\text{ii}}^{\text{P}}} + \frac{[\text{ADP}][\text{P}_\text{i}]}{K_{\text{ii}}^{\text{ADP·P}}}} + [\text{ATP}]}. \quad (3.139)$$

Simplifying the denominator and dividing the numerator and denominator by K_{M} yields

$$S = \frac{d \cdot k_{\text{cat}}^{00} \cdot \frac{[\text{ATP}]}{K_{\text{M}}^{00}}}{1 + \frac{[\text{ATP}]}{K_{\text{M}}^{00}} + \frac{[\text{ADP}]}{K_{\text{i}}^{\text{ADP}}} + \frac{[\text{P}_\text{i}]}{K_{\text{i}}^{\text{P}}} + \frac{[\text{ADP}][\text{P}_\text{i}]}{K_{\text{i}}^{\text{ADP·P}}} + \frac{[\text{ATP}]}{K_{\text{M}}^{00}} \left(\frac{[\text{ADP}]}{K_{\text{ii}}^{\text{ADP}}} + \frac{[\text{P}_\text{i}]}{K_{\text{ii}}^{\text{P}}} + \frac{[\text{ADP}][\text{P}_\text{i}]}{K_{\text{ii}}^{\text{ADP·P}}} \right)}. \quad (3.140)$$

Comparing the Schief et al. model (equation 3.140) with our model of binding (equation 3.127), we note many parallels. Dividing $d \cdot k_{\text{cat}}^{00}$, from the Schief model gives the probability of ATP binding to the motor. Note that the hydrolysis rate k_{cat}^{00} is what we denote γ. The numerators are of the same form with $K_T = K_{\text{M}}^{00}$. The Schief model contains three additional terms in the denominator, as compared to our model. These three terms imply three additional binding states, ATP and ADP bound, ATP and phosphate bound, or all three species bound.

Model Comparisons		
Parameter	Schief Model	Our Model
k_{cat}^{00}	$113.2s^{-1}$	$114.5s^{-1}$
K_M^{00}	28.1μM	26.2μM
K_i^P	9mM	8.9mM
K_i^{ADP}	34.6μM	24.5μM
$K_i^{ADP\cdot P}$	95mM	−714mM
K_{ii}^P	200mM	-
K_{ii}^{ADP}	23mM	-
$K_{ii}^{ADP\cdot P}$	30mM	-

Table 3.4: We compare the fitted parameters from our model versus the fitted parameters found by the Schief model. Overall the fits are in agreement with the exception of the Menten constant for the ADP and phosphate bound state.

We report the fitted parameters found by the Schief model, as well as the comparable values we determined in table 3.1, in table 3.4.

The values found by both models are very similar with the exception of the $K_{D\cdot P}$ value. The Schief model yields a positive value about an order of magnitude lower than our model. The low Schief value results in a larger overall K_M, which in our model pushes the fit farther away from the measured data. This makes the Schief $K_{D\cdot P}$ the worst of all the fits for both species present according to figure 3.48. However, with this exception, we have excellent agreement with all of our other parameters. Finally, the Schief model has three additional parameters, the K_{ii}. These are all very large, in the tens to hundreds of millimolar, and are multiplied by $K_T = 23$ μM, as seen in equation 3.140. This renders the cross terms effectively negligible to the model and causes the Schief model to be equivalent to our model.

3.10 Power Estimates

For decades, the question of how energy is invested in cellular processes has been of great interest. In the 1970s, several independent threads converged on these same questions with one set of efforts focused on the cost of cytoplasm [26, 27], others focused on the apparently futile cycles of GTP hydrolysis in protein translation [28] and yet others investigating the role of GTP hydrolysis in the context of microtubules [29, 30]. Our aim in this section is to build on these early efforts (and many others) to carefully characterize the power cost of a variety of processes that attend the rearrangements of the motors and microtubules that occur during aster formation in our experiments. Broadly speaking, the philosophy of the approach is

to make a list of various processes that we know take place during aster formation and to examine quantitative estimates of the power associated with these processes. Conceptually, the structure of all of the estimates will be the same, with the generic functional form

$$\text{power of process} = J_{process} \times \Delta\mu_{process}. \tag{3.141}$$

Here we have defined the quantity $\Delta\mu_{process}$ as the free energy cost of a unit process such as a single step of a motor or the movement of a single molecule up a gradient. $J_{process}$ refers to the flux associated with the process of interest, meaning how many unit processes occur per unit time. For example, in the context of constantly pumping ions up a concentration gradient, $\Delta\mu_{process}$ refers to the free energy cost of taking a single ion from one side of the membrane to the other. Similarly, the flux in that case would be given by a phenomenological linear transport law relating the concentration jump across the membrane to the flux itself. Using this quantitative structure, we carry out a series of estimates for each of the processes we think is implicated in the structural rearrangements of our motor-microtubule systems.

Experimentally Measured Power

During aster formation, we measure $\approx f \times 10^8$ ATPs are consumed per second, as shown in the main text Figure 2.3. As noted above, we aim to put this measured value into context through a series of estimates geared towards understanding the power of various processes that attend the formation of an aster. In particular, we are intrigued by the relative costs of processes such as the entropy of orientational ordering, the reduction in volume (i.e., pV work), the maintenance of gradients and so on. Each of the sections below examines one such process in detail.

Estimate of the Power of Stepping Motors

At the mechanistic level, we know what is happening to the ATP. It is being consumed by motors. Hence, the simplest statement about the ATP consumption is that every time a motor takes a step it hydrolyzes an ATP. As a proof of principle check, we ask if the power expenditure based on the measured motor hydrolysis rate matches the experimentally measured power. We measure a motor hydrolysis rate of $\gamma \approx 0.5 \frac{\text{ATP}}{\text{s·motor}}$. If all motor proteins consume ATP at this rate, we can multiply the hydrolysis rate by the number of motors in the system to find the expected power. Our experiments contain 1 μM motors, in an initial cylindrical volume of

$$V_i = \pi R^2 d = \pi \times (125\,\mu\text{m})^2 \times (70\,\mu\text{m}) \approx 3 \times 10^6\,\mu\text{m}^3, \tag{3.142}$$

which translates to

$$N_{\text{mot}} = C_i V_i = 10^{-6}\,\frac{\text{mol}}{\text{L}} \times \left(10^3\,\frac{\text{L}}{\text{m}^3}\right) \times \left(3 \times 10^{-12}\,\text{m}^3\right) \times \left(6 \times 10^{23}\,\frac{\text{MT}}{\text{mol}}\right) \approx 2{\times}10^9\ \text{motors}. \tag{3.143}$$

Thus the power expected of the system is

$$P = N_{\text{mot}}\gamma = 0.5\frac{\text{ATP}}{\text{s}\cdot\text{motor}} \times \left(2 \times 10^9\ \text{motors}\right) \approx 10^9\,\frac{\text{ATP}}{\text{s}}. \tag{3.144}$$

Compared to the $f \times 10^8\,\frac{\text{ATP}}{\text{s}}$ measured in our experiment, this estimate is within a factor of a few of the measured ATP consumption rate. In this sense, the experimental measurements are coherent with what we know about the agents that are consuming ATP. But our question is really a deeper one. We ask what is it that the motors are doing with their capacity to do work through the application of forces?

Estimate of the Power of Aster Contraction via pV Work

During the process of aster formation, the volume occupied by the microtubules that make up that aster decreases. Initially, microtubules of fixed length are uniformly distributed in a cylinder with a height, h, and radius, R. This cylinder corresponds to the region where we project light to induce motor dimerization, which drives aster formation. Some time after turning on the light, $\Delta\mathcal{T}$, the microtubules are organized in a sphere with radius, r, where $R > r$. This process is illustrated in Figure 3.51. Here, we perform a simple estimate to determine the pressure-volume work to contract an ideal gas of microtubules into a smaller aster volume. We are cognizant that a collection of microtubules is not a gas, but we suspect this the entropic cost will exceed the value we estimate here. We express the pressure of the microtubule gas as a function of volume based on the ideal gas law as

$$PV = Nk_{\text{B}}T \Rightarrow P = \frac{Nk_{\text{B}}T}{V}, \tag{3.145}$$

and input it into the equation for pressure-volume work

$$W = -\int_{V_i}^{V_f} P dV = -\int_{V_i}^{V_f} \frac{Nk_{\text{B}}T}{V} dV = -Nk_{\text{B}}T \ln\left(\frac{V_f}{V_i}\right), \tag{3.146}$$

where V_f is the aster sphere volume and V_i is the cylindrical microtubule gas volume. Note that V_f is smaller than V_i which implies that $V_f/V_i < 1$, and hence the work done is positive since the system is compressed. We now use numbers characteristic of our experiments to calculate the amount of work performed in the process of contracting the network into its final shape. First, we take the initial cylindrical

volume to be

$$V_i = \pi R^2 d = \pi \times (125\,\mu\text{m})^2 \times (70\,\mu\text{m}) \approx 3 \times 10^6\,\mu\text{m}^3, \tag{3.147}$$

and the final spherical aster volume to be

$$V_f = \frac{4}{3}\pi r^3 = \frac{4}{3}\pi \times (30\,\mu\text{m})^3 \approx 10^5\,\mu\text{m}^3. \tag{3.148}$$

Given the initial concentration of microtubules $C_i = 1$ nM, we can find the number of microtubules as

$$N_{\text{MT}} = C_i V_i = 10^{-9}\frac{\text{mol}}{\text{L}} \times \left(10^3 \frac{\text{L}}{\text{m}^3}\right) \times \left(3 \times 10^{-12}\,\text{m}^3\right) \times \left(6 \times 10^{23}\,\frac{\text{MT}}{\text{mol}}\right) \approx 2 \times 10^6\,\text{MT}. \tag{3.149}$$

We can now combine all of these results to find the pressure-volume work as

$$W = -2 \times 10^6 \times \ln\left(\frac{1}{30}\right)\, k_{\text{B}}T \approx 7 \times 10^6\, k_{\text{B}}T. \tag{3.150}$$

Under physiological conditions the energy derived from an ATP hydrolysis event is $\approx 20\, k_{\text{B}}T$ [31]. Thus, in ATP units the work is equivalent to

$$W \approx 7 \times 10^6\, k_{\text{B}}T \times \frac{\text{ATP}}{20\, k_{\text{B}}T} = 4 \times 10^5\ \text{ATP}. \tag{3.151}$$

We can also compute the power of volume contraction by dividing the work by the time it takes to form the aster. In our experiments, asters form in approximately 10 minutes, thus

$$P = \frac{W}{\Delta\mathcal{T}} = \frac{4 \times 10^5 \text{ATP}}{600\ \text{s}} \approx 10^3\,\frac{\text{ATP}}{\text{s}}. \tag{3.152}$$

From this estimate, we find that the pressure-volume contribution to the power of aster contraction is negligible since the pV work effect is five orders of magnitude smaller than measured powers. We will approach this same question differently using ideas of nematohydrodynamics in a later section.

The Entropy Cost of Bundling

Here we investigate the power to reduce the entropy of the system by dimerizing motor proteins. For this simple thought experiment suggested to us in conversations with Erwin Frey, we compare the number of microstates of a pair of independent microtubules, not bridged by motors, in comparison to linked microtubules by a dimerized motor pair. Say that two independent microtubules of length l are placed on separate one dimensional tracks with lattice sites at a spacing a, the step size of the motor. If each track is twice the length of a microtubule, $2l$, then there are

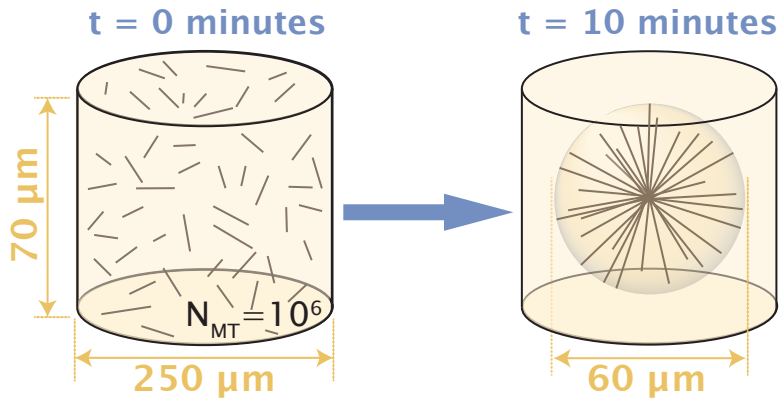

Figure 3.51: **The work of aster compression.** At the beginning of the experiment, microtubules are uniformly mixed throughout a cylinder of projected light. After some time, $\mathcal{T}$, microtubules organize into a spherical aster with a volume smaller than the initial cylinder volume.

l/a lattice sites that the microtubule center can occupy, see Figure 3.52. For two independently moving microtubules, this amounts to $(l/a)^2$ microstates. Thus the entropy of the independent microtubule case is

$$S_{\text{indep}} = 2k_{\text{B}} \ln\left(\frac{l}{a}\right). \tag{3.153}$$

If we now imagine a motor protein aligning the two microtubules, we now consider both microtubules to be on the same track. The microtubules now must move together. For the sake of this estimate, lets say that the microtubules are perfectly aligned with their ends at the same positions. The number of microstates of the coupled system is now only l/a, giving an entropy of

$$S_{\text{coup}} = k_{\text{B}} \ln\left(\frac{l}{a}\right). \tag{3.154}$$

We can compute the free energy of the microtubule coupling as

$$\begin{aligned} \Delta G = -T\Delta S = -T(S_{\text{coup}} - S_{\text{indep}}) \\ \Delta G = k_{\text{B}}T \ln\left(\frac{l}{a}\right). \end{aligned} \tag{3.155}$$

The length of stabilized microtubules in our experiment are $1\,\mu$m and the size of a motor step is 8 nm. Plugging in numbers, we find the free energy to couple two microtubules is

$$\Delta G = k_{\text{B}}T \ln\left(\frac{1000\text{ nm}}{8\text{ nm}}\right) \approx 5\,k_{\text{B}}T \approx 0.25\text{ ATP}, \tag{3.156}$$

where ATP $= 20\,k_{\mathrm{B}}T$ [31]. Say we wanted all of the microtubules in our aster system to fo rm one aligned bundle. Calculating the energy to couple all 2×10^6 microtubules together, the total energy is

$$\Delta G_{\mathrm{tot}} = \Delta G \times N_{\mathrm{MT}} = 5 \times 10^5 \text{ ATP}. \tag{3.157}$$

If the bundle is formed on the same timescale as the aster, about 10 minutes, the power of bundling is

$$P = \frac{\Delta G}{t} = \frac{5 \times 10^5 \text{ ATP}}{600 \text{ s}} \approx 10^3 \frac{\text{ATP}}{\text{s}}. \tag{3.158}$$

This estimate is five orders of magnitude smaller that the measured power, indicating that the entropic cost of microtubule coupling through motor dimerization is negligible.

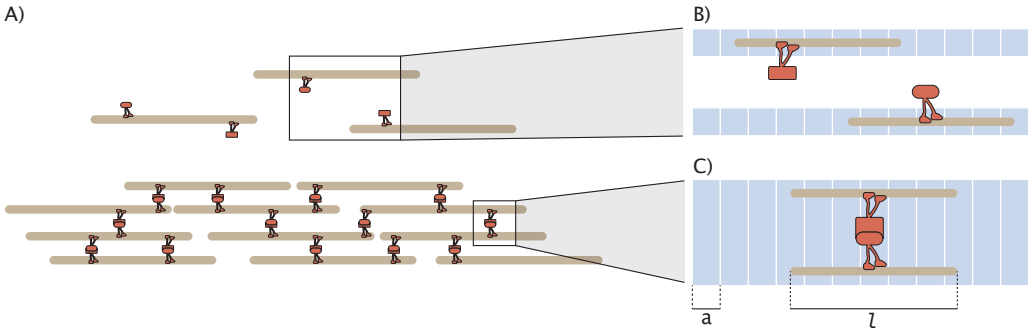

Figure 3.52: **Microtubule coupling.** A) Cross-linked microtubules form a bundle. B) Two microtubules on separate 1D tracks moving independently. C) Two microtubules aligned on the same track moving in unison.

Estimate of Power Associated with Dragging a Microtubule

One of the ways in which motors act is by producing motion. Like with most all real world motions, these processes dissipate energy. That is, some of the energy is transferred from the center of mass of the motor-cargo complex to the microscopic motions of the molecules making up the surrounding medium. This is revealed as dissipation. Here we ask what fraction of the ATP being consumed by each motor is converted into heat energy. In particular, we compute the power of a motor protein dragging a microtubule into an aster. This power can be expressed as

$$P = F_{\mathrm{D}} v, \tag{3.159}$$

where F_{D} is the drag force and v is the velocity of the motor.

To estimate the magnitude of this dissipation, we use the Stokes law to compute the drag force. Before making the calculation itself, we first examine the Reynolds number which gives us a measure of the dissipative forces and tells us whether we are in the regime of validity of the Stokes law. Since Stokes' law requires the system to be at low Reynolds number, we first make the following upper bound calculation for the Reynolds number in our experiment, namely,

$$Re = \frac{\rho v l}{\mu} = \frac{\left(10^3 \, \frac{\text{kg}}{\text{m}^3}\right) \times \left(10^{-7} \, \frac{\text{m}}{\text{s}}\right) \times \left(3 \times 10^{-5} \, \text{m}\right)}{10^{-3} \frac{\text{N}\cdot\text{s}}{\text{m}^2}} \approx 10^{-6}, \tag{3.160}$$

where $\rho = 1000\,\text{kg/m}^3$ is the fluid density, $v = 10^{-7}\,\text{m/s}$ is the measured motor speed of our NCD motors, $l = 3 \times 10^{-5}\,\text{m}$ is the measured aster radius, and $\mu = 0.003\,\text{N}\cdot\text{s/m}^2$ is the viscosity [32]. We see that the Reynolds number satisfies $Re << 1$. Since our experiment meets the low Reynolds number criterion, we can use the Stokes law ($F_D = 6\pi\mu r v$) for the drag force in equation 3.159, resulting in a power of the form

$$P_{\text{per MT}} = 6\pi\mu r v^2, \tag{3.161}$$

where r is an effective radius as we will describe below.

We begin with the most extreme model of the drag force which is to imagine a microtubule as a sphere. This approach gives us a first order-of-magnitude look at the scale of the mechanical power associated with fluid drag. This calculation provides an upper bound as it assumes the moving object to be a sphere, which we will take to a have a radius of half the length of a microtubule, as depicted in Figure 3.53. Using our measurements for microtubule length, $1\,\mu$m, and motor speed, $100\,$nm/s, we find the power for a single motor to drag a microtubule is

$$P_{\text{per MT}} = 6\pi \times \left(3 \times 10^{-3} \, \frac{\text{N}\cdot\text{s}}{\text{m}^2}\right) \times \left(5 \times 10^{-7} \, \text{m}\right) \times \left(10^{-7} \, \frac{\text{m}}{\text{s}}\right)^2 \approx 0.3 \, \frac{\text{pN}\cdot\text{nm}}{\text{s}}. \tag{3.162}$$

Taking $k_\text{B}T = 4\,\text{pN}\cdot\text{nm}$ and the energy of ATP hydrolysis $\Delta\mu_{\text{ATP}} = 20\,k_\text{B}T$, we can convert to units of ATP/s, resulting in

$$P_{\text{per MT}} = 4 \times 10^{-3} \, \frac{\text{ATP}}{\text{MT}\cdot\text{s}}. \tag{3.163}$$

The concentration of motor proteins to microtubules is 1000-fold, so if every single microtubule was being dragged into the aster at the same time, the maximum power from dragging microtubules would be the power per microtubule, as found in equation3.162, multiplied by the number of microtubules, as estimated in equation 3.149,

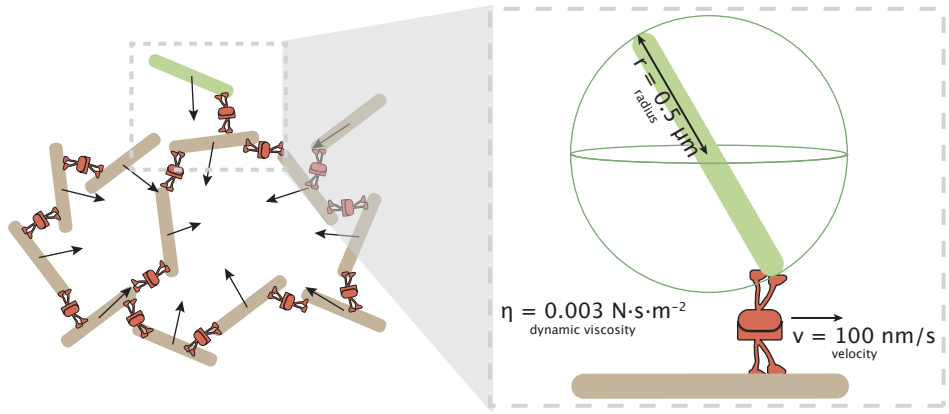

Figure 3.53: **Drag on a Microtubule.** This figure illustrates the set up to calculate the drag on a motor protein carrying a microtubule. On the left, many microtubules are dragged into the center of mass to create an aster. The inset shows the force of drag due to pulling a single microtubule. As an upper bound, the microtubule is depicted as a sphere with a diameter of the microtubule length, allowing the application of Stokes' law.

resulting in

$$P = P_{\text{per MT}} \times N_{\text{MT}} = \left(4 \times 10^{-3} \, \frac{\text{ATP}}{\text{s} \cdot \text{MT}}\right) \times \left(2 \times 10^{6} \text{ MT}\right) \approx 10^{4} \, \frac{\text{ATP}}{\text{s}}. \quad (3.164)$$

Again, we find that this estimate is far lower than our measured power by four orders of magnitude. Note that we can go farther and more precisely treat the fluid drag on a cylinder, taking care to distinguish motion parallel or perpendicular to the long axis of the microtubule. But these estimates lead to an even smaller power and we leave them as an exercise for the reader.

Though it will result in an even smaller estimate, we now refine our previous estimates. We refine our sphere estimate, to more accurately represent the surface area of a cylinder. Our previous estimate significantly overestimates the size of the microtubule by taking the sphere diameter to be the length of the microtubule. Now we will compute the spherical drag for a sphere with the same surface area as our microtubule. For a cylindrical microtubule of length $l = 1\,\mu$m as measured, and a radius $r_{\text{cyl}} = \frac{25 \text{ nm}}{2} \approx 10$ nm [31], the surface area is

$$S_{\text{cyl}} = 2\pi r_{\text{cyl}} l + 2\pi r_{\text{cyl}}^2 \approx 2\pi \times 10^{-2} \, \mu\text{m}^2. \quad (3.165)$$

We now find the spherical radius for a sphere with the same surface area as a cylinder,

$$\begin{aligned} S_{\text{sph}} &= 4\pi r_{\text{sph}}^2 = 2\pi(r_{\text{cyl}} l + r_{\text{cyl}}^2) = S_{\text{cyl}} \\ \Rightarrow r_{\text{sph}} &= \left(\frac{1}{2}(r_{\text{cyl}} l + r_{\text{cyl}}^2)\right)^{-2} = \left(\frac{1}{4\pi} S_{\text{cyl}}\right)^{-2}. \end{aligned} \quad (3.166)$$

Thus in our case,

$$r_{\text{sph}} = \left(5 \times 10^{-3}\right)^{-2} \, \mu\text{m} \approx 7 \times 10^{-2} \, \mu\text{m}. \tag{3.167}$$

Applying Stokes' Law for the new radius, we find

$$P_{\text{per MT}} = -6\pi \left(3 \times 10^{-3} \, \frac{\text{N} \cdot \text{s}}{\text{m}^2}\right) \left(7 \times 10^{-8} \, \text{m}\right) \left(10^{-7} \, \frac{\text{m}}{\text{s}}\right)^2 \tag{3.168}$$

$$\approx f \times 10^{-2} \, \text{pN} \cdot \text{nm} \approx f \times 10^{-4} \, \frac{\text{ATP}}{\text{s} \cdot \text{MT}}, \tag{3.169}$$

for each microtubule and

$$P = P_{\text{per MT}} \times N_{\text{MT}} = \left(f \times 10^{-4} \, \frac{\text{ATP}}{\text{s} \cdot \text{MT}}\right) \left(2 \times 10^6 \, \text{MT}\right) \approx 10^3 \, \frac{\text{ATP}}{\text{s}}, \tag{3.170}$$

for the process of dragging all microtubules. This is one order of magnitude lower than our previous estimate.

Nematic Order Parameter

Here, we attempt to find the free energy of organizing a two dimensional aster using the order parameter, $\mathbf{Q}$. We denote the orientation of each microtubule as

$$\mathbf{u} = (\cos\theta, \, \sin\theta) \tag{3.171}$$

and the order tensor as

$$Q_{ij} = \langle u_i u_j \rangle - \frac{1}{2}\delta_{ij} = \left\langle \begin{pmatrix} \cos^2\theta - \frac{1}{2} & \cos\theta \sin\theta \\ \cos\theta \sin\theta & \sin^2\theta - \frac{1}{2} \end{pmatrix} \right\rangle. \tag{3.172}$$

We assert that the aster is perfectly ordered, as locally all the microtubules point at the same θ. This eliminates the average surrounding the order parameter resulting in,

$$Q_{ij} = \begin{pmatrix} \cos^2\theta - \frac{1}{2} & \cos\theta \sin\theta \\ \cos\theta \sin\theta & \sin^2\theta - \frac{1}{2} \end{pmatrix}. \tag{3.173}$$

In the form written, Q_{ij} is in Cartesian coordinates, however the matrix elements are written in terms of θ, a polar coordinate. We write the elements in terms of Cartesian elements, where $\cos\theta = \frac{x}{\sqrt{x^2+y^2}}$ and $\sin\theta = \frac{y}{\sqrt{x^2+y^2}}$,

$$Q_{ij} = \begin{pmatrix} \frac{x^2}{x^2+y^2} - \frac{1}{2} & \frac{xy}{x^2+y^2} \\ \frac{xy}{x^2+y^2} & \frac{y^2}{x^2+y^2} - \frac{1}{2} \end{pmatrix}. \tag{3.174}$$

Note that this tensor is both traceless,

$$\begin{aligned} Q_{11} + Q_{22} &= \frac{x^2}{x^2+y^2} - \frac{1}{2} + \frac{y^2}{x^2+y^2} - \frac{1}{2} = 0 \\ \Rightarrow Q_{11} &= -Q_{22}, \end{aligned} \tag{3.175}$$

and symmetric,

$$Q_{ij} = \begin{pmatrix} Q_{11} & Q_{12} \\ Q_{21} & Q_{22} \end{pmatrix} = \begin{pmatrix} Q_{11} & Q_{21} \\ Q_{12} & Q_{22} \end{pmatrix} = Q_{ji} \tag{3.176}$$

given that,

$$Q_{12} = \frac{xy}{x^2+y^2} = Q_{21}. \tag{3.177}$$

Free Energy Density

With the nematic order parameter in toe, we can now compute the free energy density gradient using the Landau-Ginsberg theory. According to Julia Yeomans' lecture notes [33], there are two components to the free energy density: the bulk free energy density, which follows the Landau-de Gennes expression,

$$F_{\text{bulk}} = \frac{A}{2}(Q_{ij}Q_{ji}) + \frac{B}{3}(Q_{ij}Q_{jk}Q_{ki}) + \frac{C}{4}(Q_{ij}Q_{ji})^2, \tag{3.178}$$

and the elastic free energy density, which in 2D is,

$$F_{\text{el}} = \underbrace{\frac{L_1}{2}(\partial_k Q_{ij})^2}_{\text{splay}} + \underbrace{\frac{L_3}{2}Q_{ij}(\partial_i Q_{kl})(\partial_j Q_{kl})}_{\text{bend}}. \tag{3.179}$$

All together, the free energy density in terms of Q_{ij} is,

$$\begin{aligned} F = F_{\text{bulk}} + F_{\text{el}} =& \frac{A}{2}(Q_{ij}Q_{ji}) + \frac{B}{3}(Q_{ij}Q_{jk}Q_{ki}) + \frac{C}{4}(Q_{ij}Q_{ji})^2 + \cdots \\ &+ \frac{L_1}{2}(\partial_k Q_{ij})^2 + \frac{L_3}{2}Q_{ij}(\partial_i Q_{kl})(\partial_j Q_{kl}) + \cdots . \end{aligned} \tag{3.180}$$

Here, we will evaluate each listed term. We begin with the power series and examine up to fourth order. First expanding the summation notation of the quadratic term, we find

$$\begin{aligned} Q_{ij}Q_{ji} &= \sum_j \sum_i Q_{ij}Q_{ji} \\ &= \sum_j (Q_{1j}Q_{j1} + Q_{2j}Q_{j2}) \\ &= Q_{11}Q_{11} + Q_{21}Q_{12} + Q_{12}Q_{21} + Q_{22}Q_{22}. \end{aligned} \tag{3.181}$$

Due to the tracelessness of Q_{ij}, $Q_{11}^2 = Q_{22}^2$, and due to the matrix being symmetric, $Q_{12} = Q_{21}$, thus, we can simplify the result to

$$Q_{ij}Q_{ji} = 2Q_{11}^2 + 2Q_{12}^2. \tag{3.182}$$

Plugging in the matrix elements of equation 3.190, the quadratic term evaluates to

$$\begin{aligned} Q_{ij}Q_{ji} &= 2\left(\frac{x^2}{x^2+y^2} - \frac{1}{2}\right)^2 + 2\left(\frac{xy}{x^2+y^2}\right)^2 \\ &= 2\left(\frac{x^4}{(x^2+y^2)^2} - \frac{x^2}{x^2+y^2} + \frac{1}{4} + \frac{x^2y^2}{(x^2+y^2)^2}\right) \\ &= 2\left(\frac{x^4}{(x^2+y^2)^2} - \frac{x^4+x^2y^2}{(x^2+y^2)^2} + \frac{1}{4} + \frac{x^2y^2}{(x^2+y^2)^2}\right) \\ &= \frac{1}{2}. \end{aligned} \tag{3.183}$$

Let us now compute the cubic term,

$$\begin{aligned} Q_{ij}Q_{jk}Q_{ki} &= \sum_k \sum_j \sum_i Q_{ij}Q_{jk}Q_{ki} \\ &= \sum_k \sum_j (Q_{1j}Q_{jk}Q_{k1} + Q_{2j}Q_{jk}Q_{k2}) \\ &= \sum_k (Q_{11}Q_{1k}Q_{k1} + Q_{21}Q_{1k}Q_{k2} + Q_{12}Q_{2k}Q_{k1} + Q_{22}Q_{2k}Q_{k2}) \\ &= Q_{11}Q_{11}Q_{11} + Q_{21}Q_{11}Q_{12} + Q_{12}Q_{21}Q_{11} + Q_{22}Q_{21}Q_{12} \\ &\quad + Q_{11}Q_{12}Q_{21} + Q_{21}Q_{12}Q_{22} + Q_{12}Q_{22}Q_{21}Q_{22}Q_{22}Q_{22} \\ &= Q_{11}^3 + 3Q_{11}Q_{12}^2 + 3Q_{22}Q_{12}^2 + Q_{22}^3. \end{aligned} \tag{3.184}$$

By the symmetry of Q_{ij},

$$Q_{ij}Q_{jk}Q_{ki} = Q_{11}^3 + 3Q_{11}Q_{12}^2 + 3Q_{22}Q_{12}^2 + Q_{22}^3, \tag{3.185}$$

and given that the matrix is traceless,

$$Q_{ij}Q_{jk}Q_{ki} = Q_{11}^3 + 3Q_{11}Q_{12}^2 - 3Q_{11}Q_{12}^2 + (-Q_{11})^3 = 0, \tag{3.186}$$

so the cubic term vanishes. We now compute the quartic term using the result from equation 3.182

$$\begin{aligned} (Q_{ij}Q_{ji})^2 &= \left(\sum_j \sum_i Q_{ij}Qji\right)^2 \\ &= \left(2Q_{11}^2 + 2Q_{12}^2\right)^2. \end{aligned} \tag{3.187}$$

Thus, the quartic term is simply the square of the quadratic term, which evaluates to

$$(Q_{ij}Q_{ji})^2 = \left(\frac{1}{2}\right)^2 = \frac{1}{4}. \tag{3.188}$$

We now compute the derivative terms. We write the partial first derivatives of Q_{ij} as follows.

First Derivatives:

$$\frac{\partial}{\partial x}Q_{ij} = \begin{pmatrix} \partial_1 Q_{11} & \partial_1 Q_{12} \\ \partial_1 Q_{21} & \partial_1 Q_{22} \end{pmatrix} = \begin{pmatrix} \frac{2xy^2}{(x^2+y^2)^2} & \frac{y(-x^2+y^2)}{(x^2+y^2)^2} \\ \frac{y(-x^2+y^2)}{(x^2+y^2)^2} & -\frac{2xy^2}{(x^2+y^2)^2} \end{pmatrix} \tag{3.189}$$

$$\frac{\partial}{\partial y}Q_{ij} = \begin{pmatrix} \partial_2 Q_{11} & \partial_2 Q_{12} \\ \partial_2 Q_{21} & \partial_2 Q_{22} \end{pmatrix} = \begin{pmatrix} -\frac{2x^2y}{(x^2+y^2)^2} & \frac{x(x^2-y^2)}{(x^2+y^2)^2} \\ \frac{x(x^2-y^2)}{(x^2+y^2)^2} & \frac{2x^2y}{(x^2+y^2)^2} \end{pmatrix}. \tag{3.190}$$

Note that the matrices representing the first derivatives are also traceless and symmetric, meaning $\partial_k Q_{11} = -\partial_k Q_{22}$ and $\partial_k Q_{12} = \partial_k Q_{21}$.

Computing the first term in the elastic free energy density, we find

$$\begin{aligned}(\partial_k Q_{ij})^2 &= \sum_k \sum_j \sum_i (\partial_k Q_{ij})^2 \\ &= \sum_k \sum_j (\partial_k Q_{1j})^2 + (\partial_k Q_{2j})^2 \\ &= \sum_k (\partial_k Q_{11})^2 + (\partial_k Q_{12})^2 + (\partial_k Q_{21})^2 + (\partial_k Q_{22})^2 \\ &= (\partial_1 Q_{11})^2 + (\partial_2 Q_{11})^2 + (\partial_1 Q_{12})^2 + (\partial_2 Q_{12})^2 + (\partial_1 Q_{21})^2 + (\partial_2 Q_{21})^2 + (\partial_1 Q_{22})^2 + (\partial_2 Q_{22})^2.\end{aligned} \tag{3.191}$$

By the properties $Q_{11} = -Q_{22}$, and $Q_{12} = Q_{21}$,

$$(\partial_k Q_{ij})^2 = 2(\partial_1 Q_{11})^2 + 2(\partial_2 Q_{11})^2 + 2(\partial_1 Q_{12})^2 + 2(\partial_2 Q_{12})^2. \tag{3.192}$$

Plugging in the matrix elements,

$$\begin{aligned}(\partial_k Q_{ij})^2 &= \frac{8x^2y^4}{(x^2+y^2)^4} + \frac{8x^4y^2}{(x^2+y^2)^4} + \frac{2y^2(-x^2+y^2)^2}{(x^2+y^2)^4} + \frac{2x^2(x^2-y)^2}{(x^2+y^2)^4} \\ &= \frac{2}{x^2+y^2}.\end{aligned} \tag{3.193}$$

We now compute the second term in the elastic free energy density and use the simplifications that Q_{ij} is symmetric and traceless,

$$\begin{aligned}
Q_{ij}(\partial_i Q_{kl})(\partial_j Q_{kl}) &= \sum_l \sum_k \sum_j \sum_i Q_{ij}(\partial_i Q_{kl})(\partial_j Q_{kl}) \\
&= \sum_l \sum_k Q_{11}(\partial_1 Q_{kl})^2 + 2Q_{12}(\partial_1 Q_{kl})(\partial_2 Q_{kl}) + Q_{22}(\partial_2 Q_{kl})^2 \\
&= Q_{11}(\partial_1 Q_{11})^2 + 2Q_{11}(\partial_1 Q_{12})^2 + Q_{11}(\partial_1 Q_{22})^2 \\
&\quad + 2Q_{12}(\partial_1 Q_{11})(\partial_2 Q_{11}) + 4Q_{12}(\partial_1 Q_{12})(\partial_2 Q_{12}) + 2Q_{12}(\partial_1 Q_{22})(\partial_2 Q_{22}) \\
&\quad + Q_{22}(\partial_2 Q_{11})^2 + 2Q_{22}(\partial_2 Q_{12})^2 + Q_{22}(\partial_2 Q_{22})^2 \\
&= 2Q_{11}(\partial_1 Q_{11})^2 + 2Q_{11}(\partial_1 Q_{12})^2 \\
&\quad + 4Q_{12}(\partial_1 Q_{11})(\partial_2 Q_{11}) + 4Q_{12}(\partial_1 Q_{12})(\partial_2 Q_{12}) \\
&\quad - 2Q_{11}(\partial_2 Q_{11})^2 - 2Q_{11}(\partial_2 Q_{12})^2 \\
&= 2Q_{11}\Big[(\partial_1 Q_{11})^2 + (\partial_1 Q_{12})^2 - (\partial_2 Q_{11})^2 - (\partial_2 Q_{12})^2\Big] \\
&\quad + 4Q_{12}\Big[(\partial_1 Q_{11})(\partial_2 Q_{11}) + (\partial_1 Q_{12})(\partial_2 Q_{12})\Big].
\end{aligned} \tag{3.194}$$

Plugging in matrix values and simplifying with Mathematica, this term reduces to

$$Q_{ij}(\partial_i Q_{kl})(\partial_j Q_{kl}) = -\frac{1}{x^2+y^2}. \tag{3.195}$$

Putting everything together, we reveal an equation for the free energy density throughout an ordered aster

$$F = \frac{A}{2}\left(\frac{1}{2}\right) + \frac{C}{4}\left(\frac{1}{4}\right) + \cdots + \frac{L_1}{2}\frac{2}{x^2+y^2} - \frac{L_3}{2}\frac{1}{x^2+y^2} + \cdots . \tag{3.196}$$

We can translate this back into polar coordinates using the transforms $r = \sqrt{x^2+y^2}$, $\cos\theta = \frac{x}{\sqrt{x^2+y^2}}$ and $\sin\theta = \frac{y}{\sqrt{x^2+y^2}}$

$$F = \frac{4A+C}{16} + \frac{2L_1 - L_3}{2}\frac{1}{r^2} + \cdots . \tag{3.197}$$

Now it is left to find the energy of the aster state by integrating the free energy density over the area of the aster. We integrate over all angles from $0 \leq \theta \leq 2\pi$ and

radius values from a core cutoff, R_c to the aster radius R,

$$\begin{aligned} E &= \int_0^{2\pi} \int_{R_c}^{R} F\, r\, \mathrm{d}r\, \mathrm{d}\theta \\ &= \int_0^{2\pi} \int_{R_c}^{R} \left(\frac{4A + C}{16} r + \frac{2L_1 - L_3}{2r} \right) \mathrm{d}r\, \mathrm{d}\theta \\ &= \frac{4A + C}{8} \pi (R^2 - R_c^2) + (2L_1 - L_3)\pi \ln\left(\frac{R}{R_c}\right). \end{aligned} \tag{3.198}$$

Now that we have solved the equation for the energy of the ordered state, we can input parameters to find the energy scale of perfect order.

Order of Magnitude Estimate

To get a sense of scale of the energy in equation 3.198, we explore literature values for the constants in front of each term. Zhang et al. use modeling, simulations, and experiments to find how the elasticity of a liquid crystal (LC) depends on filament length, density, and rigidity. Their system, a thin film nematic of actin and microtubules, follows the same free energy density form as equation 3.197. In their study, they measure elastic constants, K, using elastic beam theory. They find that $L_1 = \frac{K}{2q_0^2}$, where L_1 is the coefficient of the $(\partial_k Q_{ij})^2$, same as us, and q_0 is the scalar order parameter. Thus, if we assume the L_1 term is at least of the same order as the other terms, we can get an order of magnitude estimate for the ordered energy of the aster. Since our aster is assumed to be perfectly ordered, we take $q_0 = 1$. Zhang et al. find $K \sim f \times 10^{-1}$ pN [34]. Thus, $L_1 \approx 0.1$ pN. Note that for the constant L_1 to have units of piconewtons, the free energy density must be integrated over a volume rather than an area. Since their system was a very thin film of $\delta_z = 300$ nm, their system is still quasi 2D in comparison to their large film area $4\,\mathrm{mm}^2$. While the thickness of the aster is non-trivial, we will simply proceed with this estimate to find the energy scale of ordering. Thus, we will integrate over z, the thickness of the aster, in our estimate,

$$E = \frac{4A + C}{8} \pi z (R^2 - R_c^2) + (2L_1 - L_3)\pi z \ln\left(\frac{R}{R_c}\right). \tag{3.199}$$

Taking the aster radius to be $R \approx f \times 10\,\mu$m, the cutoff radius to be $R_c \approx 1\,\mu$m, and the thickness to be $z \approx 100\,\mu$m, we find the value of the L_1 term of the energy,

$$E \sim 2\pi L_1 z \ln\left(\frac{R}{R_c}\right) = 2\pi \times 10^{-1}\ \mathrm{pN} \times 10^5\ \mathrm{nm} \times \ln(f \times 10) \approx f \times 10^5\ \mathrm{pN \cdot nm}. \tag{3.200}$$

With the conversion ATP $= 20\, k_B T \left(\frac{4\,\text{pN}\cdot\text{nm}}{k_B T}\right) = 80\,\text{pN}\cdot\text{nm}$, the free energy of the ordered aster is $f \times 10^3$ ATP. If an aster takes around 10 minutes to form, then the power of organization is

$$P = \frac{f \times 10^3\ \text{ATP}}{600\ \text{s}} = f\,\frac{\text{ATP}}{\text{s}}. \tag{3.201}$$

This is VERY low in comparison with our measured power of $10^8\ \frac{\text{ATP}}{\text{s}}$. While other studies have found K constant values as large as 10 pN [35], this would only increase our power by a factor of 100, still six orders of magnitude smaller than the measured value. Thus, the power of ordering microtubules appears to be negligible.

3.11 Key Numbers

Size of a protein

The volume of a protein is thought to scale linearly with the number of amino acids in the sequence [31]. When a sequence is unavailable, the average amino acid (a.a.) weighs 100 Da, providing an easy conversion from molecular weight. Rubisco is a well characterized protein with a molecular weight of 55 kDa, a sequence length of 500 a.a., and a diameter of $3 - 6$ nm. Thus if we want to create a rule for scaling protein radii, we can write

$$r \approx 2\ \text{nm} \times \left(\frac{\#\ \text{a.a.}}{500\ \text{a.a.}}\right)^{1/3} \approx 2\ \text{nm} \times \left(\frac{\text{MW}}{55\ \text{kDa}}\right)^{1/3}. \tag{3.202}$$

Our experiments contain two proteins, motors and the ATP probe. Our motor proteins weigh approximately 100 kDa, giving a radius of

$$r_{\text{motor}} \approx 2\ \text{nm} \times \left(\frac{100\ \text{kDa}}{55\ \text{kDa}}\right)^{1/3} \approx 2.4\ \text{nm}. \tag{3.203}$$

The ATP probe has a sequence length of 1800 base pairs, which corresponds to 600 a.a. since each amino acid contains three base pairs. Thus, the radius of the ATP probe is

$$r_{\text{probe}} \approx 2\ \text{nm} \times \left(\frac{600\ \text{a.a.}}{500\ \text{a.a.}}\right)^{1/3} \approx 2.1\ \text{nm}. \tag{3.204}$$

Reynold's Number

We can show that our system is at low Reynold's number, meaning viscous forces dominate using the definition,

$$Re = \frac{\rho v l}{\mu}, \tag{3.205}$$

where ρ is the density, v is the velocity, l is the characteristic length scale, and μ is the viscosity. Our reaction mix contains 30% glycerol in water based reagents at room temperature. We take the density of our mix to be $\rho \sim 1000\,\frac{\text{kg}}{\text{m}^3}$ and the viscosity to be $\mu = 2.4 \times 10^{-3}\,\text{N}\cdot\text{s}/\text{m}^2$ based on a calculator developed at the University of Reading [32]. For the velocity, we will take an upper bound for motor speeds, $v = 1\frac{\mu\text{m}}{\text{s}}$ [36]. And for the characteristic length scale, we will take the motor decay length as previously measured in our lab, $l = 15\,\mu$m [37]. This evaluates to a Reynold's number of

$$Re \approx 6 \times 10^{-6} << 1. \tag{3.206}$$

Diffusion Constants

Given that our system is at low Reynold's number (Equation 3.206), we can compute an expected diffusion constant for molecules in our system using the Stokes-Einstein equation,

$$D = \frac{k_\text{B}T}{6\pi\mu r}, \tag{3.207}$$

where μ is the viscosity of the media and r is the radius of the molecule. Using the viscosity of our system ($\mu = 2.4 \times 10^{-3}\,\text{N}\cdot\text{s}/\text{m}^2$ [32]), the diffusion constant of a species only depends on its radius,

$$D = \frac{k_\text{B}T}{6\pi\mu r} = \frac{4\,\text{pN}\cdot\text{nm}}{6\pi r(2.4 \times 10^{-3}\,\text{pN}\cdot\text{s}/\mu\text{m}^2)} \approx \frac{90\text{ nm}}{r}\,\frac{\mu\text{m}^2}{\text{s}}, \tag{3.208}$$

given that $k_\text{B}T \approx 4\,\text{pN}\cdot\text{nm}$. We can now compute the relevant diffusion constants for each molecule in the experiment: ATP has a radius of 0.7 nm, (BNID 106798), which leads to a diffusion coefficient of

$$D_\text{ATP} \approx 130\,\mu\text{m}^2/\text{s}. \tag{3.209}$$

Our motor proteins have a radius of about 2.4 nm (equation 3.203), giving a diffusion constant of

$$D_\text{motor} \approx 40\,\mu\text{m}^2/\text{s}. \tag{3.210}$$

Tubulin has a length of 4 nm [31], so we will take a radius of 2 nm, giving a diffusion constant of

$$D_\text{tubulin} \approx 45\,\mu\text{m}^2/\text{s}. \tag{3.211}$$

Microtubules have an experimentally measured length of 1 μm, so we will take a radius of 500 nm giving a diffusion constant of

$$D_\text{MT} \approx 0.2\,\mu\text{m}^2/\text{s}. \tag{3.212}$$

The ATP probe (Queen A81D) has a radius of about 2 nm (equation 3.204), same as tubulin, giving the diffusion constant of the probe

$$D_{\text{Queen A81D}} \approx 45\,\mu\text{m}^2/\text{s}. \tag{3.213}$$

Binding Rates and Bound Fractions

If we know the on/off rates or the equilibrium constant for two species and the total initial concentrations of each species, we can determine the bound fraction of a ligand to a receptor at equilibrium. Taking $[L]$ and $[R]$ for the concentrations of free ligands and receptors respectively, and $[LR]$as the bound concentration of ligands and receptors, we write the chemical equation,

$$[L] + [R] \underset{k_{\text{off}}}{\overset{k_{\text{on}}}{\rightleftharpoons}} [LR], \tag{3.214}$$

with an equilibrium constant defined as

$$K_{\text{eq}} = \frac{k_{\text{off}}}{k_{\text{on}}} = \frac{[\text{L}][\text{R}]}{[\text{LR}]}. \tag{3.215}$$

Assuming we know the total concentration of the ligand and receptor species, regardless of their binding states, we specify the total concentration of ligands as,

$$l = [\text{L}] + [\text{LR}] \tag{3.216}$$

and of receptors as,

$$r = [\text{R}] + [\text{LR}]. \tag{3.217}$$

The probability of ligands being bound to receptors is,

$$p_b = \frac{[LR]}{l}, \tag{3.218}$$

which we can write in terms of the equilibrium constant using Equation 3.215,

$$p_b = \frac{[L][R]}{K_{\text{eq}} l}. \tag{3.219}$$

Substituting equations 3.216 and 3.217, we can solve for the bound probability in terms of the total ligand and receptor concentrations and the equilibrium constant as follows,

$$p_b = \frac{(l - [LR])(r - [LR])}{K_{\text{eq}} l}. \tag{3.220}$$

Expanding the numerator,

$$p_b = \frac{lr - [LR]r - l[LR] + [LR]^2}{K_{\text{eq}} l} = \frac{1}{K_{\text{eq}}}\left(r - \frac{[LR]}{l}(r + l) + l\frac{[LR]^2}{l^2}\right), \tag{3.221}$$

and substituting $\frac{[LR]}{l} = p_b$,

$$p_b = \frac{1}{K_{\text{eq}}}\left(r - p_b(r+l) + l p_b^2\right). \tag{3.222}$$

We are left with a quadratic equation in terms of p_b,

$$l p_b^2 - p_b(K_{\text{eq}} + r + l) + r = 0 \tag{3.223}$$

solving for the fraction of bound species, we employ the quadratic formula,

$$p_b = \frac{K_{\text{eq}} + r + l - \sqrt{(-K_{\text{eq}} - r - l)^2 - 4lr}}{2l}, \tag{3.224}$$

noting that we must chose the "minus," square root subtracted, form to ensure that $p_b > 0$. Using this equation, the fraction of bound species at equilibrium can easily be determined!

Motor to Microtubule

Reference [37] measured the equilibrium constant for NCD Kinesin motors to be approximately 50 μM. In our experiment, we add approximately 1 μM of tubulin. If each tubulin has 13 binding sites, we will take 13 μM of tubulin binding sites as the total receptor concentration, r. For the ligand, we add approximately 1 μM of motor proteins, which we take as the total ligand concentration, l. Plugging these values into equation 3.224, we find the bound fraction of motor proteins is,

$$\begin{aligned} p_b &= \frac{50 + 13 + 1 - \sqrt{(-50 - 13 - 1)^2 - 4 \times 1 \times 13}}{2 \times 1} \\ &= \frac{64 - \sqrt{4044}}{2} \\ &= \frac{64 - 63.6}{2} \\ &= 0.2, \end{aligned} \tag{3.225}$$

indicating that approximately 20% of motor proteins are bound at equilibrium.

ATP to Probe

The ATP probe we use, Queen A81D [2], is a mutant of the Queen-7μ probe, developed in 2014 by the same group [2], using the epsilon subunit of *Bacillus* PS3. The authors characterized the dissociation constant of ATP to the probe at room temperature and found $K_{\text{d}} \sim 7\,\mu$M [18]. If we allowed the ATP probe to equilibrate

with our initial concentration of ATP, before any motor hydrolysis, we can compute an upper bound for the bound fraction of ATP. Initially, we pipette 500 μM of ATP into the reaction with approximately 3 μM of the ATP probe. Using equation 3.224, we solve for the bound fraction of ATP at equilibrium,

$$\begin{aligned} p_b &= \frac{7+3+500-\sqrt{(-7-3-500)^2-4\times 500\times 3}}{2\times 500} \\ &= \frac{510-\sqrt{254100}}{1000} \\ &= \frac{510-504}{1000} \\ &= 0.006, \end{aligned} \tag{3.226}$$

so only 0.6% of ATP is bound to the probe at equilibrium at a given time. Thus, at high ATP conditions, the effect of ATP binding to the probe should not impact the binding dynamics of ATP to motor proteins. However, as the experiment runs, ATP is hydrolyzed by the motor proteins. We can compute the binding fraction in the limit that the concentration approaches zero. Plugging $l = 0$ into equation 3.224, we find $p_b = \frac{0}{0}$, which invites us to envoke l'hôpital's rule. The first derivative of the numerator with respect to l is

$$1 - \frac{1}{2}\frac{-2(-K_{\text{eq}}-r-l)-4r}{\sqrt{(-K_{\text{eq}}-r-l)^2-4lr}} = 1 - \frac{K_{\text{eq}}-r}{\sqrt{(-K_{\text{eq}}-r-l)^2-4lr}} \tag{3.227}$$

and the first derivative of the denominator with respect to l is simply 2. Thus,

$$\lim_{l\to 0} p_{\text{b}} = \frac{1}{2} - \frac{1}{2}\frac{K_{\text{eq}}-r}{K_{\text{eq}}+r}. \tag{3.228}$$

Plugging in the dissociation constant and total concentration of ATP probe,

$$\lim_{l\to 0} p_{\text{b}} = \frac{1}{2} - \frac{7-3}{2\times 10} = 0.5 - 0.2 = 0.3. \tag{3.229}$$

Hence, as ATP becomes scarce in the system, we can expect the binding to the ATP probe to slow the motor dynamics. Plotting equation 3.224 as a function of ATP concentration when $K_{\text{eq}} + r = 10\,\mu$M, we find agreement in the limit of $l \to 0$, as shown in figure.

References

[1] Bibi Najma et al. "Competing instabilities reveal how to rationally design and control active crosslinked gels." In: *Nature Communications* 13.1 (2022), p. 6465.

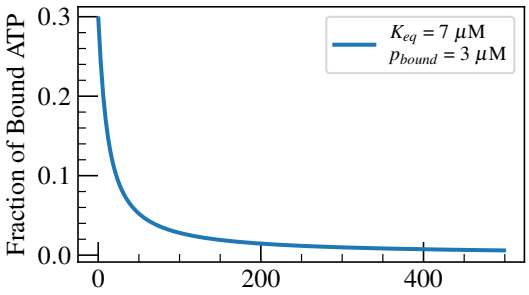

Figure 3.54: **Fraction of ATP bound to the ATP reporter as function of ATP.** At high ATP concentrations, the fraction of ATP bound to the probe is small, not impacting the amount of available ATP in the bulk.

[2] Hideyuki Yaginuma and Yasushi Okada. "Live cell imaging of metabolic heterogeneity by quantitative fluorescent ATP indicator protein, QUEEN-37C." In: *BioRxiv* (2021), pp. 2021–10.

[3] Bibi Najma et al. "Microscopic interactions control a structural transition in active mixtures of microtubules and molecular motors." In: *Proceedings of the National Academy of Sciences* 121.2 (2024), e2300174121.

[4] Teledyne Photometrics. *Camera Test Protocol*. `https://www.photometrics.com/learn/camera-test-protocol`. Accessed: (2024). 2019.

[5] Nilanjan Dey. "Uneven illumination correction of digital images: A survey of the state-of-the-art." In: *Optik* 183 (2019), pp. 483–495.

[6] Hernan G Garcia and Rob Phillips. "Quantitative dissection of the simple repression input–output function." In: *Proceedings of the National Academy of Sciences* 108.29 (2011), pp. 12173–12178.

[7] L Montgomery Smith, Dennis R Keefer, and SI Sudharsanan. "Abel inversion using transform techniques." In: *Journal of Quantitative Spectroscopy and Radiative Transfer* 39.5 (1988), pp. 367–373.

[8] Stephen Gibson et al. *PyAbel/PyAbel: v0.9.0*. Version v0.9.0. Dec. 2022. DOI: `10.5281/zenodo.7438595`. URL: `https://doi.org/10.5281/zenodo.7438595`.

[9] Daniel Sage et al. "DeconvolutionLab2: An open-source software for deconvolution microscopy." In: *Methods* 115 (2017), pp. 28–41.

[10] Max Born and Emil Wolf. *Principles of optics: electromagnetic theory of propagation, interference and diffraction of light*. Elsevier, 2013.

[11] Eugene Hecht. *Optics*. 4th. San Francisco: Addison Wesley, 2003. ISBN: 978-0805385663.

[12] Hagai Kirshner et al. “3-D PSF fitting for fluorescence microscopy: implementation and localization application.” In: *Journal of microscopy* 249.1 (2013), pp. 13–25.

[13] Sjoerd Stallinga and Bernd Rieger. “Accuracy of the Gaussian point spread function model in 2D localization microscopy.” In: *Optics express* 18.24 (2010), pp. 24461–24476.

[14] Bo Zhang, Josiane Zerubia, and Jean-Christophe Olivo-Marin. “Gaussian approximations of fluorescence microscope point-spread function models.” In: *Applied optics* 46.10 (2007), pp. 1819–1829.

[15] Marco Prato et al. “Efficient deconvolution methods for astronomical imaging: algorithms and IDL-GPU codes.” In: *Astronomy & Astrophysics* 539 (2012), A133.

[16] François Aguet, Dimitri Van De Ville, and Michael Unser. “Model-based 2.5-D deconvolution for extended depth of field in brightfield microscopy.” In: *IEEE Transactions on Image Processing* 17.7 (2008), pp. 1144–1153.

[17] Hiromi Imamura et al. “Visualization of ATP levels inside single living cells with fluorescence resonance energy transfer-based genetically encoded indicators.” In: *Proceedings of the National Academy of Sciences* 106.37 (2009), pp. 15651–15656.

[18] Hideyuki Yaginuma et al. “Diversity in ATP concentrations in a single bacterial cell population revealed by quantitative single-cell imaging.” In: *Scientific Reports* 4.1 (2014), p. 6522.

[19] D. L. Jones, R. C. Brewster, and R. Phillips. “Promoter architecture dictates cell-to-cell variability in gene expression.” In: *Science* 346.6216 (2014), pp. 1533–6.

[20] Rosalind Wenshan Pan et al. “Deciphering regulatory architectures of bacterial promoters from synthetic expression patterns.” In: *PLOS Computational Biology* 20.12 (2024), e1012697.

[21] Ahmed A Heikal et al. “Molecular spectroscopy and dynamics of intrinsically fluorescent proteins: coral red (dsRed) and yellow (Citrine).” In: *Proceedings of the National Academy of Sciences* 97.22 (2000), pp. 11996–12001.

[22] Christian Eggeling et al. “Photobleaching of fluorescent dyes under conditions used for single-molecule detection: evidence of two-step photolysis.” In: *Analytical chemistry* 70.13 (1998), pp. 2651–2659.

[23] Rob Phillips et al. *Physical biology of the cell*. Garland Science, 2012.

[24] William R. Schief et al. “Inhibition of kinesin motility by ADP and phosphate supports a hand-over-hand mechanism.” In: *Proceedings of the National Academy of Sciences* 101.5 (2004), pp. 1183–1188.

[25] David L Coy, Michael Wagenbach, and Jonathon Howard. "Kinesin takes one 8-nm step for each ATP that it hydrolyzes." In: *Journal of Biological Chemistry* 274.6 (1999), pp. 3667–3671.

[26] A. H. Stouthamer. "Theoretical study on amount of ATP required for synthesis of microbial cell material." In: *Antonie Van Leeuwenhoek Journal of Microbiology* 39.3 (1973), pp. 545–565.

[27] M. Lynch and G. K. Marinov. "The bioenergetic costs of a gene." In: *Proceedings of the National Academy of Sciences of the United States of America* 112.51 (2015), pp. 15690–15695.

[28] John J. Hopfield. "Kinetic proofreading: A new mechanism for reducing errors in biosynthetic processes requiring high specificity." In: *Proceedings of the National Academy of Sciences of the United States of America* 71.10 (1974), pp. 4135–9.

[29] T. L. Hill and Marc W. Kirschner. "Bioenergetics and kinetics of microtubule and actin filament assembly-disassembly." In: *Int Rev Cytol* 78 (1982), pp. 1–125.

[30] Tim J. Mitchison and Marc W. Kirschner. "Properties of the Kinetochore In vitro. II. Microtubule Capture and ATP-Dependent Translocation." In: *Journal of Cell Biology* 101.3 (1985), pp. 766–777.

[31] Ron Milo and Rob Phillips. *Cell biology by the numbers*. Garland Science, 2015.

[32] Chris Westbrook. *Calculate density and viscosity of glycerol/water mixtures*. Accessed: 2024. 2018. URL: %7Bhttps://www.met.reading.ac.uk/~sws04cdw/viscosity_calc.html%7D.

[33] Julia M Yeomans. "The hydrodynamics of active systems." In: *La Rivista del Nuovo Cimento* 40.1 (2017), pp. 1–31.

[34] Rui Zhang et al. "Interplay of structure, elasticity, and dynamics in actin-based nematic materials." In: *Proceedings of the National Academy of Sciences* 115.2 (2018), E124–E133.

[35] Rui Zhang et al. "Dynamic structure of active nematic shells." In: *Nature Communications* 7.1 (2016), p. 13483.

[36] Mark Schnitzer and Steven Block. "Kinesin hydrolyses one ATP per 8-nm step." In: *Nature* 388 (1997), pp. 386–390.

[37] Rachel A. Banks et al. "Motor processivity and speed determine structure and dynamics of microtubule-motor assemblies." In: *Elife* 12 (2023), e79402.

Chapter 4

FUNDAMENTAL POWER REQUIREMENTS TO BUILD OR MAINTAIN BIOCHEMICAL GRADIENTS

4.1 Abstract

Organisms organize and respond to a plethora of different gradients. Perhaps the most famous such gradient patterns the anterior-posterior axis of cells in the fly embryo, but many further examples abound. Organelles and cell membranes sustain electrochemical gradients; motile cells respond to chemoattractant gradients; tumors and biofilms develop oxygen gradients; and gradients in biodiversity even develop along evironmental axes such as elevation. In our own experimental work with light-controlled microtubule-motor systems, we and others have found how molecular assemblies spontaneously organize into star-shaped "asters" that feature an approximately spherically-symmetric and exponentially-decaying arrangement of motors; these aster structures and gradients evoke biologically-relevant structures such as the mitotic spindle. Our experiments have also measured the distribution of ATP in space and time as well as spatially-resolved measurements of the power consumed. These measurements report that asters often consume power almost ten times faster while they are forming and changing rapidly than at late stages. We hypothesize this discrepancy between early and late dissipation is due to fundamental differences in the energetic costs to build and maintain such gradients. In this paper, we explore these questions and their broad implications using simple ideas from statistical physics.

4.2 The Power of Biological Processes

Living things build and depend on exquisite patterns of chemicals in space and time. Precisely how much energy must these systems pay to incite these patterns, and then to defy their decay towards equilibrium homogeneity? Does building or maintaining structures demand greater biochemical energy and power expenditures? How do these expenditures stack up against the broader cellular economy of metabolic expenditures?

These big questions enjoy rich history. How cells invest energy over a wide set of tasks is a mystery that has gained urgency in many guises, especially in the 1970s. Early researchers asked how much energy growing microbial cells need to duplicate

their contents, finding the surprise that cells spend significantly more energy than apparently required to duplicate biomass [1, 2]. Recent, even more precise, work and modeling validate these mismatches [3] and highlight that microbes have significant expenditures unexplained by material construction costs alone. Cells far beyond microbes, including eukaryotic and plant cells, also show levels of dissipation awaiting full and complete accounting [4, 5]. Clearly, cells perform many energetically-costly functions beyond copying biomass that can participate in such total metabolic demands. These include kinetic proofreading (explaining how apparently futile cycles of GTP hydrolysis accomplish greater accuracy in protein translation and other biological transformations) [6], and GTP hydrolysis regulating the polymerization of microtubules [7, 8]. Hydrolyzing ATP may also facilitate more sensitive [9] or flexible [10] signaling in gene regulation, or additionally reduce noise in signaling networks [11], than permitted at equilibrium. Beyond these charismatic examples, exactly what other capabilities that cells unlock as they spend energy is a frontier that invites huge discoveries, particularly facilitated by new experimental technologies that resolve cellular dissipation in unprecedented regimes of physiology.

One fundamental destiny for cellular energy expenditures surely must be to assemble the extraordinary patterns of biomolecular components in space and time that orchestrate living matter. Writing in 1970, Francis Crick, Mary Munro, and coworkers pursued imaginative calculations complementing the work of Alan Turing that asked how diffusion and cellular production can establish morphogenetic gradients in embryonic development [12, 13]. These formative works assessed the plausibility and constraints of such mechanisms to establish gradients by particularly focusing on the time required to set up gradients on cellular and organismal length scales, identifying feasible regimes where gradients can be established in acceptable developmental times [13]. The time to assemble structure is just one feature affecting how biological gradients develop, however. More contemporary works often investigate the accuracy attainable while forming discrete sets of combinatorial structures [14] under different kinetic and dissipative protocols. Another blooming thread comes from results of modern stochastic thermodynamics that link the work extractable from a nonequilibrium system in a certain state (say matter arranged in space) from the Kullback Leibler divergence between that initial state and a terminal equilibrium distribution (say matter absent a gradient) [15, 16]. How such advancements may be generalized to understand the energetic costs of building and maintaining continuous biological patterns of special interest, not just from static comparisons of initial and final conditions but at local and temporal detail, is a challenge that gains both

urgency and tractability from the development of new precision measurements.

In this paper, we aim to build on these early efforts (and many others) to carefully characterize the power costs of forming gradients in new experimental measurements. We illustrate calculations in the context of how molecular motors and microtubules assemble asters in experiments we have done in which light is used to transiently crosslink motors. In these experiments, a homogeneous mixture of microtubules and motors is induced to form these ordered structures by light-induced crosslinking of the motors. Our measurements revealed that during the early stages of aster formation, the power is nearly 10-fold higher than at the late stages of aster formation. We suspect that this discrepancy is due to the substantial difference in the energetic cost to build an aster vs to maintain it. In this paper, we explore that hypothesis. While our discussion often transacts in the specific language and details of gradients of molecular motors along microtubules, the ingredients of these calculations are highly generic and may apply to make predictions and infer bounds about the costs and strategies to build versus maintaining gradients in myriad guises across biology, agnostic of particular mechanisms.

Conceptually, the structure of the estimates will all be the same, with the generic functional form

$$\text{power of process} = J_{\text{process}} \times \Delta\mu_{\text{process}}. \tag{4.1}$$

Here we have defined the quantity $\Delta\mu_{\text{process}}$ as the free energy cost of a unit process such as a single step of a motor or the movement of a single molecule up a gradient. J_{process} refers to the flux associated with the process of interest, meaning how many unit processes occur per unit time. For example, in the context of constantly pumping ions up a concentration gradient, $\Delta\mu_{\text{process}}$ refers to the free energy cost of taking a single ion from one side of the membrane to the other. Similarly, the flux in that case would be given by a phenomenological linear transport law relating the concentration jump across the membrane to the flux itself. Using this quantitative structure, we carry out a series of estimates for various models of gradient formation and maintenance.

Power to Maintain a Motor Gradient

As noted in our earlier work, the largest power estimate out of the suite of processes that occur during aster formation is associated with the formation of the gradient of motors. Because of the gradient in motor density across the aster, it is of interest to estimate the free energy required to maintain that gradient. We begin by examining

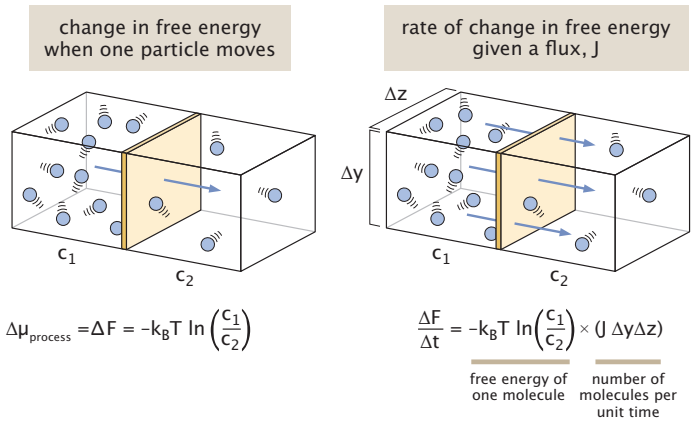

Figure 4.1: **The change in free energy when a particle is transported in a gradient.** (A) The free energy change upon moving a particle from the left reservoir to the right reservoir. (B) The total free energy dissipated as many particles move in the presence of a gradient. Adapted from Hueschen and Phillips, The Restless Cell.

the free energy cost of a one-dimensional gradient to set notation and to explain the concept and follow that discussion by the case of interest involving spherical symmetry. The concept of the estimate is to compute the free energy change when we take one particle from a region with one concentration and put that particle in a nearby region with a slightly different concentration.

Figure 4.1(A) makes this explicit by illustrating the free energy change associated with moving a single molecule from a reservoir at one concentration to a second reservoir at a different concentration. We consider a scenario in which the entirety of the free energy change is entropic (e.g., we do not consider situations involving gravitational or electrostatic potentials), meaning that the free energy is defined as

$$F = -TS, \tag{4.2}$$

where S is the entropy. We interest ourselves in the change in free energy

$$\Delta F = F_{\text{final}} - F_{\text{initial}} = -TS_{\text{final}} + TS_{\text{initial}}. \tag{4.3}$$

To compute the entropy change, we need to compute the entropy of the solutions on both sides of the partition, both before and after we have taken a molecule from the left side and placed it on the right side. The total entropy is given by

$$S_{\text{tot}} = S_1 + S_2 \tag{4.4}$$

where the subscripts refer to the two compartments. Using the Boltzmann definition of entropy, we have

$$S_{\text{tot}}^{(\text{final})} = k_B \ln W_1^{(\text{final})} + k_B \ln W_2^{(\text{final})}, \tag{4.5}$$

with a similar expression for the entropy in the initial state. This can be simplified to the form

$$S_{\text{tot}}^{(\text{final})} = k_B \ln (W_1^{(\text{final})} W_2^{(\text{final})}), \tag{4.6}$$

which makes sense given that the total number of microscopic states is equal to the product of the number of states in the first box and the number of states in the second box.

In a lattice model, we make the abstraction that space is subdivided into tiny lattice sites with a characteristic dimension of 1 nm^3 (i.e., molecular sizes). To compute the number of microstates W, we count the number of ways of arranging our L_i motors among the Ω lattice sites as

$$W_i(L_i) = \frac{\Omega!}{L_i!(\Omega - L_i)!}. \tag{4.7}$$

When $\Omega \gg L_i$ (i.e. the dilute limit), we can make the much simpler approximation

$$W_i(L) = \frac{\Omega^{L_i}}{L_i!}, \tag{4.8}$$

which amounts to the idea that every motor can sit on any of the Ω lattice sites.

We can now write the change in free energy which is strictly entropic as

$$\Delta\mu = -k_B T \left(\ln \frac{\Omega^{L_1+1}}{(L_1+1)!} \frac{\Omega^{L_2-1}}{(L_2-1)!} - \ln \frac{\Omega^{L_1}}{L_1!} \frac{\Omega^{L_2}}{L_2!} \right), \tag{4.9}$$

where we revert to the notation $\Delta\mu$ since this is the free energy change of the unit process of moving one molecule from one side of the partition to the other. This can be simplified to

$$\Delta\mu = -k_B T \ln \frac{L_1!}{(L_1+1)!} \frac{L_2!}{(L_2-1)!} \approx -k_B T \ln \frac{L_2}{L_1}. \tag{4.10}$$

We can rewrite this in a more familiar form using the language of concentrations. If we multiply numerator and denominator within the logarithm by Ωv, where v is the volume of a single lattice site in our lattice model, then $\Omega v = V_{tot}$ and hence $c_1 = L_1/V_{tot}$ and $c_2 = L_2/V_{tot}$, permitting us to write

$$\Delta\mu = k_B T \ln \frac{c_2}{c_1}. \tag{4.11}$$

Now, as seen in the right panel of Figure 4.1 if we want to find the total rate of free energy change, we need to multiply the free energy per particle by the total number

of particles transported between the two adjacent reservoirs per unit time using the flux resulting in

$$\left(\frac{\Delta F}{\Delta t}\right) = -\Delta\mu(J\Delta y\Delta z). \tag{4.12}$$

The factor $J\Delta y\Delta z$ counts the number of molecules carried down the gradient per unit time and the minus sign guarantees that if the left reservoir has more molecules than the left, then $\Delta F/\Delta t < 0$. We now interest ourselves in the case where the concentration is slowly varying, permitting us to write

$$\left(\frac{\Delta F}{\Delta t}\right) = k_B T \ln \frac{c(x+\Delta x)}{c(x)} \times (J\Delta y\Delta z), \tag{4.13}$$

where we have introduced the notation $c_1 = c(x)$ and $c_2 = c(x+\Delta x)$. Note now we switched the sign because we inverted the ratio in the logarithm with the concentration on the right now appearing in the numerator. Note that this expression is valid regardless of whether $c_1 > c_2$ or $c_2 > c_1$ since in those two cases the flux is in opposite directions and our expression reflects that. By invoking Fick's law we now have

$$\left(\frac{\Delta F}{\Delta t}\right) = k_B T \ln \frac{c(x+\Delta x)}{c(x)} \times \left(-D\frac{dc}{dx}\right)\Delta y\Delta z. \tag{4.14}$$

By carrying out the Taylor expansion $c(x+\Delta x) = c(x) + (\partial c/\partial x)\Delta x$, we can rewrite the logarithmic term as

$$\begin{aligned} \ln \frac{c(x+\Delta x)}{c(x)} &= \ln\left[\frac{c(x) + \frac{\partial c}{\partial x}\Delta x}{c(x)}\right] \\ &= \ln\left[1 + \frac{1}{c}\frac{\partial c}{\partial x}\Delta x\right]. \end{aligned} \tag{4.15}$$

Finally, we invoke a second Taylor series in the form $\ln(1+\epsilon) \approx \epsilon$, resulting in the simple and powerful expression

$$\left(\frac{\Delta F}{\Delta t}\right) = -D k_B T \frac{1}{c(x)}\left(\frac{\partial c(x)}{\partial x}\right)^2 \Delta x\Delta y\Delta z. \tag{4.16}$$

This result tells us the free energy loss for two adjacent planes if the gradient is allowed to dissipate. We can now put this all together to explore the free energy dissipated over a continuous concentration field. In this case, we take the expression seen in eqn. 4.16 and add up the contribution from each set of planes in our discrete representation of the concentration field. We can work out the minimum power to maintain such a gradient where we imagine every time a molecule goes down its gradient, energy is consumed to push it back where it came from. Given this

approach, we can now tackle the question of estimating the power associated with maintaining the radial motor gradient in our asters. However, to do so, we first need to reinterpret the one-dimensional analysis done here to the case of a three-dimensional, but spherically symmetric concentration gradient.

The Power Required to Maintain a Three-Dimensional Gradient

Building on the analysis of the previous section which was performed in one-dimension, we now turn our attention to a three-dimensional structure with a spherically symmetric concentration gradient of motors of the form $c(r)$, where r is the radial distance from the aster center. Figure 4.2(A) shows the amendment that needs to be made to the one-dimensional analysis, where now in the three dimensional case, the "boxes" are spherical shells. Interestingly, the expression we derived earlier goes through essentially unchanged except that now we consider the radial concentration, and instead of integrating over planes along the x-direction, we now integrate over spherical shells in the r direction. Given these adjustments, the power to sustain a gradient is now given as

$$P = k_{\mathrm{B}}TD \int_0^{2\pi} \int_0^{\pi} \int_0^{\infty} \frac{1}{c(r)} \left(\frac{\partial c(r)}{\partial r} \right)^2 r^2 \sin\theta \, dr \, d\theta \, d\phi, \tag{4.17}$$

where D is the diffusion constant and $c(r)$ is the radial concentration profile.

To get a qualitative feeling for the power scales, we begin by considering a fixed, radial distribution of motors described as a decaying exponential of the form

$$c(r) = c_0 e^{-r/\lambda}, \tag{4.18}$$

where c_0 is the motor concentration at $r = 0$ and λ is the decay length. Plugging this profile into eqn. 4.17, we can immediately compute the power that must be expended to prevent the diffusive relaxation of this gradient as

$$\begin{aligned} P &= 4\pi k_{\mathrm{B}}TD \int_0^{\infty} \frac{e^{r/\lambda}}{c_0} \left(-\frac{c_0}{\lambda} e^{-r/\lambda} \right)^2 r^2 \, dr \\ &= \frac{4\pi k_{\mathrm{B}}TDc_0}{\lambda^2} \int_0^{\infty} r^2 \, e^{-r/\lambda} dr. \end{aligned} \tag{4.19}$$

Integrating by parts, we find that the integral evaluates to $\lambda^2 \int_0^{\infty} r^2 \, e^{-r/\lambda} dr = 2\lambda^3$ yielding,

$$P = 8\pi k_{\mathrm{B}}TDc_0\lambda. \tag{4.20}$$

Without the prefactors, this result can also be inferred by dimensional analysis.

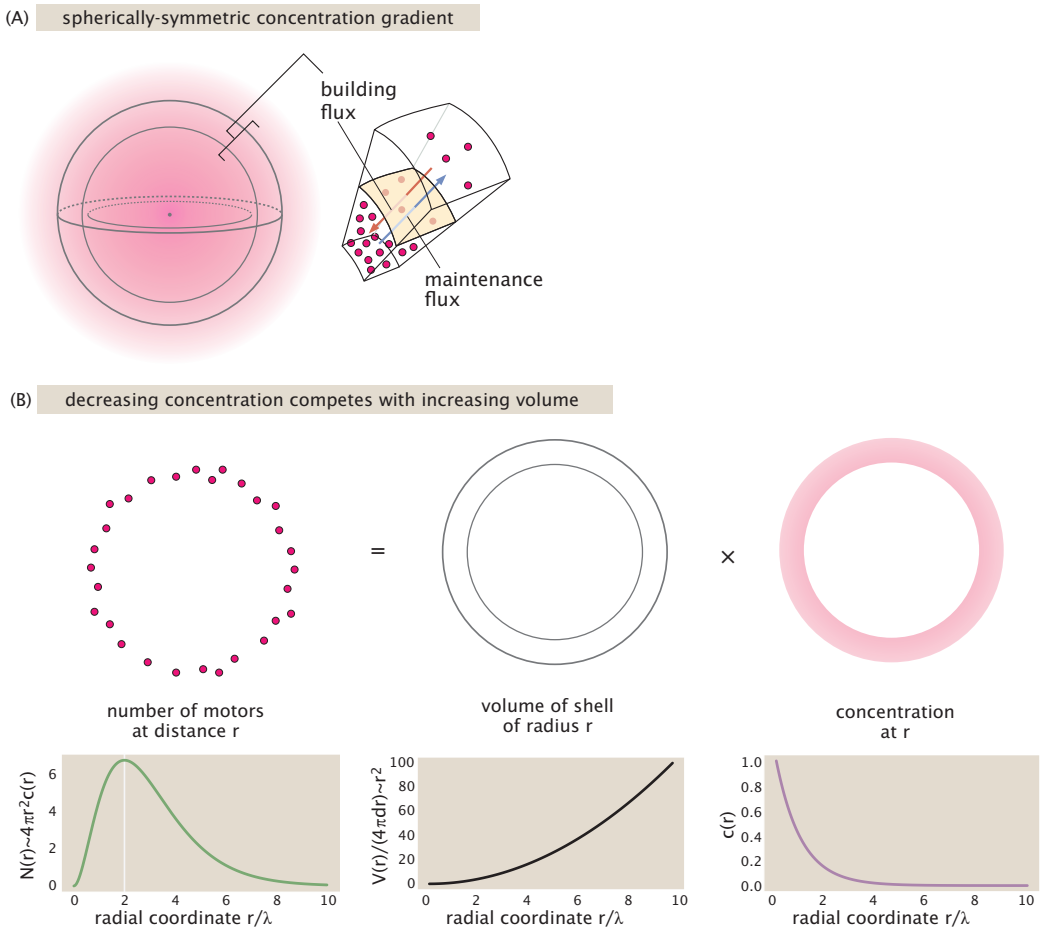

Figure 4.2: **Dissipation in a spherically symmetric concentration gradient.** (A) Maintaining a spherically symmetric concentration gradient results from a competition between the outward diffusive flux and the inward active flux provided by motors moving on microtubules. (B) There is a peak in the distribution of motors as a function of radial distance resulting from the competition between the monotonically decreasing motor concentration and the geometric effect that the spherical shells get larger with increasing r.

Estimate of the magnitude of power to prevent diffusive spreading

To get a feeling for the numbers, we appeal to the measurements described in our experimental paper for which the asters are approximately described by a radial concentration field of the form $c(r) = c_0 e^{-r/\lambda}$, with parameters $c_0 \approx 1\ \mu M$ and $\lambda \approx 30\ \mu m$. Given these values, we first ask roughly how many motors there are in this aster region, found as

$$\#\text{ of motors in aster} = \int_{\text{aster}} dV c_0 e^{-r/\lambda} = 8\pi c_0 \lambda^3. \tag{4.21}$$

This result can be seen by using integration by parts on the radial integral, though intuitively, dimensional analysis recommends this functional form to within numerical factors. Given that $c_0 = 1\mu M \approx 10^3/\mu m^3$ and $\lambda \approx 30\mu m$, we find that the number of motors in the aster is

$$\#\text{ of motors in aster} = 8\pi c_0 \lambda^3 \approx 8\pi \times \frac{10^3}{\mu m^3} \times (f \times 10\ \mu m)^3 \approx 10^9 \text{ motors.} \tag{4.22}$$

If every one of those motors was consuming only one ATP per second, the resulting power is precisely the scale we find in our measurements which is of the order of 10^9 ATP/s.

We can compare this simple order of magnitude guess with the cost to maintain the gradient computed above. In particular, using eqn. 4.20, we find

$$P = 8\pi k_{\text{B}} T D c_0 \lambda \approx (f{\times}10){\times}k_B T{\times}(10\,\frac{\mu m^2}{s}){\times}\left(\frac{10^3}{\mu m^3}\right){\times}(f{\times}10\,\mu m) \approx 5{\times}10^5\,\frac{\text{ATP}}{\text{s}}. \tag{4.23}$$

The numbers we took here for the size of the aster were for " late times" and thus we need to make a more careful analysis for the change in aster size over time to provide a full picture of the dynamics of the power in space and time. The present calculation really serves as a first cut to get a feeling for the numbers.

The Spatial Distribution of Power

The three dimensional dissipation calculated above suggests interesting spatial effects in the measured power. As seen in Figure 4.2, the radially decaying concentration gradient implies that although the concentration may be higher at smaller radii, the number of motors in a given radial shell is not maximum at the origin. This means that there is the possibility of nonmonotonic power as a function of radius. The key idea is illustrated in Figure 4.2(B), where we see that the number

of motors as a function of distance from the origin is peaked. This is the result of a competition between the volume of the shells with increasing r (which increases) and the decrease in motor concentration as a function of distance as shown in the lower right panel.

To get a feeling for this effect, we once again turn to our model of a static, spherically symmetric gradient and show that there is a maximum in the power as a function of radius. Our first task is to compute the power in a spherical shell at radius r. One way to think of the power associated with such a spherical shell at radius r is to evaluate eqn. 4.17 only between r and $r + \Delta r$, resulting in

$$P = 4\pi r^2 k_{\mathrm{B}} T D \frac{1}{c(r)} \left(\frac{\partial c(r)}{\partial r} \right)^2 \Delta r. \tag{4.24}$$

If we now exploit the known concentration profile $c(r) = c_0 \exp(-r/\lambda)$ and substitute it into eqn. 4.24, we find the power in the shell at radius r is given by

$$\frac{\partial F}{\partial t}(r) = -(\text{const.}) \times r^2 e^{-r/\lambda}, \tag{4.25}$$

where we have suppressed all constants such as D, c_0, λ, π, etc. This very simple expression now permits us to show that for our simplified model of a static aster, there is a maximum in the dissipation rate as a function of r given by

$$\frac{d}{dr}\left(\frac{\partial F}{\partial t}(r) \right) = -(\text{const.}) \times \left[2re^{-r/\lambda} - \frac{r^2}{\lambda} e^{-r/\lambda} \right] = 0 \tag{4.26}$$

resulting in a maximum in the power dissipation at radius $r = 2\lambda$

To be thorough, we were also curious about the implications of asymmetries in the aster since three-dimensional imaging demonstrates that our asters are not completely spherical, but have a preferred long axis in the illumination direction. Here we consider the opposite extreme in which the aster is a cylinder instead. In this case, the power as a function of radial distance from the cylinder axis is given by

$$\frac{\partial F}{\partial t}(r) = 2\pi r \Delta z \left(-D \frac{\partial c}{\partial r} \right) \frac{1}{c} \frac{\partial c}{\partial r} \Delta r k_B T. \tag{4.27}$$

This expression has units of power (i.e. J/s) and tells us the power dissipated in the annulus at radius r. This expression raises the question of how the power dissipated depends upon the radius, and specifically, is there a maximum. If we once again exploit the fact that the concentration has cylindrical symmetry and is characterized by $c(r) = c_0 \exp(-r/\lambda)$, then we see that we have

$$\frac{\partial F}{\partial t}(r) = -(\text{const.}) \times r e^{-r/\lambda}, \tag{4.28}$$

where we once again suppress the constants such as D, Δr, etc. This result implies in turn that

$$\frac{d}{dr}\left(\frac{\partial F}{\partial t}(r)\right) = -(\text{const.}) \times \left[e^{-r/\lambda} - \frac{r}{\lambda}e^{-r/\lambda}\right] = 0 \tag{4.29}$$

which implies that the maximum dissipation occurs at $r = \lambda$.

The calculations we have done thus far are both interesting and suggestive for interpreting the measured ATP consumption in our aster experiments. However, the discussion here was based upon a variety of simplifying assumptions, the most important of which is that the aster is fixed in shape over time. However, we know that asters evolve in time from the moment that light is used to cross link the motors leading to a time-dependent aster size and motor concentration. In the next sections, we consider the difference between the power to construct and maintain an aster which explicitly acknowledges this time dependence. Of course, to construct an aster and the motor concentration gradient requires more than diffusion. There are active fluxes and we now examine the power of these fluxes.

The Power Required to Build a Three-Dimensional Gradient

Figure 4.3 shows the power consumption over time during representative aster formation experiments, which suggest that ATP is spent nearly an order of magnitude faster at early times than at late times in the dynamics of aster formation after light-induced motor dimerization occurs. This widens the gap between our largest measured dissipations and our best quantitative estimates for the origins of the power. As a result, in the current section, we graduate our earlier estimates to confront the transient power in the earlier stages of aster formation.

What is the basis of the large discrepancy between power consumption at early and late times in the aster formation process? One provocative possibility is that the formative physics of asters at early times fundamentally demand separate, and plausibly greater, nonequilibrium expenditures than those required to just maintain an aster's structure once it has formed at late times.

To bear on these questions and learn about what they say about the precise destinies of ATP expenditure in pattern formation, here we calculate the free energy cost per time required to both build a concentration gradient in time, and to maintain it at a given state. Combining these calculations with representative phenomenology of motor distributions, we find much support for the latter idea that the power required to assemble a nonuniform profile can be hundreds of times larger than the power cost merely to maintain it (during some stages of aster formation). However, remarkably,

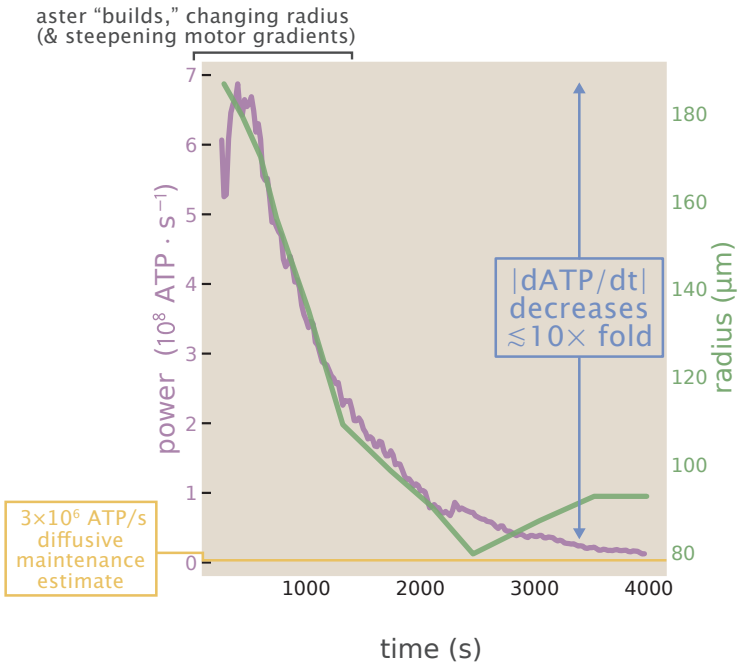

Figure 4.3: **Experimental data motivating the question of how much power it takes to build versus maintain an aster's concentration gradients.** The x-axis is time and the y-axis is the power, making it evident that the power consumption changes over time as the microtubule-motor system evolves towards its nonequilibrium aster steady state.

the relative importance of building power and maintenance power often switches over the course of an aster's trajectory, and more generally can vary over space, time, and values of biophysical parameters. We introduce an amusing and natural "dissipative Peclét number" definable locally or globally in spacetime that neatly organizes and characterizes this competition between dissipative origins.

Building versus maintaining *arbitrary* (spherically-symmetric) gradients

As simple steps towards the enduring question of how much gradients cost energetically, consider some active agent spending energy to maintain—or even grow—a concentration gradient over space. This activity, administering some material flux $\mathbf{J}_A$, must defy the spontaneous diffusive flux $\mathbf{J}_D$ of the substance that tends to relax the concentration gradient to uniformity. For a gradient to persist or build, these diffusive and active fluxes operate in opposing directions, making the concentration evolve according to a net flux $\Delta\mathbf{J} \equiv \mathbf{J}_A + \mathbf{J}_D$.

For concreteness, when the concentration profile is spherically-symmetric (varying

only along the radial coordinate r), and without loss of generality under the convention that more substance is found at small r than at large r (namely $\frac{\partial c}{\partial r} \leq 0$), the agent's flux J_A has a negative sign, $J_A \leq 0$, and the diffusive flux is positive, $J_D = -D\frac{\partial c}{\partial r} \geq 0$. Calling the net flux $J_r = \Delta J$ since it is in the radial direction, these conventions cast the net flux as $J_r = J_D - |J_A|$. (If the gradient is merely maintained, neither decaying nor steepening, then the net flux is zero and $|J_A| = |J_D|$: the active agent moves just enough material thus spending just enough energy to counteract the spontaneous diffusive flux that would result if it were not acting. While building a gradient, the agent's total active flux is thus partitioned into a maintenance flux matching diffusion, plus any attained nonzero net flux $|\Delta J| > 0$ steepening the gradient,

$$|J_A(r,t)| = |J_D(r,t)| + |J_r(r,t)|. \tag{4.30}$$

We can examine the mathematical underpinnings of this question as follows. Let the total free energy density at position $\mathbf{r}$ and time t be $f(\mathbf{r},t)$. Note that the free energy density should depend on time and space only via the concentration field $c(\mathbf{r},t)$, that is $f \equiv f(c(\mathbf{r},t))$. Then the total free energy $F^{\text{tot}}(t)$ of the system is its integral over all space,

$$F^{\text{tot}}(t) = \int d^3\mathbf{r}\; f(c(\mathbf{r},t)), \tag{4.31}$$

and the total power is the time derivative of this total free energy, giving,

$$\begin{aligned} \mathrm{P}^{\text{tot}}(t) &= \frac{dF^{\text{tot}}}{dt} && (4.32)\\ &= \frac{\partial}{\partial t}\int d^3\mathbf{r}\; f(c(\mathbf{r},t)) = \int d^3\mathbf{r}\; \frac{\partial f(c(\mathbf{r},t))}{\partial t} && (4.33)\\ &= \int d^3\mathbf{r}\frac{\partial f(c)}{\partial c}\frac{\partial c(\mathbf{r},t)}{\partial t}. && (4.34) \end{aligned}$$

Note that the chemical potential is by definition the change in free energy with respect to a change in particle number, or (dividing a local volume element by a volume) equivalently the change in free energy density with respect to concentration, $\mu(\mathbf{r},t) \equiv \frac{\partial f}{\partial c}$. In addition, note that conservation of mass gives the standard continuity equation in the concentration field: the local rate at which concentration changes is the divergence of the net flux $\mathbf{J}(\mathbf{r},t)$ without any homogeneous local sources,

$$\frac{\partial c}{\partial t} + \nabla \cdot \mathbf{J}_{\text{net}} = 0, \tag{4.35}$$

so we can express the $\frac{\partial c}{\partial t}$ in the integrand of Eq. 4.34 in terms of the net flux's divergence, $\frac{\partial c}{\partial t} = -\nabla \cdot \mathbf{J}_{\text{net}}$, yielding,

$$\mathrm{P}^{\text{tot}}(t) = \int d^3\mathbf{r} \frac{\partial f(c)}{\partial c} \frac{\partial c(\mathbf{r}, t)}{\partial t} \tag{4.36}$$

$$= -\int d^3\mathbf{r}\, \mu(\mathbf{r}, t)\, \nabla \cdot \mathbf{J}_{\text{net}}. \tag{4.37}$$

Eq. 4.37 is a volume integral of a scalar field (the chemical potential μ) times the divergence of a vector field (the net flux J_{net}). This permits us to invoke a consequence of the divergence theorem, which (see `https://en.wikipedia.org/wiki/Divergence_theorem#Corollaries`) delivers the vector identity that,

$$\int dV\, [\mathbf{F} \cdot (\nabla g) + g\, (\nabla \cdot \mathbf{F})] = \oint d\partial V\ \ (g\mathbf{F} \cdot \mathbf{n}) \tag{4.38}$$

$$\rightarrow \int dV\, g\, (\nabla \cdot \mathbf{F}) = \oint d\partial V\ \ (g\mathbf{F} \cdot \mathbf{n}) - \int dV \mathbf{F} \cdot (\nabla g)\,. \tag{4.39}$$

Identifying g as μ and $\mathbf{F}$ as $\mathbf{J}_{\text{net}}$ in this vector identity, we see that the power can be written as a volume integral of a gradient in the chemical potential coupled with the flux, minus a surface integral,

$$\mathrm{P}^{\text{tot}}(t) = \int d^3\mathbf{r}\, \mathbf{J}_{\text{net}} \cdot (\nabla \cdot \mu) - \oint dA\ \mu(\mathbf{J}_{\text{net}} \cdot \mathbf{n}). \tag{4.40}$$

For a system with no explicit dissipative action at infinity, the surface integral should vanish. This gives,

$$\mathrm{P}^{\text{tot}}(t) = \int d^3\mathbf{r}\, \mathbf{J}_{\text{net}} \cdot (\nabla \cdot \mu)\,. \tag{4.41}$$

Given a chemical potential $\mu(r) = \mu_0 + k_B T \ln c(r,t)/c_0$ varying in space (for a standard state concentration c_0 and standard potential μ_0), the local change in chemical potential imposed by moving a particle of substance an infinitesimal distance dr is,

$$d\mu = \frac{\partial \mu}{\partial r} dr \tag{4.42}$$

$$= dr\ k_B T\ \frac{1}{c(r,t)} \frac{\partial c}{\partial r}. \tag{4.43}$$

This free energy cost couples with the earlier fluxes to define the areal power densities σ of maintaining and building the gradient,

$$\underbrace{\sigma_A(r,t)}_{\text{W m}^{-2}\text{ s}^{-1}} \equiv |J_A(r,t)| \frac{\partial \mu}{\partial r} dr = \underbrace{|J_D(r,t)| \frac{\partial \mu}{\partial r}}_{\equiv \rho_D, \text{W m}^{-3}\text{ s}^{-1}} dr + \underbrace{|J_r(r,t)| \frac{\partial \mu}{\partial r}}_{\equiv \rho_r, \text{W m}^{-3}\text{ s}^{-1}} dr. \tag{4.44}$$

Here we also defined the volumetric power densities $\rho_D(r,t)$ and $\rho_r(r,t)$; their values $4\pi r^2\rho(r,t)dr$ give the power attributable to a shell of radial thickness dr around the radial position r, and when integrated radially over space give the total power for these processes.

Integrating this density over all space attacks the question of whether the total power to build a gradient, or that to maintain it against diffusion, dominates. We can express the magnitude of the total power spent by a source as

$$P_{\text{tot}}(t) = \int \left(\frac{\partial \mu}{\partial r} dr\right) \underbrace{4\pi r^2}_{\text{area through which flux passes}} (|J_D| + |J_r|)\,. \tag{4.45}$$

This allows us to explicitly quantify the partitioning of total power into the power P_{build} attributable to building and power P_{maintain} to maintain the gradient, namely,

$$P_{\text{tot}}(t) = \underbrace{\int dr\, 4\pi r^2 \frac{\partial \mu}{\partial r} |J_D(r,t)|}_{\equiv P_{\text{maintain}}(t)} + \underbrace{\int dr\, 4\pi r^2 \frac{\partial \mu}{\partial r} |J_r(r,t)|}_{\equiv P_{\text{build}}(t)}\,. \tag{4.46}$$

To compute the relative magnitudes of these terms, we must specify the governing fluxes.

How does a specified time evolution of a concentration field $c(r,t)$ set the fluxes governing these dissipative expressions? Recall that by continuity, a flux has a divergence that sets the rate of change of concentration; if the flux $\mathbf{J} \equiv [J_r, J_\theta, J_\phi]$ is spherically-symmetric (making all angular derivatives vanish, $\partial_\theta, \partial_\phi \to 0$), then,

$$\frac{\partial c(r,t)}{\partial t} = -\vec{\nabla} \cdot \mathbf{J} \tag{4.47}$$

$$= -\frac{1}{r^2}\frac{\partial}{\partial r}\left[r^2 J_r\right]. \tag{4.48}$$

This means that

$$-r^2 \frac{\partial c}{\partial t} = \frac{\partial}{\partial r}\left[r^2 J_r\right], \tag{4.49}$$

or integrating with respect to space from $r = 0$ to $r = r$,

$$-\int_0^r dr\, r^2 \frac{\partial c}{\partial t} = r^2 J_r\Big|_{r=r} - r^2 J_r\Big|_{r=0}\,. \tag{4.50}$$

Since we expect the flux $J_r(r = 0, t)$ to vanish at the origin (since there is no point source or sink there), the latter term vanishes, establishing that the radial flux is given by the radially-integrated rate-of-change of concentration,

$$J_r(r,t) = -\frac{1}{r^2}\int_{r=0}^{r} dr\, r^2 \frac{\partial c}{\partial t}. \tag{4.51}$$

On the maintenance side, Fick's first law tells us the flux required to compensate for diffusion is given by,

$$|J_D(r,t)| = \left| -D\frac{\partial c}{\partial r} \right| \tag{4.52}$$

$$= D\left| \frac{\partial c}{\partial r} \right|. \tag{4.53}$$

Taken together, Equations 4.43, 4.51, and 4.53 give precise answers to the question asked by Eq. 4.46 of how the powers to maintain or build any prescribed concentration profile $c(r,t)$ compare. To gain further insight, we now examine the consequences and lessons of these expressions by adopting specific concentration profiles $c(r,t)$.

Number-conserving, steepening, exponential concentration gradients

We now turn to the question of a spatially varying concentration gradient, $c(r,t)$. The key difference from the examples of section 4.2 is that now we consider the case in which the spatial extent of the gradient is varying over time (i.e. $\lambda(t)$). This model is physically-plausible and—it transpires—analytically-convenient. This model is motivated by two stylized facts. First, motors do exhibit approximately exponential distributions in space at some time points and over relevant spatial regions. See the conceptual description of such distributions in Figures 4.4(A) and (B) as well as exemplary phenomenology of some empirical motor distributions in Figure 4.5.

Second, physically, we believe there really should be conservation of total motors. Consider a spherically-symmetric time varying concentration gradient given by,

$$c(r,t) = c_0(t)\exp\left[-\frac{r}{\lambda(t)}\right], \tag{4.54}$$

where $c_0(t)$ is the concentration at the radial origin of the gradient ($r = 0$), namely the motor peak, and $\lambda(t)$ is a time-varying length scale of the gradient characterizing the spatial evolution of the field. The total number of motors is given by

$$N(t) = \int_{r=0}^{\infty} dr\, 4\pi r^2 c(r,t) = 8\pi\lambda(t)^3 c_0(t). \tag{4.55}$$

Now, to impose conservation of motors, we demand this integral amount to a constant value N, setting the amplitude prefactor $c_0(t)$ as,

$$c_0(t) \equiv \frac{N}{8\pi}\frac{1}{\lambda(t)^3}. \tag{4.56}$$

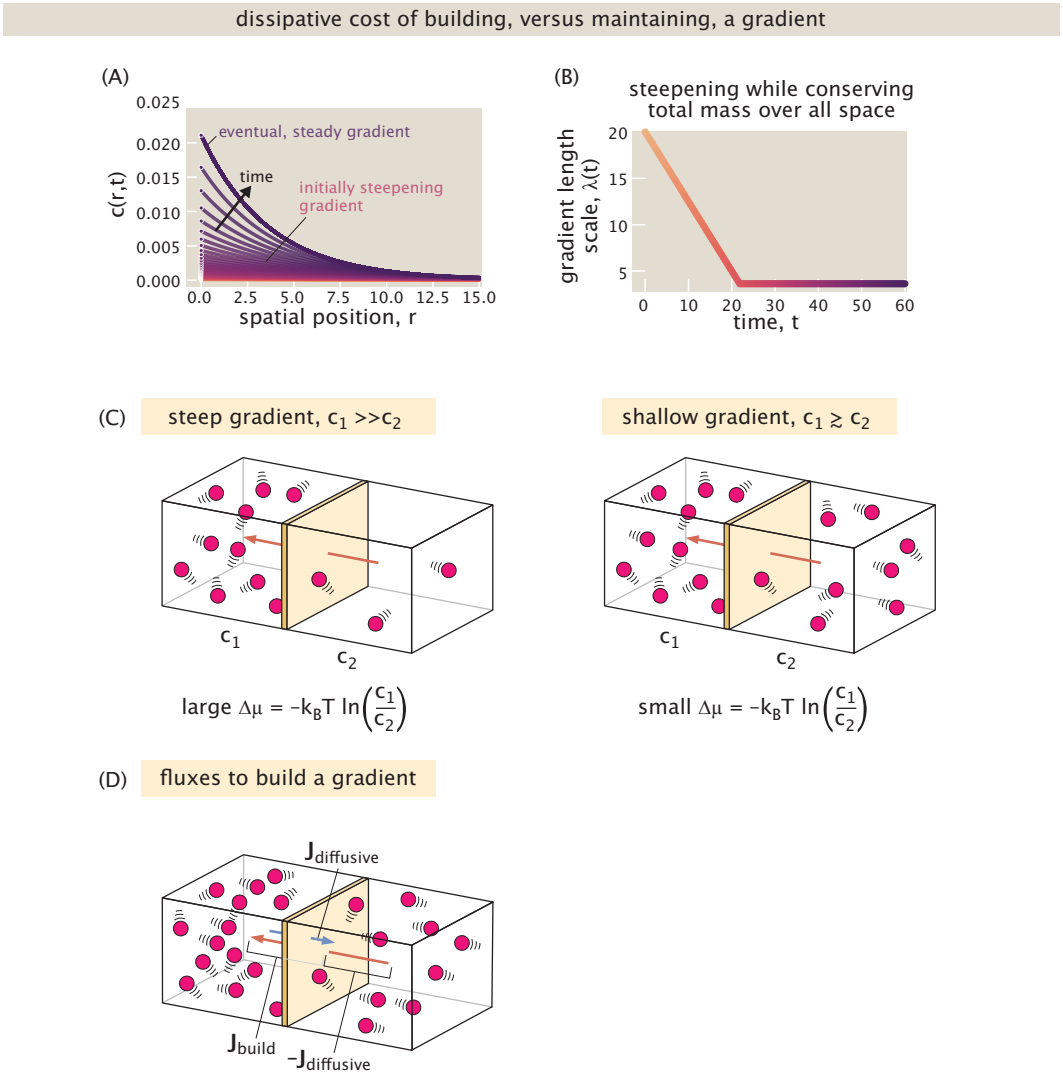

Figure 4.4: **The dynamics of building a gradient.** (A) The concentration profile as a function of time. (B) The length scale of the exponential gradient over time. (C) Schematic of the free energy cost of a steep and a shallow gradient. (D) The fluxes associated with building a gradient.

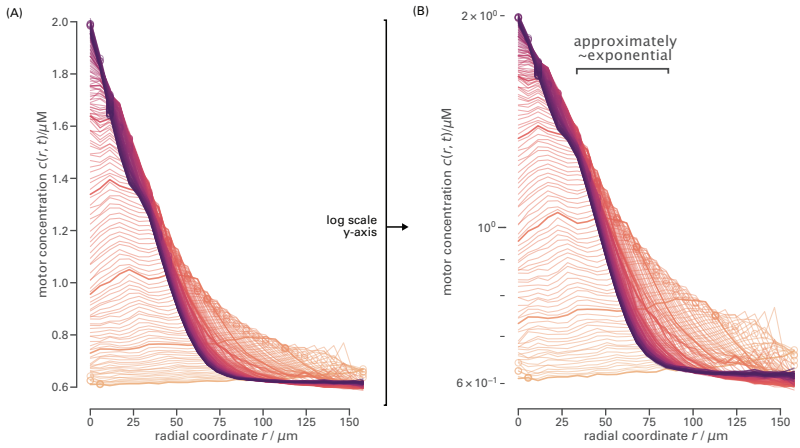

Figure 4.5: **Example motor distributions over space, angularly averaged to show variation of motor concentration over radial coordinate r.** Different lines (in distinct colors) show progression in time. (A) Motors steepen their gradients in time, as visible on linearly-scaled a y-axis. (B) Some regions of the aster are acceptably described as approximately exponentially declining with radial position r away from the center, as demonstrated by acceptably straight line on a semilog plot of the same data in (A).

This sets the spacetime evolution as,

$$c(r,t) = \frac{N}{8\pi}\frac{1}{\lambda(t)^3}\exp\left[-\frac{r}{\lambda(t)}\right]. \tag{4.57}$$

Given such a time-dependent concentration profile, we are poised to examine the power associated with both building and maintaining the gradient.

Resulting (net and diffusive) fluxes of steepening, exponential concentration gradients

Now, we substitute the conservative time evolution profile $c(r,t)$ of Eq. 4.57 into the expression for the net flux derived earlier using the continuity equation. First, we compute the relevant corresponding time derivative $\frac{\partial c}{\partial t}$ as

$$\frac{\partial c}{\partial t} = \frac{N}{8\pi}\left(-3\frac{1}{\lambda(t)^4}\partial_t\lambda\exp\left[-\frac{r}{\lambda(t)}\right] + \frac{1}{\lambda(t)^3}\exp\left[-\frac{r}{\lambda(t)}\right]\frac{r\partial_t\lambda}{\lambda(t)^2}\right) \tag{4.58}$$

$$= \frac{N}{8\pi}\left(\frac{\partial_t\lambda}{\lambda(t)^4}\exp\left[-\frac{r}{\lambda(t)}\right]\left(\frac{r}{\lambda(t)} - 3\right)\right) \tag{4.59}$$

$$= c(r,t)\frac{1}{\lambda(t)}\frac{\partial\lambda}{\partial t}\left(\frac{r}{\lambda(t)} - 3\right). \tag{4.60}$$

Substituting this time derivative into our flux expression Eq. 4.51 gives,

$$J_r(r,t) = -\frac{1}{r^2}\left[\int_{r=0}^{r} dr\, r^2\, \frac{N}{8\pi}\left(\frac{\partial_t \lambda}{\lambda(t)^4}\exp\left[-\frac{r}{\lambda(t)}\right]\left(\frac{r}{\lambda(t)}-3\right)\right)\right] \tag{4.61}$$

$$= -\frac{N}{8\pi}\frac{\partial_t \lambda}{\lambda(t)^4}\frac{1}{r^2}\left[\frac{1}{\lambda(t)}\int_{r=0}^{r} dr\, r^3\, \exp\left[-\frac{r}{\lambda(t)}\right] - 3\int_{r=0}^{r} dr\, r^2 \exp\left[-\frac{r}{\lambda(t)}\right]\right]. \tag{4.62}$$

We evaluate each remaining integral in turn. The first integral $\int_{r=0}^{r} dr\, r^3\, \exp\left[-\frac{r}{\lambda(t)}\right]$ evaluates to $6\lambda(t)^4 - \exp\left[-\frac{r}{\lambda(t)}\right]\lambda(t)\left(r^3 + 3r^2\lambda(t) + 6r\lambda(t)^2 + 6\lambda(t)^3\right)$. The second integral $\int_{r=0}^{r} dr\, r^2 \exp\left[-\frac{r}{\lambda(t)}\right]$ gives $2\lambda(t)^3 - \exp\left[-\frac{r}{\lambda(t)}\right]\lambda(t)\left(r^2 + 2r\lambda(t) + 2\lambda(t)^2\right)$. These give the remarkably-simple weighted-difference

$$\frac{1}{\lambda(t)}\int_{r=0}^{r} dr\, r^3\, \exp\left[-\frac{r}{\lambda(t)}\right] - 3\int_{r=0}^{r} dr\, r^2 \exp\left[-\frac{r}{\lambda(t)}\right] = -\exp\left[-\frac{r}{\lambda(t)}\right] r^3. \tag{4.63}$$

In fact, this simplicity can be anticipated directly by an integration-by-parts result. First, let's start with an integral of the form $\int dr\, r^n e^{-r/\lambda}$. The derivative of the integrand $r^n e^{-r/\lambda}$ is just,

$$\frac{\partial}{\partial r} r^n e^{-r/\lambda} = n r^{n-1} e^{-r/\lambda} - r^n \frac{1}{\lambda} e^{-r/\lambda}. \tag{4.64}$$

Now, integrate each term: this gives $r^n e^{-r/\lambda}$ again on the left side, and two terms involving similar integrals on different integrands on the right side, namely,

$$\int dr\, \left[\frac{\partial}{\partial r} r^n e^{-r/\lambda}\right] = n\int dr\, r^{n-1} e^{-r/\lambda} - \frac{1}{\lambda}\int dr\, r^n e^{-r/\lambda} \tag{4.65}$$

$$\rightarrow r^n e^{-r/\lambda} = n\int dr\, r^{n-1} e^{-r/\lambda} - \frac{1}{\lambda}\int dr\, r^n e^{-r/\lambda}. \tag{4.66}$$

This result directly gives the net flux cancellation above.

Accordingly, the net (building) material flux adopts the charmingly-concise final form,

$$J_r(r,t) = -\frac{N}{8\pi}\frac{\partial_t \lambda}{\lambda(t)^4}\frac{1}{r^2}\left[-\exp\left[-\frac{r}{\lambda(t)}\right] r^3\right] \tag{4.67}$$

$$= r\frac{\partial_t \lambda}{\lambda(t)}\frac{N}{8\pi}\frac{1}{\lambda(t)^3}\exp\left[-\frac{r}{\lambda(t)}\right] \tag{4.68}$$

$$= r\frac{\partial_t \lambda}{\lambda(t)} c(r,t). \tag{4.69}$$

This building flux expression exhibits some crucial properties.

First, we check this expression's units: $\frac{\partial_t \lambda}{\lambda}$ gives units of per time; r gives units of length; and $c(r,t)$ gives units of inverse cubic length. Together these quantities give per length squared per time, as required of any flux. Second, consider the sign of this net flux. A gradient that is steepening has a shrinking characteristic length scale $\lambda(t)$ in time, making $\partial_t \lambda < 0$; this makes $J_r(r,t) < 0$ correspondingly negative (net inwards flux). This sign of the net flux is physically correct: for an extant concentration gradient with greatest concentration in the center at small r and smaller concentration at larger r, we have $\frac{\partial c}{\partial r} < 0$, so a source flux that steepens this imbalance will be indeed pointed inwards, and the opposing diffusive flux $J_D = -D\frac{\partial c}{\partial r} > 0$ will be positive (pointing outwards).

Third, note that the net flux is proportional to temporal rate of change of the length scale λ divided by its current value, which is equivalent to $\frac{\partial_t \lambda}{\lambda(t)} = \frac{\partial \ln \lambda/\lambda_0}{\partial t}$ for some reference length λ_0. That is, the magnitude of the net flux is larger when the governing length scale changes its value faster relative to/*in units of* its current value. If the governing length scale does not change at all in time, $\partial_t \lambda = 0$, then the net flux also vanishes.

Third, note that the flux scales with the radial position r. This can counteract the tendency for concentrations to be smaller at larger r. Specifically, at a fixed time (e.g. setting the value of $\frac{\partial_t \lambda}{\lambda}$ to some fixed constant) the spatial position r where the magnitude of this net building flux J_r is largest is peaked (nonmonotonic) in r at some optimum r_*, since there is a geometric competition between the $\sim r$ term and the exponentially declining gradient in r. The position r_* of this maximum net building flux satisfies

$$0 := \frac{\partial J_r}{\partial r} = \frac{\partial_t \lambda}{\lambda}\left(r \underbrace{\frac{\partial c}{\partial r}}_{\leq 0} + c(r,t) \right) \tag{4.70}$$

$$\rightarrow r_* = \frac{-c(r,t)}{\frac{\partial c}{\partial r}} \tag{4.71}$$

$$\rightarrow r_* = \lambda(t). \tag{4.72}$$

Here, we have learned the following interesting, elegant, nonobvious fact: the maximal material net flux occurs at the radial position which is exactly the current governing exponential length scale. This spatially-maximized flux is $J_r(\lambda, t) =$

$\partial_t \lambda \; c(\lambda, t) = \partial_t \lambda \; \frac{N}{8\pi} \frac{1}{\lambda(t)^3} \frac{1}{e}$. Fourth, note that the flux scales with the absolute local concentration $c(r,t)$: scaling the concentration everywhere by some multiplicative factor α increases the corresponding flux by the same amount. Many of these properties are illustrated for the example of a linear ramp in time of the governing length scale $\lambda(t)$) in Figure 4.6.

For comparison to this net building flux, we also compute the corresponding maintenance (diffusive) flux under this simple conservative model of concentration $c(r,t)$ of Eq. 4.57, finding,

$$J_D(r,t) = -D\frac{\partial c}{\partial r} \tag{4.73}$$

$$= -D\left(-\frac{1}{\lambda(t)}\frac{N}{8\pi}\frac{1}{\lambda(t)^3}\exp\left[-\frac{r}{\lambda(t)}\right]\right) \tag{4.74}$$

$$= D\frac{1}{\lambda(t)}c(r,t). \tag{4.75}$$

Comparing building (net) and maintenance (diffusive) *material* fluxes

Now, we compare the magnitudes of the building and maintenance fluxes given by Eqs. 4.69 and 4.75 by computing their ratio. Importantly, this local ratio of the material transport flux to maintain the gradient, versus that to build the gradient, is also exactly interpretable as the ratio of power densities accomplishing these processes at each point in spacetime. This follows since the volumetric power densities of both processes are each proportional to $\frac{\partial \mu}{\partial r}\Big|_{(r,t)}$ as specified by Eq. 4.44, namely,

$$\frac{\rho_r(r,t)}{\rho_D(r,t)} = \frac{|J_r(r,t)|\frac{\partial \mu}{\partial r}}{|J_D(r,t)|\frac{\partial \mu}{\partial r}} \tag{4.76}$$

$$= \frac{|J_r(r,t)|}{|J_D(r,t)|}. \tag{4.77}$$

Proceeding to compute this ratio of the net flux $J_r(r,t)$ to the maintenance diffusive flux $J_D(r,t)$ (and recalling $|J_r| = -J_r$, we see that

$$\mathrm{Pe}^\circ(r,t) \equiv \frac{|J_r(r,t)|}{J_D(r,t)} = \frac{-r\frac{\partial_t \lambda}{\lambda(t)}c(r,t)}{D\frac{1}{\lambda(t)}c(r,t)} \tag{4.78}$$

$$= \frac{r(-\partial_t \lambda)}{D}. \tag{4.79}$$

$$= \frac{r^2/D}{r/(-\partial_t \lambda)} = \frac{\text{diffusion time}}{\text{“advection” time}}. \tag{4.80}$$

$$\tag{4.81}$$

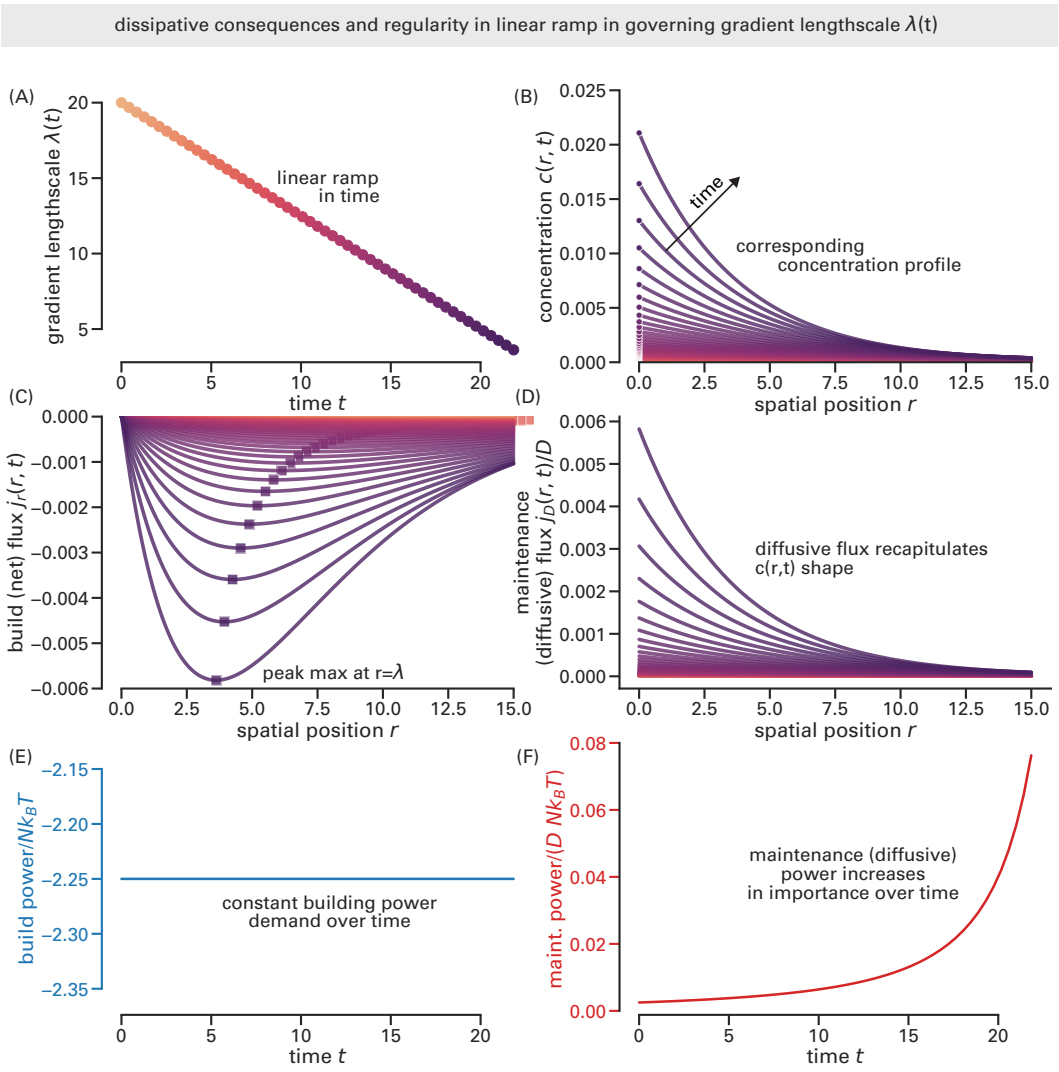

Figure 4.6: **Example of the dissipative behaviors of a steepening (number-preserving) exponential gradient in time, where the characteristic length scale $\lambda(t)$ decreases as a linear ramp in time, $\lambda(t) = \lambda_0 - \gamma t$.** (A) The illustrative linear ramp of the length scale in time, $\lambda(t) = 20 - 0.75t$, for arbitrary units of λ, t. (B) The corresponding concentration profile $c(r,t)$ over space and time (the latter indicated by distinct colors). (C) The resulting net material flux $J_r(r,t)$ required to build the gradient in this prescribed manner. Squares emphasize that the maximum flux occurs at the radial coordinate $r_* = \lambda(t)$. (D) The material flux J_D required to maintain the gradient at its current state. (E) The corresponding power $P_{\text{build}}(t)$ required to enact the steepening trajectory of the concentration gradient. This linear ramp shows a particularly simple (boring) form as $\partial_t \lambda$ is a constant for this example. (F) The maintenance (diffusive) power P_{maintain} increases with the gradient steepness, so also increases in time. (In all these traces, we measured concentration in units of the prefactor $N/8\pi$ and took the diffusion constant to be $D = 1$.)

Thus, under this model, we derive the profoundly surprising result that the relative importance of the net flux J_r needed to *build* the gradient, compared to the flux needed to *maintain* the gradient, depends *only* on whether $r\frac{\partial\lambda}{\partial t} \overset{?}{>} D$. **Interestingly, this ratio can be interpreted as a sort of local material "Péclet number" for each spatial coordinate r and (global) "advective velocity" $\partial_t\lambda$ that compete with diffusion D.** We denote this dimensionless value $\mathrm{Pe}^\circ(r,t)$, where the superscript recalls this is a material (and local) value. When this ratio is smaller than one, the diffusive flux dominates; when the ratio exceeds one, the building flux dominates.

Accordingly, in our exponential concentration gradient setting, for any nonequilibrium control scheme accomplishing a time-varying characteristic length scale $\lambda(t)$ (yielding some value of rate-of-change $\partial_t\lambda \neq 0$), there exists some radial position r past which the magnitude of the flux J_r needed to build the gradient will always exceed the magnitude of the flux J_D needed to just maintain the gradient.

Generality of the local form of this ratio being interpreted as a Péclet number. How special to the details of our chosen illustrative example $c(r,t)$ is the fact that we can precisely interpret the ratio of a net flux to a diffusive flux as some governing effective Péclet number? In fact, not special at all; *any* concentration profile or flux will admit such a description, as we now show. Dimensionally speaking, such a ratio is recognizable as,

$$\left[\frac{J_r}{J_D}\right] = \frac{\frac{1}{\text{area}} \times \frac{1}{\text{time}}}{D\frac{\text{concentration}}{\text{length}}} \tag{4.82}$$

$$= \frac{\frac{1}{\text{length}^2} \times \frac{1}{\text{time}}}{D\frac{1}{\text{length}}\frac{1}{\text{length}^3}} \tag{4.83}$$

$$= \frac{\text{length}^2 \times \frac{1}{\text{time}}}{D} \tag{4.84}$$

$$= \frac{\text{length} \times \frac{\text{length}}{\text{time}}}{D} \tag{4.85}$$

$$= \frac{\text{length} \times \text{velocity}}{D}, \tag{4.86}$$

which is exactly the form of a Péclet number.

Building and maintenance power densities are maximized at *distinct* parts of space

The radial dependence of the local Péclet number in Eq. 4.81 hints that the relative importance of building and maintenance can change over space. To understand this

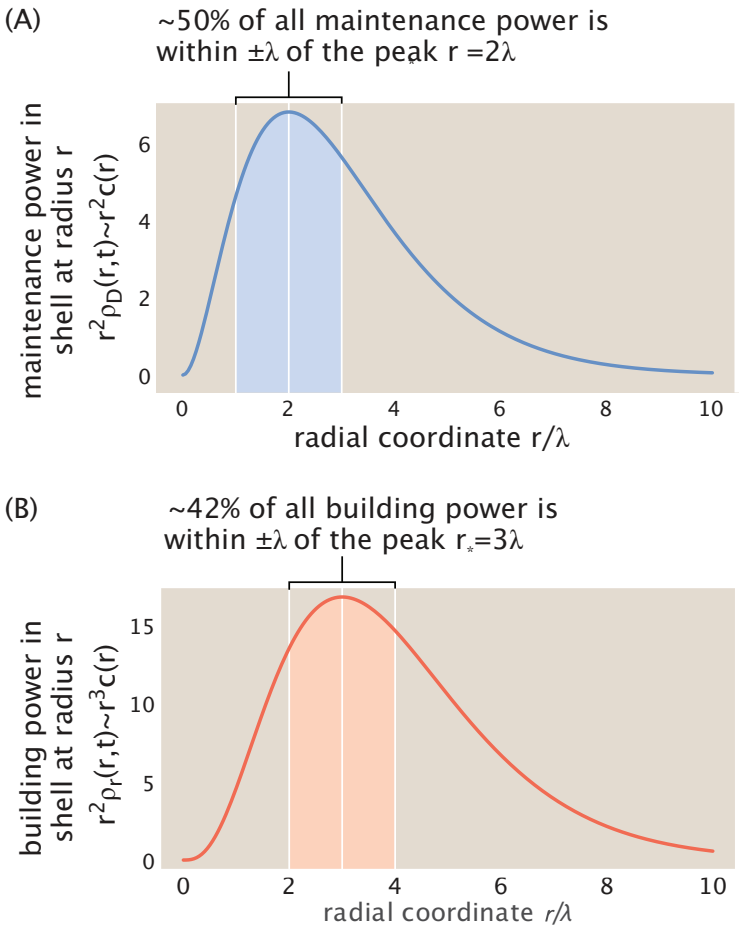

Figure 4.7: **Contrasting the locations in space where distinct dissipative mechanisms are expected to be maximal.** (A) The power attributable to a shell of radius r and unit thickness required just to maintain an exponential gradient, as specified by Eq. 4.93. This maintenance power has a spatial maximum at a radial position of $r = 2\lambda$; this localization reproduces the localization of substance in space: about half of all power over all space (from $r = 0$ to $r = \infty$) is found just within a shell within a decay length $\pm\lambda$ on either side of the dissipatively- maximal radius. (B) The power attributable to a shell of radius r and unit thickness required to further build a gradient, as specified by Eq. 4.99. This building power shows both shifted and more diffuse localization behavior than maintenance power; for instance, only $\sim 42\%$ of the total power is found within a shell at the distinct maximum of $r = 3\lambda$.

spatial dependence, we now explore further how the underlying power in a shell at a radial coordinate r varies in space quite distinctly for these two mechanisms. We preview these contrasting behaviors in Fig. 4.7.

The power attributable to a shell of radius r and thickness dr presenting a volumetric

power density $\rho(r,t)$ is

$$\text{power}(r,t) = \rho(r,t)\ 4\pi r^2\ dr. \tag{4.87}$$

Therefore, the factor $4\pi\rho(r,t)r^2$—a power per radial length increment—controls the spatial distribution of dissipation. Accordingly, we now consider the shape of this radial power density for both maintenance and building power. Substituting the fluxes captured by Eqs. 4.69 and 4.75 and chemical-potential variation (Eq. 4.105) appropriate for our exponential gradient gives the maintenance radial power density as,

$$\begin{aligned}
r^2\rho_D(r,t) &= r^2\left(|J_D(r,t)|\frac{\partial\mu}{\partial r}\right) && (4.88)\\
&= r^2\left(D\frac{1}{\lambda(t)}c(r,t)\right)\left(-k_BT\frac{1}{\lambda(t)}\right) && (4.89)\\
&= r^2c(r,t)\left(-\frac{D}{\lambda(t)^2}\ k_BT\right) && (4.90)\\
&= r^2\left(\frac{N}{8\pi}\frac{1}{\lambda(t)^3}\exp\left[-\frac{r}{\lambda(t)}\right]\right)\left(-\frac{D}{\lambda(t)^2}\ k_BT\right) && (4.91)\\
&= r^2\exp\left[-\frac{r}{\lambda(t)}\right]\left(-\frac{ND}{8\pi\lambda(t)^5}\ k_BT\right) && (4.92)\\
&\sim r^2\exp\left[-\frac{r}{\lambda(t)}\right]. && (4.93)
\end{aligned}$$

Similarly, the building radial power density is given as,

$$\begin{aligned}
r^2\rho_r(r,t) &= r^2\left(|J_r(r,t)|\frac{\partial\mu}{\partial r}\right) && (4.94)\\
&= r^2\left(r\frac{\partial_t\lambda}{\lambda(t)}c(r,t)\right)\left(-k_BT\frac{1}{\lambda(t)}\right) && (4.95)\\
&= r^3c(r,t)\left(-\frac{1}{\lambda(t)}\frac{\partial_t\lambda}{\lambda(t)}\ k_BT\right) && (4.96)\\
&= r^3\left(\frac{N}{8\pi}\frac{1}{\lambda(t)^3}\exp\left[-\frac{r}{\lambda(t)}\right]\right)\left(-\frac{1}{\lambda(t)}\frac{\partial_t\lambda}{\lambda(t)}\ k_BT\right) && (4.97)\\
&= r^3\exp\left[-\frac{r}{\lambda(t)}\right]\left(-\frac{N}{8\pi}\frac{\partial_t\lambda}{\lambda(t)^5}k_BT\right) && (4.98)\\
&\sim r^3\exp\left[-\frac{r}{\lambda(t)}\right]. && (4.99)
\end{aligned}$$

Since the exponentially-decreasing concentration $c(r,t)$ in space competes with the geometric prefactors of r^2 or r^3, respectively, in Eqs. 4.93 and 4.99, both of these

power densities have local maxima in space; these maxima occur when the power laws just start losing to the exponentially decreasing concentration field. However, notably, the spatial positions where these maxima occur are found at distinct radial optima. Specifically, the maximum of the radial maintenance power density occurs at $r_* = 2\lambda$, whereas the maximum of the radial building power density occurs at $r_* = 3\lambda$.

The majority of either type of power occurs within a moderately close vicinity of the respective maxima. To quantify just how much power is concentrated around these positions in space, we compute the fraction of this power found within a tolerance (radial distance) $\pm\delta$ of the maximum r_*, namely what we call the *localization fraction*,

$$f(\delta) \equiv \frac{\int_{r_*-\delta}^{r_*+\delta} dr\, r^2 \rho(r,t)}{\int_0^\infty dr\, r^2 \rho(r,t)}. \tag{4.100}$$

We find that the maintenance power density shows the localization fraction (about its maximum $r_* = 2\lambda$),

$$f_D(\delta) = \frac{\int_{r_*-\delta}^{r_*+\delta} dr\, r^2 \exp\left[-\frac{r}{\lambda(t)}\right]}{\int_0^\infty dr\, r^2 \exp\left[-\frac{r}{\lambda(t)}\right]} \tag{4.101}$$

$$= \frac{\frac{1}{e^2} 2\lambda \left(\left(\delta^2 + 10\lambda^2\right) \sinh\left[\frac{\delta}{\lambda}\right] - 6\delta\lambda \cosh\left[\frac{\delta}{\lambda}\right]\right)}{2\lambda^3}. \tag{4.102}$$

To get an intuitive sense of the scale at which this maintenance power is localized in space, we numerically evaluate this localization fraction with $\delta = \lambda$, which asks for the fraction of power in a shell of total radial thickness 2λ about its maximum $r_* = 2\lambda$. We find $f_D(\lambda) \approx 0.4965$, namely about $\approx 50\%$ of all the maintenance power over all space is localized to this radial region (of within a decay length on either side of the dissipatively-maximal radial position).

Next, we contrast this localization behavior to that of the building power, about its

distinct maximum $r_* = 3\lambda$. We see that,

$$f_r(\delta) = \frac{\displaystyle\int_{r_*-\delta}^{r_*+\delta} dr\, r^3 \exp\left[-\frac{r}{\lambda(t)}\right]}{\displaystyle\int_0^{\infty} dr\, r^2 \exp\left[-\frac{r}{\lambda(t)}\right]} \tag{4.103}$$

$$= \frac{\frac{1}{e^3} 2\lambda \left(6\lambda \left(2\delta^2 + 13\lambda^2\right) \sinh\left[\frac{\delta}{\lambda}\right] - \delta(\delta^2 + 51\lambda^2) \cosh\left[\frac{\delta}{\lambda}\right]\right)}{6\lambda^4}. \tag{4.104}$$

Again numerically evaluating the localization fraction with a tolerance given by the characteristic length scale, $\delta = \lambda$, we see that $f_r(\lambda) = 0.4237$: about $\approx 42\%$ of the power to build the gradient is localized in this region within a decay length in either direction around its distinct spatial maximum.

These power densities make clear a significant and interesting difference. The maintenance power density inherits its localization behavior identically from concentration. That is, the fraction of all dissipation found within a shell centered at the dissipatively-maximal radius is exactly the same as the fraction of all substance found within the same shell. (This fact, reflected by Eq. 4.89, follows since our model of an exponential concentration gradient shows that diffusive flux J_D is simply proportional to the concentration field $c(r,t)$ with no geometric prefactors and the gradient of chemical potential $\frac{\partial \mu}{\partial r}$ is constant in space.) That maintenance power density is in literal thrall to concentration is in substantial contrast to the distinct weighting of the building power, whose integrand enjoys an extra radial $\sim r^{+1}$ weight factor (as reflected by Eq. 4.95 and Eq. 4.69). Figure 4.7 summarizes and illustrates these contrasts in dissipative localization. Last, Figure 4.8 gives another high-level schematic overview of these spatial relationships.

Comparing building (net) and maintenance (diffusive) *powers*

For our specific exponential gradient, we observe the unusual fact that $\frac{\partial \mu}{\partial r}$ is independent of space r, namely,

$$\frac{\partial \mu}{\partial r} = k_B T \frac{\frac{\partial c}{\partial r}}{c(r,t)} = -k_B T \frac{1}{\lambda(t)}. \tag{4.105}$$

Armed with all the ingredients we need, we now compute each power term in turn as

$$P_{\text{build}}(t) = -4\pi \int dr\, r^2\, \frac{\partial \mu}{\partial r} \left(-\frac{1}{r^2} \int_{r=0}^{r} dr\, r^2 \frac{\partial c}{\partial t}\right) \quad \text{(by Eq. 4.51)}, \tag{4.106}$$

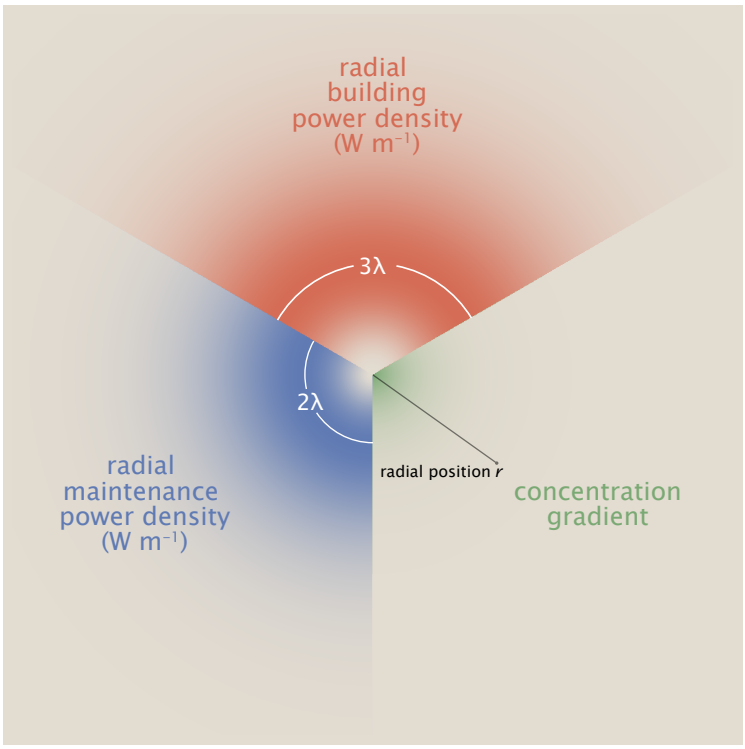

Figure 4.8: **Visualization of the distinct spatial localizations of maintenance power (blue, lower left); building power (red, top); and concentration (green, lower right).**

and

$$P_{\text{maintain}}(t) = 4\pi \int dr\, r^2 \, \frac{\partial \mu}{\partial r} \left(-D \frac{\partial c}{\partial r} \right) \quad \text{(by Fick)}. \tag{4.107}$$

Substituting this and the remaining ingredients in our particular exponential gradient

scenario, we see,

$$P_{\text{build}}(t) = -4\pi \frac{\partial \mu}{\partial r} \int_0^\infty dr\, r^2 \left(r \frac{\partial_t \lambda}{\lambda(t)} c(r,t) \right) \tag{4.108}$$

$$= -\frac{\partial \mu}{\partial r} \frac{\partial_t \lambda}{\lambda(t)} \int_0^\infty dr\, 4\pi r^2\, r c(r,t) \tag{4.109}$$

$$= -4\pi \frac{\partial \mu}{\partial r} \int dr\, r^2 \left(r \frac{\partial_t \lambda}{\lambda(t)} \frac{N}{8\pi} \frac{1}{\lambda(t)^3} \exp\left[-\frac{r}{\lambda(t)} \right] \right) \tag{4.110}$$

$$= -\frac{\partial \mu}{\partial r} \frac{4\pi}{8\pi} N \frac{\partial_t \lambda}{\lambda(t)} \frac{1}{\lambda(t)^3} \int_0^\infty dr\, r^3 \exp\left[-\frac{r}{\lambda(t)} \right], \quad \text{(Mathematica gives } \int_0^\infty dr\, r^3 e^{-r/\lambda} = 6\lambda^4\text{)}, \tag{4.111}$$

$$= -\frac{\partial \mu}{\partial r} \frac{N}{2} (\partial_t \lambda) \frac{1}{\lambda^4} 6\lambda^4. \tag{4.112}$$

$$= \frac{\partial \mu}{\partial r} 3N(-\partial_t \lambda). \tag{4.113}$$

$$= -3Nk_BT \frac{(-\partial_t \lambda)}{\lambda(t)} \tag{4.114}$$

$$= 3Nk_BT \frac{\partial \ln \lambda(t)/\lambda_0}{\partial t}. \tag{4.115}$$

(Here we could also just recall that for integer n, the value of $\int_0^\infty dr\ r^n e^{-r/\lambda}$ is $n!\lambda^{n+1}$.)

The maintenance power is

$$P_{\text{maintain}}(t) = \frac{\partial \mu}{\partial r} \int dr\, 4\pi\, r^2 \left(D \frac{1}{\lambda(t)} c(r,t) \right) \tag{4.116}$$

$$= \frac{\partial \mu}{\partial r} D \frac{1}{\lambda(t)} \underbrace{\int dr\, 4\pi\, r^2\, c(r,t)}_{=N, \text{ by Eq. 4.55.}} \tag{4.117}$$

$$= \frac{\partial \mu}{\partial r} D \frac{1}{\lambda(t)}. \tag{4.118}$$

$$= -Nk_BTD \frac{1}{\lambda(t)^2}. \tag{4.119}$$

Thus the ratios of these two powers is

$$\text{Pe}^{\lightning}(t) \equiv \frac{P_{\text{build}}(t)}{P_{\text{maintain}}(t)} = \frac{\frac{\partial \mu}{\partial r} 3N(-\partial_t \lambda)}{\frac{\partial \mu}{\partial r} D \frac{1}{\lambda(t)} N} \tag{4.120}$$

$$= \frac{3\lambda\ (-\partial_t \lambda)}{D}, \tag{4.121}$$

where we have denoted this ratio as $\text{Pe}^{\lightning}(t)$ to emphasize its nature as a dissipative (and spatially-global) Péclet number. Is this unitless? The numerator is length squared per second, consistent with the denominator, so yes.

(Interestingly, we see that taking a spatial coordinate of $r = 3\lambda$ in the local flux ratio of $\text{Pe}^{\circ}(r,t)$ in Eq. 4.81 makes that local flux ratio there equal to this total radially-integrated power ratio $\text{Pe}^{\lightning}(t)$ of Eq. 4.121.)

How does the relative importance of building versus maintenance powers change over time, as gradients steepen?

Our foregoing analysis was mathematically general, applying to any exponential gradient regardless of the trajectory of the characteristic length scale $\lambda(t)$. To proceed further, however, we must now specify some possible candidate time-evolutions $\lambda(t)$. How will the relative importance of maintenance versus building power be conserved or vary across diffrent $\lambda(t)$ profiles? Consider these three examples, which hint at the diversity of attainable behaviors.

Figure 4.6 illustrates characteristic behaviors of a concentration gradient steepening under a linearly-decreasing gradient length scale $\lambda(t)$ in time.

1. For a simple linear gradient in time, $\lambda(t) = \lambda_0 - \gamma t$ (for $t \leq \frac{\lambda_0}{\gamma}$), we see that $(\partial_t \lambda)\lambda(t) = -\gamma(\lambda_0 - \gamma t)$. This magnitude also decreases in time. In other words, the relative importance of building power to maintenance power must monotonically decrease over time. This is consistent with the fact that the building power is a constant (while maintenance power increases) in this case: see Eq. 4.114. See Figure 4.6.

2. For a power law shrinkage of the exponential gradient length scale in time, $\lambda(t) = Bt^{-\alpha}$ (with $\alpha \geq 0$ to assure that the gradient steepens), observe that

$$\partial_t \lambda = -B\alpha T^{-\alpha-1} = -\alpha \frac{\lambda(t)}{t}.$$

   Therefore, $(\partial_t \lambda)\lambda(t) = -\alpha \frac{\lambda(t)^2}{t}$, whose magnitude decreases with time t (since $\lambda(t)$ declines monotonically). In other words, the relative importance of building power to maintenance power must monotonically decrease over time.

3. For a more unusual (e.g. somewhat contrived) profile like $\lambda(t) = (1-t)^{\eta}$ for $\eta \in [0, 1/2]$, and $t < 1$, we appear to find a profile where—in contrast to the earlier examples—the magnitude of $(\partial_t \lambda)\lambda(t)$ increases in time, making the building power *increasingly* important relative to the maintenance power.

Comparing building (net) and maintenance (diffusive) *energies*

Under our model, during a time τ, the total energy spent on building is the time integral of Eq. 4.114,

$$E_{\text{build}}(\tau) = \int_{t=0}^{\tau} dt\ P_{\text{build}}(t) \tag{4.122}$$

$$= \int_{0}^{\tau} dt\ \frac{\partial \mu}{\partial r} 3N \partial_t \lambda \tag{4.123}$$

$$= 3N \int_{0}^{\tau} dt\ \left(-k_B T \frac{1}{\lambda(t)}\right) \partial_t \lambda \tag{4.124}$$

$$= -3N k_B T \int_{0}^{\tau} dt\ \frac{\partial_t \lambda}{\lambda(t)} \tag{4.125}$$

$$= -3N k_B T \int_{0}^{\tau} dt\ \frac{\partial \ln \lambda/\lambda_0}{\partial t} \tag{4.126}$$

$$= -3N k_B T \ln\left[\frac{\lambda(\tau)}{\lambda(0)}\right]. \tag{4.127}$$

Remarkably, this energy to build is *independent* of the precise timecourse $\lambda(t)$, only depending on the starting and ending length scale of the gradient!

We note with amusement that this expression Eq. 4.127 adopts precisely the same form (including numerical prefactors!) as the calculation for the work needed to contract a (microtubule) gas from an initial volume V_i and a final volume V_f in Eq. 3.146 specifying $W = -N k_B T \ln \frac{V_f}{V_i}$, if we take these volumes to be of order the characteristic length scale cubed, $V_i \sim \lambda(0)^3$ and $V_f \sim \lambda(\tau)^3$, where the cubic relation delivers our factor of three in Eq. 4.127.

In light of our discussion and estimates in this section: the fact that the order-of-magnitude estimate $\langle P_{\text{build}} \rangle = E_{\text{build}}/T = \frac{\int_0^T dt\ P_{\text{build}}(t)}{T}$ (for an observation/construction time T) is much smaller than instantaneous measured power values does *NOT* in fact say that building power is small compared to actual total power expenditures. This discrepancy says much more about the fact that *instantaneous* power values can differ a lot from the *average* of the same values, than that the *instantaneous* fundamental/theoretical building power is small compared to *instantaneous* measured total power values!

In contrast the energy to maintain is the time integral of Eq. 4.118, giving

$$E_{\text{maintain}}(\tau) = \int_{t=0}^{\tau} dt\ P_{\text{maintain}}(t) \tag{4.128}$$

$$= \int_{t=0}^{\tau} dt\ \frac{\partial \mu}{\partial r} D \frac{1}{\lambda(t)} N \tag{4.129}$$

$$= DN \int_{t=0}^{\tau} dt\ \left(-k_B T \frac{1}{\lambda(t)}\right) \frac{1}{\lambda(t)} \tag{4.130}$$

$$= -DNk_B T \int_{0}^{\tau} dt\ \frac{1}{\lambda(t)^2}. \tag{4.131}$$

Notice, as expected, that such a maintenance energy accumulates even when the length scale λ is *not* changing in time ($\partial_t \lambda \neq 0$)—and at any finite constant λ, E_{maintain} will grow with longer τ.

It is hard to bound this maintenance energy without stipulating a precise timecourse for $\lambda(t)$. But, to reach for a rough feel, say that we only know that $\lambda(t)$ decreases monotonically in time on the time interval of interest, such that $\lambda(t = \tau) \leq \lambda(t) \leq \lambda(t = 0)$. Then we can conclude the simple fact that,

$$\int_{0}^{\tau} dt\ \frac{1}{\lambda(0)^2} \leq \int_{0}^{\tau} dt\ \frac{1}{\lambda(t)^2} \leq \int_{0}^{\tau} dt\ \frac{1}{\lambda(\tau)^2} \tag{4.132}$$

$$\rightarrow \frac{\tau}{\lambda(0)^2} \leq \int_{0}^{\tau} dt\ \frac{1}{\lambda(t)^2} \leq \frac{\tau}{\lambda(\tau)^2}, \tag{4.133}$$

which means that

$$DNk_B T \frac{\tau}{\lambda(0)^2} \leq |E_{\text{maintain}}(\tau)| \leq DNk_B T \frac{\tau}{\lambda(\tau)^2}. \tag{4.134}$$

Accordingly, the ratio of these two energies is only constrained here to lie between,

$$\frac{3Nk_B T \ln\left[\frac{\lambda(\tau)}{\lambda(0)}\right]}{DNk_B T \frac{\tau}{\lambda(\tau)^2}} \leq \frac{|E_{\text{build}}(\tau)|}{|E_{\text{maintain}}(\tau)|} \leq \frac{3Nk_B T \ln\left[\frac{\lambda(\tau)}{\lambda(0)}\right]}{DNk_B T \frac{\tau}{\lambda(0)^2}} \tag{4.135}$$

$$\rightarrow \frac{3}{D} \frac{\ln\left[\frac{\lambda(\tau)}{\lambda(0)}\right]}{\frac{\tau}{\lambda(\tau)^2}} \leq \frac{|E_{\text{build}}(\tau)|}{|E_{\text{maintain}}(\tau)|} \leq \frac{3}{D} \frac{\ln\left[\frac{\lambda(\tau)}{\lambda(0)}\right]}{\frac{\tau}{\lambda(0)^2}}. \tag{4.136}$$

Empirical estimates for an example aster's motor gradients

We now consider how well the theoretical insights described above jibe with our experimental measurements. It appears that the major obvious trends—e.g., that the relative importance of building and maintenance powers can switch dramatically in time across trajectories—will be widely preserved across aster phenomenology.

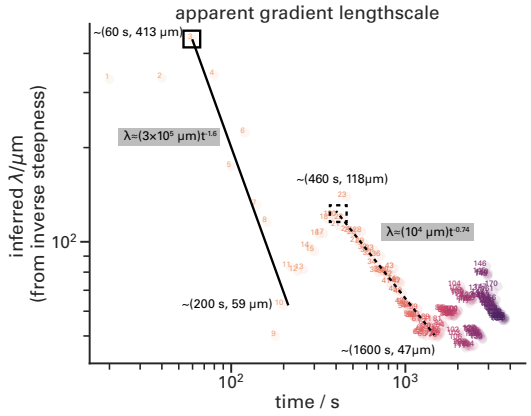

Figure 4.9: **Temporal changes in apparent length scale of motor gradients of the data in Figure 4.5.** At left, highlighted by a solid black line as a guide to the eye, an early-time steepening in the motors gives a steep approximate power law $\hat{\lambda} \approx (3 \times 10^6\ \mu\text{m})(t/1s)^{-1.6}$. The solid black square indicates a reference point $(t, \hat{\lambda}(t)) \approx (60\ s, 413\ \mu m)$ with an approximate rate-of-change of $\partial_t \hat{\lambda} \approx -11\ \mu m/s$ taken from the slope of the line. At right, a slower but still appreciable steepening resumes, marked by the dashed black line, with an approximate power law fit of $\hat{\lambda} \approx (10^4\ \mu m)(t/1s)^{-0.74}$. The dashed black square indicates a reference point at $(t, \hat{\lambda}) \approx (460\ s, 118\ \mu m)$ with an approximate rate of change of $-0.2\ \mu m/s$ taken from the slope of the dashed line.

To get a very rough sense of scale for how motor gradients actually change their characteristic length scales $\lambda(t)$ in time, we considered the same motor distributions shown earlier in the data of Figure 4.5. At each time, we found the radial position r_s at which the motor distribution was steepest in space. Then, assuming (coarsely, but not unreasonably) that these gradients were indeed locally exponentially decaying at this steepest point, we computed the approximate effective exponential gradient length scale as $\hat{\lambda}(t) = -\frac{c(r_s,t)}{\frac{\partial c}{\partial r}}$. Figure 4.9 depicts how this aster changes its apparent length scale.

Next, we—just by eye, not rigorously—extracted an apparent power law fit to each of two distinct dynamical regimes visible in the length scale's trajectory. This allows us to substitute empirically estimated values into the dissipative Péclet number of Eq. 4.121. The first regime, marked by the solid black square in Figure 4.9, implies that the building power $P_{\text{build}}(t)$ exceeds the maintenance power P_{maintain} by approximately a multiplicative factor of order,

$$\frac{P_{\text{build}}(t)}{P_{\text{maintain}}(t)} = \frac{3\lambda\ (-\partial_t \lambda)}{D} \tag{4.137}$$

$$\approx \frac{3(413\ \mu m)(-(-11\ \mu m/s))}{40\ \mu m^2/s} \tag{4.138}$$

$$\approx 340\times . \tag{4.139}$$

The second, more slowly-steepening, regime appears to register a more equal balance between building power and maintenance power, giving about

$$\frac{P_{\text{build}}(t)}{P_{\text{maintain}}(t)} = \frac{3\lambda\ (-\partial_t \lambda)}{D} \tag{4.140}$$

$$\approx \frac{3(118\ \mu m)(-(-0.2\ \mu m/s))}{40\ \mu m^2/s} \tag{4.141}$$

$$\approx 1.8\times . \tag{4.142}$$

These estimates, however coarse, argue quantitatively that **maintenance power could be dwarfed by building power to the tune of order a few hundred in the early times of an aster formation**, but show that the maintenance cost grows much more competitive at late times. □

References

[1] A. H. Stouthamer. "Theoretical study on amount of ATP required for synthesis of microbial cell material." In: *Antonie Van Leeuwenhoek Journal of Microbiology* 39.3 (1973), pp. 545–565.

[2] Ian S. Farmer and Colin W. Jones. "The energetics of Escherichia coli during aerobic growth in continuous culture." In: *European Journal of Biochemistry* 67.1 (1976), pp. 115–122.

[3] Matteo Mori et al. "Functional decomposition of metabolism allows a system-level quantification of fluxes and protein allocation towards specific metabolic functions." In: *Nature Communications* 14.1 (2023), p. 4161.

[4] Ana P. Alonso et al. "Carbon conversion efficiency and central metabolic fluxes in developing sunflower (Helianthus annuus L.) embryos." In: *The Plant Journal* 52.2 (2007), pp. 296–308.

[5] Michael J. Buono and Fred W. Kolkhorst. *Estimating ATP resynthesis during a marathon run: A method to introduce metabolism*. 2001.

[6] John J. Hopfield. "Kinetic proofreading: A new mechanism for reducing errors in biosynthetic processes requiring high specificity." In: *Proceedings of the National Academy of Sciences of the United States of America* 71.10 (1974), pp. 4135–9.

[7] T. L. Hill and Marc W. Kirschner. “Bioenergetics and kinetics of microtubule and actin filament assembly-disassembly.” In: *Int Rev Cytol* 78 (1982), pp. 1–125.

[8] Tim J. Mitchison and Marc W. Kirschner. “Properties of the Kinetochore In vitro. II. Microtubule Capture and ATP-Dependent Translocation.” In: *Journal of Cell Biology* 101.3 (1985), pp. 766–777.

[9] Javier Estrada et al. “Information integration and energy expenditure in gene regulation.” In: *Cell* 166.1 (2016), pp. 234–244.

[10] Sara D. Mahdavi et al. “Flexibility and sensitivity in gene regulation out of equilibrium.” In: *Proceedings of the National Academy of Sciences* 121.46 (2024), e2411395121.

[11] Christopher C. Govern and Pieter Rein ten Wolde. “Energy dissipation and noise correlations in biochemical sensing.” In: *Physical Review Letters* 113.25 (2014), p. 258102.

[12] Francis Crick. “Diffusion in embryogenesis.” In: *Nature* 225.5231 (1970), pp. 420–422.

[13] Mary Munro and Francis H. Crick. “The time needed to set up a gradient: Detailed calculations.” In: *Symposia of the Society for Experimental Biology*. Vol. 25. 1971, pp. 439–453.

[14] Florian M. Gartner and Erwin Frey. “Design principles for fast and efficient self-assembly processes.” In: *Physical Review X* 14.2 (2024), p. 021004.

[15] Massimiliano Esposito and Christian Van den Broeck. “Second law and Landauer principle far from equilibrium.” In: *Europhysics Letters* 95.4 (2011), p. 40004.

[16] Hong Qian. “Relative entropy: Free energy associated with equilibrium fluctuations and nonequilibrium deviations.” In: *Physical Review E* 63.4 (2001), p. 042103.

Chapter 5

MOTOR-DRIVEN MICROTUBULE DIFFUSION IN A PHOTOBLEACHED DYNAMICAL COORDINATE SYSTEM

In this collaborative project led by Soichi Hirokawa, I analyzed data and provided reagents. Specifically, I developed an image processing pipeline allowing me to analyze the speed of motor proteins based on microtubule gliding data. Additionally, I purified proteins and prepared buffers used in these experiments. This study is published and can be found with the following citation:

Soichi Hirokawa, Heun Jin Lee, Rachel A. Banks, Ana Isabel Duarte, Bibi Najma, Matt Thomson, and Rob Phillips. "Motor-driven microtubule diffusion in a photobleached dynamical coordinate system." In: *Proceedings of the National Academy of Sciences* 122.24 (2025), e2417020122. doi: 10.1073/pnas. 2417020122

Significance Statement: Individuals of active matter systems work together to generate large scale, ordered structures. However, the detailed dynamics occurring in the network bulk during this organization process are largely unknown. By photobleaching an actively contracting microtubule network, we show that filaments exhibit a local diffusion-like reorganization amid a global contraction at uniform rate, both of which can be tuned by the effective motor speed. Tuning these parameters alters the active contraction rates and effective diffusion constants, but maintains a conserved proportionality between the two. We thus find that motors play a dual role in the global contraction and local diffusive-like spread of the network.

5.1 Abstract

A hallmark feature of active matter systems is the ability of individual elements to interact and organize over length scales exceeding that of the constituent molecular players. However, the nature of internal redistribution that occurs in the bulk of the collective is less clear. Using light-dimerizable kinesin motors to spatially control the formation and contraction of a microtubule network, we deliberately photobleach a grid pattern onto the filament network serving as a transient and dynamic coordinate system to observe the deformation and translation of the remaining fluorescent squares of microtubules. We find that the network contracts at a rate set by

motor speed but is accompanied by a diffusive-like spread throughout the bulk of the contracting network with effective diffusion constant two orders of magnitude lower than that for freely-diffusing microtubules. We further find that on micron scales, the diffusive timescale is only a factor of ≈ 3 slower than that of advection regardless of conditions, showing that the global contraction and long-time relaxation from this diffusive behavior are both motor-driven but exhibit local competition within the network bulk.

Whether for schools of fish evading a sea lion or in the ordered array of microtubules comprising the spindle of dividing cells, coordinated movement and emergent patterning is a hallmark of biological dynamics across all biological scales. Curiosity surrounding the underlying principles dictating such a ubiquitous feature in biology have led to an explosion of theoretical [1, 2, 3, 4] and experimental efforts [5, 6, 7, 8, 9] to understand them. *In vitro* active matter systems offer a powerful means to study how cytoskeletal elements self-organize to generate a diverse array of networked structures. By mixing multimerized motors with filaments, a broad range of ordered patterns have been demonstrated, occurring in solutions which are spatially-homogeneous [5, 10, 9] or are locally defined through patterned light [11, 12, 13, 14]. A common observation from these assays is that the constitutive filaments rearrange in time under dynamics that appear to be primarily advective in nature. Recent efforts have led to several quantitative models that macroscopically describe the flow-like redistribution of microtubules under a range of conditions related to properties of the motors and filaments [15, 16, 17, 18, 19]. In addition to advective behavior, previous theoretical studies of contractile active gels have also shown that local fluctuations within a globally contracting network can give rise to a motor-driven diffusive-like effect among filaments [20, 21], a phenomenon that has been observed experimentally [22]. This seeming competition between active diffusion and advection invites a rigorous approach to distinguish these two effects.

In the work presented here, we incorporate fluorescence recovery after photobleaching (FRAP) into a light-controllable kinesin motor dimerization system [12, 23, 24] to characterize the interplay of motor-driven advective and diffusive dynamics. FRAP studies have typically been accompanied by various theory-based extensions of the diffusion equation to account for convective flow, reaction of molecules, or transport [25, 16, 26, 27, 28] and have been effectively applied to active *in vitro* systems to determine how filaments are redistributing into or elastically contracting

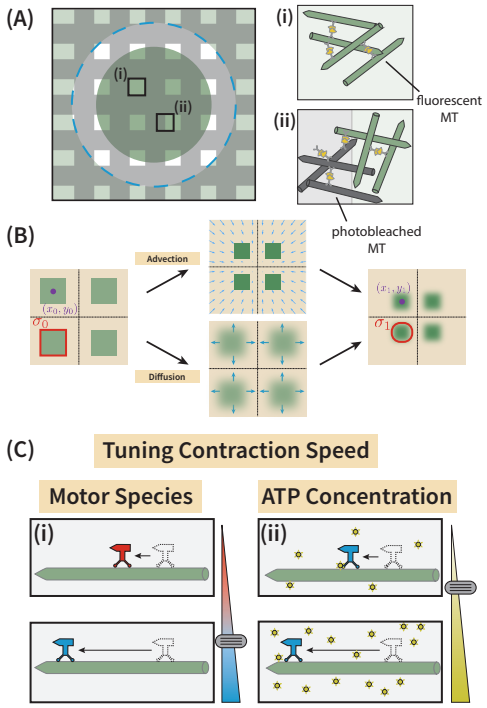

Figure 5.1: **FRAP-based approaches to studying advective and diffusive redistribution of cytoskeletal elements.** (A) Photobleaching a grid-like pattern leaves (i) squares of fluorescent microtubules (green) surrounded by (ii) non-fluorescent filaments (black) and allows us to examine the role of diffusive-like microtubule spread in the bulk of a global radially contracting network. Dashed blue circle outlines the edge of the dimerizing light inside of which the filaments couple and create a net contraction. (B) Tracking of centroids $[(x_0, y_0)$ to $(x_1, y_1)]$ and areas (σ_0 to σ_1) of the fluorescent squares allows us to quantify the advective and diffusive contributions in the contracting system. (C) The rates of these dynamics can be tuned by changing the effective motor speed through either (i) changes in the motor species or (ii) changes to the ATP concentration in the system. We tune these parameters to examine rates of contraction and bulk reorganization of microtubules in the contracting cytoskeletal network.

relative to the photobleached region [21, 29, 30, 31]. For our study, we photobleach a grid pattern onto a contracting microtubule network, which creates square fluorescent regions (Fig. 5.1(A)). By tracking the area and centroids of these regions, we are able to account for the advective contraction of the network. By measuring how the darkened photobleached lines blur, we can account for how much the microtubules in the network undergo diffusive behavior (Fig. 5.1(B)).

We find the choice of motor species [32] or the availability of ATP [33] are key parameters controlling the network dynamics (Fig. 5.1(C)). For example, by reduc-

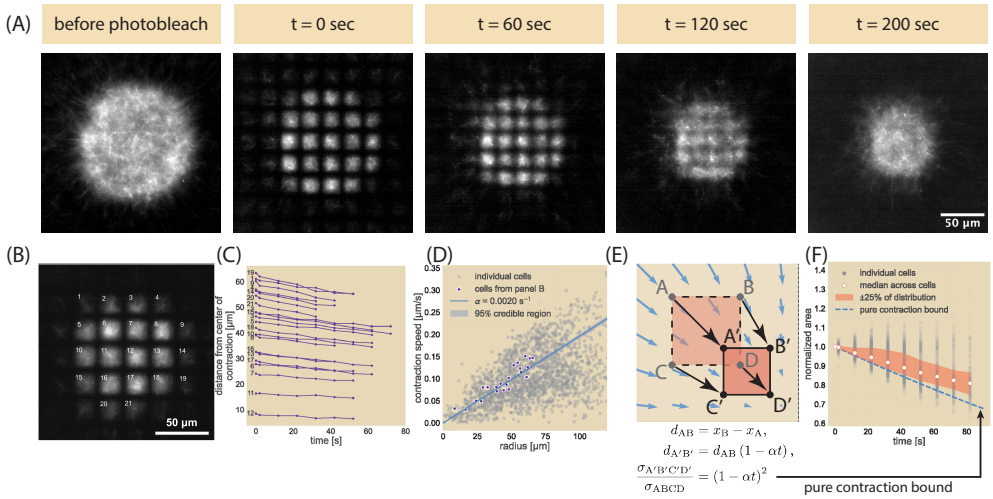

Figure 5.2: **Photobleaching a grid pattern onto the contracting microtubule network.** (A) Example dataset, where the microtubule field is photobleached and the deformations of the fluorescent regions observed using Ncd236 and 1.4 mM ATP. (B) Enumeration of individual fluorescent unit cells to (C) compute the distance of their centroids from the center of the network over time. Numbers correspond to labels from panel (B). (D) Plot of unit cell contraction speed as a function of their average distances from the center of the network, obtained by fitting the distance vs time data found in (C) to individual lines. The median contraction rate is $\alpha = 2.0 \times 10^{-3}$ s^{-1}. (E) Schematic of the unit cell deformation and expected area change under pure contraction. (F) The area of each unit cell is normalized against their initial area as obtained by the unit cell segmentation scheme and plotted as a function of time. The median normalized area is plotted in white among individual unit cells (gray). The red shaded region encompass points between the first and third quartiles of the distribution of all cells. Dashed blue line corresponds with the normalized area computed in (E) and using the median contraction rate obtained in (D).

ing motor speed, whether through decreased ATP concentration or slower motor species, the network globally contracts at a slower rate while the bulk of the network exhibits a decrease in effective diffusion constant. We further show that contraction rate and effective diffusion constant are linearly proportional measures across all of our conditions and give rise to a tightly bounded Peclét number slightly greater than one over micron length scales. While motors were understood to set the global contraction of the network, they play a second competing role within the network boundary that gives rise to a long-time relaxation on the local cytoskeletal structure.

5.2 Results

Photobleaching a grid pattern

To study the local redistribution of microtubules as the network contracts, we designed an augmented optical system that induces dimerization of kinesin through the iLid-micro system [34] in a circular region of radius 125 μm and images the microtubules [12, 24]. This modification includes a photobleaching element that allows us to photobleach a grid-like pattern into the microtubule channel at any point during contraction process (see Materials & Methods section and SI Sec S1.6). The end result is an array of squares roughly 12 μm in side length and 25 μm in center-to-center distance, much longer than the median microtubule length of $\approx$ 1.5 μm (see SI Sec S2). Fig. 5.2(A) shows an example of a grid pattern photobleached onto a microtubule network at different time points in its life history and the subsequent deformations of the bleached lines and fluorescent squares. As the image for the t = 0 sec timepoint in Fig. 5.2(A) shows, upon photobleaching the grid pattern, individual fluorescent squares, which we will call unit cells, are produced. Over a minute after photobleaching, unit cells contract toward the center of the network while the photobleached lines appear to blur away. By two minutes after photobleaching, neighboring unit cells appear to blend into each other and at later times any remnants of the photobleached pattern disappear.

Tracking fluorescent squares shows global contraction and local diffusive spread

To better quantify and understand the global network contraction dynamics, we segmented individual unit cells and measured their centroids and areas over successive frames (see SI Sec S3 and S4 for analysis). By tracking individual unit cells such as those shown in Fig. 5.2(B) and computing their distance from the center of the network over successive frames (Fig. 5.2(C)), we can determine the local contraction speeds, where we see a rough linear correspondence between distance and time. This was performed over many replicates and at different times in the contraction process (see SI Sec S5 for examples), all while maintaining the same initial size of the activation region (125 μm). We computed the slopes of each unit cell trajectory and compared the resultant speeds as a function of their distance from the network center (Fig. 5.2(D)) to find that the median contraction speed linearly increases with distance from the center, indicating a general uniform contraction rate of the entire microtubule network. We thus fit the velocity against the radius $\mathbf{r}$ with a line passing

through the origin (see SI Sec S6.1), giving the expression

$$\mathbf{v}(\mathbf{r}) = -\alpha \mathbf{r}, \tag{5.1}$$

where α is the contraction rate and thus measure a contraction rate and 95% credible region of $\alpha = 2.0 \times 10^{-3} \pm 5 \times 10^{-5}$ s^{-1}. Data separated by experimental replicates are available in SI Sec S7.

Despite the linear global contraction observed for the centroids, a more careful examination of the unit cells reveals that the network does not simply undergo purely elastic contraction. Suppose we took two points with different x-positions but the same y-position (x_A, y_A) and (x_B, y_A), respectively, such as points A and B in Fig. 5.2(E) that they have a distance d_0 of

$$d_0 = x_B - x_A, \tag{5.2}$$

where we will take $x_B > x_A$. If the two points were strictly subject to move from the velocity field given by Eq. 5.1, after time t their positions will have changed such that their distance d_1 is now

$$d_1 = \sqrt{[(x_B - \alpha x_B t - x_A + \alpha x_A t)]^2 + (y_A - \alpha y_A t - y_A + \alpha y_A t)^2}, \tag{5.3}$$

$$= (x_B - x_A)\,(1 - \alpha t)\,, \tag{5.4}$$

$$= d_0\,(1 - \alpha t)\,. \tag{5.5}$$

So the two points move closer by a factor of $1 - \alpha t$ in that time. We can make a similar argument for two points vertically separated. If we imagine this for all four points that make up the corners of a unit cell (points ABDC transforming to A'B'D'C' in Fig. 5.2(E)) and look at the change in area, we would expect that under a purely contractile active system subject to the uniform contraction rate measured from tracking the unit cell centroids, the area $A(t)$ would change from its initial size A_0 by

$$A(t) = A_0\,(1 - \alpha t)^2\,. \tag{5.6}$$

See SI Sec S8 for a more complete derivation. Fig. 5.2(F) shows the normalized area of each unit cell as a function of time in gray against this pure contraction scaling given as a blue dashed line. The median normalized area is shown as a white circle with a red outline. As can be seen by comparison with the shaded red region (representing the 50 percent of all cells that fall between the first and third quartiles of the distribution of cell areas), the majority of the experimental observations

are above the pure contraction bound. With the area being greater than that for a purely contracting network, we conclude that despite the global contraction of the network, filaments can locally spread and reorganize in the bulk. This observation is further affirmed by the merging of originally distinct fluorescent squares in the 120-second time point of Fig. 5.2(A), where a purely contractile network would cause fluorescent squares to remain distinct.

The effective diffusion constant is roughly two orders of magnitude lower than free diffusion of a microtubule

Since a purely contractile description is insufficient to fully capture the observed dynamics, we generalize our treatment of this contractile effect while accounting for diffusion by using an advection-diffusion equation to model the time evolution of the tubulin concentration $c(\mathbf{r}, t)$. Such a model has a material flux $\mathbf{J}$ of the form

$$\mathbf{J} = -D\nabla c + \mathbf{v}(\mathbf{r})\, c, \tag{5.7}$$

where D is the effective diffusion constant and $\mathbf{v}(\mathbf{r})$ is the velocity profile of the advective flow as a function of distance from the center of contraction r. As motivated by results shown in Fig. 5.2, we use the velocity field given by Eq. 5.1 with α as the computed contraction rate as shown in Fig. 5.2(D). When inserted into Eq. 5.7 and combined with the continuity equation, the advection-diffusion equation takes the form

$$\frac{\partial c}{\partial t} = -\nabla \cdot \mathbf{J}, \tag{5.8}$$

$$\frac{\partial c}{\partial t} = D\nabla^2 c + \nabla \cdot (\alpha \mathbf{r} c)\,. \tag{5.9}$$

We perform a series of careful explorations of the model in SI Sec S9-S11 to better understand the time-evolution of the concentration profile subject to Eq. 5.9 and to validate the implementation of our finite element method (FEM) using COMSOL Multiphysics®. Ultimately, these exercises confirm the importance of using a grid-like photobleaching pattern rather than a circular pattern, the latter of which would have convoluted the contributions of the radially-directed contraction with the more-isotropic diffusive-like spread. After validating our initial simulation, we turn to the use of FEM simulations on Eq. 5.9 to model our experimental results. We perform an FEM simulation of an individual unit cell, where we fix the FEM contraction rate to the experimentally-measured mean rate and sweep across various diffusion constants (see SI Sec S12 for implementation of a single unit cell in

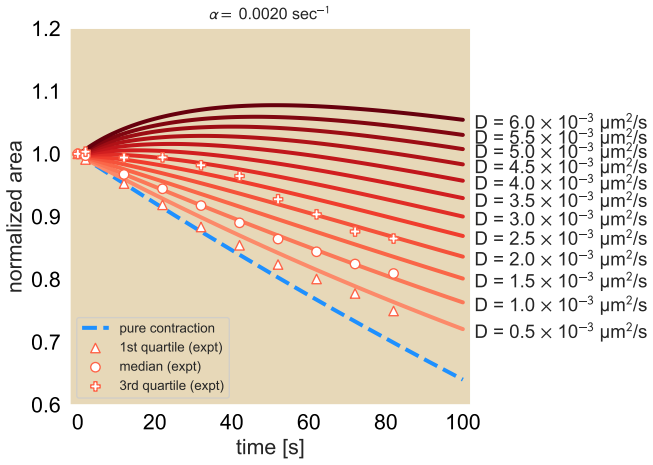

Figure 5.3: **Simulated concentration profiles for a linear advection-diffusion equation.** A family of curves for the expected normalized area of fluorescent squares subject to a fixed advection rate $\alpha = 2\times10^{-3}$ s^{-1} and varying diffusion constants. The 25th percentile (triangle), median (circle), and 75th percentile (plus sign) of the experimental area trajectories are overlaid onto the FEM results for comparison.

COMSOL). For example, for the Ncd236 motor at saturated levels of ATP, we show in Fig. 5.3 the family of normalized area trajectories for a single unit cell subject to the experimentally observed mean contraction rate of $\alpha = 2\times10^{-3}$ s^{-1}, and for diffusion constants D ranging from 5×10^{-4} to 6×10^{-3} $\frac{\mu m^2}{s}$. For comparison to the experimental data, we overlay the median (circle), the 1st quartile (triangle), and 3rd quartile (plus symbol) from the distribution of measured unit cell areas trajectories, where the quartiles give a sense of the trajectory variation. Here, we see that by minimizing least squares between the experiments and the simulation conditions, the median normalized area trajectory agrees best with the FEM trajectory with an effective diffusion constant of 1.0×10^{-3} $\frac{\mu m^2}{s}$. The first quartile of area trajectories from measurements lies between the pure contraction limit where $D_{\text{eff}} = 0$ and an effective diffusion constant $D_{\text{eff}} = 5.0 \times 10^{-4}$ $\frac{\mu m^2}{s}$. We interpret the first quartile results to mean the effective diffusion coefficient must be above 5.0×10^{-4} $\frac{\mu m^2}{s}$ in order to capture the majority of the data. The third quartile of area trajectories most closely follows the trajectory with an effective diffusion constant of $\approx 2.0 \times 10^{-3}$ $\frac{\mu m^2}{s}$ (see SI Sec S4.2 on fitting procedure), serving as a kind of upper bound. For context, the diffusion coefficients associated with the median and quartiles are all about two orders of magnitude smaller than the diffusion coefficient of a freely diffusing microtubule, which is ≈ 0.1 $\frac{\mu m^2}{s}$ (see SI Sec S2 for microtubule length;

equation for the longitudinal diffusion constant obtained from Ref [12]).

We also explored how well our FEM simulations could capture the qualitative features of the data set shown in Fig. 5.2(A), such as the merging of unit cells and the time scale of this process (see SI Sec S13). Our main finding from these efforts is, even for just qualitative comparisons, diffusion must be included in the theoretical description of the dynamics.

Changing effective motor speed proportionally changes contraction rate and effective diffusion constant

To test whether motors play a role in the diffusive-like effect, we next tuned the effective speed of the active elements, namely, the motors themselves. Two ways in which this can be done is by the choice of motor species or by changing the concentration of ATP. We chose optogenetic versions of previously characterized motor variants that span roughly an order of magnitude in speeds: Ncd236, Ncd281 [35], K401 expressed in bacteria [12], and K401 expressed in Sf9 cells [24] (See SI Sec S15 for Ncd281 construct designs and motor speeds and processivities). Fig. 5.4(A) shows the motors speeds for each of these motor types and the associated contraction rate. Interestingly, we observe a roughly linear relationship between contraction rate and motor speeds (see SI Sec S16.2). The effective diffusion coefficient also demonstrate a roughly linear trend (Fig. 5.4(B)). We note that even for the slowest motor Ncd281, a non-zero coefficient D_{eff} of 3×10^{-4} $\frac{\mu m^2}{s}$ is needed to recapitulate its corresponding unit cell area trajectories. This general tendency to increase the effective diffusion constant suggests that the motor speed may be responsible for the local microtubule effective diffusion.

We next examine how this local diffusive-like effect changes when we decrease the motor speed of a given species by reducing ATP concentrations. In order to traverse along microtubules, motors must hydrolyze ATP with each step they take. At saturated concentrations of ATP, motors can hydrolyze ATP at their maximal rate and therefore move at their maximum speed. At reduced ATP concentrations, the limited availability of ATP causes motors to hydrolyze ATP at a reduced rate, leading to an effective reduction in motor speed [36, 37, 38]. In the context of a contracting microtubule network, we hypothesize that this decrease in motor speed translates to a reduction in contraction rate, similar to the effect observed when using a slower motor species. We further hypothesize that for a constant motor concentration, reducing the concentration of ATP will increase the fraction of motors that do not

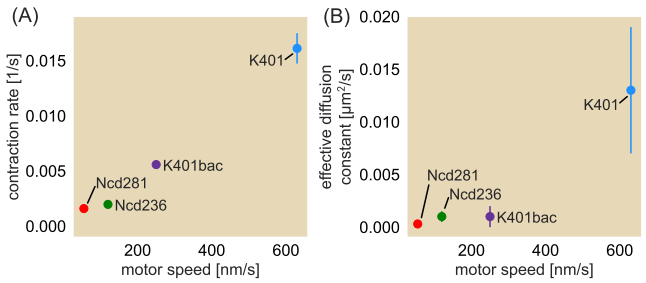

Figure 5.4: **Contraction rates and effective diffusion constants for four different motor types.** (A) Contraction rate as a function of motor speed. Here, the motors are (in order of motor speed as found in Table S2 of the SI Text) Ncd281 (red) [35], Ncd236 (green), K401 expressed in bacteria (purple), and K401 expressed in Sf9 cells (blue) [24]. (B) Corresponding effective diffusion constants as a function of motor speed where the circles denote the medians of the experimentally obtained normalized area trajectories and error bars denote the middle 50% of the distribution. Error bars for some data points are smaller than the radius for the size of the dots.

move along the microtubules and instead behave as passive crosslinkers, causing the areas of the fluorescent unit cells to fall closer to the pure contraction bound. To test this, we perform our photobleach experiment for Ncd236 and bacteria-expressed K401 at ATP concentrations spanning two orders of magnitude. We continue to use an ATP regeneration system so that the ADP concentration is negligible and therefore does not compete with ATP for the hydrolysis site [38] (see Materials and Methods). Fig. 5.5(A) and (C) show that for both Ncd236 (A) and K401 (C), as the concentration of ATP is decreased, the contraction rate of the network similarly decreases. At 25 μM ATP, the contraction rate with Ncd is roughly half of that at saturated levels. This concentration is also roughly the measured Michaelis constant of ATP hydrolysis by the motor [39]. However, at ATP concentrations below this Michaelis constant, we see that the network contraction, while still occurring for an ATP concentration of half the Michaelis constant for Ncd236, dramatically slows down. We fit the contraction rate against ATP concentration to the best fit of a Michelis-Menten equation to find that the expected Michaelis constant for ATP hydrolysis in the contracting network context (Ncd236: 30 ± 13 μM; bacterial-expressed K401: 47 ± 13 μM) is roughly the same as for measured motor speeds (Ncd236: ≈ 23 μM [39]; bacterial-expressed K401: 28.1 ± 0.9 μM [38]).

Decreasing the ATP concentration overall reduces the effective diffusion constant for Ncd236 (Fig. 5.5(B)). As the network dynamics scale with ATP concentration in a similar way to single-motor kinetics, our results show that motors are drivers of not

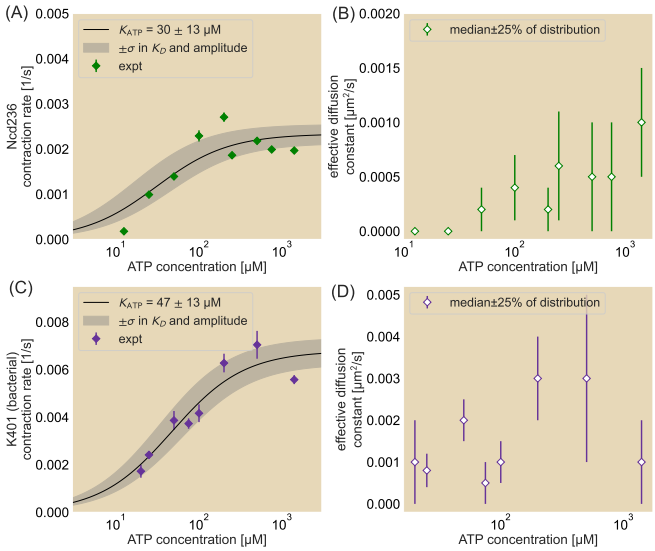

Figure 5.5: **Contraction rates and effective diffusion constants over a range of ATP concentrations.** Contraction rates (A and C) and effective diffusion constants (B and D) as a function of ATP concentration in the system. Motors used are Ncd236 (A and B) and K401 expressed in bacteria (C and D). Black line represents best fit to a Michaelis-Menten equation. Edges of the gray shaded region bounded to the left (right) using the Michaelis-Menten equation where the amplitude is the best fit plus (minus) one standard deviation and the Michaelis constant is the best fit minus (plus) one standard deviation. Effective diffusion constants fitted to the median area trajectories with error bars corresponding to fits spanning the middle 50% of the distribution motor types are presented.

only the contraction rate but also the local diffusion-like relaxation of the network. On the other hand, such a trend is less clear for bacteria-expressed K401 at some ATP concentrations (Fig. 5.5(D)). One possible explanation for the unclear trend is low motor processivity. If we consider the time a motor spends on a filament, we have $\langle \tau_{\text{on}} \rangle = k_{\text{off}}^{-1} = \frac{l \times p}{v_{\text{motor}}}$ for l the step size (8 nm), p the processivity, or the number of steps the motor takes before falling off, and v_{motor} the motor speed; in other words, the time that a microtubule is connected to the rest of the network is proportional to the processivity. This could mean that for motors of low processivity, there may be some mixing of passive diffusion and this active diffusion observed thus far. It is unclear to what extent the processivity of bacterial-expressed K401 differs from that of its Sf9-expressed variant and invites future examination to better understand the role of processivity on this diffusive-like effect. On the other hand, while Ncd236 is a non-processive motor, we suspect that cooperativity helps rescue a processive effect. It has been shown that cooperativity through multiple Ncds on

the same filament can recover a processivity similar to that of K401 [40], allowing Ncd236 to follow a general increase in effective diffusion with ATP concentration. However, the processivity of the bacterial-expressed K401 may differ from that of the highly-processive insect-expressed K401, which may play an additional role in the diffusive-like filament reorganization and making the relation between effective diffusion and ATP concentration less clear. This invites further exploration to resolve the underlying discrepancies.

Contraction rate and effective diffusion constant are unified in the Péclet number

From tuning the motor type and ATP concentration in our *in vitro* kinesin-microtubule system and measuring the resultant contraction and diffusion rates, we see when parameters increase the contraction rate of the network they also similarly increase the effective diffusion constant. This suggests a relationship between the advective and diffusive properties.

To characterize this, we make use of the Péclet number, a non-dimensional ratio

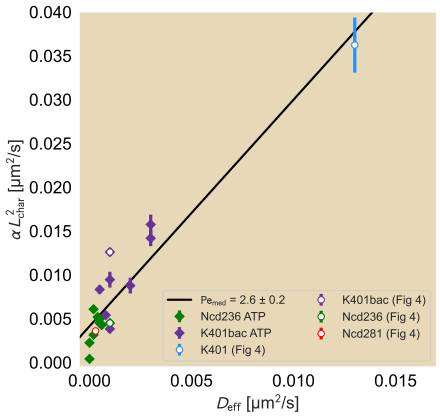

Figure 5.6: **Relation of contraction rate and effective diffusion constant**. Comparisons of contraction rate to effective diffusion constant are made for effective diffusion constants fitted to the median normalized area trajectories and obtained across all ATP concentration (diamonds) and motor species (hollow circles with colors matching those in Fig. 5.4) conditions. Contraction rates are multiplied by the square of a characteristic length scale, in this case roughly the median length of a microtubule in experiments (1.5 μm), to match the units of the effective diffusion constant. Slopes of lines are best fits of Pe, which are reported with their respective standard deviations in the legend.

between the rates of advection and diffusion in the system, given by

$$\mathrm{Pe} = \frac{\text{diffusive timescale}}{\text{advective timescale}}, \tag{5.10}$$

$$= \frac{L_{\mathrm{char}}^2/D}{L_{\mathrm{char}}/\mathrm{v}_{\mathrm{char}}}, \tag{5.11}$$

$$= \frac{\mathrm{v}_{\mathrm{char}} \times L_{\mathrm{char}}}{D}, \tag{5.12}$$

where L_{char} and $\mathrm{v}_{\mathrm{char}}$ are the characteristic length scale and characteristic advective velocity, respectively. L_{char} determines the length scale in the system over which the advective and diffusive timescales are compared. In our system, candidates for L_{char} may be as small as a typical microtubule in the assay and as large as the size of the contracting system. As the microtubule length is within an order of magnitude of the photobleached line and gives a sense of the local competition between diffusion and advection, we choose $L_{\mathrm{char}} = 1.5$ µm. We relate $\mathrm{v}_{\mathrm{char}}$ to L_{char} through the global contraction rate of the network α. In other words, $\mathrm{v}_{\mathrm{char}} = \alpha \times L_{\mathrm{char}}$. So we have

$$\mathrm{Pe} = \frac{\alpha\, L_{\mathrm{char}}^2}{D}. \tag{5.13}$$

To estimate the Péclet number, we plot the median contraction rates multiplied by the square of a characteristic length scale against the corresponding effective diffusion rates for all experimental conditions (ATP concentration as diamonds and motor species as hollow circles) in Fig. 5.6, which demonstrates a roughly linear relationship. The slope of the line gives Pe, specifically $\mathrm{Pe} = 2.6 \pm 0.2$. To get a sense for how much Pe varies due to variability within conditions, we find $\mathrm{Pe}_{25} = 4.5 \pm 0.5$ and $\mathrm{Pe}_{75} = 2.4 \pm 0.1$ for the first and third quartile datasets, respectively (see SI Sec S15), suggesting that Pe is tightly constrained. In all cases, $\mathrm{Pe} \gtrsim 1$, suggesting that the effect of diffusion is smaller than that of advection, but comparable to within an order of magnitude. This makes sense as the net effect of the unit cells, despite exhibiting a local diffusive-like effect, shrinks in area. Further, the rather narrow range in the Péclet number despite the spread in quartiles further suggests that the speed of the active elements sets both the global contraction of the network and the local spread of individual filaments. We recall that our choice of L_{char} allows us to examine the local competition between advection and diffusion. Had we chosen the side length of a unit cell or the size of the system as our size scale, we would see the increase in L_{char} results in $\mathrm{Pe} \gg 1$, demonstrating the greater dominance of the advective component over larger length scales, consistent with the net contraction in the network. Our results indicate that while advection generally dominates over

diffusion, most notably over longer length scales, the close linear relation between the two rates suggest that they are both set by the speed of the motors.

Interestingly, that a Péclet number relates the contraction rate and effective diffusion constant suggests a new interpretation of the advection-diffusion equation as written in Eq 5.9. Specifically, we can rework Eq 5.13, such that

$$D = \beta\alpha, \tag{5.14}$$

where $\beta \equiv \frac{L_{\text{char}}^2}{\text{Pe}}$. With this new relation, we next rewrite Eq 5.7 as

$$\mathbf{J} = -\underbrace{\alpha\,\mathbf{r}c}_{\text{advection}} - \underbrace{\alpha\,\beta\nabla c}_{\text{active diffusion}}, \tag{5.15}$$

such that Eq 5.9 now becomes

$$\frac{\partial c}{\partial t} = \alpha\nabla\cdot(\mathbf{r}c + \beta\nabla c)\,. \tag{5.16}$$

We emphasize again that β is dependent on quantities that are applied across all conditions namely, L_{char} and Pe, and thus is similarly fixed across the conditions examined here. Thus, if we used Pe_{med} we would obtain $\beta = 0.87\ \mu\text{m}^2$ as our value across conditions. Eq 5.16 creates a striking new viewpoint on the relation between the advective and diffusive terms. In particular, this equation tells us that there is only one parameter that varies across the conditions, namely the contraction rate α. Perhaps even more curious is the interpretation of the parameter β. Essentially, this factor tells us the coupling strength of the contraction rate on the diffusive effect in the system and suggests that tuning motor speed alone does not greatly alter this strength factor. We explore the connection between motor speed from our data and this new interpretation in Sec SI S16 as a call for further theoretical and experimental investigation of the fascinating coupling of active contraction and active diffusion. We note that a theory of the parameter β would need to account for how it depends upon motor processivity and stall force, for example.

5.3 Discussion

The dynamic cytoskeleton is critical to carrying out key processes within cells, such as the formation and maintenance of the mitotic spindle [41], cell division by cytokinesis [42], and as centers of morphogenetic information [43]. Such motor-filament structures are vital to a cell or organism, but how the constituent cytoskeletal elements reorganize to reach the same end configuration due to changes in biochemical

conditions has been unclear. In order to understand this response by the kinesin-microtubule network, we developed an experimental framework for probing the bulk redistribution of the filament network using a grid photobleaching pattern. By photobleaching the network, we observe that microtubules will undergo a diffusive-like spread that locally opposes the global, uniform contraction of the system. The diffusive-like behavior and contraction rate are jointly tuned by changes to the effective motor speed either from using different motor species or altering the ATP concentration. These effects also appear to occur from tuning crowding agents, a topic that we discuss in SI Sec S16-S17. In short, not only is the contraction an actively driven phenomenon, but so too is the diffusive-like behavior.

As we observed a general increase in effective diffusion constant with the increase in contraction rate, we further probed this relationship to find a roughly linear relationship between the two measurements. This suggests that the Péclet number, which is the ratio of the diffusive timescale to the advective one, remains roughly constant within the bulk of the contracting network regardless of the biochemical conditions we used here and further suggests that motor velocity not only sets the rate that the system contracts but also the effective diffusivity in the bulk.

Active diffusion has been observed in other active systems both *in vitro* [21, 29, 30, 31] and *in vivo* [44, 45, 46]. This phenomenon is particularly exciting in those cases where the diffusive-like motion exhibits a dependency on the availability of ATP. *In vitro*, a Michaelis-Menten like relationship has been observed between ATP concentration and the spatial rate of deformation of the system [30]. This relationship between the rate at which deformations occur and ATP concentration is consistent with our observations that both the macroscopic deformation rate and local diffusion are determined largely by an effective velocity of the motor. Furthermore, the fact that this ATP dependence also occurs in *in vivo* systems [45, 46] suggests interesting implications in the ability of cells to carry out key enzymatic reactions. One key parameter that has not yet been explored is the competition of ADP in the system. We recall that our work utilized an ATP recycling system that allowed us to ignore such competing effects. However, cells also have a supply of ADP that may compete with ATP for the ATP hydrolysis site of motors [38]. A natural extension of this study would involve systematically tuning the ratio of ATP to ADP to observe the effects of reorganization due to this competition and may provide key insights on the role of metabolic activity on altering the rates of ATP-dependent processes.

Various quantitative models have been made to recapitulate the experimentally ob-

served motor-filament dynamics [18, 11, 19, 21, 47, 23]. These models incorporate contractile stresses in the system, either through motor-driven activity or Stokeslets in the flow field, resulting in a net elastic behavior [11, 19, 23]. As we report here, a long-time relaxation term is required to create the diffusive-like filament redistribution in the network bulk. Recent treatments to introduce a long-time relaxation, as found in Ref [48], propose force-balance approaches that incorporate a viscoelastic stress to locally oppose the active stress underlying the elastic contraction. As our findings indicate that the relaxation is motor driven and transports filaments based on the direction of their orientation, we propose that an active viscoelastic-like stress term would be necessary and would need to depend on the motor speed and local polarity of the network. Indeed, other works account for the orientation $\vec{p}$ of the filaments not only for driving the movement of motors but as time-dependent variables through crosslink-generated torques [21, 47], offering encouraging pathways to recapitulate active cytoskeletal reorganization and necessitating measurements on local filament orientation.

Our work provides deeper insights into the extent of filament redistribution during network contraction, where the active element not only drives the global contractile behavior but also generates a local redistribution that can be tuned by their effective speeds. Our findings leave many unanswered and exciting questions about these self-organizing systems. Much is still not known about the origins of the network formation from the initially random orientation and uniform distribution of filaments prior to contraction. Specifically, the key criteria of the formed network, whether in the form of a density or order dependence, to drive the contraction process remain unclear. Photobleaching as applied in our work here provides a helpful macroscopic view of filament reorganization that can serve as a complement to other methods that are likely required to probe the dynamics of the filaments in the network, such as their orientation when they become coupled by the multimerized motors. Our work here offers new insights and a useful method for probing other key biochemical parameters of the cell such as different motor-microtubule ratios, admixtures of opposing motors, dynamic microtubules [49], more complex iLid-micro activation geometries [23], or with the introduction of ADP to compete against ATP-dependent reactions.

5.4 Materials and Methods

Microscopy set-up

The microscopy elements used to activate the iLid-micro dimerization and image the different fluorescence channels are similar to those found in Ross *et al.* [12]. Briefly, a digital light processing projector from Texas Instruments was used to activate the motor dimerization and image the microtubule channels. An excitation filter wheel was placed in front of the projector to filter out the different channels. Photobleaching was performed using a diode laser with a center wavelength of 642 nm. A piezoelectric mirror gimbal mount from Thorlabs was placed downstream of the laser to deflect the beam path over a small range before the laser light passes through a cylindrical lens array inserted into a direct-drive rotation mount. The gimbal mount can then sweep the projected lines laterally to thicken the photobleaching lines before the rotation mount is rotated 90° and the gimbal mount changes the deflecting angle of the beampath in the orthogonal direction. Imaging is performed using a 20x objective. More details are available in the SI Sec S1.6.

Microtubule network assay

The microtubule network formation and contraction assay is set up similarly as in Ross *et al.* [12]. Micro- and iLid-tagged motors are mixed in equal motor monomer ratios with GMPCPP-stabilized microtubules labeled with Alexa 647 in a reaction mix containing among other components ATP, ATP recycling reagents including pyruvate kinase and phosphoenolpyruvate (PEP), and pluronic as a crowding agent. While elements of the oxygen scavenging are kept in the reaction, the glucose oxidase is removed from the reaction to ensure photobleaching. Removal of these oxygen scavengers minimally affects fluorescence intensity during imaging from using the projector over the time range over which the data is analyzed, as shown in SI Sec S3.

Image acquisition arrangement

Control of the light-dimerizing activation, photobleach laser activation, and imaging are performed through the Micro-Manager (MM) software [50, 51] while photobleaching is synchronized using a series of in-house compiled executable files that control the movement of the gimbal and rotation mounts. During acquisition, a beanshell script in MM changes the projection pattern on the DLP to create a circular light pattern of radius 125 μm for the iLid activation and full field for the imaging channels. When the desired state of the microtubule network is reached for

performing photobleaching, the script completes the image acquisition cycle before turning on the photobleaching laser and calling to the executables to create the grid before the next acquisition cycle.

Motor purification

Kinesin motors are expressed using the pBiex-1 vector transfected in Sf9 suspension cells. Cells are transfected at 5-7 µg for every 15×10^6 cells at a starting concentration 10^6 cells per mL of Sf900-III media using a liposome-based transfection regent (Escort IV Transfection Reagent). Cells are harvested $\backsim$60-72 hours after transfection and purified using the FLAG affinity tag and anti-FLAG antibody resins. Proteins are stored in 50% glycerol by volume with 1.5 mM DTT, 50 µM EDTA, 50 µM EGTA, and 15 µM ATP and stored at -20°C. Full storage buffers and final concentrations of components are available in the SI.

Data Availability

All data and code are publicly available. Raw image files and COMSOL simulation file can be downloaded from the CaltechDATA research data repository under the DOI:10.22002/f23ds-f2v87. Analyzed data files and code generated by Python (for analyses) and BeanShell Scripts and C# (for hardware communication) for the work presented here are available on the dedicated GitHub repository under the DOI:10.5281/zenodo.12806576.

5.5 Acknowledgements

We thank members of the Rob Phillips lab for useful discussions. We would also like to thank the David Van Valen and Rebecca Voorhees labs for providing resources for performing the protein expression and purification. We also thank Justin Bois, Griffin Chure, Peter Foster, Sebastian Fürthauer, Victor Gomez, Stephan Grill, Catherine Ji, Frank Jülicher, Matthias Merkel, Daniel Needleman, Leïla Perié, Henk Postma, Madan Rao, Shahriar Shadkhoo, and Fan Yang. This work was supported by 1R35 GM118043 and 2R35 GM118043 Maximizing Investigators' Research Awards (MIRA) (to R.P.).

References

[1] Tamás Vicsek et al. "Novel type of phase transition in a system of self-driven particles." In: *Physical Review Letters* 75.6 (1995), pp. 1226–1229.

[2] John Toner and Yuhai Tu. “Long-range order in a two-dimensional dynamical *XY* model: how birds fly together.” In: *Physical Review Letters* 75.23 (1995), pp. 4326–4329.

[3] Sriram Ramaswamy. “The mechanics and statistics of active matter.” In: *Annual Review of Condensed Matter Physics* 1 (2010), pp. 323–345.

[4] Jonas Denk and Erwin Frey. “Pattern-induced local symmetry breaking in active-matter systems.” In: *Proceedings of the National Academy of Sciences of the United States of America* 117.50 (2020), pp. 31623–31630.

[5] François J. Nédélec et al. “Self-organization of microtubules and motors.” In: *Nature* 389.6648 (1997), pp. 305–308.

[6] Arshad Kudrolli et al. “Swarming and swirling in self-propelled polar granular rods.” In: *Physical Review Letters* 100.5 (2008), p. 058001.

[7] Nitin Kumar et al. “Flocking at a distance in active granular matter.” In: *Nature Communications* 5 (2014), p. 4688.

[8] Katherine Copenhagen et al. “Topological defects promote layer formation in *Myxococcus xanthus* colonies.” In: *Nature Physics* 17.2 (2021), pp. 211–215.

[9] Tim Sanchez et al. “Spontaneous motion in hierarchically assembled active matter.” In: *Nature* 491 (7424 2012), pp. 431–434.

[10] Thomas Surrey et al. “Physical properties determining self-organization of motors and microtubules.” In: *Science* 292.5519 (2001), pp. 1167–1171.

[11] Matthias Schuppler et al. “Boundaries steer the contraction of active gels.” In: *Nature Communications* 7.13120 (2016), pp. 1–10.

[12] Tyler D. Ross et al. “Controlling organization and forces in active matter through optically defined boundaries.” In: *Nature* 572 (2019), pp. 224–229.

[13] Rui Zhang et al. “Spatiotemporal control of liquid crystal structure and dynamics through active patterning.” In: *Nature Materials* 20.6 (2021), pp. 875–882.

[14] L M Lemma et al. “Spatio-temporal patterning of extensile active stresses in microtubule-based active fluids.” In: *PNAS Nexus* 2.5 (2023), pgad130.

[15] Ha Youn Lee and Mehran Kardar. “Macroscopic equations for pattern formation in mixtures of microtubules and molecular motors.” In: *Physical Review Letters E* 64.5 (2001), p. 056113.

[16] François Nédélec, Thomas Surrey, and A.C. Maggs. “Dynamic concentration of motors in microtubule arrays.” In: *Physical Review Letters* 86.14 (2001), pp. 3192–3195.

[17] Sumithra Sankararaman and Gautam I. Menon. “Self-organized pattern formation in motor-microtubule mixtures.” In: *Physical Review Letters E* 70.3 (2004), p. 031905.

[18] Julio M. Belmonte, Maria Leptin, and François Nédélec. “A theory that predicts behaviors of disordered cytoskeletal networks.” In: *Mol Syst Biol* 13.941 (2017), pp. 1–13.

[19] Peter J. Foster et al. “Active contraction of microtubule networks.” In: *eLife* 4.e10837 (2015), pp. 1–21.

[20] Fred C. MacKintosh and A. J. Levine. “Nonequilibrium mechanics and dynamics of motor-activated gels.” In: *Physical Review Letters* 100 (1 2008), p. 018104.

[21] Sebastian Fürthauer et al. “Self-straining of actively crosslinked microtubule networks.” In: *Nature Physics* 15 (2019), pp. 1295–1300.

[22] Igor M. Kulic et al. “The role of microtubule movement in bidirectional organelle transport.” In: *Proceedings of the National Academy of Sciences of the United States of America* 105.29 (2008), pp. 10011–10016.

[23] Zijie Qu et al. “Persistent fluid flows defined by active matter boundaries.” In: *Communications Physics* 4.198 (2021), pp. 1–9.

[24] Rachel A. Banks et al. “Motor processivity and speed determine structure and dynamics of motor-microtubule assemblies.” In: *eLife* 12 (2023), e79402.

[25] D Axelrod et al. “Mobility measurement by analysis of fluorescence photobleaching recovery kinetics.” In: *Biophysical Journal* 16.9 (1976), pp. 1055–1069.

[26] José Braga, James G. McNally, and Maria Carmo-Fonseca. “A reaction-diffusion model to study RNA motion by quantitative fluorescence recovery after photobleaching.” In: *Biophysical Journal* 92.8 (2007), pp. 2694–2703.

[27] Mohit Kumar, Mario S. Mommer, and Victor Sourjik. “Mobility of cytoplasmic, membrane, and DNA-binding proteins in *Escherichia* coli.” In: *Biophysical Journal* 98.4 (2010), pp. 552–559.

[28] Maria-Veronica Ciocanel et al. “Analysis of active transport by fluorescence recovery after photobleaching.” In: *Biophysical Journal* 112.8 (2017), pp. 1714–1725.

[29] Alexandra M. Tayar, Michael F. Hagan, and Zvonimir Dogic. “Active liquid crystals powered by force-sensing DNA-motor clusters.” In: *Proceedings of the National Academy of Sciences of the United States of America* 118.30 (2021), e210873118.

[30] Linnea M. Lemma et al. “Multiscale microtubule dynamics in active nematics.” In: *Physical Review Letters* 127.14 (2021), p. 148001.

[31] Alexandra Colin et al. “Friction patterns guide actin network contraction.” In: *Proceedings of the National Academy of Sciences of the United States of America* 120.39 (2023), e2300416120.

[32] Harukata Miki et al. “All kinesin superfamily protein, KIF, genes in mouse and human.” In: *Proceedings of the National Academy of Sciences of the United States of America* 98.13 (2001), pp. 7004–7011.

[33] Hideyuki Yaginuma et al. “Diversity in ATP concentrations in a single bacterial cell population revealed by quantitative single-cell imaging.” In: *Scientific Reports* 4.6522 (2014), pp. 1–7.

[34] Gurkan Guntas et al. “Engineering an improved light-induced dimer (iLID) for controlling the localization and activity of signaling proteins.” In: *Proceedings of the National Academy of Sciences of the United States of America* 112.1 (2015), pp. 112–117.

[35] Nicholas F. Endres et al. “A lever-arm rotation drives motility of the minus-end-directed kinesin Ncd.” In: *Nature* 439.7078 (2006), pp. 875–8.

[36] Jonathon Howard, A. J. Hudspeth, and Ronald D. Vale. “Movement of microtubules by single kinesin molecules.” In: *Nature* 342.6246 (1989), pp. 154–158.

[37] Koen Visscher, Mark J. Schnitzer, and Steven M Block. “Single kinesin molecules studied with a molecular force clamp.” In: *Nature* 400.6740 (1999), pp. 184–189.

[38] William R. Schief et al. “Inhibition of kinesin motility by ADP and phosphate supports a hand-over-hand mechanism.” In: *Proceedings of the National Academy of Sciences of the United States of America* 101.5 (2004), pp. 1183–1188.

[39] Kelly A. Foster, J. J. Correia, and Susan P. Gilbert. “Equilibrium binding studies of Non-claret disjunctional protein (Ncd) reveal cooperative interactions between the motor domains.” In: *Journal of Biological Chemistry* 273.52 (1998), pp. 35307–35318.

[40] Ken’ya Furuta et al. “Measuring collective transport by defined numbers of processive and nonprocessive kinesin motors.” In: *Proceedings of the National Academy of Sciences of the United States of America* 110.2 (2013), pp. 501–506.

[41] Christina L. Hueschen et al. “Microtubule end-clustering maintains a steady-state spindle shape.” In: *Current Biology* 29 (4 2019), 700–708.e5.

[42] Ann L. Miller. “The contractile ring.” In: *Current Biology* 21.24 (2012), R976–R978.

[43] Yonit Maroudas-Sacks et al. “Topological defects in the nematic order of actin fibres as organization centres of *H*ydra morphogenesis.” In: *Nature Physics* 17 (2021), pp. 251–259.

[44] Clifford P. Brangwynne, Fred C. MacKintosh, and David A. Weitz. "Force fluctuations and polymerization dynamics of intracellular microtubules." In: *Proceedings of the National Academy of Sciences of the United States of America* 104.41 (2007), pp. 16128–16133.

[45] Stephanie C. Weber, Andrew J. Spakowitz, and Julie A. Theriot. "Nonthermal ATP-dependent fluctuations contribute to the in vivo motion of chromosomal loci." In: *Proceedings of the National Academy of Sciences of the United States of America* 109.19 (2012), pp. 7338–7343.

[46] Ming Guo et al. "Probing the stochastic, motor-driven properties of the cytoplasm using force spectrum microscopy." In: *Cell* 158.4 (2014), pp. 822–832.

[47] Sebastian Fürthauer, Daniel J. Needleman, and Michael J. Shelley. "A design framework for actively crosslinked filament networks." In: *New Journal of Physics* 23.1 (2021), p. 013012.

[48] Fan Yang et al. "Dynamic flow control through active-matter programming language." In: *arXiv* (2022), pp. 1–9. DOI: https://doi.org/10.48550/arXiv.2208.12839.

[49] William G. Hirst et al. "Differences in Intrinsic Tubulin Dynamic Properties Contribute to Spindle Length Control in Xenopus Species." In: *Current Biology* 30.11 (2020), pp. 2184–2090.

[50] Arthur D. Edelstein et al. "Computer control of microscopes using μManager." In: *Current Protocols in Molecular Biology* (2010), pp. 14.20.1–14.20.17.

[51] Arthur D. Edelstein et al. "Advanced methods of microscope control using μManager software." In: *Journal of Biological Methods* 1.2 (2014), e11. DOI: doi:10.14440/jbm.2014.36.

Chapter 6

SUPPLEMENTARY INFORMATION FOR MOTOR-DRIVEN MICROTUBULE DIFFUSION IN A PHOTOBLEACHED DYNAMICAL COORDINATE SYSTEM

In this collaborative project led by Soichi Hirokawa, I analyzed data and provided reagents. Specifically, I developed an image processing pipeline allowing me to analyze the speed of motor proteins based on microtubule gliding data. Additionally, I purified proteins and prepared buffers used in these experiments. This study is published and can be found with the following citation:

Soichi Hirokawa, Heun Jin Lee, Rachel A. Banks, Ana Isabel Duarte, Bibi Najma, Matt Thomson, and Rob Phillips. "Motor-driven microtubule diffusion in a photobleached dynamical coordinate system". In: *Proceedings of the National Academy of Sciences* 122.24 (2025), e2417020122. doi: 10.1073/pnas. 2417020122

6.1 Materials and Methods

Motor purification

Plasmids containing the gene encoding the motor-fluorescent protein-light-activated dimerization-FLAG tag construct with the pBiex-1 vector are transfected in Sf9 suspension cells for 60-72 hours at 27°C on shakers rotating at 120 rpm. Cells are then lightly centrifuged at 500 rpm for 12 minutes to remove the supernatant before resuspending in lysis buffer (100 mM NaCl, 2 mM $MgCl_2$, 0.25 mM EDTA, 0.5 mM EGTA, 0.25 % Igepal, 3.5% sucrose by weight, 10 mM imidazole pH 7.5, 10 µg/mL aprotinin, 10 µg/mL leupeptin, 1 mM ATP, 2.5 mM DTT, and 0.5 mM PMSF) and leaving on ice for 20 minutes. Cells are then spun down for 30 minutes at 50k rpm after which the lysate is transferred to tubes containing mouse monoclonal anti-FLAG resin (Sigma A2220) and slowly rotated at 4°C for 1.5∽3 hrs to allow protein binding to the resin via the FLAG tag. Resin-bound protein are washed three times by spinning down at 2000× g, clearing the supernatant, then resuspending by tube inversion in wash buffer containing 15 mM KCl, 0.5 mM, 0.1 mM EGTA, 0.1 mM EDTA, 2 mM imidazole pH 7.5, 10 µg/mL aprotinin, 10 µg/mL leupeptin, 0.3 mM DTT, and ATP in 3 mM, 0.3 mM, and 0.03 mM concentrations for the first, second, and third washes, respectively. After the third wash, the protein are spun down again at 2000× g and most of the supernatant is removed, leaving the resin

bed and roughly an equivalent amount of supernatant by volume in the tube. The resin bed is resuspended and FLAG peptide (Sigma F4799 or Thermo Scientific A36805) is added at a final concentration of 0.5 mg/mL before rotating for 3 hrs at 4°C. After incubating to allow the peptide to outcompete the protein for resin binding, the protein are spun down again at 2000× g with the supernatant extracted and further spun down using centrifuge columns with ∽30 µm pore sizes to further separate proteins from any collected resin beads. Flow-through of clarified protein are spin concentrated using a 50 kDa filter tube to a final concentration of 2-2.5 mg/mL before diluting in 100% glycerol of the same volume for storage.

Stabilized microtubule polymerization

Fluorescently labeled stabilized microtubules are prepared as in [1, 2]. After flash thawing at 37°C and kept on ice, a combination of ≈ 1.5 mg unlabeled and 100 µg labeled tubulin are diluted to 7.5 mg/mL and 0.5 mg/mL, respectively, in M2B 6.8 containing DTT and GMP-CPP at final concentrations of 1 mM and 6mM, respectively. The tubulin mixture is then incubated on ice for 5 minutes in an ultracentrifuge tube before ultracentrifugation at 90,000 rpm at 4°C for 8 minutes. Avoiding the pellet at the the bottom, the supernatant containing tubulin monomers are then placed in a new Eppendorf tube and incubated at 37°C for 1 hour, typically in a water bath, during which the tubulin is polymerizing and stabilizing with GMPCPP. The microtubule mixture is then aliquoted into individual PCR tubes while constantly being suspended in the mixture by stirring with a pipette tip. PCR tubes are then briefly spun down with a tabletop minicentrifuge before flash-freezing with liquid nitrogen and placed in a -80°C freezer for long-term storage. Microtubules are then prepared for experiments by immersing the PCR tube in 37°C water immediately when taken out of the freezer to quickly thaw.

Glass slide treatment

Corning glass slides and No. 1.5 Deckgläser coverslips are coated with an acrylamide solution to prevent the adhesion of proteins from the light-dimerized activation assay to the surface. The acrylamide coating is done similarly to that demonstrated in [3]. Prior to application of the solution, slides and coverslips are separated by placement in appropriately sized containers and rigorously cleaned through a series of solutions and sonicating. First, slides are immersed in 1% Hellmanex to remove dirt particulates, sonicated, repeatedly rinsed with deionized water (DI H_2O), then repeatedly rinsed with ethanol. Slides are then sonicated in 200 proof

ethanol before rinsing again with DI H_2O. After rinsing, slides are sonicated in 0.1 M KOH and subsequently rinsed in double-distilled water (ddH_2O). Finally, trace metals are removed by immersing in 5% HCl for 4 hours. After repeatedly rinsing in ddH_2O, slides are stored overnight with MilliQ ultrapure water.

Upon cleaning and before the acrylamide coating, a silane solution is made first by mixing 98.5% 200 proof ethanol and 1% acetic acid before adding 0.5% trimethoxysilyl methacrylate and immediately pouring into the containers holding the slides and coverslips. After roughly 30 minutes, slides are rinsed twice in 200 proof ethanol before drying with N_2 air and baking at 110°C for 10-15 minutes to cure silane onto surface with oxygen bonding.

The polyacrylamide solution is made by mixing 950 mL ddH_2O with 50 mL 40% acrylamide and degassing under vacuum for 30 minutes. The solution is then under constant mixing on a stir plate with a stir bar during which time 350 µL TEMED and 700 mg ammonium persulfate (APS) are added to the solution. The acrylamide solution is immediately added to the slides and coverslips and incubated overnight. Slides are placed in 4°C for long-term storage.

Flow cell chamber preparation

Flow cells for all light-dimerized activation assays are prepared by thoroughly rinsing an acrylamide-coated glass slide and coverslip in ddH_2O and air drying with N_2 gas. A piece of parafilm with three channels each cut 3 mm wide is placed on the glass slide with the long axis of the channels running along the length of the slide. The coverslip is placed on top of the parafilm with pressure applied to flatten out the film. The flow cell is then briefly placed on a hot plate set at 65°C to warm the parafilm, allowing extra pressure on the contact points between the film and the glass to better seal the chambers.

Light-dimerized activation assay preparation

Photobleaching experiments require an energy mix to maintain stability and function of microtubules and motors while constantly supplying kinesin motors with ATP to contract the microtubule network. This energy mix is slightly altered from that used by Ross *et al.* [1] with the major changes being a change in acidity for K-PIPES from pH 6.8 to pH 6.1 and the absence of gluocose oxidase to allow for photobleaching. iLid- and micro-tagged motors with the same fluorescent protein

are each added to the reaction mixture at final concentrations of 40-100 nM with stabilized microtubules added at a final concentration of 1.5-2.5 μM tubulin. Concentrations of motors and tubulin are tuned to ensure that the microtubule network 1) contracts into an aster, which can fail to occur with too few motors or tubulin, and 2) without an influx of microtubules from outside of the light-activation region, which can occur from too much tubulin or too many motors dimerizing in the absense of light. Once the tubulin and motor concentrations are determined that meet these criteria for a given motor species, all subsequent replicates are fixed at these concentrations. All experiments are run within less than an hour of incubation time beyond which the influx of microtubules from the unilluminated reservoir tends to occur at higher frequency, as has recently been noted as a long-range connectivity of the network [4].

Optical set-up

The sample is imaged and photobleached using a super planar fluorescence 20x objective from Nikon (numerical aperture 0.45). Image acquisition is performed using a FLiR Blackfly monochrome camera (BFLY-U3-23S6M-C) with three filters in front of it: a Semrock Brightline dual-band pass filter centered at 577 nm (28.3 nm FWHM bandwidth) and 690 nm (55.1 nm FWHM bandwidth); and a Semrock StopLine single-notch filter at 532 nm (17 nm notch bandwidth) to suppress transmission of the YFP laser to the camera.

Activation of motor dimerization and imaging of the microtubules is performed using a digital light projector DLP Lightcrafter Display 4710 EVM Gen2 from Texas Instruments. The DLP projects white light while a motorized filter wheel sets the transmissible range of wavelengths onto the sample (beam blocker for no light, 460/50 nm filter for blue light for iLid-micro dimerization and 630/38 for microtubule imaging). Photobleaching of microtubules is performed using a 645 nm laser. The laser path is set to pass through a cylindrical lens array that transforms the collimated light pattern into a series of lines along one axis. The cylindrical lens array is mounted onto a rotation mount to allow for photobleaching of vertical and horizontal lines to generate the grid pattern. To ensure that the photobleached lines persist for multiple frames of the image, the laser passes through a gimbal-mounted mirror that deflects the beam over a small range of angles. By deflecting the laser light off of the mirror through two lenses with the same focal length f and a second, stationary mirror placed $4 \times f$ away from the gimbal-mounted mirror before passing the laser through the cylindrical lense array, the transformed laser lines can be swept

out. We use this beam steering approach to photobleach thicker lines.

To perform the activation and imaging patterns, we supply μManager with TIFF image stacks of matching pixel dimensions as the projector and use a Beanshell script modified from Ross *et al.* [1] to use the correct TIFF image in the stack. The TIFF stack contains a blank image (all pixel values 0) for when the laser is turned on (which is also used in conjunction with the beam blocker to prevent light from passing onto the sample outside of the activation and imaging cycles); a maximum pixel intensity image for the microtubule imaging, and a circular pattern in a blank background for the circular iLid-micro dimerization activation pattern of radius 125 μm. The primary modification to the Beanshell script is the incorporation of a user-defined timer for when the photobleaching will be performed. The timer is set so that the photobleaching occurs during the contraction phase of the microtubule self-organization, varying from shortly after the microtubule network has formed to shortly before the microtubule no longer visibly contracts in volume (a period of roughly 5 minutes for Ncd236 at saturated ATP). Fig 6.8 provides three examples of the photobleaching occuring at early, intermediate, and late contraction. We emphasize again that the initial iLid-micro dimerizing light pattern is fixed in all three cases. To photobleach the network (when the timer is reached), the imaging pauses while the Beanshell script turns on the laser and executes a series of custom written executables that sweep out the laser lines to create thicker parallel photobleached lines, turn off the laser, rotate the cylindrical lense array, then reactivate the laser and sweep out the laser lines in the orthogonal direction to generate the grid pattern. Upon finishing this command, the laser is shut off and imaging resumes. The entire photobleaching is performed within a roughly 10-15 second window.

6.2 Microtubule Length Extraction

Stabilized microtubules imaged under total internal reflection fluorescence (TIRF) microscopy such as the ones shown in Fig. 6.1(A) were analyzed similar to that discussed in [1] in order to extract their lengths. Briefly, due to the uneven illumination that can occur in the image, images were first background corrected using a local thresholding method known as Niblack thresholding [5] with window size of 3 pixels and k value of 0.001, which determines how many standard deviations below the mean pixel value that one sets the cut-off in the window. Although the array is a series of pixel values to be weighed against the original image, we found that this array already improved the image contrast. With this improved contrast but

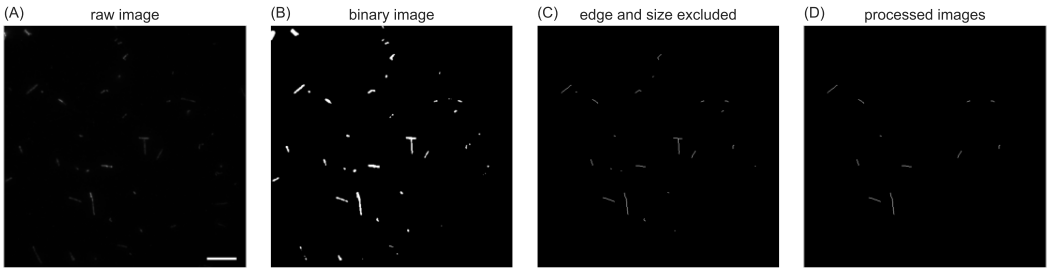

Figure 6.1: **Processing steps of microtubule images.** (A) Raw image. Scale bar denotes 10 μm. (B) Images processed after computing a Niblack threshold and using Otsu thresholding on the Niblack threshold array. (C) Putative MTs skeletonized after removing objects too close to the image border or too small. (D) Removal of any MTs that cross over each other to get the final MTs used for analysis.

considering that the result is still a nonbinary image, we used Otsu thresholding on the Niblack theshold array to extract the microtubules from the background. The result is shown in Fig. 6.1(B).

Using the binary image which contains extracted microtubules, we imposed a morphological closing algorithm to reconnect any microtubules that were broken during the Niblack thresholding from being picked up as signal. This closing was performed using a 3 pixel x 3 pixel square array, suggesting that disconnected microtubules needed to be within $3\sqrt{2}$ pixels of each other at their ends to be connected again. From here, we removed any microtubules that were too close to the edge of the image as they may extend outside of the camera field of view and removed any objects that were fewer than 10 pixels in area as we considered them too small to know with enough certainty whether they were microtubules or small blemishes in the image. Putative microtubules underwent a morphological thinning so that they were converted to one-pixel wide lines along which we could compute their lengths. The result of the edge and size exclusion and skeletonizing are shown in Fig. 6.1(C).

As a final step before measuring the lengths, we removed any microtubules that seem to cross over. This was performed by removing objects where two line segments along the same microtubule strand formed angles of at least 75°, leaving behind a processed image such as Fig. 6.1(D). From here, we used any remaining microtubules and measured their lengths and compiled them. Fig. 6.2 shows empirical cumulative distribution functions of these microtubules from the five MT polymerization assays performed over the course of the work presented here. n

denotes the number of microtubules that were extracted from the image processing and used in the distributions for each replicate. Here, we see that for most of the work performed the MTs had lengths between $1-3$ μm with median lengths between $1.5-2.1$ μm.

6.3 Image Processing: Global Drift Correction

For computational efficiency in later image processing steps, photobleached images are cropped to contain only the region where the collective filament network is present. We first find the center of the contracting network for the image immediately preceding photobleaching. To do so, the image is smoothed with a Gaussian blur and thresholded with the Yen thresholding method [6]. After removing objects that are at the image edge or small objects, the largest segmented object is taken. The properties of this object are then taken, included a pixel-weighted centroid and its major axis length.

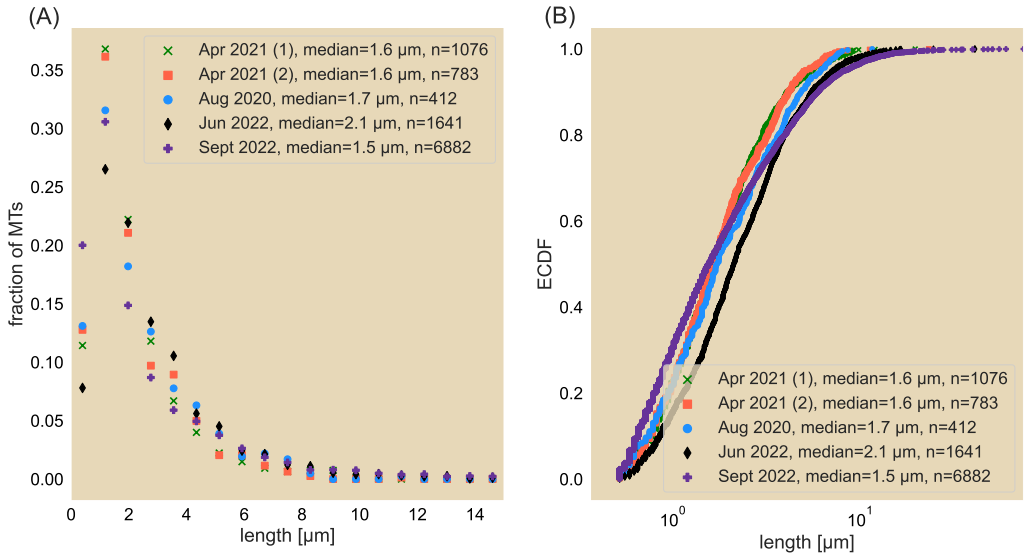

Figure 6.2: **Distributions of microtubule length from microtubules stabilized from polymerization preparations for experiments used in this manuscript.** Microtubules were prepared five times over the course of the work presented here, thus shown as five different datasets. Left plot shows the histogrammed length distribution as a linear x-scale of length while the right plot shows the same data as an empirical cumulative distribution function (ECDF) as a logarithmic x-scale. The two polymerization preparations performed in April 2021 were performed separately by two of the authors of this manuscript on the same day. *n* denotes the number of microtubules whose lengths were obtained in the distributions.

For cropping the first photobleached image, we start by cropping a window in the image using the pixel-weighted centroid as the image center and 130% of the major axis length as the length of the window. This buffer to the window cropping typically ensures that contracting networks that are drifting can still be easily tracked and cropped. To more efficiently crop the image, we then take this cropped window and use a heavy Gaussian blur (σ = 30 pixels) and subtract this from the cropped photobleached image. We then normalize the image and use Otsu thresholding [7] to identify putative fluorescent unit cells. We roughly identify the unit cells by removing those that are close to the edge of the image as well as objects that are smaller than 36 μm^2, which would be far smaller than a unit cell. Unit cells are further cleaned up by filling in any small holes in the unit cell with a morphological closing before taking the pixel-weighted centroid using all of the unit cells together to get a rough position of the network center. This process is then repeated on the next photobleached frame using the new centroid for the image center and the original window length over the desired number of photobleach frames. These cropped images are then used for further, more careful processing of the unit cells.

6.4 Quantifying Microtubule Unit Cell Dynamics

In this work, we sought to characterize the bulk redistribution of microtubules through local deformations and translations within the contracting network. To develop a processing method that would allow us to quantify the advective and diffusive components of the network, we first set out to determine whether the microtubule number is conserved in the system. A part of this determination, which relies heavily upon the fluorescence signal, depends upon whether the imaging system also affects the signal over time through passive photobleaching. We seek to assess these factors in SI Secs. 6.4 and 6.4 below.

Imaging system negligibly photobleaches microtubules

One concern in analyzing microtubule fluorescence over time is whether the optical system decreases its signal due to secondary photobleaching effects from the projector, which is used to illuminate the field of view for imaging purposes and perform the iLid-micro light stimulation. To investigate this, we imaged the microtubule field without activating the iLid-micro dimerization using the same exposure times (200 ms) and different imaging frequencies depending upon the speed at which contraction takes place, between 3 seconds and 10 seconds per frame. We then examined the mean image intensity and standard deviation of the pixel intensity as

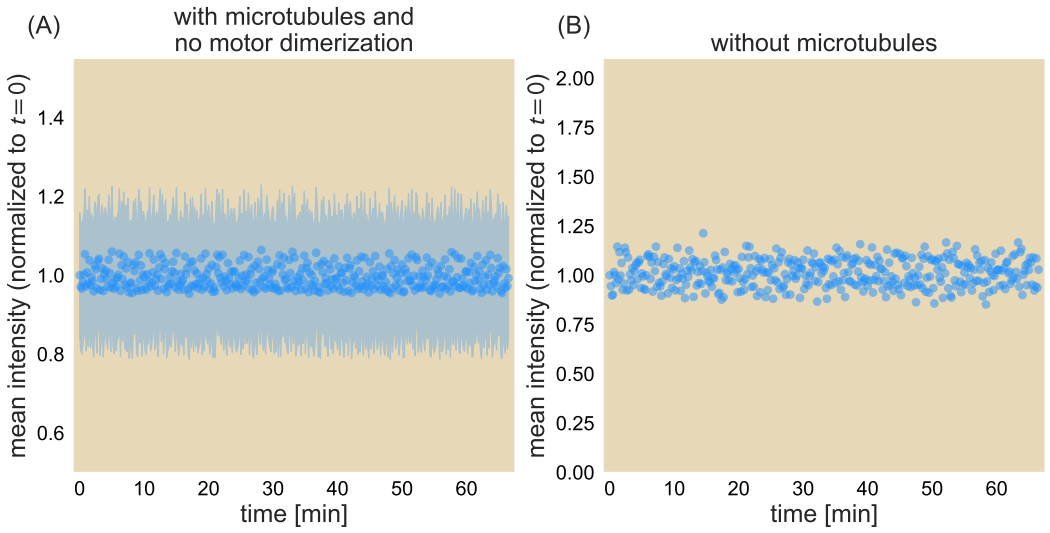

Figure 6.3: **Image intensity of the microtubule field as a function of time.** (A) Mean intensity of the microtubule field normalized against that of the first image. Blue shaded region represents one standard deviation in the mean intensity (normalized by the same initial mean value). (B) Mean intensity of the same fluorescence channel in the absence of microtubules.

a function of time.

Fig. 6.3(A) illustrates the effects of the projector on the microtubule field. The mean intensity of the field of view, as normalized against the mean intensity at $t = 0$ seconds, indicates that the fluorescence field fluctuates within a few percent but does not appear to decrease over an hour. These fluctuations are likely due to fluctuations from the image acquisition set-up itself, as Fig. 6.3(B) shows the normalized mean intensity of the microtubule fluorescence channel but in the absence of microtubules. Here, we see that that the integrated intensity fluctuates over the short term but does not appear to exhibit a global decrease, further supporting that the small fluctuations in fluorescence intensity in successive imaging stages comes from the imaging system. Nevertheless, we conclude that the fluorescence intensity is well preserved over the course of experiments and does not require corrections during image processing.

Net flux of microtubules goes into the imaging plane

As the projector does not passively photobleach the microtubule channel (SI Sec. 6.4), we next ask whether there is a loss of microtubules during the contraction process. Microtubules may disconnect from the contracting network and diffuse

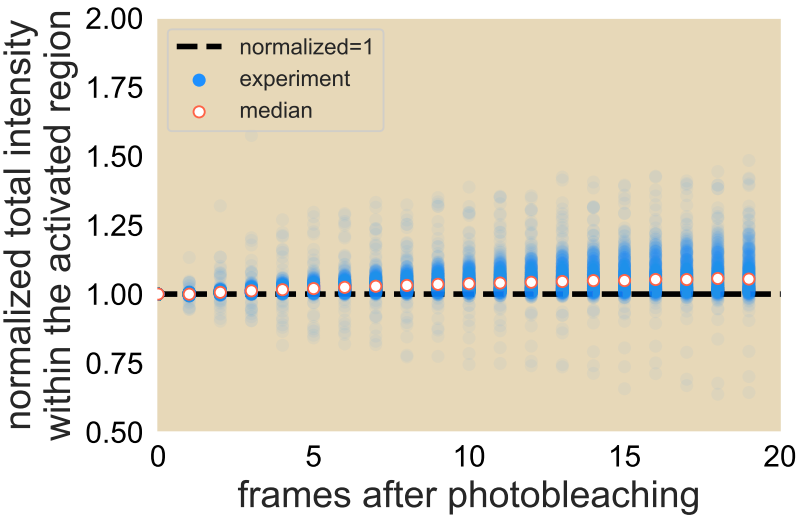

Figure 6.4: **Integrated intensity of the photobleached contracting network over image frames.** White dots denote the median value across all experiments.

away. For example, as we use an epifluorescent imaging set-up, if microtubules are lost from the network by moving out of the plane of imaging, they will project a low, more diffuse signal onto the image. In contrast, microtubules that move into the plane of focus will exhibit a higher signal. Similarly, microtubules lost at the periphery in the image plane will lead to a reduced integrated intensity across the entire network.

To determine the effects of flux across the focal plane, we measure the integrated fluorescence signal of the contracting network after photobleaching. This is done by integrating the fluorescence signal of the activated network as it contracts away from the unilluminated reservoir. We then examine the normalized integrated signal over time.

Fig. 6.4 shows that the integrated intensity of the contracting network increases in time. Over 20 imaging frames, the fluorescence increases by about 5%, suggesting a roughly 0.25% increase between frames. While some of the observed increase in intensity can be accounted for by those datasets where the contracting network is not fully disconnected from the unilluminated reservoir and thus introducing more microtubules at the periphery, we suspect that the majority of this increase comes from an increase of microtubules that are entering the imaging plane. This observation makes sense as we expect a growing concentration of microtubules

entering the imaging plane due to network contraction. Had we accounted for this increase in intensity over successive frames, our results would at best have led to a greater area of the unit cells than the ones we computed, which would produce greater effective diffusion constants. Even so, we argue that the roughly quarter of a percent increase between frames is relatively minor and conclude that the total microtubule count remains roughly constant over the course of the experiment.

Number conservation of unit cells

Due to the negligible photobleaching effects of the projector on the network and the small influx of microtubules in the imaging plane, we make the assumption that the total number of microtubules for the entire network is conserved. We further assume that at the local level, the number of fluorescent microtubules that compose a unit cell is also conserved. As a result, we choose to identify and track unit cells in time by conserving their integrated fluorescence intensity.

Fluorescent unit cells of a photobleached microtubule network are thus segmented in the cropped image sets where the microtubules outside of the activation region are neglected. For each image, we identify the unit cells by first enhancing the contrast between the fluorescence signal of the unit cells and the background through the subtraction of a heavily Gaussian blurred form of the image (σ = 20 pixels) and subtracting off this blur from the original image. Pixel values are then normalized across the image to fall between 0 and 1.

In order to identify each fluorescent square, we tested a variety of thresholding schemes using the Sci-kit Image package for Python. In summary, the following thresholding schemes are:

- Isodata – identifies those threshold values where, when each pixel is grouped according to whether it lies above or below the threshold value, the threshold value is the average of the two binned groups.
- Li – iteratively computes the cross-entropy between the image and a binary image with a different thresholding value. The returned threshold value is that which reduces the cross entropy [8].
- Mean – computes the mean pixel value across the image [9].

- Otsu – finds the threshold that minimizes the sum of the variances of the background and foreground [7].
- Triangle – computes a line from the peak in the histogram to the last histogram bin (if the peak is shifted to the left of the histogram). A second perpendicular line is drawn from this line toward the first histogram bin it touches. The corresponding x-value gives the threshold [10].
- Yen – computes the minimum cross-entropy between the image and thresholded binary image while accounting for the bit depth of the image [6].

Furthermore, we seek the method that best identifies the unit cells not only in the bulk that will appear as squares but also those that lie along the periphery that may not appear as complete squares after the photobleaching is applied but are nevertheless part of the network.

Fig 6.5 shows these various thresholding schemes performed on the background-subtracted image (top right) with comparisons to the original raw image (top left). We see that while the isodata thresholding approach misses many of the fluorescent squares, other thresholding schemes reasonably render the threshold of the squares. We notice that the Li, Otsu, triangle and Yen thresholding schemes miss unit cells on the periphery of the network, especially if they are not squares as in those found toward the center of the microtubule network. To keep track of their dynamics, we elect to use the mean thresholding algorithm, which from visually comparing the threshold to the raw data better represents the unit cells, including those unit cells on the network periphery. After the thresholding is applied, the segmented image is cleaned up by removing segmented objects that are too small (less than a third of the area of a unit cell immediately after photobleaching) and objects that are larger than the area of a unit cell. A morphological closing is performed where any holes smaller than 3 pixels $\times$ 3 pixels within a fluorescent unit cell is closed. These small holes may arise from a local minimum in signal that falls in the background regime during thresholding. With the segmented images from the first frame, the centroid position, area, and total fluorescence of each unit cell are computed. For total fluorescence, we compute the pixel intensity by taking the raw image signal and subtracting the average background signal inherent to the camera. Fig 6.6(A) provides a schematic of the resultant thresholding to initially identify unit cells.

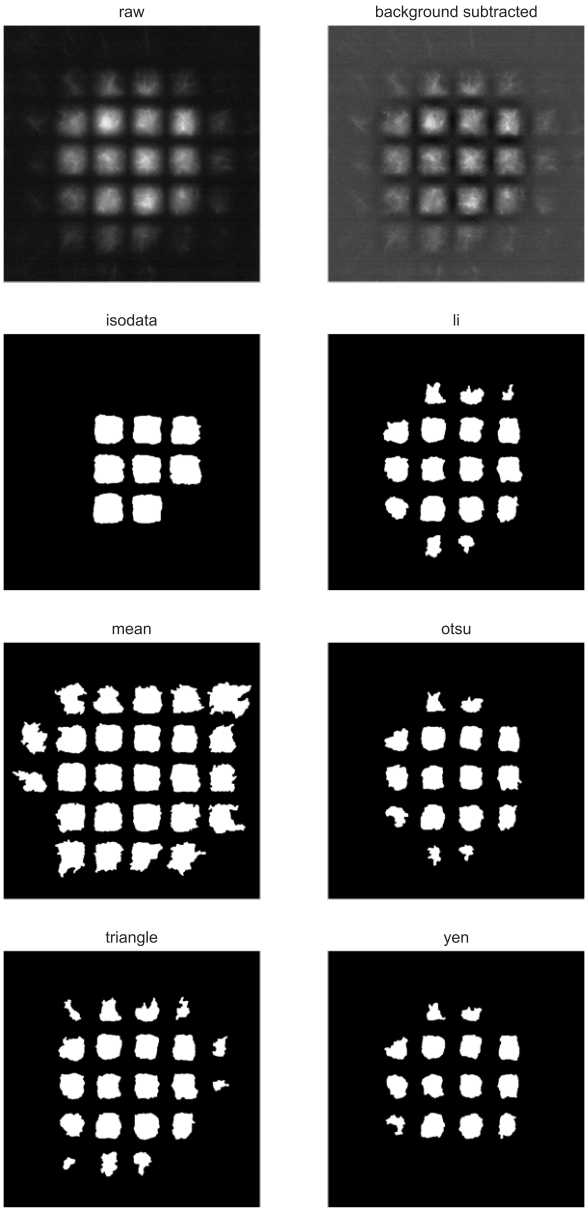

Figure 6.5: **Various thresholding schemes of fluorescent squares.** Top two images correspond to the raw (left) and background-subtracted (right) images. The thresholding schemes used, in order, were isodata, Li, mean, Otsu, triangle, and Yen thresholding methods. Due to the under-representation of unit cell fluorescent signal for all the other methods, we opt for the mean thresholding scheme to identify unit cells.

As schematized in Fig 6.6(B) and (C), images of subsequent time points are processed with the intention of preserving the integrated fluorescence of each unit cell, which corresponds with our argument that fluorescent microtubules are conserved for each unit cell. We first subtract the background signal and segment unit cells

with the same threshold value as for the $t = 0$ timepoint. However, as unit cells begin to deform due to their fluorescent microtubules dispersing, the integrated fluorescence signal of the newly segmented unit cells will differ from that of the first time point, which translates to a different number of fluorescent microtubules. As a result, for images after the first frame immediately succeeding photobleaching, we expand or reduce the segmentation of unit cells by adding or subtracting pixels around their boundaries until we obtain the same total fluorescence as the $t = 0$ timepoint. Fig. 6.6(C) elaborates on the scheme for correcting to obtain the same integrated intensity as in the initial time frame to within a specified tolerance. To do this, each unit cell is then paired with itself from the previous time step by determining nearest centroids. Due to the minimal reduction in fluorescence intensity from the projector during imaging as discussed in Sec 6.4, we compare the total fluorescence intensity of the segmented unit cell in the frame of interest to that of the same unit cell from the first frame. 1 layer of pixel beyond (within) the boundary of the unit cell are histogrammed and Otsu thresholded to distinguish microtubule regions to background regions. The pixels that make up the foreground (background) according to the thresholding are then added (subtracted) until the integrated fluorescence falls within 0.01 tolerance of the original fluorescence intensity.

To understand how the choice of relative tolerance in the integrated fluorescence affects that computed effective diffusion constant D_{eff}, we performed the unit cell segmentation and tracking under different tolerance levels. Fig 6.7 shows that while a tolerance below 0.015 leads to a constant effective diffusion constant, increasing the tolerance above this point leads to a monotonic decrease in the D_{eff}. This suggests that the area trajectories of unit cells can be highly sensitive to the tolerance given to the microtubule preservation count. This control also indicates that the area trajectories of unit cells are not markedly different below the 0.015 tolerance and yields robust measurements of the area trajectories and by extension fits of the effective diffusion constants.

Unit cell centroids, areas, and fluorescence intensities are then computed in addition to the pixel-weighted center of the entire contracting network after this intensity-adjusted processing for all of the unit cells. Image processing of a unit cell terminates when it is found to overlap with another unit cell during the fluorescence intensity correction scheme as this indicates that the unit cells have begun to merge and by the next time point thus microtubules from one unit cell can no longer be distinguished

from those of the other.

6.5 Photobleaching Performed at Different Times During Contraction

While all experiments in the manuscript involve activating a circular region of the motor-microtubule system with a radius of 125 μm, that is, all experiments are assumed to have the same amount of total tubulin, replicates may differ by the time during the contraction process when the network is photobleached. SI Fig. 6.8 shows three such cases of this photobleaching on three separate replicates: (A) shortly after the microtubule network has formed and begun to contract, (B) roughly halfway between the initial and final sizes of the network, and (C) towards the end of contraction. In all three cases, we observe a diffusive-like effect in the bulk of the network. Data for each individual replicate is available in SI Sec 6.7.

6.6 Data Analysis

Contraction rate computation

In the main text, we use the centroids of fluorescent unit cells obtained in SI Sec. 6.4 to demonstrate that contraction speed of the microtubule network scales linearly with distance from the network center. We first obtain the speed that each unit cell centroid is moving toward the center as a function of time. For each unit cell, we observe a linear relation between the centroid distance from the network center and time after photobleaching of the form

$$r = v_c\, t + r_0, \tag{6.1}$$

where r is the unit cell centroid distance from the network center, v_c is the speed of the unit cell (which will take to be positive here but directed toward the origin), t is the time since photobleaching, and r_0 is the initial centroid distance from the network center immediately after photobleaching.

Based on the extracted contraction speed and distances for all of the unit cells for a given motor type, we noted a linear relation between radius r and centroid speed v_c of the form

$$v_c = \alpha\, r + v_0, \tag{6.2}$$

where α is the contraction rate in units of inverse time and v_0 is the contraction speed at the network center. To this end, we aim to compute α and v_0. Although we expect the speed at the network center to be 0, we relax this assumption for our analysis. To more carefully compute the rate of contraction of the network and

determine the range of credibility of the computed rate, we use a Bayesian approach. Specifically, we compute the probability of α and v_0 given the contraction speed and distance of each unit cell from the network center $(r_0, v_c)_i$, $P\left(\alpha, v_0 | \{(r_0, v_c)_i\}\right)$, where i denotes each unit cell. Here, we use the centroid distance immediately after photobleaching but found that another criterion such as the median of the centroid distance over the course of the time window analyzed does not dramatically affect the results due to the relatively small travel ($\frac{\Delta r}{r_0} < 10\%$ for Δr the distance traveled over the entire time course) the unit cells undergo.

We note from Bayes' Theorem that

$$P\left[\alpha, v_0 | \{(r_0, v_c)_i\}\right] = \frac{P\left[\{(r_0, v_c)_i\} | \alpha, v_0\right] P\left(\alpha, v_0\right)}{P\left[\{(r_0, v_c)_i\}\right]}, \tag{6.3}$$

$$= \frac{\prod_i P\left[(r_0, v_c)_i | \alpha, v_0\right]}{\prod_i P\left[(r_0, v_c)_i\right]} P\left(\alpha, v_0\right), \tag{6.4}$$

$$\propto \prod_i P\left[(r_0, v_c)_i | \alpha, v_0\right] P\left(\alpha, v_0\right), \tag{6.5}$$

where we drop the denominator on the right-hand side as it does not involve the parameters we want to find, thus making the two sides proportional to each other. Here, $P\left[(r_0, v_c)_i | \alpha, v_0\right]$ is the likelihood distribution of getting the $(r_0, v_c)_i$ that we did given α and v_0 while $P\left(\alpha, v_0\right)$ is the prior distribution of our two parameters.

We expect that our priors on α and v_0 are independent of each other, so we can break up the probability function into a product of two functions

$$P\left(\alpha, v_0\right) = p\left(\alpha\right) p\left(v_0\right). \tag{6.6}$$

Meanwhile, we can rearrange each likelihood function as a product of two probabilities. The probability of getting $(r_0, v_c)_i$ given our parameters is also the probability of getting $v_{c,i}$ given our parameters and $r_{0,i}$ times the probability of getting $r_{0,i}$, or

$$P\left((r_0, v_c)_i | \alpha, v_0\right) = P\left(v_{c,i} | \alpha, v_0, r_{0,i}\right) P\left(r_{0,i}\right), \tag{6.7}$$

$$\propto P\left(v_{c,i} | \alpha, v_0, r_{0,i}\right), \tag{6.8}$$

where we change to a proportionality again as $P\left(r_{0,i}\right)$ is independent of our parameters. Here, we expect that our contraction speed for a given unit cell $v_{c,i}$ comes from a Normal distribution where the mean value is $\alpha\, r_{0,i} + v_0$ and standard deviation σ. This means that we will also need a prior on σ. This means that our distribution

really takes the form of

$$P\left(\alpha, v_0, \sigma | \left\{(r_0, v_c)_i\right\}\right) \propto P(\alpha)\, P(v_0)\, P(\sigma) \prod_i P\left(v_{c,i} | \alpha, v_0, \sigma, r_{0,i}\right). \tag{6.9}$$

As a result, we say that our likelihood takes the form

$$v_{c,i} \backsim \text{Normal}\left(\alpha r_{0,i} + v_0, \sigma^2\right). \tag{6.10}$$

We then defined our priors to be that α is drawn from the half-normal distribution where $\alpha > 0$ as we are working with speeds of contraction, σ is also drawn from a half-normal distribution and enforced to be positive, and v_0 is drawn from a normal distribution about $v = 0$. We make the offset a normal rather than a half-normal distribution as there may be a value of $r > 0$ for which the contraction stops, which for a positive slope would mean a negative speed at $r = 0$. Put together, we have the following priors

$$\alpha \backsim \text{Half-Normal}(0, 1), \tag{6.11}$$

$$\sigma \backsim \text{Half-Normal}(0, 1), \tag{6.12}$$

$$v_0 \backsim \text{Normal}(0, 1). \tag{6.13}$$

We sampled the joint distribution of (α, v_0, σ) by Hamiltonian Markov chain Monte Carlo using the Stan probabilistic program [11]. From each (α, v_0) that is sampled we compute the mean value $\mu = \alpha\, r + v_0$ for $0 \leq r \leq R$ where R is the distance of the farthest centroid from the network center and report the median and 95% credible region in Fig. 2 and 4-6 of the main text.

Computing the best fit effective diffusion constant

In the main manuscript, we use an advection-diffusion model to compute an effective diffusion constant to quantify the difference in area between the experimental normalized area trajectories and the pure contraction bound (signifying no diffusion). To do so, we used the finite element method (FEM) on individual unit cells of initially uniform concentration subject to the advection-diffusion equation as described in Eq. 3 of the main manuscript. We then processed the simulated concentration field data with a similar integrated particle count method as described in SI Sec. 6.4 in order to compute the area of the unit cells in time. This analysis gives rise to a family of normalized area trajectories for a fixed contraction rate and variable diffusion constant. In order to compute the effective diffusion constant from, say, the median normalized area trajectories from a given set of experimental conditions,

we take the simulated area trajectory for one of the diffusion constants and the area trajectory of the experimentally-obtained contraction rate and compute the sum of the square of the difference between the two trajectories across time. For each of the quartiles, the effective diffusion constant is computed as the one whose area trajectory minimizes the sum of the differences squared.

6.7 Experimental Variation of Contraction Speed and Normalized Area Trajectories

Individual replicates of contraction speed and normalized area trajectories

In the main manuscript, we computed the contraction rate using all of the replicates of a given set of experimental conditions. However, to exhibit experimental variation between replicates, we present in Fig. 6.9 the contraction speed and normalized area data for all of the replicates involving Ncd236 at 1400 μM ATP and 0.5 mg/mL pluronic. Note that the line in the contraction speed is the same as shown in Fig. 2(D) of the main manuscript where the contraction rate $\alpha = 0.002$ sec^{-1} for comparison of how each replicate compares to the computed line. This contraction rate is also used for the pure contraction bound shown on the normalized area data. The time noted at the top of each contraction speed plot marks the time into the experiment that the photobleaching was performed, with the plots organized in order of ascending time into the experiment of photobleaching. We note that while the variability in times depends in part on the time needed for the microtubule network to form and begin contracting, it is more generally dependent on how far into the contraction process the network has progressed. Thus, later times generally denote replicates where the microtubule network is approaching the end of the contraction phase. We note that the contraction speed and area trajectory data across replicates suggest no clear trend in either of these metrics against the time into contraction.

We also take note of some of the early contraction photobleach datasets, notably corresponding to time points 302 sec (first one), 322 sec, 342 sec, and most notably 662 sec and 682 sec, where the contraction speed appears to be lower than the line particularly at high radii. We again emphasize that these replicates were photobleached early in the contraction process and possibly while the network is still forming. One potential interpretation of the low velocities is that this early on in the contraction rate, there is a delayed response between the contraction happening at the center and the contraction happening toward the extremities. Another possibility is that there may be unexpected chemical effects that cause the network

in these replicates to take more time to form and lead to odd contraction effects. As these contraction speeds fall below the linear contraction profile shown in red, we suspect that this means that removing these datasets would translate to a new linear contraction profile with a higher slope, e.g., a higher contraction rate and would further translate to a sharper decrease in the normalized area trajectory of a purely contracting unit cell, thus having little bearing on the observation that the unit cells exhibit a diffusive-like effect. However, for the sake of transparency, we elect to keep these datasets in the reporting.

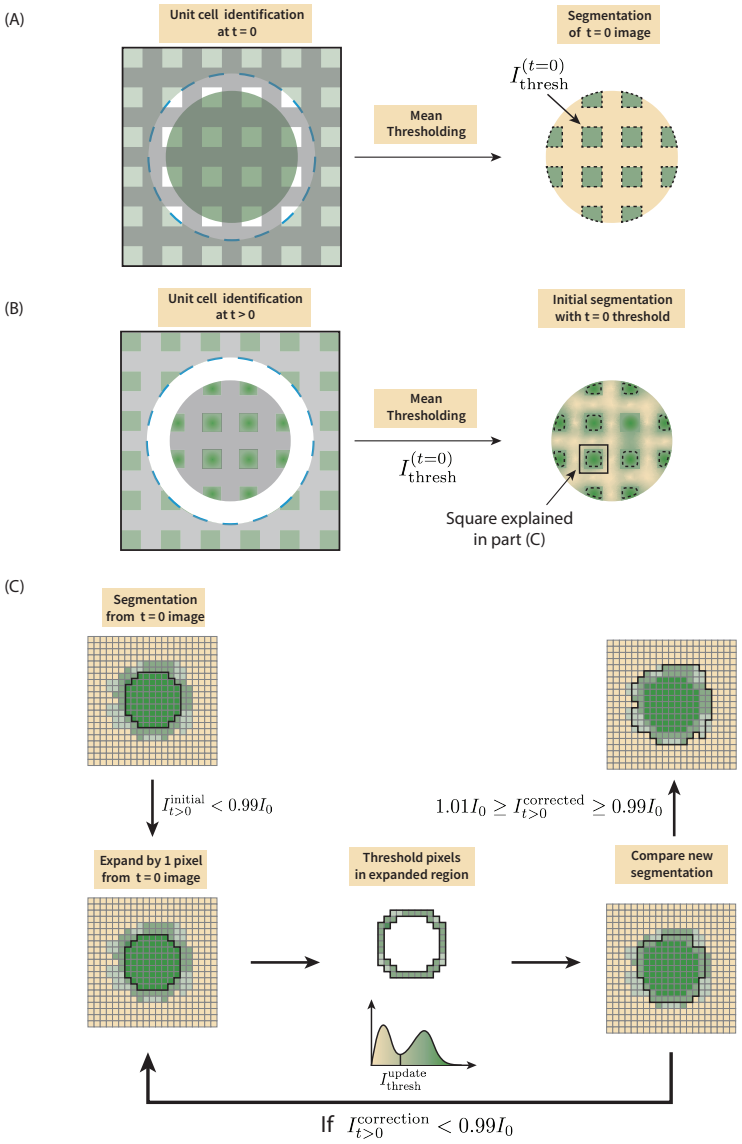

Figure 6.6: **Unit cell segmentation correction scheme.** (A) Unit cells in the first image after photobleaching are segmented using mean thresholding to obtain an initial threshold value $I_{\text{thresh}}^{(t=0)}$. Dashed blue circle denotes the extent of the projected light within which motors dimerize, causing the network to couple and contract (green circle). (B) Unit cells of later frames are initially segmented using $I_{\text{thresh}}^{(t=0)}$. (C) The integrated intensity of each unit cell after the initial segmentation $I_{t>0}^{\text{initial}}$ is compared against that for the $t = 0$ case, I_0. In instances where $I_{t>0} < 0.99I_0$, the pixels in a single layer beyond the segmentation boundary are histogrammed and thresholded to distinguish pixels containing microtubules with those regions that make up the background. These pixels with signal are then added, the integrated intensity is recomputed and compared again to I_0. The process is repeated until the integrated intensity falls within 1% of I_0.

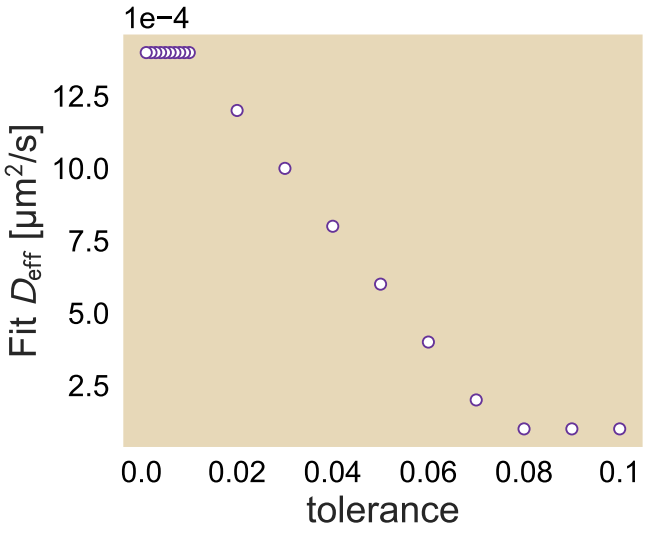

Figure 6.7: **Effective diffusion constant fits against various tolerances in the relative unit cell fluorescence.** The tolerance is the fractional difference in fluorescence intensity between the unit cell in the first frame and the unit cell at a later time point. Dataset used on Ncd236 at saturated ATP concentration (1.4 mM).

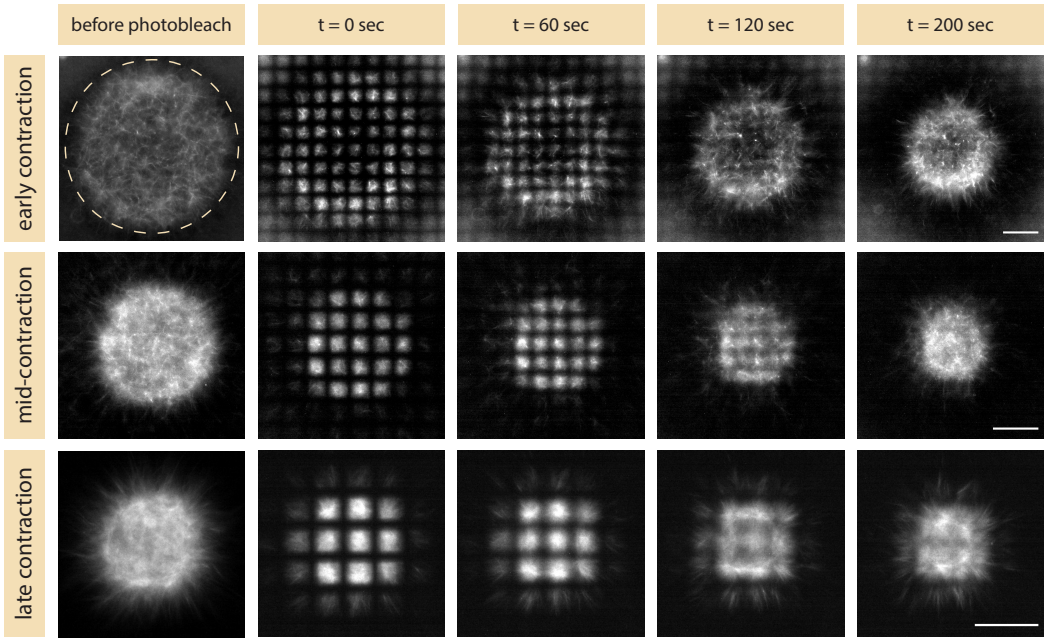

Figure 6.8: **Photobleaching a grid pattern onto the contracting microtubule network.** Here, three different time points during microtubule network contraction are shown where photobleaching is applied: (A) early in contraction as the network pulls away from the reservoir of uncoupled microtubules; (B) in the middle of the contracting phase; and (C) toward the end of contraction before the network no longer appears to shrink. From left to right, columns of images correspond to various times relative to photobleaching: immediately before photobleaching, immediately after photobleaching (0 seconds), then 60 seconds, 120 seconds, and 200 seconds after photobleaching. Dashed line in the pre-bleached early contracting microtubule network outlines the circular activation pattern used for iLid- and micro-tagged motor dimerization. Scale bars in the t = 200 sec column apply to their respective rows of images. All three examples correspond to experiments using Ncd236 and 1.4 mM ATP, which are the two parameters tuned later. All experiments in the manuscript use the same circular activation pattern of radius 125 μm regardless of time into contraction process when the photobleaching occurs.

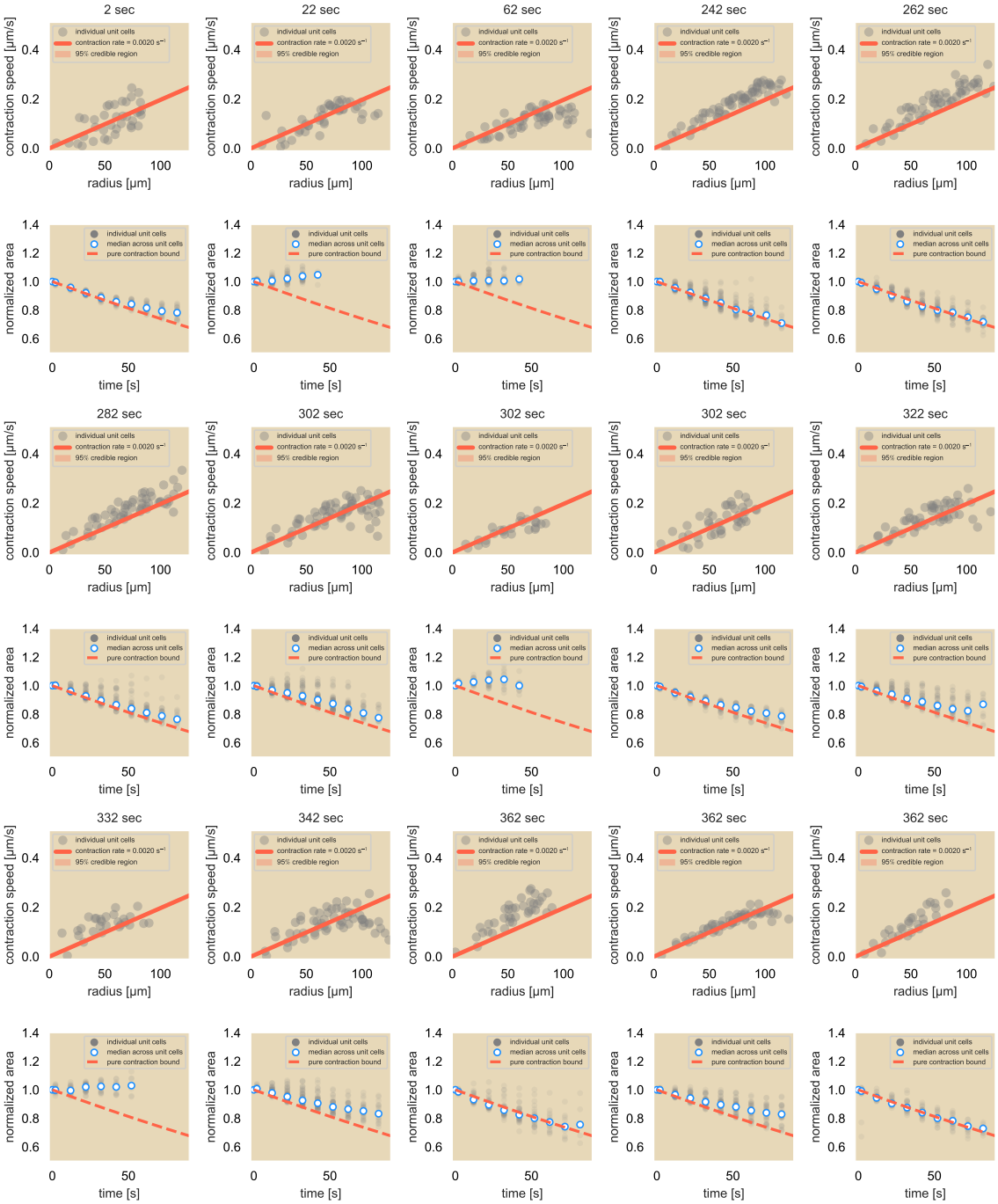
2 sec
22 sec
62 sec
242 sec
262 sec
282 sec
302 sec
302 sec
302 sec
322 sec
332 sec
342 sec
362 sec
362 sec
362 sec
contraction speed [μm/s]
radius [μm]
normalized area
time [s]
individual unit cells
contraction rate = 0.0020 s⁻¹
95% credible region
median across unit cells
pure contraction bound

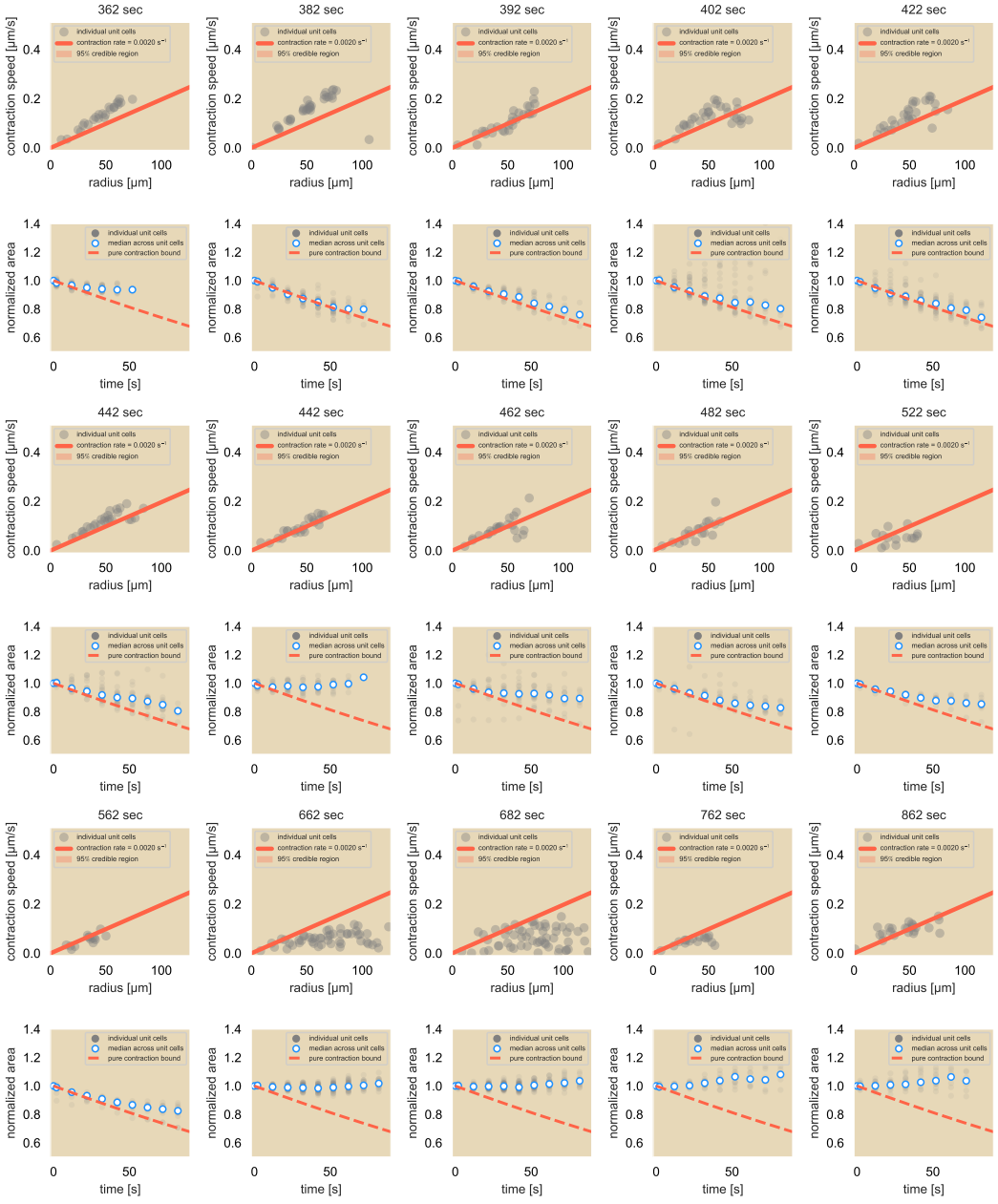

Figure 6.9: **Contraction speed (odd rows) and normalized area trajectory (even rows) of each experimental replicate using 0.5 mg/mL pluronic, 1400 μM ATP, and Ncd236.** The lines in the plots of contractions speed data and in the plots of the area trajectory are the same as in Fig. 2(D) and 2(F), respectively, of the main manuscript. The time at the top of each contraction speed plot marks the time into the experiment that the photobleaching was performed.

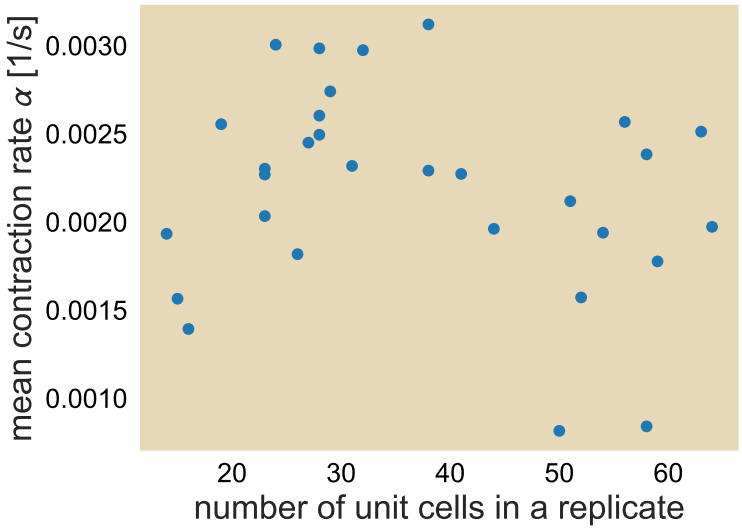

Figure 6.10: **Median contraction rate of each replicate as a function of their number of unit cells.** Contraction rate measured for all replicates of Ncd236 at 1.4 mM ATP and 0.5 mg/mL of pluronic.

Contraction Rate per Replicate

Although we computed a contraction rate compiling all of the replicates, we examine the spread in the median contraction rate for each case. Fig. 6.10 shows the median contraction rate α of each replicate as a function of the number of unit cells that make up the photobleached network for that replicate. This corresponds inversely with how far into the contraction process that we wait before photobleaching the network, that is, fewer unit cells corresponds to photobleaching network when it is smaller from having contracted further. Here, we see that most of the contraction rates are strongly concentrated between 0.0015 and 0.0025 s^{-1}. Furthermore, we do not identify a clear trend between the contraction rate and how far along the network is in the contraction process. As a result, we do not find that the computing the contraction rate from combining all of the replicates will result in a dramatically different outcome from if we treat each replicate individually.

6.8 Deformation of a Square Due Solely to Contraction

In the main text, we observed that each fluorescent unit cell on average conserves its area while its center of mass moves toward the network center with speed that is linearly dependent on the distance from the center. We compute the expected area of each unit cell had the network elastically contracted due solely to the observed

global contraction. We define the contraction velocity field $\mathbf{v}(x, y)$ as

$$\mathbf{v}(x, y) \equiv -\alpha \left(x\hat{x} + y\hat{y} \right), \tag{6.14}$$

where α is the contraction rate as computed in SI Sec. 6.6 and reported in the main manuscript. This means that after a time interval Δt a point (x, y) subject to this advective flow will be displaced in the x- and y- directions according to

$$\Delta X = v_x \Delta t = -\alpha x \Delta t, \tag{6.15}$$

$$\Delta Y = v_y \Delta t = -\alpha y \Delta t, \tag{6.16}$$

so the point at the later time (x', y') relates to its earlier time point by

$$x' = x + \Delta X = x \left(1 - \alpha \Delta t\right) \tag{6.17}$$

$$y' = y + \Delta Y = y \left(1 - \alpha \Delta t\right). \tag{6.18}$$

Suppose we looked at the four corners of a unit cell, labeled as A, B, C, D as depicted in Fig. 6.11. If we assign their coordinates as

$$\mathrm{A} \rightarrow (x_\mathrm{A}, y_\mathrm{A}), \tag{6.19}$$

$$\mathrm{B} \rightarrow (x_\mathrm{B}, y_\mathrm{B}), \tag{6.20}$$

$$\mathrm{C} \rightarrow (x_\mathrm{C}, y_\mathrm{C}), \tag{6.21}$$

$$\mathrm{D} \rightarrow (x_\mathrm{D}, y_\mathrm{D}). \tag{6.22}$$

Under a rectangular geometry, we can choose two vertices diagonally across from each other on the rectangle and write their x- and y- coordinates with the coordinates of the other two diagonal vertices, so with a choice of using coordinates from A and D, the coordinates for B and C become

$$\mathrm{A} \rightarrow (x_\mathrm{A}, y_\mathrm{A}), \tag{6.23}$$

$$\mathrm{B} \rightarrow (x_\mathrm{D}, y_\mathrm{A}), \tag{6.24}$$

$$\mathrm{C} \rightarrow (x_\mathrm{A}, y_\mathrm{D}), \tag{6.25}$$

$$\mathrm{D} \rightarrow (x_\mathrm{D}, y_\mathrm{D}). \tag{6.26}$$

Under the deformation mapping, their new coordinates, labeled as A′, B′, C′, and D′ get mapped on as

$$\mathrm{A}' \rightarrow \left[x_\mathrm{A} \left(1 - \alpha \Delta t\right), y_\mathrm{A} \left(1 - \alpha \Delta t\right)\right], \tag{6.27}$$

$$\mathrm{B}' \rightarrow \left[x_\mathrm{D} \left(1 - \alpha \Delta t\right), y_\mathrm{A} \left(1 - \alpha \Delta t\right)\right], \tag{6.28}$$

$$\mathrm{C}' \rightarrow \left[x_\mathrm{A} \left(1 - \alpha \Delta t\right), y_\mathrm{D} \left(1 - \alpha \Delta t\right)\right], \tag{6.29}$$

$$\mathrm{D}' \rightarrow \left[x_\mathrm{D} \left(1 - \alpha \Delta t\right), y_\mathrm{D} \left(1 - \alpha \Delta t\right)\right]. \tag{6.30}$$

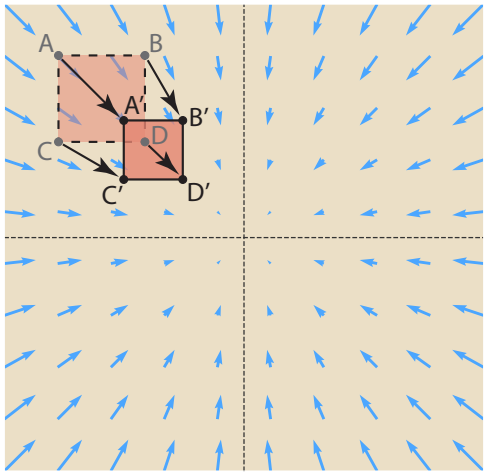

Figure 6.11: **Schematic of unit cell contraction due purely to the advective velocity field.** An advective velocity field scales linearly with distance from the origin while pointing radially inward and is shown in blue. The points at the corners of the square (A, B, C, D) are mapped after some time Δt to the points (A′, B′, C′, D′).

Eqs. 6.30 tells us that under this particular velocity field, any two points that are horizontally or vertically aligned will maintain the same horizontal or vertical alignment, respectively, even at later times. Thus, a square will preserve its shape in time.

We next examine what happens to the area of a unit cell had the only effect been the global contraction. In this case, we can compare the area of the square before and after the deformation. To compute the area swept out by (A,B,C,D), we multiply the line segment between B and D, L_{BD} with the line segment between C and D, L_{CD}:

$$\sigma_{(\mathrm{A,B,C,D})} = L_{\mathrm{BD}} \times L_{\mathrm{CD}}, \tag{6.31}$$

$$= \left[\sqrt{(x_{\mathrm{B}} - x_{\mathrm{D}})^2 + (y_{\mathrm{B}} - y_{\mathrm{D}})^2}\right] \times \left[\sqrt{(x_{\mathrm{D}} - x_{\mathrm{C}})^2 + (y_{\mathrm{D}} - y_{\mathrm{C}})^2}\right], \tag{6.32}$$

$$= (y_{\mathrm{A}} - y_{\mathrm{D}}) \times (x_{\mathrm{D}} - x_{\mathrm{A}})\,. \tag{6.33}$$

As noted from Eq. 6.26, we used the fact that $x_{\mathrm{B}} = x_{\mathrm{D}}$, $y_{\mathrm{B}} = y_{\mathrm{A}}$, $x_{\mathrm{C}} = x_{\mathrm{A}}$, and $y_{\mathrm{C}} = y_{\mathrm{D}}$ to simplify the equation down in terms of two coordinates. In comparison,

the area of the deformed unit cell swept out by (A′, B′, C′, D′) takes the form

$$\sigma_{(\mathrm{A}',\mathrm{B}',\mathrm{C}',\mathrm{D}')} = L_{\mathrm{B}'\mathrm{D}} \times L_{\mathrm{C}'\mathrm{D}'}, \tag{6.34}$$

$$= \left[\sqrt{(x_{\mathrm{B}'} - x_{\mathrm{D}'})^2 + (y_{\mathrm{B}'} - y_{\mathrm{D}'})^2}\right] \times \left[\sqrt{(x_{\mathrm{D}'} - x_{\mathrm{C}'})^2 + (y_{\mathrm{D}'} - y_{\mathrm{C}'})^2}\right], \tag{6.35}$$

$$= (y_{\mathrm{A}'} - y_{\mathrm{D}'}) \times (x_{\mathrm{D}'} - x_{\mathrm{A}'}), \tag{6.36}$$

$$= [y_{\mathrm{A}}(1 - \alpha\Delta t) - y_{\mathrm{D}}(1 - \alpha\Delta t)] \times [x_{\mathrm{D}}(1 - \alpha\Delta t) - x_{\mathrm{A}}(1 - \alpha\Delta t)], \tag{6.37}$$

$$= (y_{\mathrm{A}} - y_{\mathrm{D}})(1 - \alpha\Delta t) \times (x_{\mathrm{D}} - x_{\mathrm{A}})(1 - \alpha\Delta t), \tag{6.38}$$

$$= (y_{\mathrm{A}} - y_{\mathrm{D}}) \times (x_{\mathrm{D}} - x_{\mathrm{A}})(1 - \alpha\Delta t)^2, \tag{6.39}$$

$$= \sigma_{(\mathrm{A},\mathrm{B},\mathrm{C},\mathrm{D})}(1 - \alpha\Delta t)^2. \tag{6.40}$$

Thus we find that the area of the unit cell subject solely to the contraction would decrease by $(1 - \alpha\Delta t)^2$ after a time period Δt. This comes in contrast to the results that we found experimentally where the area of the fluorescent unit squares remains greater than the pure contraction bound during the contraction process suggesting a mechanism that disperses microtubules against the global contraction.

6.9 2D Linear Advection-Diffusion Model

In the work presented in the main manuscript, we argue for an advection-diffusion model to describe the redistribution of microtubules in the bulk of the contracting network. In this section, we explore Eq 3 as shown in the manuscript to examine whether the model could reasonably recapitulate the experimental observations as a tool for computing an effective diffusion constant for the diffusive-like spread of microtubules in the bulk. While the main manuscript uses the finite element method (FEM) to simulate the area change of a concentration of particles localized to a square, as is the case for microtubules of a unit cell, we first develop an intuition for this equation for a series of initial conditions and at steady state. To validate the FEM approach before applying it to the unit square case, we numerically and analytically solve these initial conditions and directly compare them. This theoretical analysis is meant to explore the filament concentration when subject to a linear contraction velocity profile. We note here that we later invoke the Sturm-Liouville Theorem, which we elaborate on in SI Sec 6.10.

In the 2D telescoping case, we assume that we are carrying out an aster assay experiment where we dimerize motors (and thus couple microtubules) in a circular

region of radius R. We assume that the distributions of motors and microtubules are strictly radially dependent and thus have no angular dependence. Finally, we model the velocity profile of the microtubule movement by assuming radially inward advection of particles where those that lie further away from the origin move faster than those toward the center as given by

$$\mathbf{v} = -\alpha r \hat{r}. \tag{6.41}$$

The advection-diffusion equation then takes the form

$$\frac{\partial c}{\partial t} = D\nabla^2 c - \nabla \cdot (\mathbf{v}c), \tag{6.42}$$

$$= \frac{D}{r}\frac{\partial}{\partial r}\left(r\frac{\partial c}{\partial r}\right) + \alpha\frac{1}{r}\frac{\partial}{\partial r}(r^2 c), \tag{6.43}$$

$$= D\frac{\partial^2 c}{\partial r^2} + \frac{D}{r}\frac{\partial c}{\partial r} + \alpha r\frac{\partial c}{\partial r} + 2\alpha c, \tag{6.44}$$

$$= D\frac{\partial^2 c}{\partial r^2} + \left(\frac{D}{r} + \alpha r\right)\frac{\partial c}{\partial r} + 2\alpha c, \tag{6.45}$$

$$\frac{1}{D}\frac{\partial c}{\partial t} = \frac{\partial^2 c}{\partial r^2} + \left(\frac{1}{r} + \frac{\alpha r}{D}\right)\frac{\partial c}{\partial r} + \frac{2\alpha c}{D}. \tag{6.46}$$

We first follow the procedure of separation of variables $c(r,t) = \Phi(r)T(t)$ and determine that the time-dependent component takes on the familiar form of $e^{-Dk^2 t}$. This ansatz is then applied to Eq. 6.46 and we rewrite the spatial component of the concentration as

$$-k^2\Phi = \frac{\mathrm{d}^2\Phi}{\mathrm{d}r^2} + \left(\frac{1}{r} + \frac{\alpha r}{D}\right)\frac{\mathrm{d}\Phi}{\mathrm{d}r} + \frac{2\alpha\Phi}{D}, \tag{6.47}$$

$$0 = r\frac{\mathrm{d}^2\Phi}{\mathrm{d}r^2} + \left(1 + \frac{\alpha r^2}{D}\right)\frac{\mathrm{d}\Phi}{\mathrm{d}r} + \left(\frac{2\alpha}{D} + k^2\right)r\Phi. \tag{6.48}$$

We will define a new length scale $\lambda^2 \equiv \frac{D}{\alpha}$ as well as a change of variables $\rho \equiv \frac{r}{\lambda}$ and $\tilde{k} \equiv \lambda k$. In this case, Eq. 6.48 takes the altered form

$$0 = \rho\frac{\mathrm{d}^2\Phi}{\mathrm{d}\rho^2} + (1+\rho^2)\frac{\mathrm{d}\Phi}{\mathrm{d}\rho} + \left(2 + \tilde{k}^2\right)\rho\Phi. \tag{6.49}$$

By following a prescription on which we elaborate further in SI Sec 6.10, we obtain a weighting function that will help us compute the eigenfunctions using Eq. 6.69, namely,

$$m(\rho) = e^{\frac{\rho^2}{2}}. \tag{6.50}$$

When we multiply Eq. 6.49 by the multiplicative function, we get

$$0 = \rho\, e^{\frac{\rho^2}{2}} \frac{\mathrm{d}^2\Phi}{\mathrm{d}\rho^2} + (1+\rho^2) e^{\frac{\rho^2}{2}} \frac{\mathrm{d}\Phi}{\mathrm{d}\rho} + \left(2 + \tilde{k}^2\right) \rho\, e^{\frac{\rho^2}{2}} \Phi, \tag{6.51}$$

$$\frac{\mathrm{d}}{\mathrm{d}\rho}\left[\rho\, e^{\frac{\rho^2}{2}} \frac{\mathrm{d}\Phi}{\mathrm{d}\rho}\right] + 2\rho\, e^{\frac{\rho^2}{2}} \Phi = -\tilde{k}^2 \rho\, e^{\frac{\rho^2}{2}} \Phi. \tag{6.52}$$

Through the Sturm-Liouville Theorem as described in SI Sec 6.10, specifically Eq. 6.52, we find that the weighting function differs from the multiplicative function due to the inclusion of the prefactor ρ. In this case, the weighting function $w(\rho)$ as well as $p(\rho)$ and $q(\rho)$ are given as

$$w(\rho) = p(\rho) = q(\rho) = \rho\, e^{\frac{\rho^2}{2}}. \tag{6.53}$$

Furthermore, we observe that the eigenvalues take the form $\tilde{k}^2$. Solutions of Φ from Eq. 6.52 are obtained from Wolfram Alpha and take the form

$$\Phi_{\mathrm{ss}}(\rho) = c_{\mathrm{ss}}\, e^{-\frac{\rho^2}{2}}, \tag{6.54}$$

$$\Phi_{\mathrm{dyn}}(\rho) = c_1\, e^{-\frac{\rho^2}{2}}\, {}_1F_1\left(-\frac{\tilde{k^2}}{2}; 1; \frac{\rho^2}{2}\right) + c_2\, G^{2,0}_{1,2}\left(\frac{\rho^2}{2}\middle| \begin{matrix} -\frac{\tilde{k}^2}{2} \\ 0, 0 \end{matrix}\right), \tag{6.55}$$

where $G^{m,n}_{p,q}\left(z\middle| \begin{matrix} a_1,\ldots,a_p \\ b1,\ldots,b_q \end{matrix}\right)$ is the Meijer G-function (we split up the eigenfunctions as dynamic and steady-state terms for now). We note here that the arguments of the Meijer G-function are such that the function diverges at the origin. As our system is defined as $0 \leq r \leq R$, we can say that $c_2 = 0$. Thus, our eigenfunctions are

$$\Phi_{\mathrm{ss}}(\rho) = c_{\mathrm{ss}}\, e^{-\frac{\rho^2}{2}}, \tag{6.56}$$

$$\Phi_{\mathrm{dyn}}(\rho) = c_1\, e^{-\frac{\rho^2}{2}}\, {}_1F_1\left(-\frac{\tilde{k^2}}{2}; 1; \frac{\rho^2}{2}\right), \tag{6.57}$$

where we note that in the case of $\tilde{k} = 0$, we go from the dynamic eigenfunction to the static eigenfunction.

No-flux boundary condition

In the work presented here, there is no inflow or outflow of material at the boundary. Thus, we impose the boundary condition $\mathbf{J}\Big|_{r=R} = 0$. This means that

$$J_r\Big|_{r=R} = D\frac{\mathrm{d}\Phi}{\mathrm{d}r} - v(R)\Phi(R) = D\frac{\mathrm{d}\Phi}{\mathrm{d}r}\Big|_{r=R} + \alpha R \Phi(R) = 0. \tag{6.58}$$

We then need to ensure that the boundary condition is satisfied for the dynamic eigenfunction. We start by taking the derivative of the eigenfunction:

$$\frac{\mathrm{d}\Phi}{\mathrm{d}r} = -\frac{c_1\,\rho}{\lambda}\,e^{-\frac{\rho^2}{2}}\left[\frac{\tilde{k}^2}{2}\,{}_1F_1\left(1-\frac{\tilde{k}^2}{2};2;\frac{\rho^2}{2}\right)+{}_1F_1\left(-\frac{\tilde{k}^2}{2};1;\frac{\rho^2}{2}\right)\right], \tag{6.59}$$

$$\left.\frac{\mathrm{d}\Phi}{\mathrm{d}r}\right|_{r=R} = -\frac{c_1\,\alpha R}{D}\,e^{-\frac{\alpha R^2}{2D}}\left[\left(\frac{Dk^2}{2\alpha}\right){}_1F_1\left(1-\frac{Dk^2}{2\alpha};2;\frac{\alpha R^2}{2D}\right)+{}_1F_1\left(-\frac{Dk^2}{2\alpha};1;\frac{\alpha R^2}{2D}\right)\right], \tag{6.60}$$

so when applied to the boundary condition, we get

$$D\left.\frac{\mathrm{d}\Phi}{\mathrm{d}r}\right|_{r=R}+\alpha R\Phi(R) = -c_1\,\alpha R\,e^{-\frac{\alpha R^2}{2D}}\left(\frac{Dk^2}{2\alpha}\right){}_1F_1\left(1-\frac{Dk^2}{2\alpha};2;\frac{\alpha R^2}{2D}\right) \tag{6.61}$$

$$-\,c_1\,\alpha R\,e^{-\frac{\alpha R^2}{2D}}\,{}_1F_1\left(-\frac{Dk^2}{2\alpha};1;\frac{\alpha R^2}{2D}\right) \tag{6.62}$$

$$+\,c_1\,\alpha R\,e^{-\frac{\alpha R^2}{2D}}\,{}_1F_1\left(-\frac{Dk^2}{2\alpha;1;\frac{\alpha R^2}{2D}}\right). \tag{6.63}$$

We are then left with the simplified equation,

$$\left(\frac{Dk^2}{2\alpha}\right){}_1F_1\left(1-\frac{Dk^2}{2\alpha};2;\frac{\alpha R^2}{2D}\right)=0. \tag{6.64}$$

Here, $k=0$ is satisfied, which yields the steady-state solution. Fig. 6.12 shows the zeros when we set $\frac{R}{\lambda}=3.16$. The first few non-zero eigenvalues are then $\tilde{k}=0.474$,

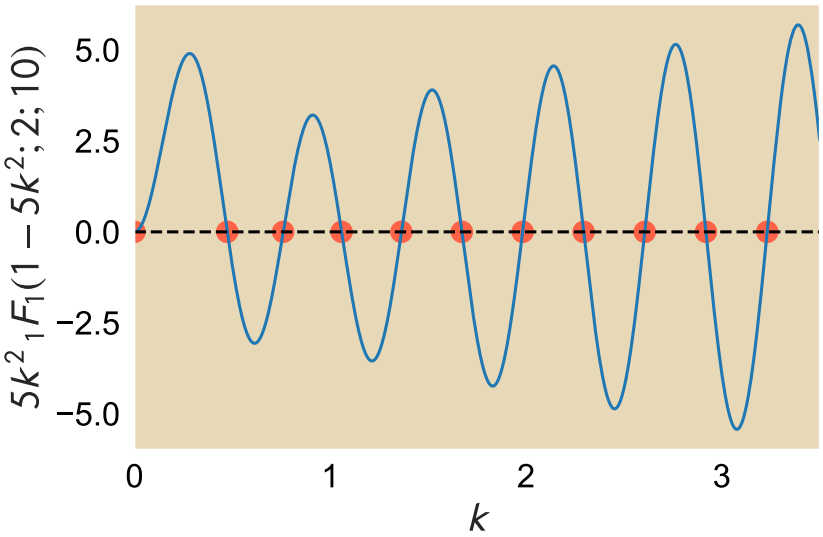

Figure 6.12: **Zeros of k for $\frac{\lambda^2k^2}{2}\,{}_1F_1\left(1-\frac{\lambda^2k^2}{2};2;\frac{R^2}{2\lambda^2}\right)=0$ where $\frac{R}{\lambda}=3.16$.** Red dots are overlayed with the points where the Kummer confluent hypergeometric function crosses the x-axis.

0.759, 1.058, 1.354, and 1.672. Here, we observe a similar oscillator pattern to the zeros of the system. Once again, we see that there are multiple values of k that satisfy the boundary conditions. This means that the solution to the advection-diffusion problem once both boundary and initial conditions are satisfied, is a superposition of the different eigenfunctions:

$$c(r,t) = c_{\text{ss}}\, e^{-\frac{\alpha r^2}{2D}} + e^{-\frac{\alpha r^2}{2D}} \sum_{i=1}^{\infty} c_i e^{-Dk_i^2 t}\, {}_1F_1\Big(-\frac{Dk_i^2}{2\alpha}; 1; \frac{\alpha r^2}{2D}\Big). \tag{6.65}$$

For simplicity, we will reintroduce the length scale $\lambda \equiv \sqrt{\frac{D}{\alpha}}$ so that the equation is simplified as

$$c(r,t) = c_{\text{ss}}\, e^{-\frac{r^2}{2\lambda^2}} + e^{-\frac{r^2}{2\lambda^2}} \sum_{i=1}^{\infty} c_i e^{-Dk_i^2 t}\, {}_1F_1\Big(-\frac{\lambda^2 k_i^2}{2}; 1; \frac{r^2}{2\lambda^2}\Big). \tag{6.66}$$

We turn next to the Sturm-Liouville Theory in SI Sec 6.10 before applying these equations to three simple initial conditions as validation of the theory and the finite element methods (FEM) approach.

6.10 Sturm-Liouville Theory

The Sturm-Liouville theory says that all well-behaved second-order linear ordinary differential equations that can be written in the form

$$\frac{\mathrm{d}}{\mathrm{d}x}\Big[p(x)\frac{\mathrm{d}y}{\mathrm{d}x}\Big] + q(x)\, y(x) = -\lambda\, w(x)\, y(x), \tag{6.67}$$

have real eigenvalues with an orthonormal basis of eigenfunctions. Curiously, these equations also have a prescription for determining these eigenfunctions. Importantly, $w(x)$ is the weighting function, which provides the means for satisfying the orthogonality relations for finding coefficients of each term in the series solution to the partial differential equation. Specifically, if we were to write the ODE in the form

$$P(x)\, y''(x) + Q(x)\, y'(x) + R(x)\, y(x) = f(x), \tag{6.68}$$

for functions $P(x)$, $Q(x)$, $R(x)$, and $f(x)$, then there is a multiplicative function that can be determined by

$$m(x) = \exp\Big(\int \frac{Q(x) - P'(x)}{P(x)} \mathrm{d}x\Big). \tag{6.69}$$

This multiplicative function is then multiplied to Eq. 6.68 and recast into the form shown in Eq.6.67. Thus, with $P(\tilde{x}) = 1$ and $Q(\tilde{x}) = \tilde{x}$,

$$m(\tilde{x}) = \exp\Big(\int \tilde{x}\,\mathrm{d}\tilde{x}\Big), \tag{6.70}$$

$$= \exp\Big(\frac{\tilde{x}^2}{2}\Big), \tag{6.71}$$

and the ODE takes the form

$$0 = \frac{\mathrm{d}}{\mathrm{d}\tilde{x}}\Big[e^{\frac{\tilde{x}^2}{2}}\frac{\mathrm{d}\Phi}{\mathrm{d}\tilde{x}}\Big] + \Phi\Big(1+\tilde{k}^2\Big)e^{\frac{\tilde{x}^2}{2}}, \tag{6.72}$$

or in the form of Eq. 6.67,

$$\frac{\mathrm{d}}{\mathrm{d}\tilde{x}}\Big[e^{\frac{\tilde{x}^2}{2}}\frac{\mathrm{d}\Phi}{\mathrm{d}\tilde{x}}\Big] + e^{\frac{\tilde{x}^2}{2}}\Phi = -\tilde{k}^2 e^{\frac{\tilde{x}^2}{2}}\Phi, \tag{6.73}$$

so that $p(x) = q(x) = w(x) = e^{\frac{\tilde{x}^2}{2}}$ and $\lambda = \tilde{k}^2$.

Next, we show the orthogonality conditions of the eigenfunctions. Suppose that solving Eq. 6.67 creates a series of eigenfunctions $\{y_j(x)\}$. Suppose that a given eigenfunction $y_i(x)$ has the eigenvalue λ_i so that

$$\frac{\mathrm{d}}{\mathrm{d}x}\Big[p(x)\frac{\mathrm{d}y_i}{\mathrm{d}x}\Big] + q(x)\,y_i(x) = -\lambda_i\,w(x)\,y_i(x). \tag{6.74}$$

Suppose that each eigenfunction of the system, bounded by $a \le x \le b$, obeys the boundary conditions

$$\alpha_1 y_i(a) + \alpha_2 y_i'(a) = 0, \tag{6.75}$$

$$\beta_1 y_i(b) + \beta_2 y_i'(b) = 0. \tag{6.76}$$

To test the orthogonality conditions, we multiply both sides by $y_j(x)$, a particular eigenfunction of the differential equation, and integrate over the entire system,

$$\int_a^b \frac{\mathrm{d}}{\mathrm{d}x}\Big[p(x)\frac{\mathrm{d}y_i}{\mathrm{d}x}\Big]y_j(x) + q(x)\,y_i(x)\,y_j(x)\mathrm{d}x = -\lambda_i\int_a^b w(x)\,y_i(x)\,y_j(x)\mathrm{d}x, \tag{6.77}$$

$$p(x)\frac{\mathrm{d}y_i}{\mathrm{d}x}y_j(x)\Big|_a^b - \int_a^b p(x)\frac{\mathrm{d}y_i}{\mathrm{d}x}\frac{\mathrm{d}y_j}{\mathrm{d}x}\mathrm{d}x + \int_a^b q(x)\,y_i(x)\,y_j(x)\mathrm{d}x = -\lambda_i\int_a^b w(x)\,y_i(x)\,y_j(x)\mathrm{d}x. \tag{6.78}$$

Had Eq. 6.74 involved $y_j(x)$ and we multiplied both sides of the equation by $y_i(x)$, then Eq. 6.78 would have the subscripts reversed:

$$p(x)\frac{\mathrm{d}y_j}{\mathrm{d}x}y_i(x)\Big|_a^b - \int_a^b p(x)\frac{\mathrm{d}y_i}{\mathrm{d}x}\frac{\mathrm{d}y_j}{\mathrm{d}x}\mathrm{d}x + \int_a^b q(x)\,y_i(x)\,y_j(x)\mathrm{d}x = -\lambda_j\int_a^b w(x)\,y_i(x)\,y_j(x)\mathrm{d}x. \tag{6.79}$$

Suppose we subtracted Eq. 6.79 from Eq. 6.78 and applied our boundary conditions:

$$-(\lambda_i - \lambda_j)\int_a^b w(x)\, y_i(x)\, y_j(x)\mathrm{d}x = p(x)\frac{\mathrm{d}y_i}{\mathrm{d}x}y_j(x)\Big|_a^b - p(x)\frac{\mathrm{d}y_i}{\mathrm{d}x}y_j(x)\Big|_a^b, \tag{6.80}$$

$$-(\lambda_i - \lambda_j)\int_a^b w(x)\, y_i(x)\, y_j(x)\mathrm{d}x = p(b)\Big[\frac{\mathrm{d}y_i}{\mathrm{d}x}\Big|_b y_j(b) - \frac{\mathrm{d}y_j}{\mathrm{d}x}\Big|_b y_i(b)\Big] - p(a)\Big[\frac{\mathrm{d}y_i}{\mathrm{d}x}\Big|_a y_j(a) - \frac{\mathrm{d}y_j}{\mathrm{d}x}\Big|_a y_i(a)\Big], \tag{6.81}$$

$$-(\lambda_i - \lambda_j)\int_a^b w(x)\, y_i(x)\, y_j(x)\mathrm{d}x = p(b)\Big[\frac{\beta_1}{\beta_2}y_i(b)\, y_j(b) - \frac{\beta_1}{\beta_2}y_i(b)\, y_j(b)\Big] - p(a)\Big[\frac{\alpha_1}{\alpha_2}y_i(a)\, y_j(a) - \frac{\alpha_1}{\alpha_2}y_i(a)\, y_j($$

(6.82)

$$-(\lambda_i - \lambda_j)\int_a^b w(x)\, y_i(x)\, y_j(x)\mathrm{d}x = 0. \tag{6.83}$$

If $i = j$, then the left-hand side is already zero.

$$-\lambda_i\int_a^b w(x)\Big[y_i(x)\Big]^2\mathrm{d}x = p(x)\frac{\mathrm{d}y_i}{\mathrm{d}x}y_i(x)\Big|_a^b - \int_a^b p(x)\Big[\frac{\mathrm{d}y_i}{\mathrm{d}x}\Big]^2\mathrm{d}x + \int_a^b q(x)\Big[y_i(x)\Big]^2\mathrm{d}x. \tag{6.84}$$

We will return to the case where $i = j$ to find the coefficients of eigenfunction. If $i \neq j$, then the eigenvalues are different here and the integral is zero:

$$\int_a^b w(x)\, y_i(x)\, y_j(x)\mathrm{d}x = 0, \text{for } i \neq j. \tag{6.85}$$

Eq. 6.84 serves as a convenient equation for analytically solving the coefficients for each eigenfunction.

6.11 The Recovery of a Typical FRAP-like Disc is Time-Sensitive in the Advection-Diffusion Model.

As we derive in the SI Sec. 6.9, the general solution to the PDE

$$\frac{\partial c}{\partial t} = D\nabla^2 c + \nabla\cdot\Big[\alpha\mathbf{r}c\Big], \tag{6.86}$$

assuming no angular dependence, takes the form

$$c(r,t) = c_{\mathrm{ss}}\, e^{-\frac{r^2}{2\lambda^2}} + e^{-\frac{r^2}{2\lambda^2}}\sum_{i=1}^{\infty} c_i e^{-Dk_i^2 t}\, {}_1F_1\Big(-\frac{\lambda^2 k_i^2}{2}; 1; \frac{r^2}{2\lambda^2}\Big), \tag{6.87}$$

where c_{ss} is the coefficient for the steady-state concentration term, $\lambda \equiv \sqrt{\frac{D}{\alpha}}$, k_i are the eigenvalues specific to the boundary condition, c_i are the coefficients based on initial conditions, and ${}_1F_1(a;b;z)$ is the Kummer confluent hypergeometric function

$${}_1F_1(a;b;z) = \sum_{l=0}^{\infty}\frac{(a)_l}{(b)_l}\frac{z^l}{l!}, \tag{6.88}$$

where the Pochhammer symbol $(a)_l = \frac{(a+l-1)!}{(a-1)!}$. The most well-known example of Eq. 6.88 is the case where $a = b$, which yields ${}_1F_1(a;a;z) = e^z$. The eigenvalues $\{k_i\}$ are found by satisfying the boundary conditions and are those terms that satisfy the equation

$$\left(\frac{\lambda^2 k_i^2}{2}\right){}_1F_1\left(1 - \frac{\lambda^2 k_i^2}{2}; 2; \frac{R^2}{2\lambda^2}\right) = 0. \tag{6.89}$$

Eq. 6.87 shows that the steady-state profile of the concentration is a Gaussian distribution with standard deviation λ.

We now seek to identify the coefficients of the terms, which are specific to the initial conditions. Here, we will analytically examine three cases for initial conditions: 1) uniform concentration, 2) a uniform concentration except with molecules removed in the region $r \leq R_0$ as found in many FRAP assays, and 3) a FRAP-like removal of molecules in the region $r \leq R_0$ after the system initially reaches a steady-state Gaussian concentration profile. As our goal is to validate our FEM simulations through agreement with some initial conditions that can be analytically determined, we directly compare analytical and FEM solutions.

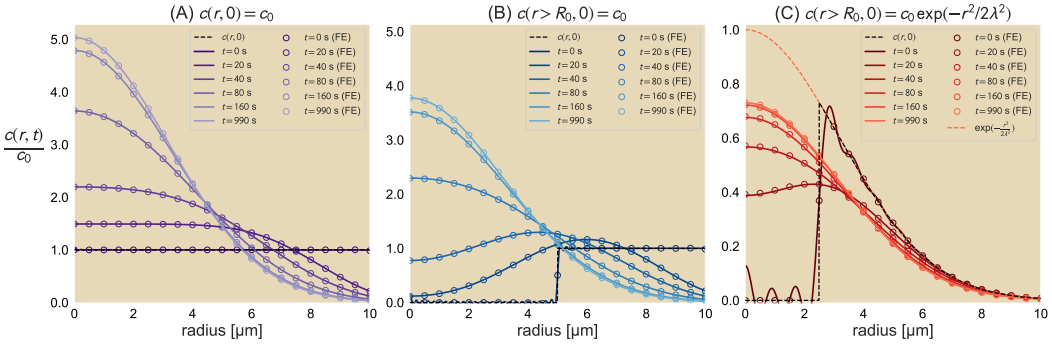

Figure 6.13: **Radial advection-diffusion for various initial conditions.** (A) Uniform concentration throughout the system. (B) Uniform concentration for $r > R_0$ and no molecules for $r \leq R_0$. (C) A Gaussian distribution for $r > R_0$ and no molecules for $r \leq R_0$. Analytical solutions are presented as solid lines while solutions obtained by finite elements are shown as hollow points. The initial condition for each situation is shown as a dashed black line. For all studies, $D = 0.1\ \frac{\mu m^2}{s}$, $R = 10\ \mu m$, and $v_m = 0.1\ \frac{\mu m}{s}$. For (B), we set $R_0 = \frac{R}{2}$ while for (C) we set $R_0 = \frac{R}{4}$. For (C), the steady-state profile prior to removing molecules for $r \leq R_0$ is shown as a dashed red line. All analytical solutions use the first 12 eigenvalues that satisfy Eq. 6.89.

Uniform concentration

We start with the case where the concentration is uniform everywhere,

$$c(r,0) = c_0. \tag{6.90}$$

The solution to the PDE with this initial condition takes the form of

$$c(r,t) = \frac{c_0}{2} e^{-\frac{r^2}{2\lambda^2}} \left\{ \frac{\frac{R^2}{\lambda^2}}{1 - e^{-\frac{R^2}{2\lambda^2}}} + \sum_{i=1}^{\infty} \frac{R^2\, e^{-D\,k_i^2 t}\, {}_1F_1\!\left(-\frac{\lambda^2 k_i^2}{2}; 2; \frac{R^2}{2\lambda^2}\right)}{\int_0^R r'\, e^{-\frac{r'^2}{2\lambda^2}} \left[{}_1F_1\!\left(-\frac{\lambda^2 k_i^2}{2}; 1; \frac{r'^2}{2\lambda^2}\right)\right]^2 \mathrm{d}r'} \times {}_1F_1\!\left(-\frac{\lambda^2 k_i^2}{2}; 1; \frac{r^2}{2\lambda^2}\right) \right\}. \tag{6.91}$$

Fig. 6.13(A) shows the concentration profile as a function of radius and for various time points given this initial condition. Here, we used $D = 0.1\ \frac{\mu m^2}{s}$, $R = 10\ \mu m$, and $v_m = 0.1\ \frac{\mu m}{s}$. Solid lines indicate different time points for the specific analytical solution given the uniform initial condition. These analytical solutions also show strong agreement with simulations performed by FEM which are denoted by hollow points. Here, we use the first 12 eigenvalues k_i for the analytical solution. Similar to the decomposition of a square wave into a sum of sinusoidal functions yielding imperfect agreement with the original function, we see here that the use of a limited number of eigenvalues that satisfy Eq. 6.89 leads to fluctuations about the original function for $t = 0$ (see SI Sec. 6.12 on Gibbs phenomenon). Nevertheless, we see that these fluctuations in the analytical condition quickly smooth out for $t > 0$. For the given parameters, the concentration at larger radii decreases quickly due to the higher advection overcoming diffusion. As shown at $t = 20$ seconds and $t = 40$ seconds, the concentration appears roughly uniform at lower concentrations but the length scale of this uniformity appears to decrease. At $t = 990$ seconds, the concentration profile reaches the Gaussian steady-state solution where the concentration gradient allows diffusion to counter the advective flow.

Uniform concentration for $r > R_0$.

We apply a similar initial condition as that used in Sec. 6.11, but remove any molecules within a distance R_0 from the origin as typically performed in FRAP experiments. This initial condition is mathematically described by

$$c(r,0) = \begin{cases} 0 & \text{if } r \le R_0, \\ c_0 & \text{if } r > R_0. \end{cases} \tag{6.92}$$

The solution for this initial condition is similar to Eq. 6.91 but with different limits of integration (see SI Sec. 6.10 on Sturm-Liouville Theory and 6.9 for application

of the theory in 2D),

$$c(r,t) = \frac{c_0}{2} e^{-\frac{r^2}{2\lambda^2}} \left\{ \frac{\frac{R^2}{\lambda^2} - \frac{R_0^2}{\lambda^2}}{1 - e^{-\frac{R^2}{2\lambda^2}}} + \sum_{i=1}^{\infty} \alpha_i e^{-D\, k_i^2 t}\, {}_1F_1\Big(-\frac{\lambda^2 k_i^2}{2}; 1; \frac{r^2}{2\lambda^2} \Big) \right\}, \tag{6.93}$$

where

$$\alpha_i = \frac{R^2\, {}_1F_1\Big(-\frac{\lambda^2 k_i^2}{2}; 2; \frac{R^2}{2\lambda^2} \Big) - R_0^2\, {}_1F_1\Big(-\frac{\lambda^2 k_i^2}{2}; 2; \frac{R_0^2}{2\lambda^2} \Big)}{\int_0^R r'\, e^{-\frac{r'^2}{2\lambda^2}} \Big[{}_1F_1\Big(-\frac{\lambda^2 k_i^2}{2}; 1; \frac{r'^2}{2\lambda^2} \Big) \Big]^2 \mathrm{d}r'}. \tag{6.94}$$

As $R_0 \to 0$ in Eq. 6.93 we recover Eq. 6.91. Fig. 6.13(B) shows traces of the concentration profile at the same times as in Fig. 6.13(A). Here, $R_0 = \frac{R}{2}$. Once again, we see that the analytical solution for $t = 0$ fluctuates about the defined initial condition but quickly smooth out and agree well with FEM results (hollow points) for $t > 0$. By removing molecules at $r \leq R_0$, a wave of molecules move toward the origin from a combination of advection toward the origin and diffusion moving molecules against the concentration gradient while the concentration at $r \to R$ recedes. Once again, we recover a Gaussian profile, but at a lower maximum than that observed in Fig. 6.13(A) due to the lower initial number of molecules.

Gaussian profile for $r > R_0$.

Finally, consider a situation where molecules in this advective-diffusive system are allowed to reach steady-state before photobleaching all molecules within a certain radius of the center $r \leq R_0$. The initial conditions would appear as

$$c(r,0) = \begin{cases} 0 & \text{if } r \leq R_0, \\ c_0\, e^{-\frac{r^2}{2\lambda^2}} & \text{if } r > R_0. \end{cases} \tag{6.95}$$

We show analytically that the concentration profile is

$$c(r,t) = c_0 e^{-\frac{r^2}{2\lambda^2}} \left\{ \frac{e^{-\frac{R_0^2}{2\lambda^2}} - e^{-\frac{R^2}{2\lambda^2}}}{1 - e^{-\frac{R^2}{2\lambda^2}}} - \frac{1}{2} \sum_{i=1}^{\infty} \beta_i e^{-Dk_i^2 t}\, {}_1F_1\Big(-\frac{\lambda^2 k_i^2}{2}; 1; \frac{r^2}{2\lambda^2} \Big) \right\}, \tag{6.96}$$

where

$$\beta_i = \frac{R_0^2\, {}_1F_1\Big(1 + \frac{\lambda^2 k_i^2}{2}; 2; -\frac{R_0^2}{2\lambda^2} \Big)}{\int_0^R r'\, e^{-\frac{r'^2}{2\lambda^2}} \Big[{}_1F_1\Big(-\frac{\lambda^2 k_i^2}{2}; 1; \frac{r'^2}{2\lambda^2} \Big) \Big]^2 \mathrm{d}r'}. \tag{6.97}$$

Once again the analytical solution agrees with simulations of the same initial condition shown in Fig. 6.13(C) for $R_0 = \frac{R}{4}$. We note here that as $R_0 \to 0$ we recover

the steady-state solution again as the time-dependent terms vanish and the ratio of exponentials in the time-independent term goes to unity. Fig. 6.13(C) shows again the imperfection of the analytical solution for $t = 0$ and the initial condition but a strong agreement with FEM results. In this situation, the concentration toward the outer edge of the system remains largely unchanged as diffusion and advection are balanced toward the boundary. However, at smaller radii of the system, there is a shift in concentration as molecules enter the $r \leq R_0$ region and for the chosen parameter values, the overall concentration profile returns to a Gaussian distribution within 3 minutes.

Across all three initial conditions, we see that the concentration builds up toward the contraction center and forms a Gaussian distribution as the steady-state profile. The different time courses in the concentration profiles for these initial conditions further reveals that in experimental systems exhibiting such an advective-diffusive behavior the use of FRAP becomes sensitive to the time when photobleaching is applied. If the concentration profile in the system has already begun to move away from a uniform distribution, such as the initial contraction of a highly connected filament network, then the molecule redistribution until steady state is achieved will show different recovery profiles from that of an experiment where photobleaching is applied at a time when the system is already close to reaching the steady-state profile. Such results provide the two extremes of "fluorescence recovery" in potential *in vitro* assays that evolve from a uniform concentration to a Gaussian-shaped distribution subject to this advection-diffusion system.

We show here three cases where analytical solutions to the linear advection-diffusion equation can be determined for direct comparison to the FEM simulations. As the square unit cell is more complex, we turn fully to FEM for our measurements and comparisons to the analyzed experimental data.

6.12 Numerically solving Advection-Diffusion Equations with COMSOL

Our use of COMSOL Multiphysics® simulations are constructed with consideration of four particular details in mind: design of the geometry; set-up of the differential equations, including boundary and initial conditions; choice of mesh size; and sweeping through parameters. Elaboration of the mesh size dependence is discussed in Sec. 6.12.

Geometry

Because we analyzed fluorescent unit cells from our experimental data until they were no longer distinguishable from neighboring unit cells, we opted to simplify the FEM numerical simulation by examining the time course of a single unit cell subject to advection and diffusion. Even though unit cells in the network may be transported toward the center of contraction, as we have shown in SI Sec 6.8, the unit cell deformation from advection is not position dependent. This is similarly the case for diffusion, where its contribution to the flux of molecules is dependent on the gradient of concentration. As indicated in Fig. 6.14, the geometry of the system in the COMSOL simulations is a square of side length 20% longer than the side length of unit cell, which we take to be 10 µm. We then place the smaller square that represents the unit cell inside of the larger square such that it shares the same center. We then take the union of these two squares before applying the split operation to distinguish the unit cell from the surrounding region.

Setting up the differential equations

Although there are multiple forms of inputting partial differential equations in COMSOL, for the advection-diffusion equation studied, that is

$$\frac{\partial u}{\partial t} = D\nabla^2 u + \alpha\nabla\cdot(\mathbf{r}u)\,, \tag{6.98}$$

we elect to use the coefficient form PDE and define our variable of interest as u with units of mol/m^3 and ensure that each term in the equation carries units of mol/(m^3·s). Although our past derivations use the variable c, we use u in the differential equation due to the occurrence of the coefficient c in the coefficient form PDE in COMSOL.

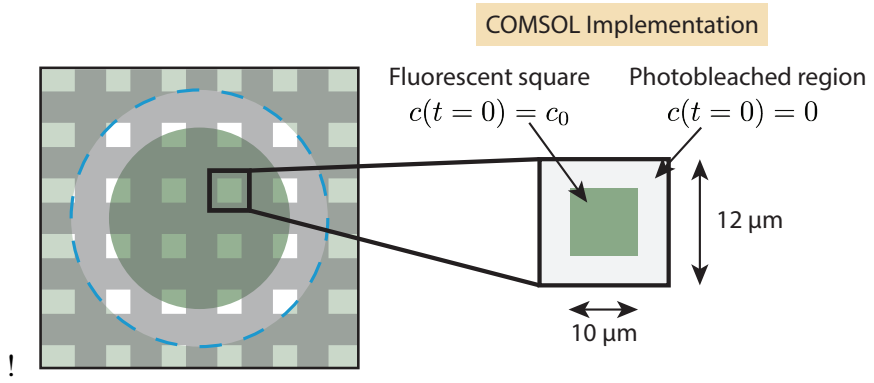

Figure 6.14: **Schematic of COMSOL set-up.** To simulate the time evolution of a single unit cell in the advection-diffusion equation, we model a single unit cell as a 10 µm x 10 µm square within a larger 12 µm x 12 µm square.

We note that the coefficient form PDE as shown in COMSOL is of the form

$$e_a \frac{\partial^2 u}{\partial t^2} + d_a \frac{\partial u}{\partial t} + \nabla \cdot (-c\nabla u - \eta u + \gamma) + \beta \cdot \nabla u + au = f, \tag{6.99}$$

where e_a, d_a, c, a, and f are scalar coefficients while η, γ, and β are vectors. We note here that in COMSOL, the term involving η is written as α, but to avoid confusion with the α used throughout our work, we change the COMSOL notation to η. Rewriting Eq. 6.98 to match the form of Eq. 6.99 gives

$$\frac{\partial u}{\partial t} + \nabla \cdot (-D\nabla u - \alpha \mathbf{r} u) = 0. \tag{6.100}$$

We can see here that to make Eq. 6.100 match Eq. 6.99, then e_a, a, all of the elements of γ, all of the elements of β, and f are all 0 while

$$d_a = 1 \text{ s}^{-1}, \tag{6.101}$$

$$c = D, \tag{6.102}$$

$$\eta = \begin{bmatrix} \alpha x \\ \alpha y \end{bmatrix}, \tag{6.103}$$

where we note that we define D to take on dimensions of length^2/time and α to have units of time^{-1} in COMSOL.

In our experiments, we are careful to ensure that there is negligible to no detectable amount of microtubules flowing from outside of the light-activated region into network. We thus impose a no-flux boundary condition by using the Zero Flux boundary condition option in COMSOL.

Applying the initial condition

We opt to make the initial condition of the unit cell of uniform concentration c_0 while the concentration in the region outside of the unit cell is initially set to 0. However, defining these two initial conditions piecewise with the geometry of the system outlined above leads to a sharp change in the gradient, which can lead to large errors and negative concentrations at high Péclet number, we instead define a rectangle function where the edges of the rectangle function are smoothed over 200 nm and have well-defined continuous derivatives to second order.

Choice of mesh size

Because we use the total particle number as a conserved quantity for computing the area of the unit cells in time, we wish to minimize the numerical error in the

FEM simulations. Of the various mesh designs, we opt to use the "Extremely fine" mesh size with the boundary between the unit cell and the surrounding system, obtained from the geometry design, to also undergo 6 iterations of refinement under the "Control Entities" tab. This boundary is heavily refined in order to minimize the occurrence and value of negative concentrations that may arise at high Péclet number. A more elaborate discussion of mesh size choice is presented in SI Sec. 6.12 on the Gibbs phenomenon.

Parameter Sweep

To perform the parameter sweep, we include the Parametric Sweep option in the Study section of the simulation and define the parameters of interest under Global Definitions → Parameters. Within the parameters, we specify the parameters D for our diffusion constant and α for our contraction rate. Under the Parametric Sweep, we can then chose D and α as our parameters to be swept. We select our range of values of α to be the different experimentally-obtained contraction rates while D ranged from 0.0001 $\mu m^2/s$ to 0.01 $\mu m^2/s$ in various increments ranging from 0.0001 $\mu m^2/s$ to 0.0005 $\mu m^2/s$. All possible combinations of D and α were permitted for the simulations.

Gibbs phenomenon in analytical solutions and mesh granularity in FEM

As we noted in the SI Sec. 6.11, upon solving the analytical solutions for three cases, there was notable discrepancy between the analytically solved concentration profile at $t = 0$ and the defined initial condition. In this section, we address the sensitivity of the analytical solutions to the number of terms in the infinite series that are kept when showing the concentration profile over time. We then discuss a similar case of sensitivities in the finite element method (FEM) which can also affect the accuracy of numerical solutions.

As shown in Fig. 6.15, the analytical solution, which is composed of the first 100 non-zero eigenvalues for the two cases involving a uniform initial concentration and the first 25 eigenvalues for the one involving the FRAPed Gaussian profile and the steady-state function, creates oscillations about the intended initial condition. This disagreement is a demonstration of the Gibbs phenomenon, as famously revealed by the imperfect decomposition of a square wave into a sum of sinusoidal functions. Fig. 6.15 demonstrates the evolution of each of the three analytical solutions examined in the main manuscript when more eigenvalues are included

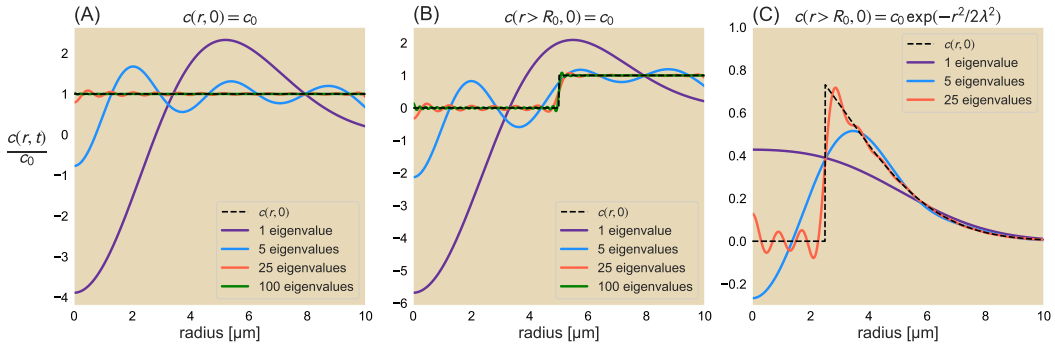

Figure 6.15: **Gibbs phenomenon for analytical solutions.** Concentration profiles of the analytical solution for the initial conditions (A) $c(r,0) = c_0$, (B) $c(r > R_0, 0) = c_0$, and (C) $c(r > R_0, 0) = c_0 \exp(-r^2/2\lambda^2)$ with the steady-state solution and the first nonzero eigenvalue solution (purple line), the first five nonzero eigenvalue solutions (blue), the first twenty-five terms (red), and for (A) and (B) the first hundred terms (green). The intended initial conditions are represented as dashed black lines.

in the solution. Specifically, for $c(r,0) = c_0$ (Fig. 6.15(A)), $c(r > R_0, 0) = c_0$ (Fig. 6.15(B)), and $c(r > R_0, 0) = c_0 \exp(-r^2/2\lambda^2)$ (Fig. 6.15(C)), all of which are represented by dashed black lines, more eigenvalues reduce the level of error between the analytical solution and the initial condition. For the two initial conditions involving a uniform concentration, the use of one eigenvalue in addition to the steady-state solution (purple line) leads to a large negative concentration at $r = 0$ but more closely recapitulate the initial conditions after using 100 non-zero eigenvalues. Deviations from the initial condition decrease dramatically by that point. This is similarly observed for the clipped Gaussian distribution: while the Gaussian tail is quantitatively captured by the the addition of only a few eigenvalues, the analytical solution begins to better recapitulate the concentration profile about $r = R_0$ with the addition of more terms in the solution. Curiously, after using more than 25 eigenvalues, the solution shows large oscillations rather than smaller ones that are smoothed out rather quickly after a small amount of time.

Just as analytical solutions are sensitive to a form of resolution to properly capture the time evolution of a variable of interest, more concretely shown through the number of eigenvalues computed and by extension the number of terms used in the infinite series, so too are there sensitivities in the FEM solution. These sensitivities must also be addressed during setup of the FEM solution to ensure that the model equation is being accurately recapitulated. In this case, a key consideration is the

choice of granularity in the mesh. As FEM involves solving the governing equation over a particular domain, having a very fine grained mesh allows for the FEM solution to more accurately reflect the true solution to the problem at the cost of computational time. On the other hand, a very coarse-grained mesh involves less computing power to solve the original equations but may coarse grain away details smaller than the element size, requiring a balance between accurately solving the original PDE(s) and computational efficiency.

Fig. 6.16 shows how the granularity of the mesh affects the FEM solutions. We compare the concentration profiles produced by FEM (solid blue lines) against the true initial condition (dashed black lines) for six different element sizes as found in the physics-controlled mesh feature in COMSOL Multiphysics: (A) extremely

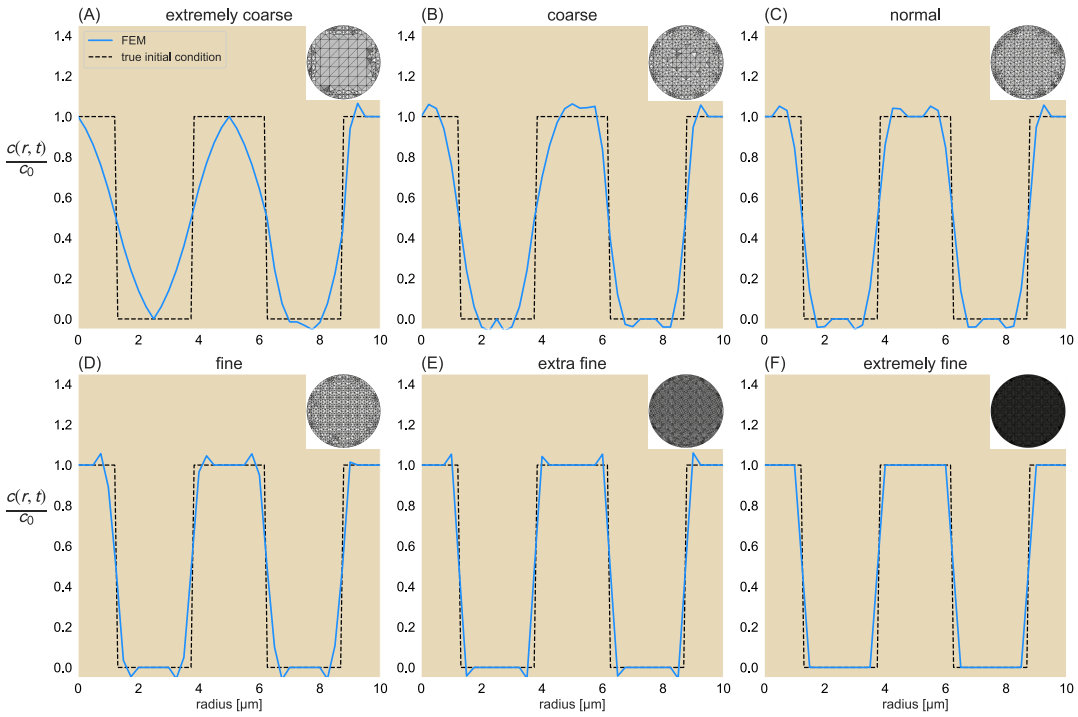

Figure 6.16: **Effects of mesh granularity on FEM solution.** Concentration profiles at $t = 0$ for six different element sizes as defined by the COMSOL Multiphysics physics-controlled mesh: (A) extremely coarse, (B) coarse, (C) normal, (D) fine, (E) extra fine, and (F) extremely fine. Finite elements output is represented by the blues lines while the true initial conditions are given as the black dashed lines. For visualization purposes, the appearance of the meshes used for the defined geometry are shown as insets in the upper righthand corner of the respective subfigures. Concentration profile is from a line trace along the horizontal axis from the origin of the geometry to the boundary.

coarse, (B) coarse, (C) normal, (D) fine, (E) extra fine, and (F) extremely fine. We see that while using the most coarse-grained feature poorly matches the desired initial condition with more of a sine wave than a square wave, successively decreasing element size (increase in mesh fineness) allows the FEM solution to more closely reflect the initial condition. Fig. 6.16(B)-(E) show that increasing the mesh fineness leaves fewer deviations from the true values, largely located near the discontinuities in the profile. The insets in the upper right of each figure shows the mesh pattern for the geometry for the study. As Fig. 6.16(F) shows, while the extremely fine mesh does not overshoot above the c_0 values or undershoot the $c(r, 0) = 0$ regions, the finite size of the elements in the mesh causes the discontinuous region to take on a value between the two regions instead. As the FEM simulation is not computationally demanding for the single unit cell case, we opt to use an Extremely Fine mesh setting.

6.13 FEM Results of Advection-Diffusion Equation on a Simulated Unit Cell Array

In the main manuscript, we measure the area of the fluorescent squares over time and compare the results to numerical simulations of an advection-diffusion equation through the FEM simulations as described in SI Sec 6.12 in order to compute effective diffusion constants. While alternative approaches to obtaining the effective diffusion constant exist, we offer this as a direct comparison to numerical experiments. For a qualitative comparison to the experimentally-observed change in the photobleached microtubule network, we present in this section the time evolution of the concentration distribution for an array of unit cells subject to linear advective and diffusive effects. For these simulations, we follow a similar procedure as outlined in SI Sec. 6.12 but on a circle of radius 60 μm and squares of side length 15 μm with a periodicity of 30 μm. Fig. 6.17 shows different time points of the concentration profile subject to the same rate of advection ($0.002\ \text{sec}^{-1}$) but different diffusion constants, namely, those measured for the median (Fig. 6.17(A)) and 3rd quartile area trajectories (Fig. 6.17(B)), an order of magnitude greater diffusion constants (Fig. 6.17(C)-(D)), and roughly the diffusion coefficient of a free microtubule (Fig. 6.17(E)). From examining the different concentration profiles in Fig. 6.17 in comparison to the experimental results shown in Fig. 2 of the manuscript, we see that once again, introducing diffusion to the system is a necessary component to recapitulate the experimentally obtained results. We further see that by eye the simulated data and experiments look most similar when simulating with an effective

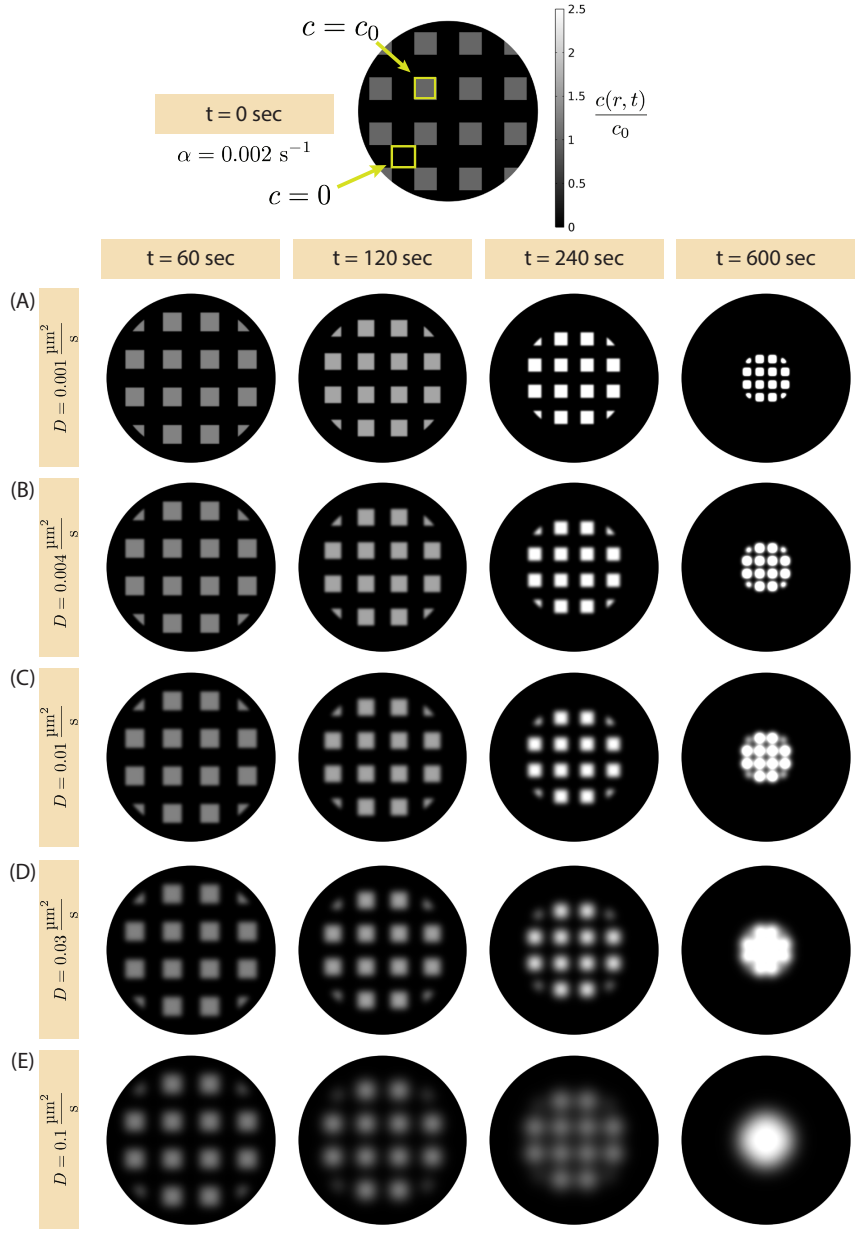

Figure 6.17: **Concentration profiles of an array of unit cells at various time points and diffusion constants.** The FEM simulation is the same as that described in SI Sec 6.12 but where each square (denoted by initial concentration c_0 as drawn with the top yellow box in the $t = 0$ sec schematic) has a side length of 15 µm and a center-to-center distance of 30 µm, with a concentration of 0 in between. In all cases, we use the same advection rate of 0.002 sec^{-1} and different diffusion coefficients: (A) 0.001 $\frac{\mu m^2}{sec}$, (B) 0.004 $\frac{\mu m^2}{sec}$, (C) 0.01 $\frac{\mu m^2}{sec}$, (D) 0.03 $\frac{\mu m^2}{sec}$, and (E) 0.1 $\frac{\mu m^2}{sec}$.

diffusion constant of 0.1 $\frac{\mu m^2}{sec}$. However, we note that as discussed in the results section "The effective diffusion constant is roughly two orders of magnitude lower

than free diffusion of a microtubule" in the manuscript and as revealed through Fig. 3, we see that when we careful quantify the area trajectories using the same metric for experiments, the diffusion constants above about 6.0×10^{-3} $\frac{\mu m^2}{sec}$ would lead to increasing area trajectories instead.

6.14 Motor Constructs

Motor Construct	Sequence Layout
micro variant	pBiex-1:FLAG-GG-mVenus-$(GSG)_2$-micro-$(GSG)_4$-Ncd281
iLid variant	pBiex-1:FLAG-GG-mVenus-$(GSG)_2$-iLid-$(GSG)_4$-Ncd281

Table 6.1: Ncd281 construct design. All constructs are designed in the pBiex-1 vector and produced by Twist Biosciences.

Motor Species	Speed (pH 6.8)	Speed (pH 6.1)	Processivity
Ncd281	53 ± 9 nm/s	55 ± 1.1 nm/s	Nonprocessive [12]
Ncd236	130 ± 30 nm/s	120 ± 10 nm/s	Nonprocessive [13, 14]
bacterial-expressed K401	220 ± 40 nm/s	250 ± 70 nm/s	unmeasured
insect-expressed K401	650 ± 70 nm/s	630 ± 100 nm/s	≈ 100 steps [13]

Table 6.2: Motor variant parameters.

While several of the motors used here in the analysis are obtained from previous work, including K401 expressed in bacteria [1], K401 expressed in insects and Ncd236 expressed in insects [13], we also designed constructs for the study of Ncd281 [12]. Specifically, the sequences are inserted into pBiex-1 vectors and includes a FLAG tag for protein purification, mVenus for motor fluorescence visualization, either a micro or iLid domain as described in [15] and Ncd281 as described in [12]. Between these different domains are multiple repeats of a 'GSG' amino acid sequence which offers flexible links between the regions. Table 6.1 illustrates these sequences. Constructs were produced by Twist Biosciences.

In addition, Table 6.2 shows the different motors presented in the manuscript, including their processivities and maximum speeds at two pHs: pH 6.8 used in previous studies [1, 13] and pH 6.1 used for many conditions here. Changes to pH have been previously shown to affect motor speeds for kinesin-1 [16, 17]. Briefly, gliding assays are performed using the motors and the same reaction mix performed at pH 6.8 as in the previous works [1, 13] and at pH 6.1 as performed in the experiments presented here. Microtubules are tracked over time using the same algorithm used for the microtubule length measurements performed in SI Sec 6.2 with the added feature of identifying nearest centroids in subsequent frames while

weighting according to microtubule length and the orientation of the filaments. Here, we find that in some instances, the motor speed at pH 6.1 is on average slower than that at pH 6.8 while in the case of bacterial-expressed K401, the higher pH is on average slower. In all cases, the speeds still fall within a standard deviation of the pH 6.8 case. Citations of their processivities are added as necessary. We note that we omit citing a processivity for the bacterial-expressed K401 as it is not known for certain whether it has the same processivity as the Sf9-expressed K401 and thus is an open question as to whether a low processivity of bacterial-expressed K401 causes a more fluctuating trend in the effective diffusion constant for the ATP titration data.

6.15 Variability in Péclet Number

In the main manuscript, we argue that a Péclet number Pe emerges regardless of the effective motor speed, tuned through ATP concentration or motor species. There, we presented this using the effective diffusion constants fitted from simuations onto the median area trajectories for these conditions. To get an idea for how sensitive Pe is to the variability found within conditions, e.g. the spread in area trajectory distribution, we compute Pe for the first and third quartiles. Fig. 6.18 shows best linear fits for each of quartiles examined where the slopes denote the respective values of Pe. Here, we find that in addition to the median Péclet number $\mathrm{Pe}_{\mathrm{med}} = 2.6 \pm 0.2$ as noted in the main manuscript, $\mathrm{Pe}_{25} = 4.5 \pm 0.5$ and $\mathrm{Pe}_{75} = 2.4 \pm 0.1$. Here, we see that despite the variability in the effective diffusion constant, Pe is less than a factor of 2 different between the quartiles, suggesting low variability in this dimensionless number.

6.16 An Expanded Investigation of the Advection-Diffusion Equation

As we showed at the end of the Results section, there is a thought-provoking reinterpretation of the advection-diffusion equation (Eq 5 in the main manuscript) that hypothesizes that the diffusion constant D is proportional to the contraction rate α. We called this proportionality constant β to be interpreted as the coupling between motor action and effective diffusion, permitting us to rewrite the advection-diffusion equation in the form

$$\frac{\partial c}{\partial t} = \alpha \nabla \cdot (\mathbf{r} c + \beta \nabla c) \,. \tag{6.104}$$

In the main manuscript, we argued that a consequence of Eq 6.104 (Eq 11 in the manuscript) is that the contraction rate, which is tied to the motor speed, is involved in both the global contraction of the network and the local diffusive-effect through

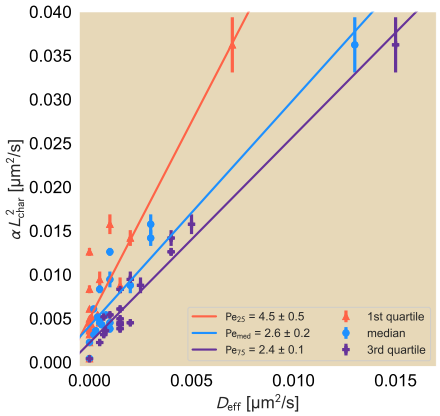

Figure 6.18: **Fits of Péclet number for the first quartile (red), median (blue), and third quartile (purple).** We remind the reader that the blue datasets are identical to what is presented in Fig. 6 of the main manuscript.

a coupling strength factor β. We now further explore the consequences of such a finding on our dataset writ large.

Data collapse of the area trajectories

An intriguing question regarding Eq. 6.104 is whether there is a way of relating all of the different area trajectories for the different biochemical conditions examined. Indeed, if we divided alpha from both sides of the equation and redefine a dimensionless time $t' = \alpha t$, we see that Eq. 6.104 becomes

$$\frac{\partial c}{\partial t'} = \nabla \cdot (\mathbf{r}c + \beta \nabla c) \,. \tag{6.105}$$

Eq. 6.105 tells us that if we were to multiply time for the different conditions, whether in the FEM simulations or the experiments, by their corresponding contraction rates α, we should see that only one quantity matters to generate the family of normalized area curves: the coupling strength factor β. Fig. 6.19 shows all of the simulated area trajectories by FEM and all of the median normalized areas from the different experimental conditions where their times are non-dimensionalized with their corresponding contraction rates. Furthermore, each of the lines are color coded to represent a different coupling strength factor β, computed by dividing the diffusion constant parameter of each curve by the corresponding contraction rate used in a given simulation. The darker the shade of blue, the higher the strength factor β. Here, we see that as expected, increasing the value of β corresponds to a normalized area trajectory deviating farther from the pure contraction bound. Furthermore, we see that by non-dimensionalizing time for all of the normalized

area trajectories, we get the different datasets to roughly result in a data collapse with one value of β. This further reinforces the idea of a close coupling between the contraction rate and the local active diffusion in the network, which we thus far quantify as this coupling term β.

Relating motor speed to contraction rate and strength factor

Next, we turn to the seeming relation between the contraction rate and motor speed. In particular, we see an enticing linear relationship between the two quantities for the different motor species in Fig 4 of the main manuscript. If we were to fit a line through the median contraction rate against measured motor speeds as reported in SI Sec 6.14, we obtain a line of slope 0.026 μm^{-1}, as shown in Fig. 6.20. We note that the y-intercept of this fit is close to 0 at -6.0×10^{-4} s^{-1}.

In addition, the ATP titration data for Ncd236 and bacterial-expressed K401 suggest that we can back-calculate the effective speeds of these motors. Specifically, we can compute the effective motor speeds from using the Michaelis-Menten equation for

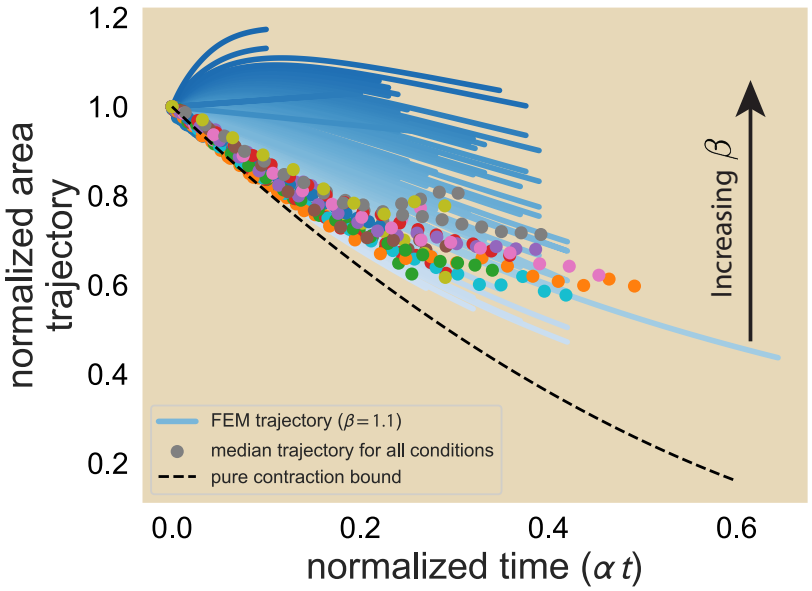

Figure 6.19: **Data collapse of the different normalized area trajectories from FEM simulations and experiments as a function of the nondimensionalized time $t' = \alpha t$.** Solid blue lines correspond with a different FEM simulation where the darker the blue the higher the value for β. Different colored points correspond to the median normalized area of each experimental condition reported in the manuscript. The dashed black line corresponds with a generic pure contraction bound $(1 - t')^2$.

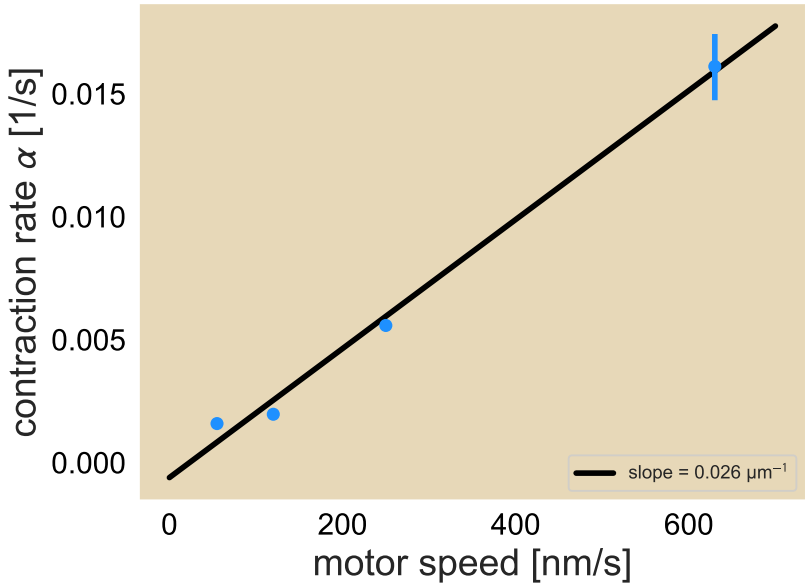

Figure 6.20: **Linear fit of contraction rate against the motor speeds as presented in Fig. 4 of the main manuscript.** Here we use the mean motor speed and the median contraction rate for each motor species. The slope of the line corresponds to 0.026 μm^{-1} and a y-intercept of -6.0×10^{-4} s^{-1}. We remind the reader that some error bars corresponding to the 95% credible region are smaller than the size of the points.

the measured Michaelis constant K_{ATP} at each ATP concentration c, or

$$v_{\text{effective}} = v_{\text{max}} \frac{\frac{c}{K_{\text{ATP}}}}{1 + \frac{c}{K_{\text{ATP}}}}. \tag{6.106}$$

As we are simply exploring the data, here we use the best fit Michaelis constants for the two motors, $K_{\text{ATP}} = 30$ μM for Ncd236 and $K_{\text{ATP}} = 47$ μM for bacterial-expressed K401. We plug these in using the motor speeds measured from the gliding assays in SI Sec 6.14 and plot their contraction rates with motor speeds. Fig. 6.21 shows the relation between contraction rate and motor speed. Here, we see that the linear relation between the two quantities appears further reinforced as strongly linear between the two plots, making a strong case for a linear relation between the global contraction rate of the network and motor speed.

We close this discussion with an examination of the relation between the motor speed and the diffusive coupling strength β. Fig. 6.22 shows such a relation between the two quantities. Here, we see that though there is some variation in the strength factor, a large proportion of the data seems to fall between a strength factor

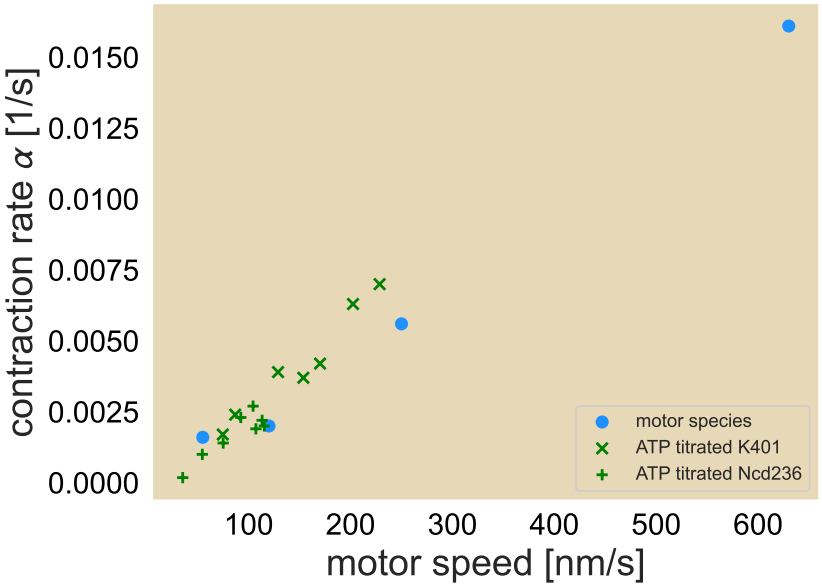

Figure 6.21: **Contraction rate against motor speeds across all conditions.** The Michaelis-Menten equation is used with the best fit Michaelis constants K_M as reported in Fig. 5 to compute the effective motor speeds at different ATP concentrations for bacterial-expressed K401 (green 'x') and Ncd236 (green '+' sign).

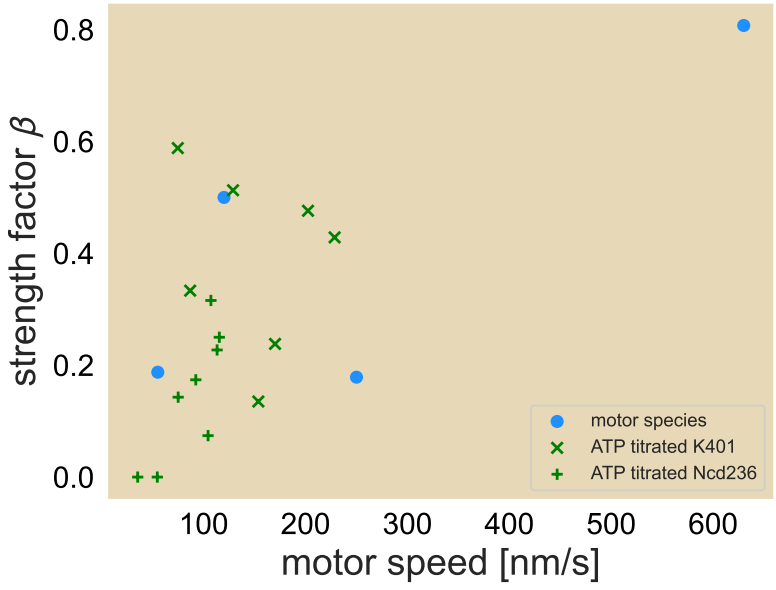

Figure 6.22: **Coupling strength as a function of motor speeds across all conditions.** Effective motor speeds for bacterial- expressed K401 (green 'x') and Ncd236 (green '+' sign) are computed using the same Michaelis-Menten conversion above.

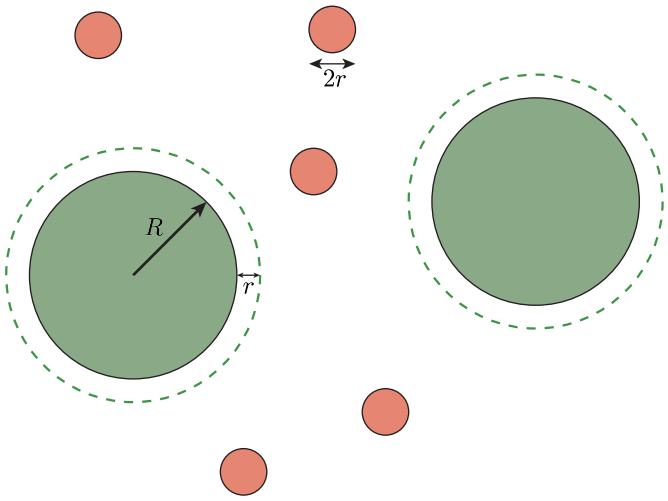

Figure 6.23: **Schematic of crowding action on two larger objects.** The crowders (red) have radius r while the two larger objects (green) have radius $R \gg r$. An additional zone around the large molecules as denoted with a dashed outline extends r away from the edge of each molecule and denotes the region within which the centers of the crowders cannot enter.

of 0.2 and 0.6. We note to the reader that for context, the different area trajectories in Fig. 3 of the main manuscript correspond to β ranging from 0.25 for $D = 5{\times}10^{-4}\ \frac{\mu m^2}{s}$ to 3 at $D = 6{\times}10^{-3}\ \frac{\mu m^2}{s}$. As a result, we can argue that this is a rather narrow range of strength factors. This observation, meant as impetus for further thought as we grapple with understanding the underlying mechanism, leaves open the question of what biochemical or motor properties might influence β and thus this diffusive-like effect.

6.17 Computing Depletion Forces

One of the most useful effects of crowding agents is their ability to induce entropic forces upon larger objects when these crowded objects are within the size of the crowding agent from each other. This may be relevant in *in vitro* active systems where the use of crowding agents help to bundle microtubules and promote self-organization. In the case of the work presented here, pluronic ($\backsim$ 12.5 kDa) acts as a crowding agent for microtubules (α and β tubulin have sizes of 50 kDa each and a one-micron long microtubule consists of $\backsim\ 1.6 \times 10^3$ tubulin). Here, to get a sense of the size of these forces, we estimate the entropic forces induced by crowders such as pluronic onto rigid polymers such as microtubules. To start, we compute the free energy change of the space that crowding agents can occupy when there are

two larger particles of radius R. We will start by solving in two dimensions where we account only for the cross-sectional area of the microtubules. We will further assume the system does not contain a high density of crowders, so we will say that there are N crowders that can be distributed across $\Omega \gg N$ lattice sites of size a. Finally, each crowder will have radius r. In the absence of the microtubules, the free energy of the crowders in a system of size A_{sys} is

$$G_{\text{open}} = -Nk_BT \ln\left(\frac{A_{\text{sys}}}{a}\right), \tag{6.107}$$

where k_BT is the thermal energy. Later on we will attempt a derivation where the number of crowders is dense enough where we need to account for their finite size. With the addition of two microtubules, the free energy G_{crowd} becomes

$$G_{\text{crowd}} = -Nk_BT \ln\left(\frac{A_{\text{sys}} - A_{\text{exc}}}{a}\right), \tag{6.108}$$

where A_{exc} is the excluded area unavailable to the crowders. This can be represented as the cross-sectional areas of the microtubules with an additional radial buffer zone of length r and depends upon the distance the two cross-sectional areas are from each other. For now, we can compute the free energy change as

$$\Delta G \equiv G_{\text{crowd}} - G_{\text{open}} = -Nk_BT \ln\left(\frac{A_{\text{sys}} - A_{\text{exc}}}{A_{\text{sys}}}\right), \tag{6.109}$$

$$\approx Nk_BT \frac{A_{\text{exc}}}{A_{\text{sys}}}, \tag{6.110}$$

where we assumed that $A_{\text{sys}} \gg A_{\text{exc}}$.

As noted, the distance between the two microtubules has an effect on the exclusion area. If the microtubules are spaced such that a crowder can fit between them, then A_{exc} is at its maximum, where

$$A_{\text{exc}} = 2 \times \pi(R + r)^2. \tag{6.111}$$

However, if the microtubules are spaced less than a crowder apart, then there is an overlap region that is double-counted A_{overlap} (Fig. 6.24(A)). We can compute the area of overlap by recognizing that half of the overlap is the difference between the area swept out by the portion of the circle whose arclength is marked by the intersections of the two overlapping circles and the area of the triangle whose vertices contain these two intersection points and the center of the circle as noted in Fig. 6.24(B). We will label the common angle between them as 2θ.

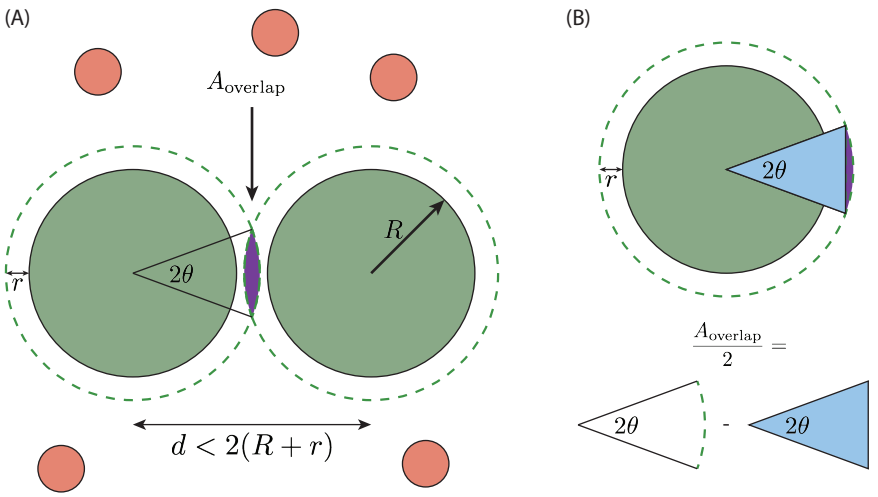

Figure 6.24: **Schematic of the overlap of two molecules.** (A) When the large molecules are separated by a distance $d < 2(R + r)$, the exclusion area contains an overlap region that is double-counted in the accounting if the areas of the two molecules and their extended zones are added. (B) The overlap area can be computed by subtracting by computing the difference between the slice of the circle whose arclength begins and ends with the two intersection points of the overlapping circles (as swept out by the angle 2θ) and the triangle whose vertices are the center of the circle and the two points where the overlapping circles intersect.

We can compute the area swept out by the circular slice as

$$A_{\text{slice}} = \int_0^{2\theta} \mathrm{d}\theta' \int_0^{R+r} r' dr', \tag{6.112}$$

$$= \theta(R + r)^2, \tag{6.113}$$

We note that the angle θ can be obtained with some trigonometry

$$\cos\theta = \frac{d/2}{R + r}, \tag{6.114}$$

$$= \frac{d}{2(R + r)}, \tag{6.115}$$

so the area of the slice as a function of the distance d is

$$A_{\text{slice}} = (R + r)^2 \cos^{-1}\left(\frac{d}{2(R + r)}\right) \tag{6.116}$$

while the area of the triangle is

$$A_{\text{triangle}} = \frac{d}{2} \times \sqrt{(R + r)^2 - \left(\frac{d}{2}\right)^2}. \tag{6.117}$$

Then the overlap region is

$$A_{\text{overlap}} = 2 \times \left(A_{\text{slice}} - A_{\text{triangle}}\right), \tag{6.118}$$

$$= 2(R+r)^2 \cos^{-1}\left(\frac{d}{2(R+r)}\right) - d \times \sqrt{(R+r)^2 - \left(\frac{d}{2}\right)^2}. \tag{6.119}$$

Suppose we made a change of variables to $d = 2(R+r) - \epsilon$ where $0 < \epsilon < 2r$. Then we can modify A_{overlap} to be

$$A_{\text{overlap}} = 2(R+r)^2 \cos^{-1}\left(\frac{2(R+r)-\epsilon}{2(R+r)}\right) - [2(R+r)-\epsilon] \times \sqrt{(R+r)^2 - \left(\frac{2(R+r)-\epsilon}{2}\right)^2}, \tag{6.120}$$

$$= 2(R+r)^2 \cos^{-1}\left(1 - \frac{\epsilon}{2(R+r)}\right) - [2(R+r)-\epsilon] \times (R+r)\sqrt{1 - \left(\frac{2(R+r)-\epsilon}{2(R+r)}\right)^2}, \tag{6.121}$$

$$\approx 2\,(R+r)^2 \sqrt{\frac{\epsilon}{(R+r)}} - [2(R+r)-\epsilon] \times (R+r)\sqrt{1 - \left(1 - \frac{\epsilon}{2(R+r)}\right)^2}, \tag{6.122}$$

$$\approx 2\,(R+r)^2 \sqrt{\frac{\epsilon}{(R+r)}} - 2\,(R+r)^2 \left(1 - \frac{\epsilon}{2(R+r)}\right)\sqrt{\frac{\epsilon}{(R+r)} - \left[\frac{\epsilon}{2(R+r)}\right]^2} \tag{6.123}$$

$$= 2\,(R+r)^2 \sqrt{\frac{\epsilon}{(R+r)}} \left\{1 - \left(1 - \frac{\epsilon}{2(R+r)}\right)\sqrt{1 - \left[\frac{\epsilon}{4(R+r)}\right]}\right\}, \tag{6.124}$$

$$\approx 2\,(R+r)^2 \sqrt{\frac{\epsilon}{(R+r)}} \left[1 - \left(1 - \frac{\epsilon}{2(R+r)}\right)\left(1 - \frac{\epsilon}{8(R+r)}\right)\right], \tag{6.125}$$

$$\approx 2\,(R+r)^2 \sqrt{\frac{\epsilon}{(R+r)}} \left[\frac{5\epsilon}{8(R+r)}\right], \tag{6.126}$$

$$= \frac{5\,(R+r)^2}{4}\left[\frac{\epsilon}{(R+r)}\right]^{3/2} \tag{6.127}$$

where we note that $\epsilon \ll (R+r)$ and expand to enough orders to maintain a dependence on ϵ. We also note that for small x, $\cos^{-1}(1-x) \approx \sqrt{2x}$. As a result,

the free energy is

$$\Delta G \approx N k_B T \frac{A_{\text{exc}}}{A_{\text{sys}}}, \tag{6.128}$$

$$= N k_B T \frac{2\pi(R+r)^2 - A_{\text{overlap}}}{A_{\text{sys}}}, \tag{6.129}$$

$$= \frac{N}{A_{\text{sys}}} k_B T \left\{ 2\pi(R+r)^2 - \frac{5\,(R+r)^2}{4} \left[\frac{\epsilon}{(R+r)} \right]^{3/2} \right\}, \tag{6.130}$$

$$= c k_B T \left\{ 2\pi(R+r)^2 - \frac{5\,(R+r)^2}{4} \left[\frac{\epsilon}{(R+r)} \right]^{3/2} \right\}, \tag{6.131}$$

where we define the crowder concentration $c = \frac{N}{A_{\text{sys}}}$. As expected, we can see that the free energy goes down as the spacing between the microtubules goes down, suggesting an energetic preference for keeping the microtubules close together.

We can compute the entropic force as the negative derivative of the free energy with respect to the distance d. We can then impose the change of variables to see that

$$F_{\text{depletion}} = -\frac{\partial \Delta G}{\partial d} = -\frac{\partial \Delta G}{\partial (2(R+r) - \epsilon)}, \tag{6.132}$$

$$= \frac{\partial \Delta G}{\partial \epsilon}, \tag{6.133}$$

$$= \frac{15}{8} c k_B T \left[(R+r)\epsilon \right]^{1/2}. \tag{6.134}$$

We can then imagine that if we operated in three dimensions, then in the case where two microtubules of length L that are aligned would have a depletion force that goes as

$$F = \frac{15}{8} c k_B T L \left[(R+r)\epsilon \right]^{1/2}. \tag{6.135}$$

Fig. 6.25 shows the relation between the depletion force and the overlap length ϵ. Here, we normalize both sides according to the axes labels. As expected, the depletion force increases as the two microtubules become closer to each other.

If we estimate that a 1 µm-long microtubule has an outer radius of $\backsim$ 10 nm and pluronic, with a mass of 12.5 kDa and a final concentration of 0.5 mg/mL in the experiments (making it 40 µM), has a radius of $\backsim$ 1 nm, then the depletion force

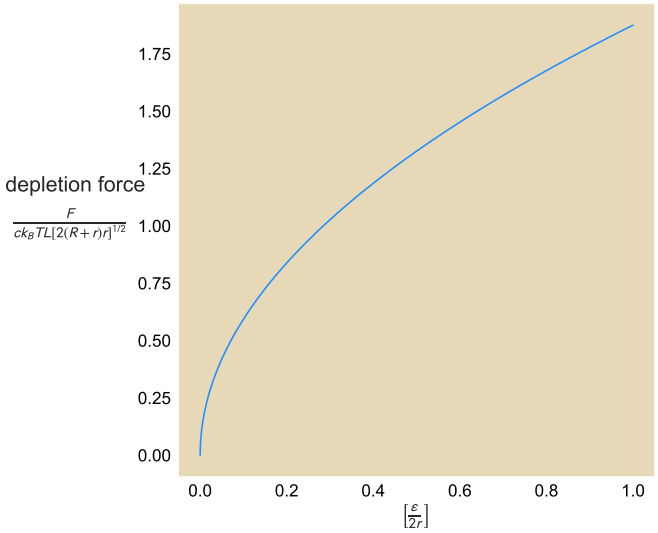

Figure 6.25: **Depletion force as a function of overlap distance ϵ.**

due to pluronic is

$$F_{\text{depletion}}^{\text{pluronic}} \backsim \frac{15}{8} \times \frac{40 \times 10^3}{\mu\text{m}^3} \times (4\,\text{pN} \cdot \text{nm}) \times (10\,\text{nm} \times 1\,\text{nm})^{1/2} \times 1\mu\text{m}, \quad (6.136)$$

$$\backsim \frac{40 \times 10^4}{\mu\text{m}^2} \times 4\,\text{pN} \cdot \text{nm}^2, \quad (6.137)$$

$$\backsim 1\,\text{pN}. \quad (6.138)$$

Thus, we can see that microtubules under the standard conditions are subjected to roughly pico-Newton forces, within the range of forces expected to be exerted by motors. We note, however, that the size of pluronic is even larger, most likely underestimating the computed entropic force.

6.18 Microtubule Bundling can Affect Both Contraction Speed and Filament Redistribution

Depletion agents such as pluronic or polyethylene glycol (PEG) play central roles in pushing active systems into contractile or extensile regimes [18, 19]. These polymers help to induce entropic forces between filaments to form bundles, which can help allow active or passive crosslinkers to induce filament coupling over larger length scales. The motor-microtubule system examined thus far includes 0.5 mg/mL pluronic, a concentration that can induce picoNewton-scale forces between microtubules (see SI Sec S7). Here, we ask what happens to the contraction and bulk filament redistribution when these entropic forces are tuned to an alteration to the concentration of pluronic. We thus implement our photobleaching scheme and

track the movement and areas of the fluorescent unit cells when the system is altered over a range of pluronic concentrations, from a complete removal of the depletion agent to a 10-fold increase in concentration, while keeping all else fixed, including motor and microtubule concentrations. Fig. 6.26 shows the contraction rate and effective diffusion constant for the bacterial-expressed K401 across a range of pluronic concentrations, including its complete absence. We find that increasing the pluronic concentration leads to a general increase in the contraction rate until 1.5 mg/mL, after which contraction does not appear to occur any faster. In the absence of pluronic, the network contracts more slowly, with a rate roughly 2/3 the rate of the 1.5 mg/mL pluronic concentration. We note the dramatic decrease at the standard experimental conditions using 0.5 mg/mL pluronic, which lies below even the complete absence of pluronic. We hypothesize that this inconsistency comes from the storage of pluronic in the standard set of experiments being different than the storage conditions used for the pluronic when performing the titration series. Briefly, under standard conditions, the pluronic is stored in the base reaction buffer used in the experimental assay involving K-PIPES, $MgCl_2$, EGTA, and KOH. It is possible that under long-term storage in this media, the pluronic behaves differently and as a result exhibits a different effect for the standard reaction.

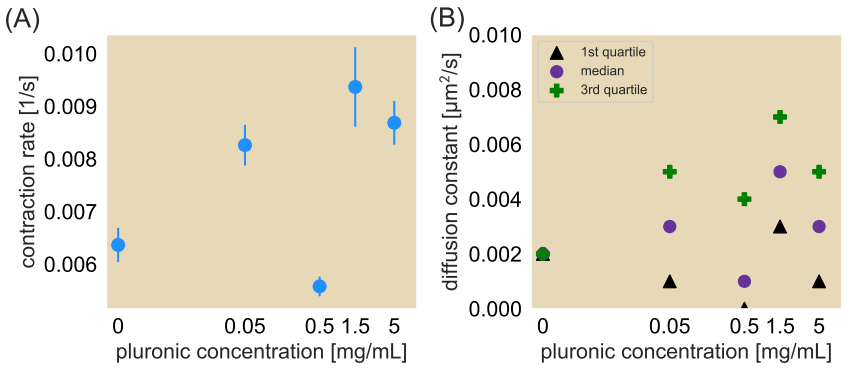

Figure 6.26: **The effect of pluronic on the network contraction rate and effective diffusion constant.** (A) Contraction rate and (B) diffusion constant as a function of pluronic concentration as presented here use bacteria-expressed K401 motors. The effective diffusion constants shown here are obtained from best fits to the 1st quartile (triangle), median (circle), and 3rd quartile (plus symbol) of the normalized area trajectories. We note the outlier at 0.5 mg/mL in panel (A) likely corresponds with different storage conditions of the pluronic than from the rest of the other pluronic concentrations used in this study, which may have had a biochemical impact in the assay.

When we computed the effective diffusion constants for the different quartiles as shown in Fig. 6.26(B), we found with the increase in pluronic a general increase in effective diffusion constant for the 3rd quartile and median data, but a roughly constant effective diffusion constant for the 1st quartile data. Interestingly, we note that the general increase and decrease of the effective diffusion constants also appears to follow the contraction rate at the corresponding pluronic concentration, suggesting a close relation between the two.

While crowding is commonly implemented in inducing organization in *in vitro* active matter systems and has become a focus of attention as a tunable parameter [20, 21], only recently has crowding been systematically studied to understand its effects on bulk reorganization of a cytoskeletal network [22]. Nevertheless, to our knowledge, we show some of the first experimental studies systematically tuning the effects of crowding on bulk reorganization and observe that entropic forces have more of a binary effect on the contraction rate: in the absence of pluronic, the network contracts more slowly and by adding even 0.1 mg/mL of crowding agent the network contracts more quickly without much more increase in contraction dynamics at higher concentrations. This suggests that entropic forces on the order of pico-Newton scales are sufficient to aid in the formation of a contracted filament network. This is roughly in the same order of magnitude as stall forces for motors, further supporting the role of crowding as generating similar effects to passive crosslinkers.

References

[1] Tyler D. Ross et al. “Controlling organization and forces in active matter through optically defined boundaries.” In: *Nature* 572 (2019), pp. 224–229.

[2] Nefeli Georgoulia. *Tubulin polymerization with GTP/GMPCPP/Taxol*. 2012. URL: https://mitchison.hms.harvard.edu/files/mitchisonlab/files/tubulin_polymerization_with_gtp.pdf.

[3] Stephen J. DeCamp. *Dogic lab - acrylamide coating protocol.* 2016. URL: https://www.stephenjdecamp.com/uploads/6/4/9/1/64916107/dogic_lab_acrylamide_coating_protocol.pdf.

[4] Shichen Liu et al. “Force propagation in active cytoskeletal networks.” In: *arXiv preprint arXiv:2401.04217* (2024).

[5] Wayne Niblack. *An introduction to digital image processing*. Prentice-Hall International, 1986.

[6] Jui-Cheng Yen, Fu-Juay Chang, and Shyang Chang. “A new criterion for automatic multilevel thresholding.” In: *IEEE Transactions on Image Processing* 4.3 (1995), pp. 370–378.

[7] Nobuyuki Otsu. “A threshold selection method from gray-level histograms.” In: *IEEE Transactions on Systems, Man, and Cybernetics: Systems* 9.1 (1979).

[8] Chun Hung Li and C. K. Lee. “Minimum cross entropy thresholding.” In: *Pattern recognition* 26.4 (1993), pp. 617–625.

[9] Chris A. Glasbey. “An analysis of histogram-based thresholding algorithms.” In: *CVGIP: Graphical models and image processing* 55.6 (1993), pp. 532–537.

[10] Gregory W. Zack, William E. Rogers, and Samuel A. Latt. “Automatic measurement of sister chromatid exchange frequency..” In: *Journal of Histochemistry & Cytochemistry* 25.7 (1977), pp. 741–753.

[11] Bob Carpenter et al. “Stan: A probabilistic programming language.” In: *Journal of Statistical Software* 76 (2017), pp. 1–32.

[12] Nicholas F. Endres et al. “A lever-arm rotation drives motility of the minus-end-directed kinesin Ncd.” In: *Nature* 439.7078 (2006), pp. 875–8.

[13] Rachel A. Banks et al. “Motor processivity and speed determine structure and dynamics of motor-microtubule assemblies.” In: *eLife* 12 (2023), e79402.

[14] Christian Hentrich and Thomas Surrey. “Microtubule organization by the antagonistic mitotic motors kinesin-5 and kinesin-14.” In: *Journal of Cell Biology* 189.3 (2010), pp. 465–480.

[15] Gurkan Guntas et al. “Engineering an improved light-induced dimer (iLID) for controlling the localization and activity of signaling proteins.” In: *Proceedings of the National Academy of Sciences of the United States of America* 112.1 (2015), pp. 112–117.

[16] Babu J. N. Reddy et al. “Heterogeneity in kinesin function.” In: *Traffic* 18.10 (2017), pp. 658–671.

[17] Fawaz Baig et al. “Dissecting the pH sensitivity of kinesin-driven transport.” In: *The Journal of Physical Chemistry B* 128.48 (2024), pp. 11855–11864.

[18] Tim Sanchez et al. “Spontaneous motion in hierarchically assembled active matter.” In: *Nature* 491 (7424 2012), pp. 431–434.

[19] Bibi Najma et al. “Competing instabilities reveal how to rationally design and control active crosslinked gels.” In: *Nature Communications* 13.6465 (2022), pp. 1–10.

[20] Vahid Nasirimarekani et al. “Tuning the properties of active microtubule networks by depletion forces.” In: *Langmuir* 37.26 (2021), pp. 7919–7927.

[21] Bibi Najma et al. “Microscopic interactions control a structural transition in active mixtures of microtubules and molecular motors.” In: *Proceedings of the National Academy of Sciences of the United States of America* 121.2 (2024), e2300174121.

[22] Wei-Xiang Chew et al. “Effects of microtubule length and crowding on active microtubule network organization.” In: *iScience* 26.2 (2023), p. 106063.